

AD A056343

AFATL-TR-77-129

(2)

LEVEL II

# Missile Aerodynamic Parameter and Structure Identification from Flight Test Data

THE ANALYTIC SCIENCES CORPORATION  
SIX JACOB WAY  
READING, MASSACHUSETTS 01867

DDC  
RECEIVED  
JUL 18 1978  
FCB

NOVEMBER 1977

FINAL REPORT FOR PERIOD FEBRUARY 1977-OCTOBER 1977

Approved for public release; distribution unlimited



**Air Force Armament Laboratory**

AIR FORCE SYSTEMS COMMAND • UNITED STATES AIR FORCE • EGLIN AIR FORCE BASE, FLORIDA

78 07 06 032

FILE COPY

UNCLASSIFIED

SECURITY CLASSIFICATION OF THIS PAGE (When Data Entered)

REPORT DOCUMENTATION PAGE		READ INSTRUCTIONS BEFORE COMPLETING FORM
1. REPORT NUMBER	2. ORG. ACCESSION NO.	3. RECIPIENT'S CATALOG NUMBER
(18) AFATL-TR-77-129	(9) Final rept. Feb-Oct 77	
4. TITLE (and Subtitle)	5. TYPE OF REPORT & PERIOD COVERED	
(6) MISSILE AERODYNAMIC PARAMETER AND STRUCTURE IDENTIFICATION FROM FLIGHT TEST DATA.	Final Report: February 1977 to October 1977	
7. AUTHOR(s)	8. PERFORMING ORGANIZATION REPORT NUMBER	
(10) James E. Kain, Charles M. Brown, Jr. Jang G. Lee	(14) TASC (15) F08635-77-C-0062	
9. PERFORMING ORGANIZATION NAME AND ADDRESS	10. PROGRAM ELEMENT, PROJECT, TASK AREA & WORK UNIT NUMBERS	
The Analytic Sciences Corporation Six Jacob Way Reading, Massachusetts 01867 (7) 41	Program Element: 62602F JON 16 20680107	
11. CONTROLLING OFFICE NAME AND ADDRESS	12. REPORT DATE	
Air Force Armament Laboratory Armament Development and Test Center Eglin Air Force Base, Florida 32542	(11) Nov 1977	
14. MONITORING AGENCY NAME & ADDRESS (if different from Controlling Office)	13. SECURITY CLASS. (of this report)	
	UNCLASSIFIED	
16. DISTRIBUTION STATEMENT (of this Report)		15a. DECLASSIFICATION/DOWNGRADING SCHEDULE
Approved for public release; distribution unlimited		
17. DISTRIBUTION STATEMENT (of the abstract entered in Block 20, if different from Report)		
18. SUPPLEMENTARY NOTES		
Available in DDC.		
19. KEY WORDS (Continue on reverse side if necessary and identify by block number)		
Extended Kalman Filter Aerodynamic Parameter Identification Structure Identification Six-Degrees-of-Freedom Missile Modeling Postflight Data Processing EKF Algorithm Dynamic Modeling Errors		
20. ABSTRACT (Continue on reverse side if necessary and identify by block number)		
An extended Kalman filter algorithm for aerodynamic parameter identification from missile postflight data is developed and verified for realistic test conditions. The algorithm includes a general purpose six-degrees-of-freedom missile airframe model suitable for representing a variety of missile configurations. Verification studies consider low order "linear" aerodynamic models and higher order models with extensive nonlinear and pitch-yaw coupling effects. The sensitivity of filter		

DD FORM 1 JAN 73 473

EDITION OF 1 NOV 65 IS OBSOLETE

UNCLASSIFIED

SECURITY CLASSIFICATION OF THIS PAGE (When Data Entered)

UNCLASSIFIED

SECURITY CLASSIFICATION OF THIS PAGE(When Data Entered)

20. Abstract (Continued)

performance to initial conditions, measurement data rate and accuracy, input selection, and modeling errors is investigated. A structure identification technique is used to select the most probable aerodynamic model for a given data set from a group of candidate models. In addition, actual flight test data from a complex aerodynamically controlled vehicle is processed with the filter algorithm. The resulting identified model is shown to be an improvement over the preflight model.

UNCLASSIFIED

## PREFACE

This report documents the Missile Aerodynamic Coefficient and Structure Identification Study performed by The Analytic Sciences Corporation for the Air Force Armament Laboratory, Eglin Air Force Base, under Contract No. F08533-77-C 0062. The study was performed during the period February 1977 to October 1977. Mr. E. S. Sears managed the program for the Laboratory. The authors wish to express their appreciation to the engineering staff at AFATL for their suggestions during the missile airframe modeling and missile flight sensor modeling portions of this study.

This report has been reviewed by the Information Officer (OI) and is releasable to the National Technical Information Service (NTIS). At NTIS it will be available to the general public, including foreign nations.

This technical report has been reviewed and is approved for publication.

FOR THE COMMANDER:

*Clifford H. Allen, Jr.*  
CLIFFORD H. ALLEN, JR., Colonel, USAF  
Chief, Guided Weapons Division

✓		
BY		
DISTRIBUTION/RECEIVED DATE		
Dist. AVAIL. 01/12/80		
A		

78 07 06 032

## TABLE OF CONTENTS

SECTION	TITLE	PAGE
I	INTRODUCTION	1
	Background	1
	Technical Approach	3
	Organization of the Report	5
II	THE MISSILE AIRFRAME MODEL	6
	Overview	6
	Coordinate Frames and Notation	8
	Missile Equations of Motion	11
	Thrust and Mass Models	14
	Aerodynamic Modeling	18
III	MISSILE FLIGHT TEST MEASUREMENTS	25
	Acceleration Measurements	25
	Rate Gyro Measurements	26
	Angle-of-Attack and Sideslip Measurements	27
	Range and Attitude Sensor Measurements	29
IV	THE EXTENDED KALMAN FILTER FOR PARAMETER IDENTIFICATION	32
	Kalman Filter Equations	32
	Extended Kalman Filter Equations	38
	Implementation Considerations	41
	The Partitioned Form	41
	Partial Derivatives	43
	Identification Options	44
	Computational Requirements	44
V	ALGORITHM VERIFICATION WITH SYNTHETIC DATA	48
	Introduction	48
	A Nominal Test Case	51
	Flight Sensor Studies	66
	Sensor Noise	66
	Sensor Selection	71
	Sensor Modeling	75
	Wind Studies	78
	Estimation of Nonlinear Aerodynamic Effects	81
	Additional Performance Studies	87
	Synthetic Data Processing for a Case Exhibiting Large Mach Number Variations	90

## TABLE OF CONTENTS (Concluded)

SECTION	TITLE	PAGE
VI	AERODYNAMIC MODEL STRUCTURE IDENTIFICATION	97
	Background	97
	Experimental Results	100
VII	GBU-15 FLIGHT TEST DATA PROCESSING	109
	Background	109
	Flight Test Description	110
	The A Priori Model	114
	Identification Results	120
VIII	CONCLUSIONS AND RECOMMENDATIONS	146
	Summary and Conclusions	146
	Recommendations	150
APPENDIX A	IDENTIFICATION ALGORITHM OUTPUT	151
APPENDIX B	STRUCTURE IDENTIFICATION USING THE EXTENDED KALMAN FILTER	173
APPENDIX C	TELEMETRY DATA FROM A GBU-15 FLIGHT TEST	178
REFERENCES		191

## LIST OF FIGURES

FIGURE	TITLE	PAGE
1	Inertial and Body Coordinate Systems	9
2	Planar Thrust Misalignment and CG Travel Diagram	17
3	Measurement Processing with the Kalman Filter	36
4	Structure of an Extended Kalman Filter	38
5	Pitch Control for Nominal Test Case	54
6	Yaw Control for Nominal Test Case	55
7	Typical Perturbation Force Input for the Nominal Test Case	56
8	A Priori Measurement Time-History	58
9	Computed Pitch Rates Using Final Parameter Estimates, A Priori Initial Conditions and no Process Noise	62
10	Computed Pitch Rate Using A Priori Parameter Values, Perfect Initial Conditions and Correct Process Noise	63
11	Computed Pitch Rate Using Final Parameter Values, Perfect Initial Conditions, and Correct Process Noise	63
12	Angle-of-Attack from Alternate Nominal Test Case	64
13	Sideslip from Alternate Nominal Test Case	65
14	Residuals for Case 1	68
15	Residuals for Case 2	68
16	Residuals for Case 4	71
17	z-Axis Wind Estimation Error With Large Initial State Uncertainty and Large $\alpha$ - $\delta$ Sensor Errors	82
18	z-Axis Wind Estimation Error With Large Initial State Uncertainty and Small $\alpha$ - $\delta$ Sensor Errors	82
19	Angle-of-Attack Profile for the 36-Parameter Cases	86
20	Sideslip Profile for the 36-Parameter Cases	86
21	Mach Number Profile for AFATL Interceptor	91
22	Angle-of-Attack Profile for AFATL Interceptor	92
23	Sideslip Profile for AFATL Interceptor	92

# LIST OF FIGURES (Concluded)

FIGURE	TITLE	PAGE
24	Functional Diagram of the Structure Identification Algorithm	100
25	Probability that $H_i$ is True when $H_1$ is True, for $i = 1, 2$ , and 3	105
26	Probability that $H_i$ is True when $H_1$ is True, for $i = 1$ and 2	105
27	Probability that $H_i$ is True when $H_1$ is True, for $i = 1$ and 3	106
28	Probability that $H_i$ is True when $H_2$ is True, for $i = 1, 2$ , and 3	106
29	Probability that $H_i$ is True when $H_2$ is True, for $i = 1$ and 3	107
30	Probability that $H_i$ is True when $H_3$ is True, for $i = 1, 2$ , and 3	108
31	Physical Characteristics of the GBU-15	110
32	Measured Wind Data for GBU-15 Test Flight	113
33	Comparison of Measured Speed of Sound and Density With Standard Values	114
34	Representative Wind Tunnel Data	116
35	Predicted and Actual Measurement Comparison for Segment I	122
36	Predicted and Actual Measurement Comparison for Segment II	126
37	Predicted and Actual Measurement Comparison for Segment III	130
38	Comparison of Predicted and Actual Sideslip for Segment III With Input Measurement Assumed to Represent Negative Sideslip	136
39	Predicted and Actual Measurement Comparison With Fixed Initial Parameter Values	138
40	Predicted and Actual Measurement Comparison With Fixed Final Parameter Values	142



# LIST OF TABLES

TABLE	TITLE	PAGE
1	Direction Cosine Transformation Matrix Elements	10
2	Aerodynamic Force Coefficients	23
3	Aerodynamic Pitch Moment -- $C_M$	23
4	Aerodynamic Yaw Moment -- $C_N$	24
5	Aerodynamic Roll Moment -- $C_L$	24
6	Summary of the Extended Kalman Filter	40
7	Dynamic States, Measurements and Parameters	45
8	Algorithm Computational Options	46
9	Program Specifications	46
10	Filter Initialization and Performance Summary for Nominal Test Case	52
11	Nominal Test Case Aerodynamic Model	53
12	Nominal Initial-Dynamic State Statistics	53
13	Nominal Measurement Noise Levels	55
14	Filter Performance Summary for Alternate Nominal Test Case	65
15	Noise Sensitivity Studies	66
16	Parameter Identification Performance With Increased Measurement Noise	67
17	Parameter Identification Performance With Reduced Measurement Noise	70
18	Sensor Selection Studies	72
19	Parameter Estimation Accuracy Without a Longitudinal Accelerometer	73
20	Parameter Estimation Accuracy With Accelerometer and Rate Gyros Only	74
21	Parameter Identification Performance With Position and Attitude Measurements	76
22	Systematic Errors Sensitivity Studies	77
23	The Effects of Systematic Measurement Error on Parameter Identification	78

# LIST OF TABLES (Concluded)

TABLE	TITLE	PAGE
24	Wind Studies	80
25	Parameter Identification Summary for 36-Parameter Cases	85
26	Additional Performance Studies	88
27	Additional Filter Performance Studies	89
28	Identification Accuracy With Partial Parameter Set	90
29	Aerodynamic Model for AFATL Interceptor	93
30	Approximate Aerodynamic Parameter Values for AFATL Interceptor	94
31	Truth Model Parameter Values	101
32	Filter Model Parameter Initial Statistics	103
33	Summary of Radar Data Processing for Three Flight Segments	112
34	GBU-15 Airframe Data	115
35	GBU-15 Parameter Data	119
36	Adjusted Measurement Noise Levels	120
37	Final GBU-15 Parameter Estimates	134
38	Additional Parameters Investigated	136

## SECTION I INTRODUCTION

### BACKGROUND

A major problem during the design of a modern high performance tactical missile is predicting and modeling the aerodynamic forces and moments it will experience. This problem is particularly difficult for missiles which must execute extreme maneuvers to intercept high-g targets. The mathematical model of the airframe's aerodynamic behavior is needed for autopilot and guidance law design and for a preliminary evaluation of the missile's performance. Thus, the initial design effort normally includes many hours of wind tunnel testing to determine an aerodynamic model. Due to the problems of tunnel and mount interference, dimensional scaling, and the reduction of the force and moment data to a suitable analytical form, the aerodynamic model obtained may be highly inaccurate. In addition, the missile airframe configuration may be modified during the design to improve expected performance, increase control effectiveness, or for other engineering reasons. Modifications to the aerodynamic representation accounting for such changes are often based on a limited amount of additional wind tunnel testing or on the best estimates of the aerodynamic designer.

The true test of the missile simulation model used during the design and preliminary evaluation comes during flight test. Postflight data processing involves reconstruction of the flight using data taken during the test. Discrepancies between expected and actual flight behavior in many cases point to inaccuracies in the aerodynamic model. In addition, unknown effects such as thrust vector misalignment,

off-nominal thrust levels, and flight sensor model uncertainties lead to additional discrepancies. Using the flight test data to improve the aerodynamic model is a crucial phase of missile design which typically results in airframe and/or autopilot modifications to improve regions of questionable performance.

In the study documented here, a method of postflight data processing is investigated which directly addresses the airframe modeling problem. An extended Kalman filter is designed to estimate a variety of aerodynamic model and measurement parameters and a structure identification procedure is demonstrated which selects among candidate models. A general purpose six-degrees-of-freedom missile flight test model is developed which allows flexibility in sensor selection and parameterization, as well as rapid reprogramming to accommodate a variety of missile airframes.

The concept of aerodynamic model determination from flight data has been applied with success to aircraft (Reference 1). An aircraft during flight test can be well instrumented with expensive and possibly redundant flight data sensors, which can be used repeatedly. In addition, control surface inputs can be designed which intentionally separate complex aerodynamic effects or excite aircraft motion in a confined flight condition. This allows relatively simple aerodynamic models that are valid for special cases. Flight tests can be repeated if sensor or telemetry problems arise.

By comparison, a missile flight test program presents a more difficult aerodynamic identification problem. Because of the cost and the destructive nature of missile flight testing, only a relatively few flight tests are scheduled.

Also flight tests may have a variety of objectives in addition to verifying or determining the aerodynamic model. Thus the freedom to exercise control surfaces for the purposes of aerodynamic parameter estimation may be restricted. Since a single missile flight will likely involve large and rapid variation in flight condition, aerodynamic simplifications applying only to restricted flight regions must be minimized.

The major difference between missile and aircraft aerodynamic parameter estimation methods lies in the airframe modeling detail required. Full six-degrees-of-freedom kinematics along with time-varying thrust, mass, center of gravity and inertias are modeled in order to characterize the tactical missile throughout the operating flight regime. This modeling complexity along with the desired flexibility and generality of the resulting postflight data processing algorithm places a considerable burden on the particular parameter estimation algorithm used. The algorithm must be computationally efficient; it must produce accurate parameter estimates in spite of modeling uncertainty, and user convenience must be maximized.

#### TECHNICAL APPROACH

The application of modern estimation methods to the processing of measurements from complex dynamic systems has become commonplace in many fields of engineering. In particular, the problem of system identification, or parameter estimation, has received much attention. Given the equations necessary to describe the dynamic process (the state equations), the associated measurement equations, and the system and measurement noise statistics, the application of modern estimation methods is well understood (Reference 2).

It is known that if the system mathematical description is accurate and if the equations are linear, the Kalman filter gives "optimal" estimates of the system states. For this discussion, an optimal estimator is defined as one producing lower root mean square (rms) estimation errors than any other estimation technique. In addition to being an optimal estimator, the Kalman filter automatically computes the rms accuracy of its estimates.

The linearity restriction mentioned above is rarely satisfied in realistic physical problems such as the one considered here. Thus, it is common to linearize the system equations about the current system state estimates in order to determine an "approximately optimal" system estimate. If the system is "nearly linear" in the region which contains the system states and estimates, then this type of filter provides a nearly optimal estimate. This approach, used here, has been highly successful in a variety of engineering applications and is called the Extended Kalman Filter (EKF).

In applying the EKF to parameter identification, the equations of motion -- i.e., the model structure -- are assumed to be known to within a set of uncertain parameters. The parameter vector, e.g., the set of aerodynamic coefficients, is distinguished from the vehicle's dynamic state vector -- positions, velocities, etc. The parameter vector is adjoined to the dynamic state vector to form an augmented state vector. The EKF for the augmented state can be applied in a straightforward manner. After measurement processing, that portion of the augmented state representing the parameter vector yields parameter estimates. Parameter estimation accuracy is obtained from the final augmented state covariance matrix.

A model structure identification method is also developed and evaluated in this report. The method requires that several candidate structures be postulated and the defining parameters estimated. The system models are statistically compared using information stored during the course of processing with each EKF, and the most probable system model is selected.

## ORGANIZATION OF THE REPORT

This report is organized as follows: Section II discusses the six-degrees-of-freedom airframe dynamics and the aerodynamic parameterization. Frequently encountered missile flight instrumentation is described in Section III along with the associated math models. Section IV describes the EKF, presents a partitioned form of the conventional extended Kalman filter tailored specifically for the large-scale parameter identification problem, and discusses the implementation of the EKF for the airframe identification problem. Section V presents aerodynamic parameter estimation results obtained utilizing computer-generated synthetic measurements from a typical short range air-to-air missile. A structure identification method is developed in Section VI and test cases are presented which demonstrate its ability to select the correct aerodynamic model structure from a family of candidate models. Section VII discusses an application of the identification algorithm to actual flight data taken from an aerodynamically controlled airframe. Section VIII summarizes the study and presents the major conclusions.

## SECTION II

### THE MISSILE AIRFRAME MODEL

#### OVERVIEW

The generalized six-degrees-of-freedom missile airframe model used in this effort includes 12 fundamental state variables:

- Three missile inertial velocity components in body axes
- Three inertial positions to locate the missile center of gravity (CG)
- Three rotation rates of the body axes with respect to inertial space
- Three Euler angles to locate the body axes in inertial space.

A generalized aerodynamic model provides force and moment coefficients as a function of the following inputs:

- Angle-of-attack
- Angle-of-sideslip
- Mach number
- Control deflections
- Inertial rotation rates
- Angle-of-attack and sideslip rates
- Total relative velocity magnitude.

This model utilizes a Taylor's Series expansion for the aerodynamic force and moment coefficients in terms of the above



input variables. Terms up to third order are considered, with appropriate terms selected by considering a variety of missile configurations, as well as utilizing the symmetrical nature of the general missile airframe with respect to a single plane of symmetry (Reference 3). The aerodynamic moments are assumed to be referenced to a fixed point on the missile airframe, and must be translated to account for CG travel while thrusting. The flight time-histories of three composite control surface deflections are provided -- the pitch, yaw, and roll control deflections. The level of modeling detail assumed is typical of that used in postflight trajectory reconstruction from flight data.

The earth is assumed flat and nonrotating for the duration of the missile flight. An atmosphere model provides density, pressure, speed of sound and inertial wind velocity as a function of altitude. For missile flight tests at high altitudes the wind can contribute significantly to the effective angle-of-attack. The effects of atmospheric wind on missile aerodynamic forces and moments is accurately represented.

The missile airframe may be thrusting with variable mass, moments of inertia, and CG locations. Thrust values are determined by an input table of sea level thrust versus flight-time, with corrections for thrust variation with altitude. The mass, inertia and CG properties are computed proportional to the integral of thrust (impulse), requiring as inputs only the launch and burnout values of mass, inertia, and CG location.

The six-degrees-of-freedom missile model described above is not exact in that a variety of second order effects are neglected such as body bending, etc. It is common practice

in the engineering application of Kalman filtering methods to account for these known (and sometimes unknown) model details by assuming random inputs (process noise) to the dynamic equations of motion. To this end, six additional random states are added to the 12 fundamental airframe states. These can be used to represent modeling uncertainties such as bending effects, unsteady aerodynamics, wind gusts, or control deflection measurement errors. Three random force states and three random moment states are modeled. The rms magnitude and bandwidth for each disturbance state are required inputs to describe these random effects.

#### COORDINATE FRAMES AND NOTATION

Two coordinate frames are used frequently in the missile airframe model; these are an inertial frame and a missile body-fixed frame. The direction cosine matrix computed from an appropriate set of Euler angles provides the necessary transformation between frames. Superscripts I (inertial frame) and B (body frame) are used to indicate the particular frame associated with the coordinates of a given vector.

The inertial coordinate frame assumes a flat non-rotating earth and is fixed at launch. The origin of the I-frame is located on the surface of the earth below the launch point (Figure 1). The x and y inertial directions are horizontal while the z axis is down. The x axis is oriented in the downrange direction while y is crossrange to the right. Note that altitude is in the negative z direction in this set of coordinates.

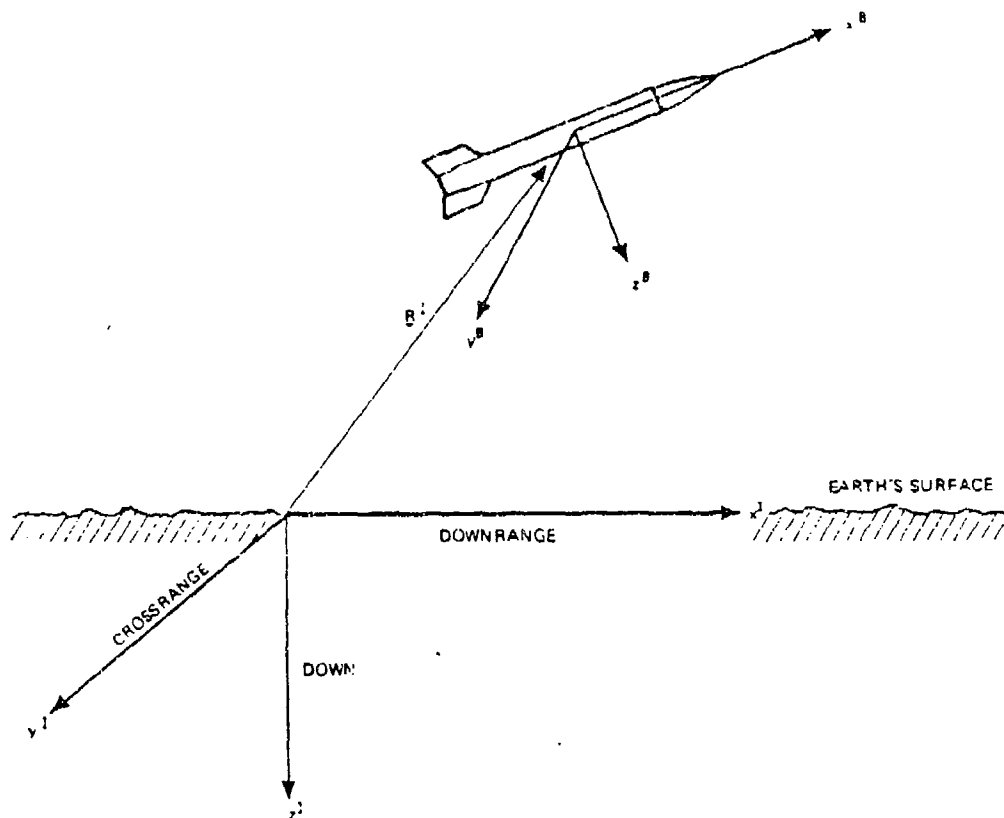


Figure 1. Inertial and Body Coordinate Systems

The body coordinate frame is located along principal body axes; i.e., all cross products of inertia are zero (Figure 1). The x-axis is along the centerline positive forward. The y- and z-axis define the missile control planes; i.e., missile control commands are given in the x-z plane (pitch plane) and the x-y plane (yaw plane). The origin of the body frame is the missile CG.

The transformation between inertial and body axes is accomplished via the direction cosine transformation. This transformation is defined in terms of three Euler angles.

$\phi$  = roll angle

$\theta$  = pitch attitude

$\psi$  = yaw attitude

A complete description of these angles is contained in Reference 4. The resulting direction cosine transformation from body to inertial ( $C_B^I$ ) is given by Table 1.

TABLE 1. DIRECTION COSINE TRANSFORMATION MATRIX ELEMENTS

$i, j$	$[C_B^I]_{ij}$
1,1	$\cos\phi \cos\theta$
1,2	$\sin\phi \sin\theta \cos\psi - \cos\phi \sin\psi$
1,3	$\cos\phi \sin\theta \cos\psi + \sin\phi \sin\psi$
2,1	$\cos\theta \sin\phi$
2,2	$\sin\phi \sin\theta \sin\psi + \cos\phi \cos\psi$
2,3	$\cos\theta \sin\theta \sin\psi - \sin\phi \cos\psi$
3,1	$-\sin\theta$
3,2	$\sin\phi \cos\theta$
3,3	$\cos\phi \cos\theta$

Certain notation conventions used in the missile model are presented below:

- All vectors are underscored
- A dot over a quantity indicates its total time-derivative
- Elements of a vector are subscripted by the appropriate index, i.e.,  $w_3$  is the third component of the vector  $\underline{w}$

- A "x" between two three-element vectors represents the cross product, i.e.,  $\underline{w} \times \underline{v}^B$ .
- The cross product equivalent matrix  $\tilde{w}$  is given by

$$\tilde{w} = \begin{bmatrix} 0 & -w_3 & w_2 \\ w_3 & 0 & -w_1 \\ -w_2 & w_1 & 0 \end{bmatrix} \text{ such that } \underline{w} \times \underline{v}^B = \tilde{w} \underline{v}^B$$

- The quantity  $\underline{g}^I$  will be used to represent the gravity vector in inertial coordinates, i.e.,

$$\underline{g}^I = \begin{bmatrix} 0 \\ 0 \\ g \end{bmatrix}$$

- The direction cosine transformation relating the I- and B-frames is given by  $C_I^B$  where, for example

$$\underline{v}^B = C_I^B \underline{v}^I$$

Thus  $C_I^B$  transforms vectors from the I- to the B-frame. The inverse of  $C_I^B$  will be designated  $C_B^I$  so that

$$\underline{v}^I = C_B^I \underline{v}^B$$

#### MISSILE EQUATIONS OF MOTION

The nonlinear differential equations which must be propagated to determine the 12 fundamental missile states consist of the four interrelated three-element vector equations summarized below:

$$\dot{\underline{v}}^B = \frac{QAC_f}{m} + \frac{f_T}{m} + C_I^B \underline{g}^I - \underline{w} \times \underline{v}^B + \underline{r}_f \quad (1)$$

$$\dot{\underline{r}}^I = C_B^I \underline{v}^B \quad (2)$$

$$\dot{\underline{w}} = \left[ \underline{I}_N^{-1} \right] \left\{ QAD \underline{C}_{10} - QACF \times \underline{C}_f + \underline{m}_T - \begin{pmatrix} w_2 w_3 (I_z - I_y) \\ w_3 w_1 (I_x - I_z) \\ w_1 w_2 (I_y - I_x) \end{pmatrix} + \underline{r}_m \right\} \quad (3)$$

$$\dot{\underline{\psi}} = \begin{pmatrix} \dot{\phi} \\ \dot{\theta} \\ \dot{\psi} \end{pmatrix} = \begin{pmatrix} w_1 + (\sin \phi w_2 + \cos \phi w_3) \tan \theta \\ \cos \phi w_2 - \sin \phi w_3 \\ (\sin \phi w_2 + \cos \phi w_3) / \cos \theta \end{pmatrix} \quad (4)$$

The left sides of these four equations represent the derivatives of the 12 fundamental missile states, defined as follows:

$\underline{v}^B$  = missile velocity with respect to inertial space in body axes

$\underline{r}^I$  = missile CG position vector in inertial space

$\underline{w}$  = missile rotation rates with respect to inertial space always understood to be expressed in body coordinates

$\underline{\psi}$  = a vector made up of the three Euler angles which locate the body axes orientation with respect to inertial space.

The following symbols are used above and will be further defined in subsequent subsections:

$Q$  = dynamic pressure

$A$  = aerodynamic reference area

$\underline{C}_f$  = aerodynamic force coefficients

$m$  = mass

$\underline{f}_T$  = thrust vector in body axes

$\underline{r}_f$  = acceleration perturbation input

$\underline{I}_N$  = inertia matrix containing inertias  $I_x, I_y, I_z$

$D$  = aerodynamic reference length

$C_m$  = aerodynamic moment coefficients

$\underline{cg}$  = vector from aerodynamic reference point to the CG

$\underline{m}_T$  = thrust moment vector

$\underline{r}_m$  = perturbation moment vector

The right side of Equation 1 includes the summation of all forces acting on the missile. The five terms on the right side of the equation, from left to right, represent the following:

- Aerodynamic forces in body axes
- Thrust forces in body axes
- Projection of gravity onto body axes
- Coriolis contributions
- Random perturbation effects.

Equation 2 defines the rate of change of missile inertial position as the transformation of the body-referenced velocity  $\underline{y}^B$ . The right side of Equation 3 represents the summation of all moments acting on the airframe. The quantity  $[I_N^{-1}]$  is the diagonal inertia matrix; the five terms included within the braces in Equation 3, from left to right, represent the following:

- Aerodynamic moments about the body-fixed aerodynamic reference point
- Aerodynamic moment translation to CG location
- Thrust moment about the CG

- Gyroscopic coupling terms
- Random moment perturbation terms.

Equation 4 represents the dynamics of the Euler angle states; these equations are derived in Reference 4.

#### THRUST AND MASS MODELS

The analytical expressions for aerodynamic and thrust forces and moments are in some cases highly airframe-specific. Thus, the general purpose airframe model proposed here may not be applicable in all cases. Nevertheless, there is considerable commonality between the majority of missile airframe models so that few changes will be necessary to represent a variety of airframe types.

Variations among different missile airframes are separated into two categories,

- Thrust-mass characteristics
- Aerodynamic representation.

The time-varying thrust and mass characteristics of an arbitrary missile are fundamentally related. The nature of this relationship is used here to minimize the inputs required to define a specific missile configuration.

A missile thrust versus time profile at sea level is assumed in tabular form. Linear interpolation provides a continuous sea level thrust ( $T_{s1}$ ) time-history. The mass



flow rate is assumed proportional to  $T_{sl}$  so that mass and mass-related characteristics can be modeled as linear functions of the thrust integral. The missile mass characteristics required are:

- Mass ( $m$ )
- Moments of inertia about body axes (assumed principal axes)  $I_x$ ,  $I_y$ ,  $I_z$  with diagonal inertia tensor,

$$\begin{bmatrix} I_N \end{bmatrix} = \begin{bmatrix} I_x & 0 & 0 \\ 0 & I_y & 0 \\ 0 & 0 & I_z \end{bmatrix}$$

- Coordinates of CG travel from the aerodynamic reference point, (cg-a three element vector).

The time-variation of these seven mass-related variables is computed from the launch (full) values, the burnout (empty) values and the thrust versus time table. In particular,

$$m(t) = m_1 - \left( \frac{\int_0^t T_{sl}(\tau) d\tau}{\int_0^{t_b} T_{sl}(\tau) d\tau} \right) (m_1 - m_{bo}) \quad (5)$$

where

$m(t)$  = missile mass at time  $t$

$t_b$  = time at burnout

$T_{sl}(t)$  = sea level thrust at time  $t$

$m_1$  = launch mass

$m_{bo}$  = burnout mass

The moments of inertia and CG travel are computed in a similar manner.

Sea level thrust is corrected to account for altitude variations using the exhaust gas exit ( $a_{ex}$ ). The resulting thrust at altitude T is given by

$$T = T_{sl} + (p_0 - p(\text{alt})) a_{ex} \quad (6)$$

where

$p_0$  = sea level reference pressure  
(2116 lb/sq ft)

$p(\text{alt})$  = actual pressure altitude from the  
atmosphere model\*

The primary thrust direction is along the positive body x-axis. Thrust vector misalignments and/or thrust vector control produce lateral forces and thrust moments. The model presented here accounts for thrust misalignment but does not explicitly consider thrust vector controls (TVC). Note that TVC and thrust misalignments are modeled in a similar manner, so that the framework for a TVC model is included.

Figure 2 shows a planar representation of the thrust moment effects. Note the body axes are assumed fixed at the missile CG which may be located arbitrarily with respect to the geometric missile centerline. The point of thrust attachment to the missile airframe, as well as the aerodynamic reference point, are assumed to be fixed along the missile geometric centerline. The vector cg gives the CG travel from the stationary aerodynamic reference point. The cg vector

---

\*The 1962 ARDC reference atmosphere is assumed in this study.

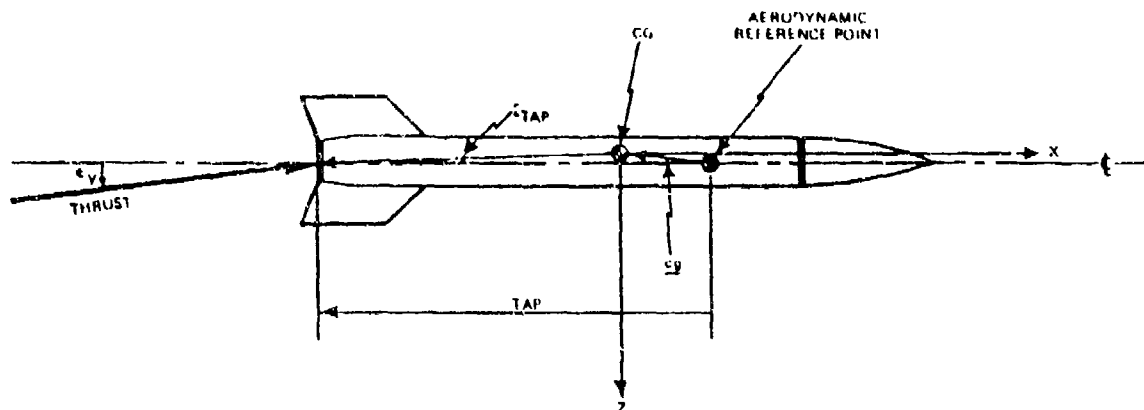


Figure 2. Planar Thrust Misalignment and CG Travel Diagram

points towards the CG and is specified in body axes. The thrust attachment point along the geometric centerline is referenced from the aerodynamic reference point. The variable TAP indicates the distance from the aerodynamic reference point to the thrust attachment point; the positive direction is indicated in Figure 2.

Small angular thrust vector misalignments  $\epsilon_y$  and  $\epsilon_z$  are considered as positive thrust rotations about the y and z body axes. The thrust vector in body axes is given by,

$$\underline{f}_1 = \begin{pmatrix} 1.0 \\ \epsilon_z \\ -\epsilon_y \end{pmatrix} \quad (7)$$

A vector from the CG position to the thrust attachment point is given by,

$$\underline{r}_{TAP} = \begin{pmatrix} -TAP - CG_x \\ -CG_y \\ -CG_z \end{pmatrix} \quad (8)$$

The thrust moment about the CG is given by:

$$\underline{m}_t = \underline{r}_{TAI} \times \underline{f}_t \quad (8)$$

## AERODYNAMIC MODELING

Six-degrees-of-freedom aerodynamic models are, in most cases highly vehicle specific, utilizing a variety of one-, two-, and three-dimensional tables, as well as Taylor series expansions, trigonometric expansions and other analytic functions, to characterize the wind tunnel data. The common link between the various aerodynamic models is in the set of independent variables which must be related to the aerodynamic forces and moments. These variables are defined in this section.

The relative velocity vectory  $\underline{v}_r$  defines the movement of the missile through the surrounding air mass. The wind velocity ( $\underline{v}_w$ ) is defined as the movement of the surrounding air mass with respect to the inertial coordinate system. Consequently, the relative velocity is given by,

$$\underline{v}_r = \underline{v}^B - C_I^R \underline{v}_w \quad (10)$$

The velocity  $\underline{v}_w$  is assumed to be a function only of altitude. Wind versus altitude tables must be supplied to the model.

The relative velocity is expressed in terms of the relative velocity magnitude ( $v_m$ ) and two angles which define the position of the relative velocity vector in body axes. Two sets of relative velocity vector orientation angles are used frequently in missile models. Angle-of-attack ( $\alpha$ ) and angle-of-sideslip ( $\beta$ ) are used exclusively for aircraft and

for winged missiles with a dominant single plane of symmetry. For these vehicles sideslip is controlled to be small and this fact often simplifies the mathematical representation of the yaw plane aerodynamic model.

For missiles with two planes of symmetry, e.g., cruciform missiles, aerodynamics are frequently modeled as functions of aerodynamic roll  $\phi_A$  and total angle-of-attack  $\alpha_T$ . This permits the use of the known vehicle symmetry to simplify the aerodynamic representation (References 5 and 6).

Angle-of-attack and sideslip are sometimes required to be Euler angles relating the body axes to a "wind axes" system -- i.e., a coordinate system with one axis along the relative velocity direction. In this case,  $\alpha$  and  $\beta$  are defined by:

$$\alpha = \tan^{-1} (v_{r_3}/v_{r_1}) \quad (11)$$

$$\beta = \sin^{-1} (v_{r_2}/v_m) \quad (12)$$

where

$$v_m = (v_{r_1}^2 + v_{r_2}^2 + v_{r_3}^2)^{1/2} \quad (13)$$

The angle-of-attack and sideslip can be used to characterize the aerodynamics of missiles with both single and dual plane of symmetry. This more general formulation is adopted here. Nevertheless, it is recognized that in special cases the  $(\alpha_T, \phi_A)$  representation may lead to reduced order parameterizations and thus more efficient parameter identification.

An alternate definition of sideslip is frequently used in missile modeling where the "wind axes" are rarely required. This definition is used here and is given by,

$$\delta = \tan^{-1} (v_{r2}/v_{r1}) \quad (14)$$

This sideslip definition does not result in an Euler angle set. The similarity between the  $\alpha$  and  $\beta$  computations of Equations 11 and 14 allows some simplification of the aerodynamic model for cruciform missiles.

A generalized missile model in  $\alpha$  and  $\beta$  cannot assume  $\delta$  small. In many cases  $\alpha$  and  $\beta$  may be equally large. Nevertheless the assumption of at least one plane of symmetry -- the xz plane -- will be used to simplify the aerodynamic model.

The model given here assumes all aerodynamic forces and moments to be linear in mach number about some reference value,  $M_0$ . This assumption limits the region of applicability of the model to flight segments where Mach variations are small. The speed of sound  $v_s$  is required for the computation of mach number  $M$ . The speed of sound is computed as a function of missile altitude. Mach number is given by:

$$M = v_m/v_s \quad (15)$$

Both aerodynamic forces and moments are assumed proportional to dynamic pressure  $Q$ .

$$Q = \rho v_m^2/2 \quad (16)$$

where the atmospheric density  $\rho$  is computed as a function of altitude from the atmosphere model. In addition, the aero-

dynamic force in Equation 1 is proportional to some specified reference area  $A$  while the aerodynamic moments (Equation 3) are proportional to the product of reference area and reference distance,  $AD$ .

In addition to  $\alpha$ ,  $\beta$ , and  $M$  the aerodynamic coefficients are functions of the aerodynamic control surface deflections. Missile control surface deflections are commonly governed by three independent commands. These commands are designed to produce torques about the three body axes thus achieving control in pitch, yaw, and roll. The pitch, yaw, and roll control deflections are required by the generalized model presented here.

Measurement of control surface deflection requires instrumentation of actuator response -- a measurement frequently not required for operational missile configurations. In some cases actuator response measurements may not be available or may be impractical. A more easily obtained measurement is the control surface command which results from the autopilot subsystem. These commands are related to the actual deflections through the actuator dynamics. Actuator dynamics are typically wide bandwidth with respect to the dominant airframe frequency response, and thus may be ignored in some cases. If control surface command rather than actual actuator response is used to model the airframe input, the effects of actuator dynamic lag should be investigated. This can be complicated since actuator lags may involve calculation of aerodynamic hinge moments, detailed motor modeling and/or hydraulic servo models. The model presented here assumes that measurements of actual control deflections are available.

Six independent variables required for aerodynamic modeling have been described thus far -- angle-of-attack, sideslip, mach number, and three control deflections. These quantities define the static behavior of the aerodynamics, i.e., a vehicle fixed with respect to the airflow will experience forces and moments as functions of these quantities. Most wind tunnel studies provide only static empirical force and moment relationships. Additional dynamic forces and moments arise as a result of the time-variation of the airframe with respect to the airflow.

The dynamic aerodynamic effects are often computed analytically using theoretical aerodynamic concepts. Dynamic wind tunnel testing methods are sometimes used (Reference 7). The most common dynamic terms considered are the aerodynamic damping moments. In addition, magnus terms are sometimes added which couple the pitch and yaw aerodynamics when roll rates exist. The additional variables required to represent the dynamic terms are missile rotation rates --  $p$ ,  $q$  and  $r$  representing rotation rates about body x-, y- and z-axes, respectively -- as well as  $\dot{\alpha}$  and  $\dot{\beta}$ . The standard normalizing factor  $D/2v_m$  is used to normalize the dynamic aerodynamic terms.

A generalized mathematical model in the form of Taylor series expansions relates the 12 independent variables to the 6 aerodynamic forces and moments. This model is defined in terms of time-invariant parameters in order to make use of parameter identification methods. The complete aerodynamic model is given by Tables 2 through 5.



TABLE 2. AERODYNAMIC FORCE COEFFICIENTS

AXIAL FORCE

$$C_x = C_{x_\alpha} \alpha + C_{x_\alpha} 2\alpha^2 + C_{x_\beta} 2\beta^2 + C_{x_\alpha} 3\alpha^3 + C_{x_{\delta p}} 2\delta p^2 \\ + C_{x_{\delta q}} 2\delta q^2 + C_{x_{\delta i}} 2\delta i^2 + C_{x_{\delta qa}} \delta qa + C_{x_{\delta r}} \delta r + C_{x_M} \left( \frac{M-M_0}{M_0} \right)$$

NORMAL FORCE

$$C_z = C_{z_0} + C_{z_\alpha} \alpha + C_{z_\alpha} 2\alpha^2 + C_{z_\beta} 2\beta^2 + (C_{z_\beta} 2 + C_{z_\beta} 2\alpha^2) \beta^2 \\ + (C_{z_{\delta q}} + C_{z_{\delta qa}} \alpha + C_{z_{\delta q\beta}} \beta^2) \delta q + C_{z_{\delta i}} \frac{qD}{2V_m} + C_{z_M} \left( \frac{M-M_0}{M_0} \right)$$

LATERAL FORCE

$$C_y = C_{y_\beta} \beta + C_{y_\beta} 3\beta^3 + (C_{y_\alpha} 2 + C_{y_\beta} 2\alpha^2) \alpha^2 + C_{y_{\alpha\beta}} \alpha\beta \\ + (C_{y_{\delta r}} + C_{y_{\delta ru}} 2\alpha^2 + C_{y_{\delta r\beta}} \beta) \delta r + C_{y_{\delta q}} \delta q + C_{y_j} \frac{pD}{2V_m} + C_{y_r} \frac{rD}{2V_m} + C_{y_M} \left( \frac{M-M_0}{M_0} \right)$$

TABLE 3. AERODYNAMIC PITCH MOMENT --  $C_M$

STATIC CONTROL FIXED TERMS

$$C_{M_0} + C_{M_\alpha} \alpha + C_{M_\alpha} 2\alpha^2 + C_{M_\beta} 2\beta^2 + (C_{M_\beta} 2 + C_{M_\beta} 2\alpha^2) \beta^2$$

CONTROL EFFECTS

$$(C_{M_{\delta q}} + C_{M_{\alpha\delta q}} \alpha + C_{M_{\alpha} 2\delta q} \alpha^2 + C_{M_{\beta} 2\delta q} \beta^2 + C_{M_{\delta p}} 2\delta p^2 + C_{M_{\delta r}} 2\delta r^2 + C_{M_{p\delta q}} \frac{pD}{2V_m}) \delta q \\ + (C_{M_{\delta q}} 2 + C_{M_{\alpha} 2\delta q} 2\alpha^2) \delta q^2$$

DYNAMIC TERMS -- PITCH DAMPING AND MAGNUS EFFECTS

$$(C_{M_{\dot{q}}} + C_{M_{\alpha} \dot{\alpha}} + C_{M_{\beta} \dot{\beta}} + C_{M_{q\alpha}} \alpha) \frac{D}{2V_m}$$

MACH DEPENDENCE

$$C_{M_M} \left( \frac{M-M_0}{M_0} \right)$$

TABLE 4. AERODYNAMIC YAW MOMENT --  $C_N$

<u>STATIC CONTROL FIXED TERMS</u>
$C_{N_{\alpha}} + C_{N_{\beta}} \beta^3 + (C_{N_{\alpha}^2} + C_{N_{\alpha}^2 \beta}) \alpha^2 + C_{N_{\alpha \beta}} \alpha \beta$
<u>CONTROL EFFECTS</u>
$\left( C_{N_{\delta r}} + C_{N_{\delta r}} \beta + C_{N_{\delta r}} \beta^2 + C_{N_{\delta r}} \alpha^2 + C_{N_{\delta r}} \alpha \beta + C_{N_{\delta r}} \delta r^2 + C_{N_{\delta r}} \delta q^2 + C_{N_{\delta r}} \frac{p}{2v_m} \right) \delta r$ $+ (C_{N_{\delta r}} + C_{N_{\delta r}} \beta^2) r^2 + C_{N_{\delta r}} \delta p$
<u>DYNAMIC TERMS -- YAW DAMPING AND MAGNUS EFFECTS</u>
$(C_{N_r} + C_{N_r} \beta + C_{N_{p \alpha}} + C_{N_{r \beta}} + C_{N_p}) \frac{p}{2v_m}$
<u>MACH DEPENDENCE</u>
$C_{N_M} \left( \frac{M-M_0}{M_0} \right)$

TABLE 5. AERODYNAMIC ROLL MOMENT --  $C_L$

<u>STATIC CONTROL FIXED TERMS</u>
$C_{L_{\alpha}} + C_{L_{\beta}} \beta + C_{L_{\alpha}^2} \alpha^2 + C_{L_{\beta}^2} \beta^2 + C_{L_{\alpha \beta}} \alpha \beta$
<u>ROLL CONTROL EFFECTS</u>
$(C_{L_{\delta p}} + C_{L_{\delta p}} \alpha + C_{L_{\delta p}} \delta q + C_{L_{\delta p}} \alpha \delta q + C_{L_{\delta p}} \delta r^2 + C_{L_{\delta p}} \delta q^2) \delta p$
<u>COUPLING TERMS</u>
$C_{L_{\alpha \delta r}} \alpha \delta r + C_{L_{\beta \delta q}} \beta \delta q + C_{L_{\delta r}} \delta r$
<u>DYNAMIC TERMS</u>
$(C_{L_p} + C_{L_q} + C_{L_r}) \frac{p}{2v_m}$
<u>MACH DEPENDENCE</u>
$C_{L_M} \left( \frac{M-M_0}{M_0} \right)$

### SECTION III

#### MISSILE FLIGHT TEST MEASUREMENTS

Data taken during the course of missile flight testing for the purpose of post flight analysis include ground-based missile position tracking data and telemetry records from signals generated onboard the missile. The potential measurements available and their mathematical models are discussed in this section. During data processing all measurements are assumed discrete with a constant data rate.

#### ACCELERATION MEASUREMENTS

Three body-fixed accelerometers are assumed to provide specific force measurements along the body x-, y-, and z-axes. These sensors are typically located near the nose of the missile and thus also sense the effects of body rotations. They are likely to be "control quality" accelerometers subject to large biases, scale factor uncertainty, and noise.

The accelerometer measurement is modeled by

$$\underline{a}_m = \left[ I + SFE_a \right] \left\{ \frac{\underline{f}_a}{m} + \frac{\underline{f}_t}{m} + \underline{w} \times (\underline{w} \times \underline{r}_s) + \underline{\dot{w}} \times \underline{r}_s \right\} + \underline{b}_a + \underline{\xi}_a \quad (17)$$

where

$\underline{a}_m$  = measured acceleration

$\underline{f}_a$  = aerodynamic force vector

$\underline{f}_t$  = thrust force vector

$\underline{w}$  = missile rotation rate

$\underline{r}_s$  = sensor location with respect to the aerodynamic reference point, in body axes

$\xi_a$  = accelerometer measurement noise

$b_a$  = accelerometer bias error

$I$  = unit identity matrix

$SFE_a$  = diagonal matrix containing accelerometer  
scale factor errors

### RATE GYRO MEASUREMENTS

Three body fixed rate gyros are assumed. Rate gyros used in missile control are subject to bias errors, scale factor errors and acceleration sensitive errors. The rate gyro model used is given by

$$\underline{w}_m = [I + SFE_g] \underline{w} + [ASE] \underline{a}_g + \underline{b}_g + \underline{\xi}_g \quad (18)$$

where

$\underline{w}_m$  = rate gyro measurement

$SFE_g$  = diagonal matrix containing rate gyro  
scale factor errors

$\underline{b}_g$  = gyro bias drift error

$[ASE]$  = 3x3 matrix of acceleration sensitive  
drift errors

$\underline{a}_g$  = acceleration in body axes at gyro  
location

$\underline{\xi}_g$  = accelerometer white measurement noise

The gyro and accelerometer instrument packages are located at approximately the same location, so that

$$\underline{a}_g = \frac{\underline{f}_a}{m} + \frac{\underline{f}_t}{m} + C_I^B \underline{g}^I + \underline{w} \times (\underline{w} \times \underline{r}_s) + \dot{\underline{w}} \times \underline{r}_s \quad (19)$$

## ANGLE-OF-ATTACK AND SIDESLIP MEASUREMENTS

Knowledge of the relationship between the angle-of-attack and sideslip and the missile dynamic response is the key to determining the analytical model for the aerodynamic forces and moments. In some cases, angle-of-attack and sideslip can be determined implicitly using the accelerometer and gyro sensors. Alternately, the angle-of-attack and sideslip may be measured explicitly using the appropriate sensors. Accelerometers and gyros measure missile characteristics with respect to inertial space, whereas angle-of-attack and sideslip are functions of the relative velocity. If significant wind is present, the accelerometers and gyros may not provide sufficient angle-of-attack and sideslip accuracy.

For missile flight tests, the  $\alpha$ - $\beta$  sensor consists of a boom projecting ahead of the missile into the free airstream, beyond possible interference with the detached shock wave. Two wind vanes are attached to the boom and allowed rotational freedom in orthogonal planes (Reference 8). The vanes remain aligned with the relative airflow; thus the vane angles measured with respect to the fixed boom provide an indication of the angle-of-attack and sideslip at the missile nose. Measurement lags result because of vane inertias and rotational friction.

Various attempts have been made to calibrate  $\alpha$ - $\beta$  sensors by inflight calibration methods (References 9 and 10). These studies indicate poor agreement between manufacturer's calibration results and inflight verification, as well as large discrepancies in the predicted sensor lags. Consequently, effective use of the  $\alpha$ - $\beta$  sensor may require identification of a variety of sensor parameters.

The  $\alpha$  and  $\beta$  required within the aerodynamic model discussed in Section II are derived from the relative velocity at the missile CG. The  $\alpha$  and  $\beta$  as measured at the missile nose will include the effects of missile rotations with respect to the airstream. Consider the following example:

Missile velocity = 1200 ft/sec

Pitch rotation rate = 4 rad/sec

$\alpha$ - $\beta$  sensor to CG distance = 3 ft

Angle-of-attack at CG = 0

A discrepancy in angle-of-attack at the CG and angle-of-attack at the nose of 0.01 radian (0.56 degree) results. Failure to accurately model this effect may account for the in-flight calibration difficulties encountered by the referenced studies. In addition,  $\alpha$ - $\beta$  booms must be calibrated to account for bending under load (Reference 7), and they may lead to perturbations of the uninstrumented aerodynamics.

Based upon the above consideration, the following model can be used to approximate the  $\alpha$ - $\beta$  sensor output:

$$\alpha_B = \alpha - \frac{w_y r_B}{v_x} \quad (20)$$

$$\beta_B = \beta + \frac{w_z r_B}{v_x} \quad (21)$$

$$\omega_\alpha^2 \ddot{\alpha}_L + 2\zeta_\alpha \omega_\alpha \dot{\alpha}_L + \alpha_L = \alpha_B \quad (22)$$

$$\omega_\beta^2 \ddot{\beta}_L + 2\zeta_\beta \omega_\beta \dot{\beta}_L + \beta_L = \beta_B \quad (23)$$

$$\alpha_m = (1+SFE_\alpha)\alpha_L + b_\alpha + \xi_\alpha \quad (24)$$

$$\beta_m = (1+SFE_\beta)\beta_L + b_\beta + \xi_\beta \quad (25)$$

where

$\alpha_B, \beta_B$  = angle-of-attack and sideslip at nose boom

$r_B$  = distance from CG to nose boom

$\alpha_L, \beta_L$  = dynamic response of  $\alpha$ - $\beta$  sensor

$\omega_\alpha, \omega_\beta$  = natural frequency of  $\alpha$ - $\beta$  sensor

$\zeta_\alpha, \zeta_\beta$  = damping ratio of  $\alpha$ - $\beta$  sensor

$\alpha_m, \beta_m$  =  $\alpha$ - $\beta$  sensor measurements

$SFE_\alpha, SFE_\beta$  =  $\alpha$ - $\beta$  sensor scale factor errors

$b_\alpha, b_\beta$  =  $\alpha$ - $\beta$  sensor bias errors

$\xi_\alpha, \xi_\beta$  = wide bandwidth noise on  $\alpha$ - $\beta$  sensor measurement

#### RANGE AND ATTITUDE SENSOR MEASUREMENTS

Several sensors can provide missile range and attitude information. An inertial reference unit (IRU), the on-board seeker, and remote radar and theodolite ranging are discussed here.

An inertial reference unit consists of a package of precision accelerometers and gyros which provide missile position and attitude with respect to inertial space. Because of cost, only the longer range tactical missiles have an operational requirement for an IRU. Nevertheless an IRU may be provided as part of the flight test instrumentation. Position and attitude measurements from an IRU are subject to low frequency drift as a result of initial alignment errors and instrument biases. The IRU position drifts may be considerably larger than the radar position uncertainty. By correlating the radar range data with the IRU data, postflight IRU calibration

can be performed, resulting in estimates of instrument biases, scale factor errors, instrument nonorthogonalities, and initial alignments errors -- along with an optimal estimate of the missile trajectory and attitude time-history. This procedure can be performed using modern estimation methods, without a detailed missile airframe simulation. The inclusion of the postflight IRU calibration within the airframe identification algorithm is not required; however the capability of using the results from such an effort is provided.

Missile test ranges may utilize a variety of radars spaced along the missile ground track during a test flight. In addition phototheodolite sensors may be available to provide highly accurate triangulation ranging. Piecing together the various radar and/or theodolite measurements is a post-flight smoothing problem which must include detailed radar and theodolite error models; however, again an airframe model (Reference 11) is not required.

The missile inertial position estimates from combinations of radar, theodolite and IRU measurements will be considered as potentially available for the airframe identification problem. The measurements are modeled as follows:

$$\underline{r}_m^I = \underline{r}^I + \underline{\xi}_r \quad (26)$$

where

$\underline{r}_m^I$  = measured missile position vector  
 $\underline{\xi}_r$  = uncorrelated position measurement error

Modern filtering/smoothing methods frequently used for postflight trajectory generation provide not only trajectory estimates but position error statistics (i.e., the statistics of  $\underline{\xi}_r$ ), as well. Such data will interface directly with the method used in this study.



As indicated above, missile attitude can be obtained from the IRU. Attitude information may also be inferred from an onboard seeker. During a missile guidance flight test an operationally required onboard seeker may be used to track a target. In some cases the test target is fixed to the ground. During such a test the seeker attitude in body coordinates together with the target location provides a measure of missile attitude in inertial space. The attitude information and uncertainties from this measurement are highly seeker specific. Errors due to seeker gimbal dynamics, radome aberration effects and onboard signal processing must be investigated. These effects may be modeled using process and/or measurement noise.

Missile attitude information from an onboard IRU or seeker is modeled here by an Euler angle measurement,

$$\underline{v}_m = \underline{v} + \underline{\xi}_v \quad (27)$$

where

$\underline{v}_m$  = Euler angle measurement

$\underline{\xi}_v$  = uncorrelated angle measurement noise

This model assumes that IRU and seeker data reduction is performed separately, with the resulting attitude and attitude uncertainties stored for use with the identification algorithm.

## SECTION IV

### THE EXTENDED KALMAN FILTER FOR PARAMETER IDENTIFICATION

The extended Kalman filter is an extension of optimal (minimum-variance) linear filtering theory to problems which involve nonlinear dynamics and measurements, e.g., the aerodynamic coefficient estimation task. This section provides the background needed for understanding the EKF algorithm developed in this study. The discussion assumes a basic familiarity with random variables and state-space notation; additional details can be found in Reference 2.

#### KALMAN FILTER EQUATIONS

To apply Kalman filtering theory to any estimation problem, it is necessary to derive a linear, first-order, vector differential equation which models the manner in which the system states interact and propagate as functions of time. For linear systems, this equation has the general form\*

$$\dot{\underline{x}}(t) = F(t)\underline{x}(t) + G(t)\underline{w}(t) + \underline{u}(t) \quad (28)$$

where  $\underline{x}(t)$  is an  $n \times 1$  column vector representing the system state,  $F(t)$  is an  $n \times n$  dynamics matrix which defines the

---

\*Some overlap in symbol usage exists between this section and Sections II and III. The notation in this section is standardized in Reference 2, to which the reader can refer for further details.

interaction of the state vector components, and  $\underline{w}(t)$  is a  $p \times 1$  column vector of white gaussian noise inputs such that\*

$$E[\underline{w}(t)] = \underline{0}; \text{Cov}[\underline{w}] = E[\underline{w}(t)\underline{w}(\tau)^T] = Q(t)\delta(t-\tau) \quad (29)$$

The matrix  $G(t)$  is an  $n \times p$  distribution matrix which indicates how each component of  $\underline{w}(t)$  affects each component of the system state derivative, and  $\underline{u}(t)$  is a  $n \times 1$  column vector of known system inputs. Note that the  $F$ ,  $G$ , and  $Q$  matrices may be time-varying. For a missile airframe model, the elements of the state vector  $\underline{x}$  will typically be missile positions and velocities; the elements of  $\underline{w}$  will be random inputs such as airstream turbulence; and the elements of  $\underline{u}$  will be known inputs such as missile control surface deflections.

At discrete instants of time  $t_k$  it is assumed that measurements of linear combinations of the state variables are made. The equation describing this measurement process has the general form

$$\underline{z}_k = H_k \underline{x}_k + \underline{v}_k \quad (30)$$

where  $\underline{z}_k$  is a vector of  $r$  measured quantities at time  $t_k$ ,  $H_k$  is an  $r \times n$  observation matrix describing the linear combinations of state variables which comprise  $\underline{z}_k$  in the absence of noise, and  $\underline{v}_k$  is an  $r$ -vector of zero mean gaussian measurement errors with a covariance matrix  $R_k$  defined by

$$E[\underline{v}_k \underline{v}_j^T] = \begin{cases} [0] & ; \quad k \neq j \\ R_k & ; \quad k = j \end{cases} \quad (31)$$

---

\*The symbol  $E[ ]$  denotes mathematical expectation;  $\text{Cov}[\underline{w}]$  denotes the covariance matrix of  $\underline{w}$ .

At any time  $t$ , the objective of optimal estimation theory is to process all the measurements taken up to that time and produce an estimate  $\hat{\underline{x}}(t)$  of the system state  $\underline{x}(t)$  having minimum error, in a statistical sense. The optimization criterion most often chosen is that of minimizing the mean square estimation error. The minimum mean-square error estimate is calculated with the Kalman filtering algorithm.

As measurements become available, there is an instantaneous change in the knowledge of the state  $\underline{x}(t_k)$ . Denoting the optimum estimate of  $\underline{x}(t_k)$  just prior to the availability of  $\underline{z}_k$  as  $\hat{\underline{x}}_k(-)$  and the optimum estimate of the state vector immediately after processing  $\underline{z}_k$  as  $\hat{\underline{x}}_k(+)$ , the Kalman filter generates the optimum estimate of the system state according to the following algorithm:\*

$$\dot{\hat{\underline{x}}}(t) = F(t)\hat{\underline{x}}(t) + \underline{u}(t) ; \hat{\underline{x}}(t_{k-1}) = \hat{\underline{x}}_{k-1}(+) \quad (32)$$

$$\hat{\underline{x}}_k(+) = \hat{\underline{x}}_k(-) + K_k [\underline{z}_k - H_k \hat{\underline{x}}_k(-)] \quad (33)$$

where Eq. 4.1-5 is used to calculate the estimate between measurements and Eq. 4.1-6 is used to update the estimate when new data is received at each time  $t_k$ .

The quantity in brackets in Equation 33 is known as the measurement residual  $\hat{\underline{r}}_k$ . This vector quantity is the difference between the actual measurement  $\underline{z}_k$  and the optimal estimate of the measurement  $H_k \hat{\underline{x}}_k(-)$ . An important attribute of the Kalman filter is the whitening of the residual process. It can be shown that a Kalman filter produces a residual process  $\hat{\underline{r}}_k$  such that

---

\*Only the continuous form of the Kalman filter with discrete measurements is considered here.

$$E[\tilde{\underline{r}}_k \tilde{\underline{r}}_j^T] = 0 \quad k \neq j$$

In addition it is known that

$$\text{Cov} [\tilde{\underline{r}}_k \tilde{\underline{r}}_k^T] = [H_k P_k(-) H_k^T + R_k]^{-1}$$

The "whiteness" of the residual process and the consistency of the residual magnitudes with the predicted residual standard derivation is an excellent test for proper filter behavior.

The  $n \times r$  matrix  $K_k$  is the Kalman gain matrix. Let  $\tilde{\underline{x}}(t)$  denote the error made in estimating  $\underline{x}(t)$ , i.e.,

$$\tilde{\underline{x}}(t) = \hat{\underline{x}}(t) - \underline{x}(t) \quad (34)$$

and let

$$P(t) = \text{Cov}[\tilde{\underline{x}}(t)] = E[\tilde{\underline{x}}(t) \tilde{\underline{x}}(t)^T] \quad (35)$$

The gain matrix  $K_k$  is then computed using the following equations:

$$\dot{P}(t) = F(t)P(t) + P(t)F(t)^T + G(t)Q(t)G(t)^T \quad (36)$$

with  $P(t_{k-1}) = P_{k-1}(+)$  and

$$K_k = P_k(-) H_k^T [H_k P_k(-) H_k^T + R_k]^{-1} \quad (37)$$

$$P_k(+) = [I - K_k H_k] P_k(-) \quad (38)$$

where  $P_k(-)$  is  $P(t)$  just before the measurement at time  $t_k$  and  $P_k(+)$  is  $P(t)$  just after  $t_k$ . Equation 36 is used to calculate the estimation error covariance between the measurements; Equations 37 and 38 are used to calculate the Kalman

gain matrix for use in Equation 33 and to update the estimation error covariance matrix when a measurement arrives.

Figure 3 illustrates the procedure for processing measurements with the Kalman filter. The algorithm has two distinct phases. Equations 32 and 36 describe the time evolution of the state estimate and its error statistics between measurements under the influence of system dynamics and noise. This process is commonly referred to as extrapolation. Equations 33, 37, and 38 indicate how the estimate and its error covariance are updated at the measurement time to reflect the new information available. The algorithm is optimum in the minimum mean-square error sense as long as the assumed mathematical model for the system is accurate.

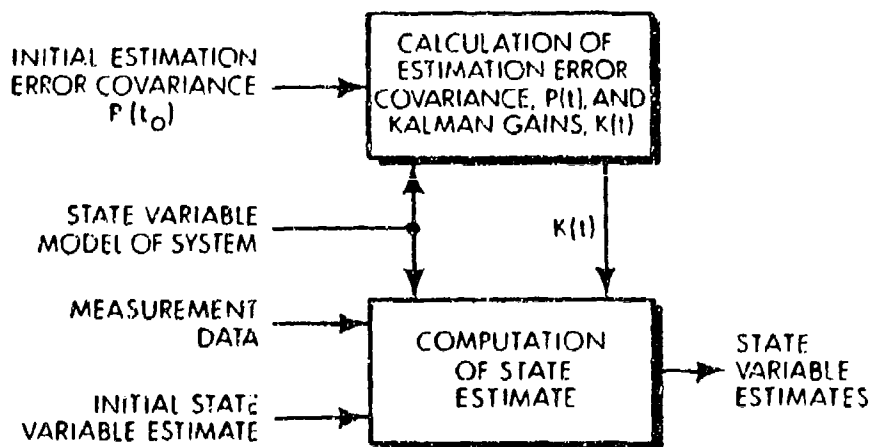


Figure 3. Measurement Processing with the Kalman Filter

A unique feature of the Kalman filter is that a measure of the estimation accuracy is automatically provided by the algorithm. The matrix  $P(t)$  is a complete description of the error statistics of the estimate. In particular, the square roots of the diagonal terms of  $P(t)$  represent the

standard deviations of the error obtained in estimating the components of  $\underline{x}(t)$ . Note that  $P(t)$  is specified for all time by Equations 36, 37 and 38. Thus estimation accuracy and the Kalman gains can be precomputed independently of the measurement sequence  $\underline{z}_k$ .

In summary, the following conditions must be met to implement an optimum Kalman filter:

- The system must be linear
- The matrices  $F(t)$ ,  $G(t)$ , and  $\underline{u}(t)$  must be known functions of time
- The vector input  $\underline{w}(t)$  must be a gaussian white noise process with known covariance matrix,  $Q(t)\delta(t-\tau)$ , and zero mean
- The measurements must obey Equation 30, and  $H_k$  must be known for all  $k$
- The measurement errors  $\underline{v}_k$  must be a gaussian white sequence with covariance matrix  $R_k$  and zero mean
- To initialize the filter equations, the initial statistics of  $\underline{x}$  must be known.

If the missile airframe identification problem could be put into a form which met all of the conditions listed above, the design of an optimal estimator would involve only the direct implementation of the Kalman filter equations. However, the airframe dynamics and measurements considered here are nonlinear; the linearity requirement is violated. Furthermore, the objective of estimating the uncertain aerodynamic coefficients, which is tantamount to estimating parameters of the matrix  $F$  in Equation 28, introduces additional nonlinearity. One means of overcoming these problems is the extended Kalman filter described in the next subsection.

## EXTENDED KALMAN FILTER EQUATIONS

Since the problem under consideration cannot be realistically modeled as a linear system, a nonlinear estimation technique must be used. The method selected here is the extended Kalman filter. The latter is essentially a conventional Kalman filter design applied to a mathematical model obtained by linearizing the system about the current state estimate. The structure of this algorithm is illustrated in Figure 4. Note that, because of the linearization procedure, the covariance calculation is now dependent upon the state estimate. Consequently, it is not possible to precompute the covariance matrix and Kalman gains, as functions of time, since they are dependent upon the measurement data. The extended Kalman filter yields very nearly optimal estimates if the linearization is accurate, i.e., as long as the state estimate is close to the true system state.

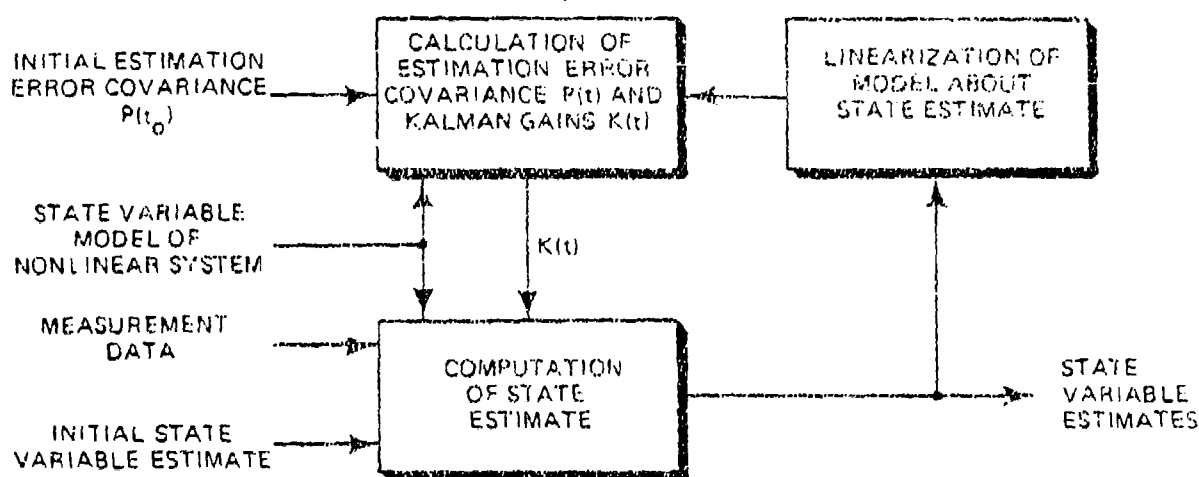


Figure 4. Structure of an Extended Kalman Filter



A reasonably general mathematical model for nonlinear stochastic systems is given by the equations

$$\dot{\underline{x}}(t) = \underline{f}[\underline{x}(t), t] + G(t)\underline{w}(t) \quad (39)$$

$$\underline{z}_k = \underline{h}_k[\underline{x}(t_k)] + \underline{v}_k ; k = 1, 2, \dots \quad (40)$$

where  $\underline{f}$  and  $\underline{h}_k$  are nonlinear differentiable functions of the state vector  $\underline{x}$ , and  $\underline{w}(t)$  and  $\underline{v}_k$  are zero mean, independent gaussian white noise processes having spectral density and covariance matrices  $Q(t)$  and  $R_k$ , respectively. The measurements  $\underline{z}_k$  are taken at discrete times  $t_k$ .

The first approach one might use to derive a filtering algorithm for  $\underline{x}(t)$  in Equation 39 is to linearize the nonlinear functions  $\underline{f}$  and  $\underline{h}_k$  about an appropriate known reference trajectory  $\bar{\underline{x}}(t)$ , and then apply conventional linear estimation theory, i.e., the Kalman filter discussed in the last subsection. Thus, denoting  $\underline{x}(t_k)$  by  $\underline{x}_k$ , the expressions

$$\underline{f}(\underline{x}, t) \approx \underline{f}(\bar{\underline{x}}, t) + \left. \frac{\partial \underline{f}}{\partial \underline{x}} \right|_{\underline{x}=\bar{\underline{x}}} (\underline{x} - \bar{\underline{x}}) \quad (41)$$

$$\underline{h}_k(\underline{x}_k) \approx \underline{h}_k(\bar{\underline{x}}_k) + \left. \frac{\partial \underline{h}_k}{\partial \underline{x}_k} \right|_{\underline{x}_k=\bar{\underline{x}}_k} (\underline{x}_k - \bar{\underline{x}}_k) \quad (42)$$

may be substituted into Equations 39 and 40 to derive the corresponding Kalman filter which estimates the variation in  $\underline{x}$ , from the reference trajectory. When the reference trajectory is chosen to be the current best estimate of the state  $\hat{\underline{x}}(t)$ , the resulting algorithm is known as an extended Kalman filter (EKF); the mechanization equations for the latter are given in Table 6 (see also Reference 2).

TABLE 6. SUMMARY OF THE EXTENDED KALMAN FILTER

System Model	$\dot{\underline{x}}(t) = \underline{f}(\underline{x}(t), t) + \underline{G}(t)\underline{w}(t) ; \underline{w}(t) \sim N(0, Q(t))$
Measurement Model	$\underline{z}_k = \underline{h}_k[\underline{x}(t_k)] + \underline{v}_k ; k = 1, 2, \dots ; \underline{v}_k \sim N(0, R_k)$
Initial Conditions	$\underline{x}(0) \sim N(\underline{\hat{x}}_0, P_0)$
Other Assumptions	$E[\underline{w}(t)\underline{v}_k^T] = 0$ for all $k$ and all $t$
State Estimate Propagation	$\underline{\hat{x}}(t) = \underline{F}[\underline{\hat{x}}(t_k), t]$
Error Covariance Propagation	$\dot{P}(t) = F[\underline{\hat{x}}(t), t] P(t) + P(t) F[\underline{\hat{x}}(t), t]^T + G(t)Q(t)G(t)^T$
State Estimate Update	$\underline{\hat{x}}_k(t) = \underline{\hat{x}}_k(-) + K_k[\underline{z}_k - \underline{h}_k[\underline{\hat{x}}_k(-)]]$
Error Covariance Update	$P_k(t) = \{1 - K_k H_k[\underline{\hat{x}}_k(-)]\} P_k(-)$
Gain Matrix	$K_k = P_k(-) H_k[\underline{\hat{x}}_k(-)]^T \{H_k[\underline{\hat{x}}_k(-)] P_k(-) H_k[\underline{\hat{x}}_k(-)]^T + R_k\}^{-1}$
Definitions	$F[\underline{\hat{x}}(t_k), t] = \frac{\partial \underline{f}(\underline{\hat{x}}(t), t)}{\partial \underline{\hat{x}}(t_k)} \bigg _{\underline{x}(t) = \underline{\hat{x}}(t)}$ $H_k[\underline{\hat{x}}_k(-)] = \frac{\partial \underline{h}_k[\underline{x}(t_k)]}{\partial \underline{x}(t_k)} \bigg _{\underline{x}(t_k) = \underline{\hat{x}}_k(-)}$

The matrix  $P(t)$  in Table 6 is a first-order approximation to the estimation error covariance matrix, and  $\underline{x}_k(-)$  and  $P_k(-)$  denote the solutions to the propagation equations at time  $t_k$  just before the  $k$ th measurement is processed. Note that the EKF equations reduce to the optimal Kalman filter outlined in the last section if

$$\underline{f}(\underline{x}(t), t) = F(t)\underline{x}(t) + \underline{u}(t) \quad (43)$$

and

$$\underline{h}_k(\underline{x}(t_k)) = H_k \underline{x}(t_k) \quad (44)$$

## IMPLEMENTATION CONSIDERATIONS

### THE PARTITIONED FORM

The application of the EKF to parameter identification is straightforward. An augmented state is defined as

$$\underline{x} = \begin{bmatrix} \underline{x}_s \\ \underline{a} \end{bmatrix}$$

where  $\underline{x}_s$  is the dynamic state vector and  $\underline{a}$  is the uncertain parameter vector. The required first order differential equation for  $\underline{x}$  is given by

$$\dot{\underline{x}} = \begin{bmatrix} \dot{\underline{x}}_s \\ \dot{\underline{a}} \end{bmatrix} = \begin{bmatrix} f(\underline{x}_s(t), \underline{a}, t) \\ \underline{0} \end{bmatrix} + \begin{bmatrix} G \underline{w}(t) \\ \underline{0} \end{bmatrix} \quad (45)$$

For large state vectors the primary computational burden of the EKF is in the propagation of the state covariance between measurements (Equation 36). As an example, consider an airframe parameter estimation problem containing 50 parameters and 18 dynamic states. For this sample case the augmented state is of length 68. The augmented state covariance matrix will have 2346 unique elements.\* Thus an extended Kalman filter for a state of order 68 would have to numerically integrate  $2346 + 68 = 2414$  scalar equations.

The numerical integration burden can be reduced by partitioning the augmented state covariance matrix into a

---

\*An  $n \times n$  symmetric covariance matrix contains  $n(n+1)/2$  unique elements.

dynamic state covariance  $P_{ss}$ , a parameter covariance  $P_{aa}$  and the state-parameter "cross covariance"  $P_{sa}$ . The augmented state covariance  $P$  is given by

$$P = \begin{bmatrix} P_{ss} & P_{sa} \\ P_{sa}^T & P_{aa} \end{bmatrix}$$

The resulting equations become

$$\dot{P}_{ss} = \underline{f}_{\underline{x}_s} P_{ss} + P_{ss} \underline{f}_{\underline{x}_s}^T + \underline{f}_{\underline{a}} P_{sa}^T + P_{sa} \underline{f}_{\underline{a}}^T + GQG^T \quad (46)$$

$$\dot{P}_{sa} = \underline{f}_{\underline{x}_s} P_{sa} + \underline{f}_{\underline{a}} P_{aa} \quad (47)$$

$$\dot{P}_{aa} = [0]$$

where elements of the matrices  $\underline{f}_{\underline{x}_s}$  and  $\underline{f}_{\underline{a}}$  are given by,

$$\left[ \underline{f}_{\underline{x}_s} \right]_{ij} = \frac{\partial f_i(\underline{x}_s, \underline{a}, t)}{\partial x_{sj}}$$

$$\left[ \underline{f}_{\underline{a}} \right]_{ij} = \frac{\partial f_i(\underline{x}_s, \underline{a}, t)}{\partial a_j}$$

Note that the parameter covariance  $P_{aa}$  is constant between measurements and thus requires no integration. For the 50-parameter, 18-state example the numerical integration requirements are now 1089 scalar equations, or a savings of over 50 percent.

## PARTIAL DERIVATIVES

Four partial derivative matrices are required by the partitioned form of the EKF.

- Partial derivatives of dynamic state derivatives with respect to dynamic states  $\underline{f}_{\underline{x}_s}$
- Partial derivatives of dynamic state derivatives with respect to parameters  $\underline{f}_{\underline{a}}$
- Partial derivatives of measurements with respect to state  $\underline{h}_{\underline{x}_s}$
- Partial derivatives of measurements with respect to parameters  $\underline{h}_{\underline{a}}$

These partial derivatives are computed analytically during the course of the numerical integration. Conventional though tedious algebraic methods are used in the derivation of these equations. Because of the required generality of the resulting filtering algorithm, no simplifying assumptions were made.

In addition to the analytic partial derivatives, a numerical partial derivative calculation has been utilized. The latter is useful for two reasons. First, it offers an independent verification of the analytic partial derivatives, and second it can provide an indication of the linearity of the dynamic equations in a region about the augmented state estimate.

The numerical partial derivative is based upon a two sided perturbation of the function to be differentiated -- i.e., both plus and minus perturbations are used. The perturbation step size is determined based on the standard deviation of the dynamic state or parameter with respect to which the derivative is to be taken. Thus linearity of the dynamics in a

statistically defined region about the state and parameter estimate is assumed in the calculation of the numerical partial derivatives. Recall that accurate linearization is one of the fundamental assumptions required in order for the EKF to be a near-optimal estimator. Thus correlation between the analytical and numerical partial derivative calculations provides both an indication of the correctness of the analytical partials as well as providing a necessary condition for optimality of the EKF parameter estimates.

#### IDENTIFICATION OPTIONS

In the most general form of the missile model presented in Sections II and III there are 22 dynamic states, 14 measurements, and approximately 150 parameters to be estimated. A summary of the quantities contained in each of these categories is given in Table 7. The filtering algorithm is structured so as to allow subsets of the most general case to be exercised with particular attention given to allowing a flexible parameter set. The aerodynamic parameters are implemented so that particular parameters may be selected for estimation while the remainder may be fixed at preset values. It is anticipated that less than 50 parameters will be estimated at one time for any particular case.

Certain options are available which reduce the computational burden during the calculation of the analytical partial derivatives. These options are listed in Table 8.

#### COMPUTATIONAL REQUIREMENTS

The present algorithm is coded in FORTRAN IV and implemented in single precision in an IBM 360/145 computer. Core requirements are approximately 340K IBM 360 bytes based

TABLE 7. DYNAMIC STATES, MEASUREMENTS AND PARAMETERS

NO.	DESCRIPTION
<u>Dynamic States</u>	
1-3	Missile Velocity in Body Axes
4-6	Missile Position in Inertial Axes
7-9	Missile Body Rotation Rate
10-12	Missile Euler Angles
13-15	Missile Acceleration Perturbation Components
16-18	Missile Moment Perturbation Components
19-20 *	$\alpha$ Sensor Dynamic States
21-22 *	$\beta$ Sensor Dynamic States
<u>Measurements</u>	
1-3	Body Fixed Accelerometers
4-6	Body Fixed Rate Gyros
7-8	$\alpha$ - $\beta$ Sensor
9-11	Position Measurements
12-14	Attitude Measurements
<u>Potential Parameter List</u>	
1-40	Aerodynamic Force Coefficients
41-100	Aerodynamic Moment Coefficients
101-103	Wind Bias Uncertainty
104 *	Atmospheric Density Uncertainty
105-106 *	Thrust Misalignment
107 *	Thrust Bias
108 *	Mass Uncertainty
109-111 *	Moments of Inertia
112-114 *	CG Locations
115-117 *	Perturbation Force Time Constant
118-120 *	Perturbation Moment Time Constant
121-123 *	Perturbation Force Scale Factor
124-126 *	Perturbation Moment Scale Factor
127-129	Accelerometer Bias
130-132	Accelerometer Scale Factor
133-135	Gyro Bias
136-138	Gyro Scale Factor
139-148 *	Gyro G Sensitivities
149-150 *	$\alpha$ - $\beta$ Sensor Natural Frequencies
151-152 *	$\alpha$ - $\beta$ Sensor Damping Ratios
153-154 *	$\alpha$ - $\beta$ Sensor Bias
155-156 *	$\alpha$ - $\beta$ Sensor Scale Factor Errors

\*These options are not presently implemented in the identification algorithm.

TABLE 8. ALGORITHM COMPUTATIONAL OPTIONS

OPTION	EXPLANATION
No Wind	All wind calculations are bypassed
No Thrust	Thrust is assumed zero and mass properties are constant
No CG Translation	No moment translation due to CG offset is considered
No $\alpha$ , $\beta$ required	The aerodynamic moments are not a function of $\alpha$ or $\beta$

on the maximum allowable\* problem dimensions given by Table 9. The two test cases given in the table, discussed in detail in Section V, provide examples of the algorithm execution times. Execution of test case 1 requires approximately 7 minutes while test case 2 required 17.5 minutes.

TABLE 9. PROGRAM SPECIFICATIONS

PROGRAM SPECIFICATION	MAXIMUM ALLOWABLE	TEST CASE 1	TEST CASE 2
Number of dynamic states	18	18	18
Number of estimated parameters	50	11	36
Number of measurements at each sample time	10	8	8
Number of measurement samples	650	100	100
Integration steps per measurement	x	1	1

\*Maximum allowable dimensions are easily modified by re-compiling the algorithm source code.



Previous experience with conversion of computer algorithms similar to the one proposed here to a CDC 6600 computer indicate an improvement in execution time of at least a factor of five. Core requirements should be within 120K CDC 6600 words.

## SECTION V

### ALGORITHM VERIFICATION WITH SYNTHETIC DATA

#### INTRODUCTION

The algorithm verification results presented in this section are based on the processing of computer-generated synthetic measurements from an airframe model of an existing short-range air-to-air intercept missile. The primary purpose of these studies is to demonstrate the validity of the extended Kalman filter as an identification algorithm, with a controlled test case. The actual state and parameter estimation errors are compared to the statistics of these errors as predicted by the algorithm. Consistency between the actual errors and the predicted statistics is an indication of proper filter performance.

Divergence of the estimation errors from the filter predicted error standard derivations can result from several sources, such as:

- Inconsistency between the measurement generator model and the filter design model
- Analytical or programming errors
- Numerical precision (word length)
- Inaccurate linearization.

The first error source is removed from consideration in the controlled experiment discussed here -- certain subprograms used within the filter algorithm are shared by the measurement generation routine insuring model consistency.

Because of the complexity and generality of the dynamic state equations, the major source of error has been with the analytical derivation and programming of the analytical partial derivative calculations. The numerical partial derivative calculation provides an independent verification of the analytical computations.

Filter inaccuracies caused by numerical precision are frequently encountered in large scale Kalman filtering problems. Special purpose filtering equations, such as square root filter algorithms (Reference 2), are often implemented solely for the purpose of avoiding word length difficulties. All results presented in this report were performed using IBM 360 single precision arithmetic. Several identification failures have occurred in instances with no process noise and low measurement uncertainty -- resulting in highly accurate parameter and state estimation accuracy. These failures were attributed to precision difficulties. With normal measurement noise and process noise inputs no precision difficulties have arisen.

Filter divergence resulting from violation of the linearity requirement is a common problem in the application of extended Kalman filters (Reference 12). This problem can sometimes be solved by using accurate initialization methods, the injection of process noise, or resorting to more complex filters based on second order Taylor series expansions, such as the second-order Gaussian filter (Reference 12). Fortunately, the cases investigated here have demonstrated remarkable linearity for large parameter and initial state uncertainty. This result has been verified through the numerical partial derivative computations mentioned previously.

A distinction between two types of models must be made in the discussion of filter evaluation with synthetic data. One model is used for generating synthetic measurements while a second model is used within the filter. For the majority of the discussion in this section, these models have identical structure -- yet differ by parameter values, state initial condition values, and process noise inputs.

The short-range air-to-air interceptor model used for generating measurements was designed to exercise the various modeling options discussed in Sections II and III. Its mass characteristics, thrust model and aerodynamic coefficients are typical of existing missile configurations. The coefficient values chosen for measurement generation were selected by a Gaussian random number generator with mean values equal to representative wind tunnel values and standard deviations of about 25 percent of the mean. The resulting aerodynamic model corresponds to no actual missile but provides a suitable demonstration case. The airframe has no pitch rate or acceleration feedback for stability augmentation and thus stable missile flight can be achieved by commanding open loop aerodynamic control surface (canards in this case) deflections. The roll aerodynamics were not modeled -- aerodynamic roll coefficients were fixed at zero -- and yet considerable roll motion was induced from the roll perturbation moments. The linear pitch, yaw and drag aerodynamic coefficients were assigned values near the low angle-of-attack wind tunnel values for the short-range interceptor.

The data shown in this section were taken during the first two seconds of missile flight. The missile velocity variation is from Mach 1.1 to Mach 1.6 during this time. Time-varying thrust and mass characteristics are modeled during this period.

## A NOMINAL TEST CASE

A test case is discussed in detail in this section in order to demonstrate the algorithm output. Subsequent subsections present variations to this case.

The aerodynamic model used consists of 11 basic pitch, yaw, and drag linear aerodynamic terms. If the missile dynamic response can be restricted to within a suitably small region about some known reference condition during the period of identification, this parameter set will accurately represent the airframe response without additional nonlinear terms. This set of coefficients is widely used for missile performance studies and autopilot design studies, and values for these terms are relatively well known prior to flight test. We assume during this test that these basic aerodynamic terms are known to within about 25 percent (one sigma). These 11 parameters, the values used for filter initialization, and the initial parameter uncertainty assumed within the filter model are given in Table 10. The "true" parameter values used for measurement generation (also shown in Table 10) were computed from a Gaussian random number generator using statistics identical to the filter model. The resulting aerodynamic force and moment model is given by Table 11.

The test flight simulated here is representative of an air launched flight from about 22,000 feet altitude at Mach 1.1. The mean initial dynamic state values and their standard deviations are given in Table 12. The initial state uncertainties are realistic for flight tests of the airframe studied here.

The aerodynamic control surface deflections for the nominal case were not designed specifically for the purpose of aerodynamic parameter estimation. The pitch and yaw control

TABLE 10. FILTER INITIALIZATION AND PERFORMANCE  
SUMMARY FOR NOMINAL TEST CASE

PARAMETER	INITIALIZATION			ESTIMATION PERFORMANCE		
	FILTER ESTIMATE	FILTER STANDARD DEVIATION	TRUE VALUE	FILTER ESTIMATE	FILTER STANDARD DEVIATION	$n_{\sigma}$
$C_{x_0}$	-1.63	0.4	-1.00	-2.05	0.0361	1.6
$C_{y_0}$	-43.55	10.0	-33.47	-34.4	0.574	1.6
$C_{y_{dr}}$	- 0.044	0.01	- 0.049	- 0.048	0.00448	0.20
$C_{z_0}$	-43.55	10.0	-42.12	-43.1	0.592	1.5
$C_{z_{dq}}$	- 0.044	0.01	- 0.041	- 0.0478	0.00601	1.1
$C_{M_n}$	-200.55	50.0	-172.24	-173.6	3.44	1.3
$C_{M_{dq}}$	2.9	0.7	3.26	3.35	0.0843	1.07
$C_{M_q}$	-12500	3000.0	10432	-10438	1022.0	0.01
$C_{M_{\theta}}$	200.55	50.0	166.53	172.9	3.30	1.9
$C_{N_{dr}}$	-2.9	0.7	-2.5	-258	0.0608	1.3
$C_{N_r}$	-12500	3000.0	12892	-10978	850	2.2

TABLE 11. NOMINAL TEST CASE AERODYNAMIC MODEL

AERODYNAMIC OUTPUT	MATHEMATICAL MODEL
x Body Force	$AQC_{x_0}$
y Body Force	$AQ(C_{y\beta}\beta + C_{y\delta r}\delta r)$
z Body Force	$AQ(C_{z\alpha}\alpha + C_{z\delta q}\delta q)$
Moment About x	0
Moment About y	$AQQ(C_{M\alpha}\alpha + C_{M\delta q}\delta q + C_{M\dot{q}}\dot{q} \frac{D}{2V_M})$
Moment About z	$AQQ(C_{N\beta}\beta + C_{N\delta q}\delta q + C_{N\dot{r}}\dot{r} \frac{D}{2V_M})$

TABLE 12. NOMINAL INITIAL DYNAMIC STATE STATISTICS

STATE	UNITS	MEAN	STANDARD DEVIATION
Body Velocity (x)	ft/sec	1160.0	100.0
Body Velocity (y)	ft/sec	0.0	20.0
Body Velocity (z)	ft/sec	0.0	20.0
Inertial Position (x)	ft	0.0	200.0
Inertial Position (y)	ft	0.0	200.0
Inertial Position (z)	ft	-22100	200.0
Body Rotation Rate About x	rad/sec	0.0	0.20
Body Rotation Rate About y	rad/sec	0.0	0.20
Body Rotation Rate About z	rad/sec	0.0	0.20
Roll Euler Angle $\phi$	rad	0.0	0.04
Pitch Euler Angle $\theta$	rad	0.0	0.04
Heading Euler Angle $\psi$	rad	0.0	0.04

deflections were extracted from simulation of an air-to-air target engagement. The pitch and yaw control histories are shown in Figures 5 and 6. An operationally required 0.4-second control input delay is indicated on these figures.

Six process noise inputs were included as perturbation inputs to the force and moment equations in generating the synthetic measurement data. Noise was processed through low pass filters to generate time-functions representative of the appropriate correlated process noise inputs. The perturbation inputs are specified by their noise bandwidth and rms magnitude. A bandwidth of 10 rad/sec (0.1-second correlation time) was selected for all perturbation inputs. The noise entering the acceleration equations ( $\underline{r}_f$ ) is given the same rms acceleration level as the acceleration measurement uncertainty --  $2 \text{ ft/sec}^2$  (0.06 g). The moment perturbations

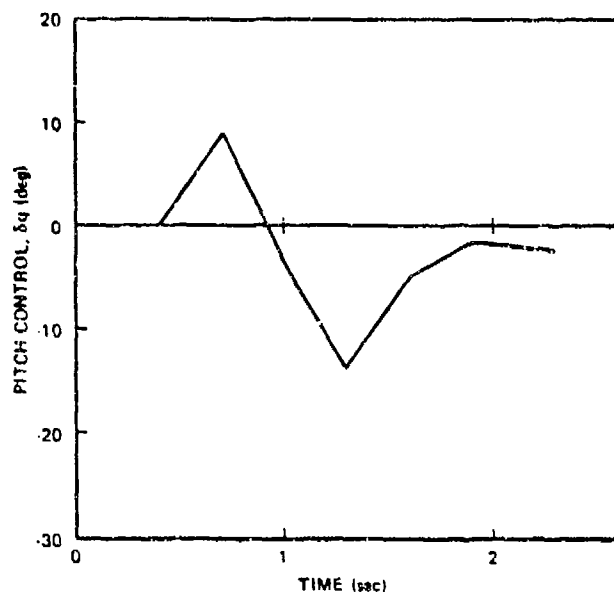


Figure 5. Pitch Control for Nominal Test Case



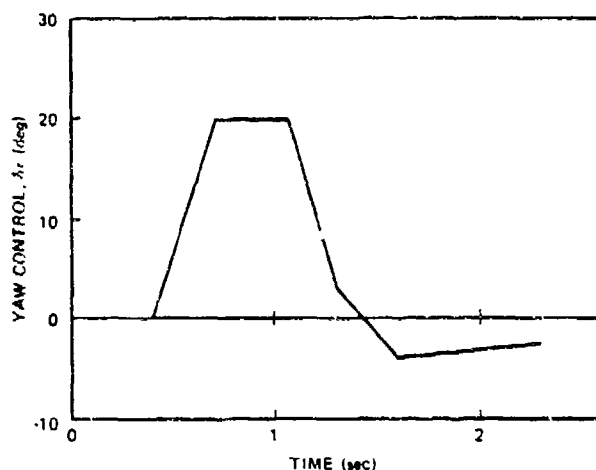


Figure 6. Yaw Control for Nominal Test Case

are given rms magnitudes of 50 ft-lb in pitch and yaw, and 10 ft-lb in roll -- roughly equivalent to a 0.3-degree rms noise level on control deflection measurement or a 5-ft/sec wind gust rms level. A typical realization of the perturbation input is given by Figure 7. This particular sample was input as the body x-axis force perturbation for the nominal case.

Measurements considered for the nominal test case were three accelerometers located near the missile nose, three body rate gyros and the  $\alpha$ - $\beta$  sensors. White noise sequences were used for the measurement error models. The noise levels (one sigma) are given in Table 13. The measurement sample rate was 50 hertz for this case.

TABLE 13. NOMINAL MEASUREMENT NOISE LEVELS

MEASUREMENTS	UNITS	STANDARD DEVIATION
All Accelerometers	ft/sec <sup>2</sup>	2.0
All Rate Gyros	rad/sec	0.02
$\alpha$ - $\beta$ Sensors	rad	0.02

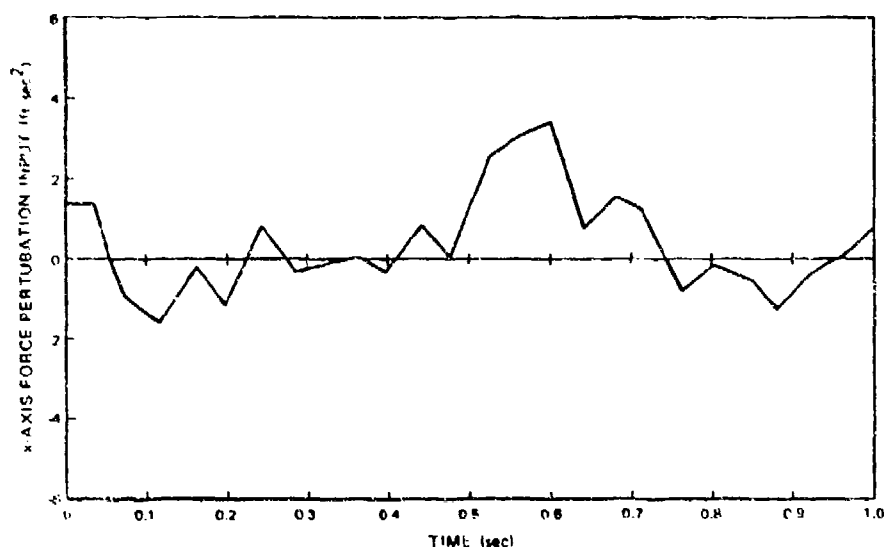


Figure 7. Typical Perturbation Force Input  
For the Nominal Test Case

The estimates of the aerodynamic coefficients used to initialize the identification algorithm must be approximately correct in order for the EKF to provide useful results. The required accuracy of the a priori model cannot be generalized and will vary from case to case. Nevertheless any obvious errors, such as control input sign errors, etc, should be removed prior to attempting parameter identification. Assistance in initial model checkout is provided by simply integrating the a priori model and comparing the result with the flight measurements. The comparison for the nominal test case discussed above is presented in Figure 8. The trajectory mismatch indicated by this figure results from initial condition errors, parameter errors, and the process noise inputs.

The roll rate response resulting from the process noise input utilized for measurement generation can be seen

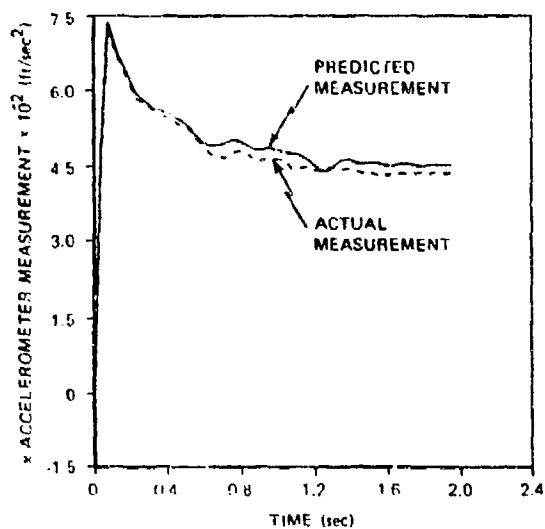
from Figure 8(d). The roll angle resulting from this case was approximately 560 degrees after 2 seconds -- realistic for an airframe without roll stabilization. The predicted roll rate is zero -- indicating no a priori information about the roll response is assumed. The predicted pitch and yaw rotation rate responses exhibit large deviations from the actual as a result of process noise and parameter uncertainty. This rotation rate sensitivity to parameter errors indicates that measurements of rotation rate should be useful for parameter identification.

The angle-of-attack and sideslip responses resulting from the control input are larger than those from a more realistic model of this airframe because of the omission of the nonlinear aerodynamic effects. Nevertheless the extreme variation in angular motion offers an excellent test of the extended Kalman filter ability to identify parameters. Identification in situations having different angle-of-attack and sideslip time-histories is discussed in the subsections to follow.

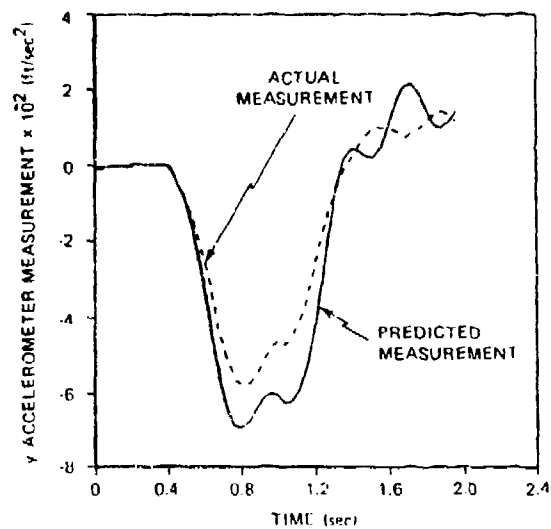
The interpretation of parameter identification results and the verification of accurate filter performance is aided by the visualization of a variety of algorithm outputs. The following variables are available from the EKF as functions of time.

- State estimate and state estimation accuracy
- Parameter estimates and parameter estimation accuracy
- EKF residual process and its one sigma bounds.

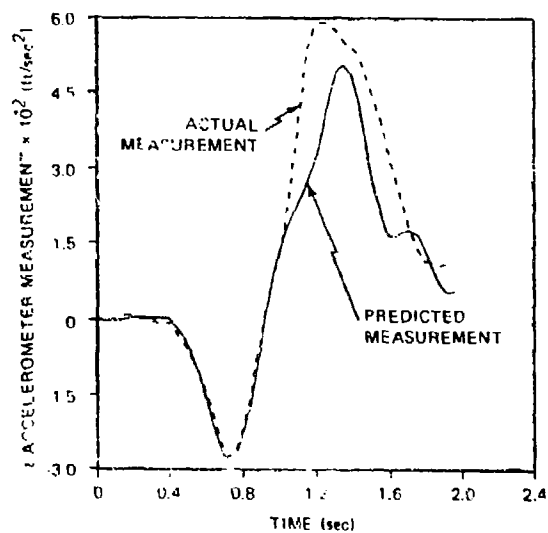
In addition, parameter-to-parameter correlation coefficients are useful since individual parameters may be highly



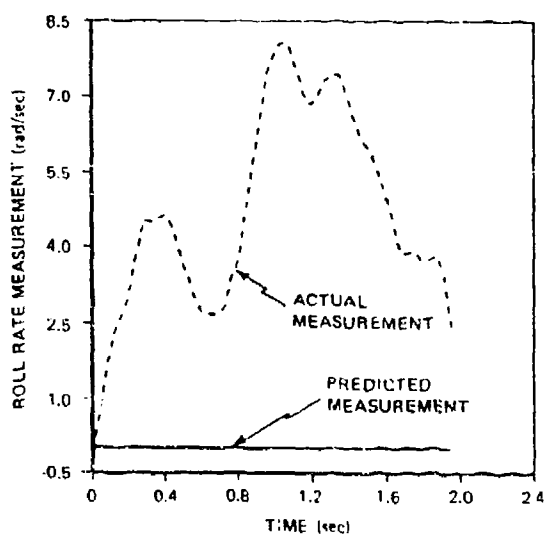
(a) x-Accelerometer



(b) y-Accelerometer

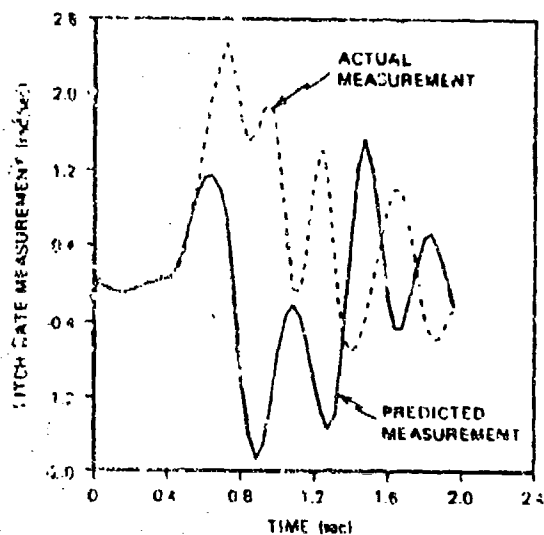


(c) z-Accelerometer

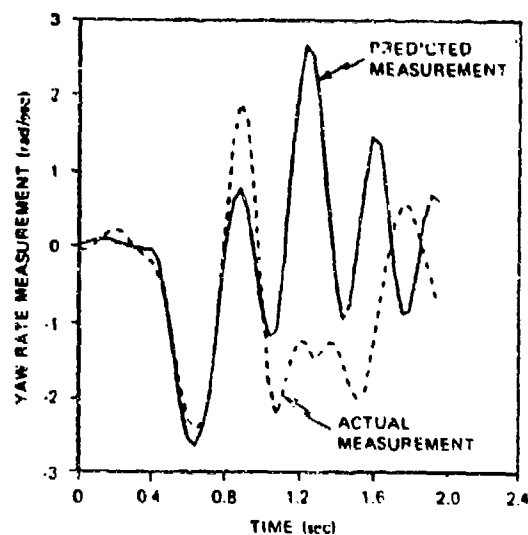


(d) Roll Rate

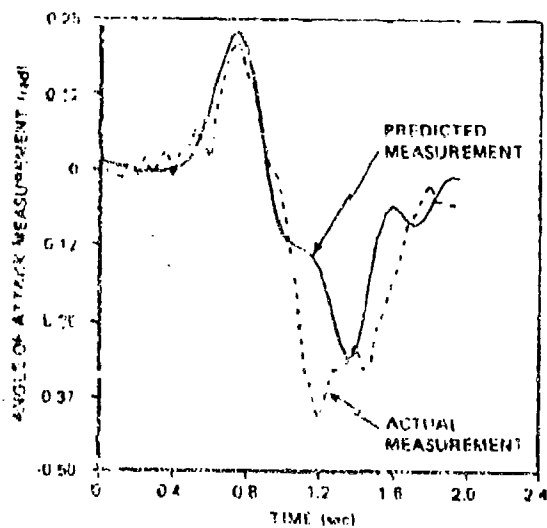
Figure 8. A Priori Measurement Time-History



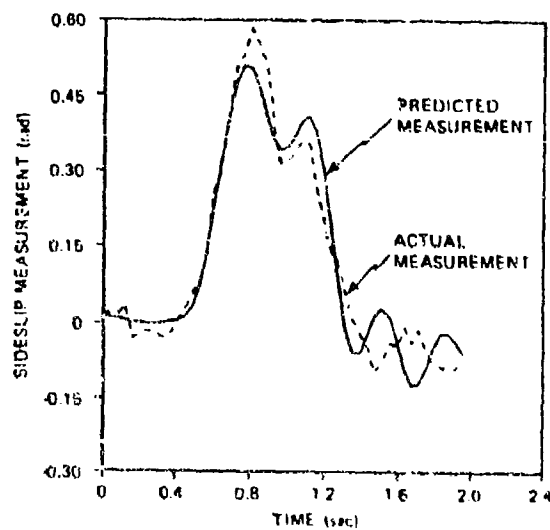
(e) Pitch Rate



(f) Yaw Rate



(g) Angle-of-Attack



(h) Sideslip

Figure 8. A Priori Measurement Time-History (Concluded)

unobservable and yet highly correlated -- indicating some linear combination of parameters may be estimated. Parameter-to-dynamic state correlations are also available and may allow insight into additional measurements which would produce better parameter observability.

When synthetic measurements are processed, the actual parameter and state values are available as well as the filter estimates. Thus, actual state and parameter estimation errors may be computed and compared to the predicted one sigma error bounds as functions of time. The parameter errors, state errors, residuals and all respective one sigma bounds for the test case discussed above are contained in Appendix A.

The results in Appendix A must be interpreted in a statistical sense -- recall that a normally distributed random quantity is within one sigma 68.3 percent of the time, within two sigma 95.5 percent of the time, and within three sigma 99.7 percent of the time. The data in Appendix A represents only one sample generated by an initial starting seed to a random number generator. A more thorough statistical analysis requires a large number of random trials and the collective interpretation of the ensemble results. This monte carlo type of filter evaluation has not been performed because of the expense of computing several monte carlo samples. Nevertheless the single sample results for state and parameter estimation contained in Appendix A are a useful indication of acceptable filter performance.

An additional performance indicator lies in the whiteness of the filter residuals. Visual verification of residual whiteness and correspondence of the residual magnitudes with their one sigma bounds shows excellent filter performance as seen in Figure A-3 of Appendix A.

A useful summary of the parameter estimation performance for the nominal case is given in Table 5. This table includes true parameter values, final filter estimates, final filter standard deviations and a figure of merit referred to as  $n_o$ . A value of  $n_o$  greater than about three indicates a highly improbable parameter error and thus, possibly poor filter performance. The value of  $n_o$  is computed according to:

$$n_{oi} = \frac{|\hat{a}_i - a_i|}{\sigma_i}$$

where

$\hat{a}_i$  = estimate of  $i^{\text{th}}$  parameter

$a_i$  = actual value of  $i^{\text{th}}$  parameter

$\sigma_i$  = filter predicted standard deviation

In practical applications where the actual model structure and parameter values are unknown, good correlation between the predicted measurements from the filter and the actual measurements is an indication of acceptable filter operation. Yet if the final parameter estimates from filtering are inserted into an otherwise a priori model, a poor correlation between computed and actual measurements may result. Small levels of omitted disturbance inputs (process noise) or erroneous state initial conditions may have a significant effect when integrated over many samples. This phenomenon is demonstrated using the nominal test case. The computed pitch rate agreement with the measured pitch rate shown by Figure 9 is not significantly improved when compared with Figure 8(e).

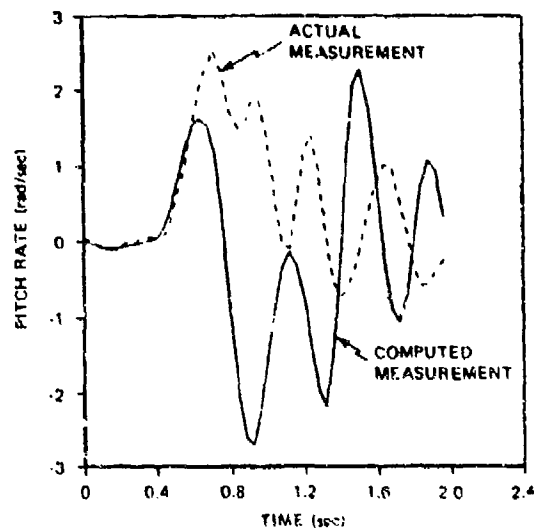


Figure 9. Computed Pitch Rates Using Final Parameter Estimates, A Priori Initial Conditions and no Process Noise

An alternative procedure can be used to indicate improved parameter accuracy when synthetic data is used. In this case, state initial conditions and process noise inputs are known perfectly. Thus, a priori parameter values can be used with perfect state initial conditions and known disturbance inputs to demonstrate the model uncertainty resulting from initial parameter errors alone. Figure 10 shows the pitch rate measurement agreement in this case. A similar trajectory produced using the final parameter estimates (with perfect state initial conditions and process noise) resulting from filtering should show improved agreement-- indicating model improvement. This is demonstrated in Figure 11 where excellent agreement is obtained between actual and predicted pitch rate measurement. Although not included here, similar excellent agreement occurs for the remaining measurements.



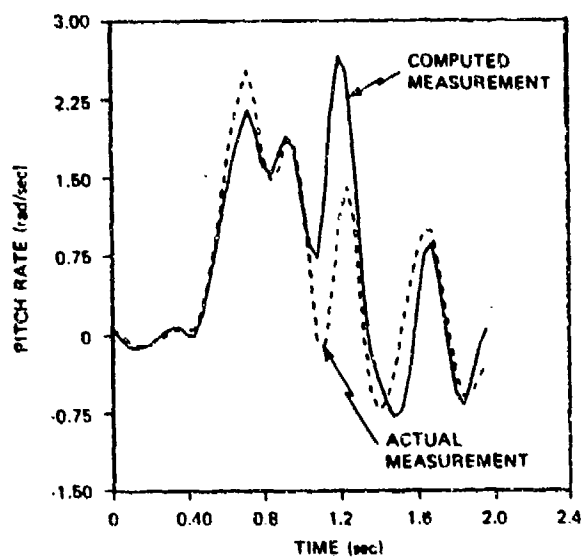


Figure 10. Computed Pitch Rate Using A Priori Parameter Values, Perfect Initial Conditions and Correct Process Noise

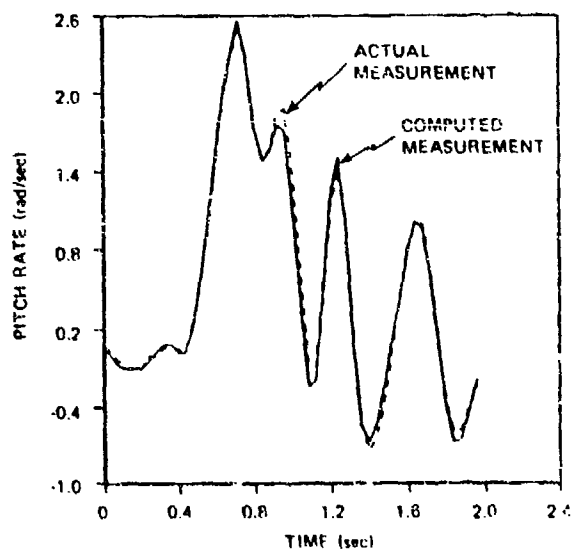


Figure 11. Computed Pitch Rate Using Final Parameter Values, Perfect Initial Conditions, and Correct Process Noise

An alternate model will be used as a reference in certain sensitivity studies to be shown in the sections to follow. This alternate nominal case includes an erroneous CG translation term and yet the resulting sensitivity studies provide useful performance data. An erroneous sign of the CG translation term resulted in a more stable airframe and smaller angle-of-attack and sideslip responses to the control inputs given in Figures 5 and 6. The angle-of-attack and sideslip responses for this case are shown in Figures 12 and 13. The initialization and measurement uncertainties are identical to those used previously. A summary of the parameter identification performance is given in Table 14. Note that the parameter estimation accuracy predicted by the filter is worse in all cases than for the previously defined nominal case (Table 10). This is a direct result of the reduced  $\alpha$  and  $\beta$  responses for this case -- also note that the values of  $n_c$  in most cases are below those in Table 10.

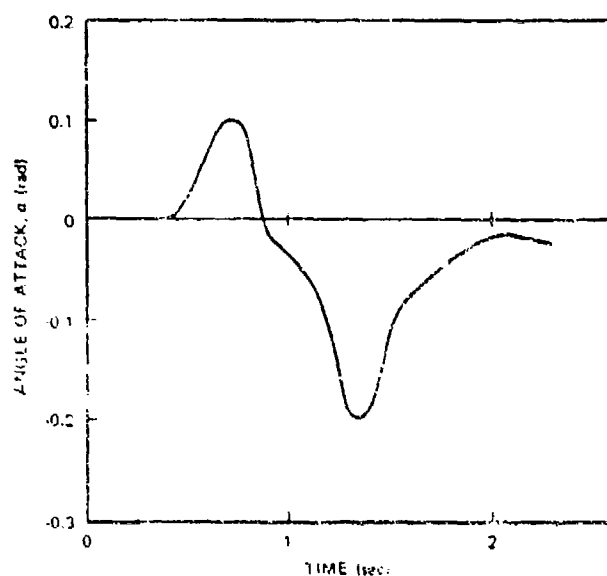


Figure 12. Angle-of-Attack from Alternate Nominal Test Case

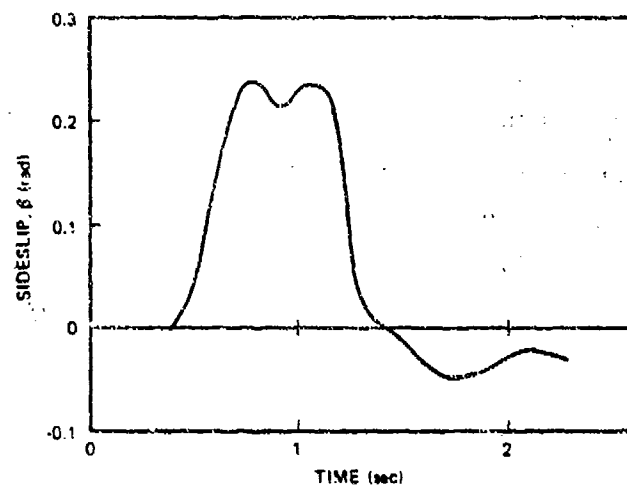


Figure 13. Sideslip from Alternate Nominal Test Case

TABLE 14. FILTER PERFORMANCE SUMMARY FOR ALTERNATE NOMINAL TEST CASE

PARAMETER	ESTIMATION PERFORMANCE		
	FILTER PARAMETER ESTIMATE	FILTER STANDARD DEVIATION	$n_{\sigma}$
$C_{x_0}$	-2.07	0.0064	1.7
$C_{y_{\beta}}$	-34.4	0.784	1.2
$C_{y_{\delta r}}$	-0.052	0.0045	0.66
$C_{z_u}$	-43.39	0.987	1.29
$C_{z_{\delta q}}$	-0.0448	0.00619	0.61
$C_{M_{\alpha}}$	-177.5	5.11	1.03
$C_{M_{\delta q}}$	3.366	0.0009	1.17
$C_{N_q}$	-13050	1186.0	2.2
$C_{N_{\beta}}$	170.45	4.47	0.67
$C_{N_{\delta r}}$	-2.53	0.066	0.44
$C_{N_r}$	-11493	973.0	1.4

## FLIGHT SENSOR STUDIES

Adequate flight instrumentation is necessary for the extraction of useful aerodynamic models from missile flight tests. Three studies are discussed in this subsection relating to flight sensors. Studies of this nature are useful for the design of flight test maneuvers and instrumentation specifications.

### SENSOR NOISE

Sensor errors can be classified into two categories for the purpose of error modeling -- random effects with no time-correlation called "white" noise, and errors which are correlated in time. White noise is easily modeled for statistical filtering, while the correlated errors require a thorough understanding of the sensor dynamics.

Test cases for four noise model variations from the nominal case are described in Table 15. A summary

TABLE 15. NOISE SENSITIVITY STUDIES

CASE	DESCRIPTION
1	Two times nominal noise modeled within the filter -- two times nominal noise used for measurement generation.
2	Two times nominal noise modeled by the filter -- nominal noise levels used for measurement generation.
3	Half nominal noise modeled in the filter -- half nominal noise used for measurement generation.
4	Half nominal noise modeled in the filter -- nominal noise used for measurement generation.

of the filter performance for the first two cases after 2 seconds of filtering is given in Table 16 along with the nominal filter performance. The parameter error is increased in both cases. In addition, values of  $n_0$  are reduced from the nominal case, indicating better predicted/actual filter correlation. Typical residual processes from these two cases are shown in Figures 14 and 15. In Figure 14, where the filter model is correct, 64 percent of the residual points are included within the one sigma bound. In Figure 15, 96 percent of the residual points are within one sigma. This result demonstrates how measurement noise statistics can be identified by inspection of the residual process and the predicted residual bound.

TABLE 16. PARAMETER IDENTIFICATION PERFORMANCE WITH INCREASED MEASUREMENT NOISE

PARAMETER	NOMINAL, $\sigma(n_0)$	CASE 1 INCREASED MEASUREMENT NOISE, CORRECT FILTER MODEL $\sigma(n_0)$	CASE 2 NOMINAL MEASUREMENT NOISE, INCORRECT FILTER MODEL, $\sigma(n_0)$
$C_{x_0}$	0.0361 (1.6)	0.0523 (1.05)	0.0541 (0.99)
$C_{y_\beta}$	0.574 (1.6)	0.899 (0.81)	0.929 (0.67)
$C_{y_{\delta r}}$	0.00448 (0.2)	0.00586 (0.05)	0.00583 (0.10)
$C_{z_\alpha}$	0.692 (1.5)	1.07 (0.78)	1.11 (0.67)
$C_{z_{\delta q}}$	0.00601 (1.1)	0.00767 (0.81)	0.00766 (0.56)
$C_{M_\alpha}$	3.44 (1.3)	4.73 (0.81)	4.91 (0.66)
$C_{M_{\delta q}}$	0.0843 (1.07)	0.1061 (0.78)	0.1087 (0.63)
$C_{M_q}$	1032 (0.010)	1061. (0.04)	1057 (0.15)
$C_{N_F}$	3.30 (1.9)	4.64 (1.08)	4.78 (0.99)
$C_{N_{\delta r}}$	0.0608 (1.3)	0.0804 (0.58)	0.0819 (0.57)
$C_{N_r}$	850 (2.2)	878.5 (2.2)	872.3 (2.2)

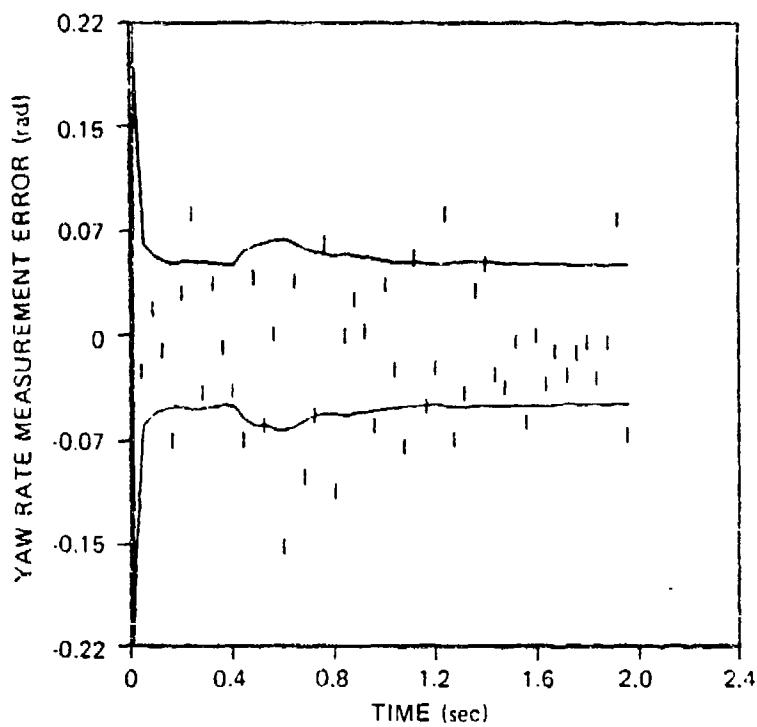


Figure 14. Residuals for Case 1

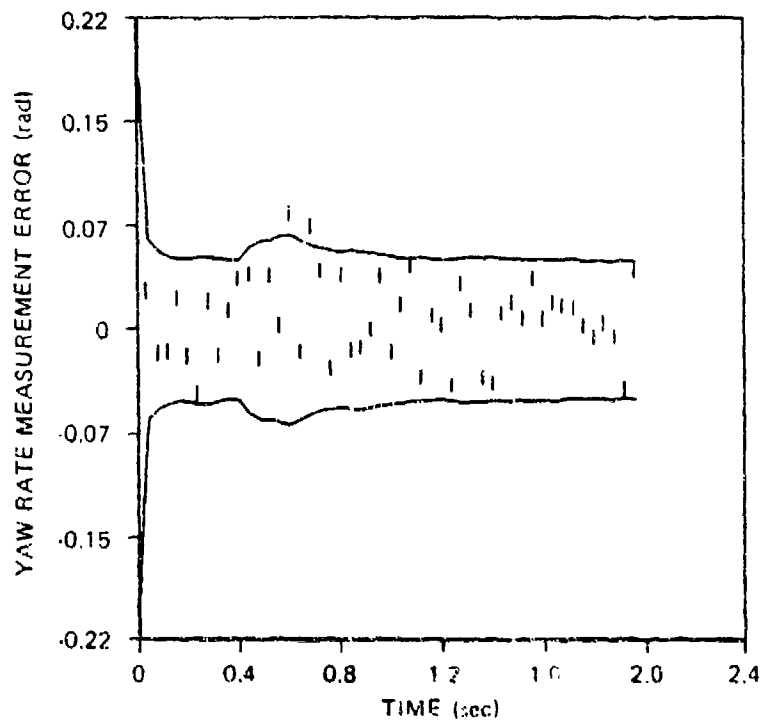


Figure 15. Residuals for Case 2

The two sensor noise cases with reduced noise levels are summarized in Table 17, and compared with the nominal estimation performance. For these cases, 0.8 second of data were processed. Parameter accuracies are improved in both cases. Note that the values of  $n_0$  are larger than for the nominal case.

Numerical difficulties were encountered with Case 4 after 1 second of integration, because the predicted residual covariance matrix became ill-conditioned. Both state and parameter estimates show signs of filter divergence prior to this point. (Note that relatively large values of  $n_0$  for this case at 0.8 second). The residual process for the angle-of-attack measurement from Case 4 is shown in Figure 16. Only 33 percent of the residual points are included within the one sigma bound.

Several characteristics of the extended Kalman Filter are demonstrated by the noise sensitivity examples discussed below:

- Predicted and actual estimation error agreement is improved with increasing measurement noise levels.
- Conservative measurement noise levels have little effect on the resulting filter estimates and result in stable filter performance (Reference 12, p. 244-251). Correct noise levels can be inferred from the resulting residual process.
- Low measurement noise levels can result in filter divergence and numerical difficulties. (This could be corrected by use of higher precision arithmetic).

TABLE 17. PARAMETER IDENTIFICATION PERFORMANCE WITH REDUCED MEASUREMENT NOISE

PARAMETER	NOMINAL (T=.8) $\sigma(n_o)$	CASE 3 REDUCED MEASUREMENT NOISE, CORRECT FILTER MODEL $\sigma(n_o)$	CASE 4 NOMINAL MEASUREMENT NOISE, INCORRECT FILTER MODEL $\sigma(n_o)$
$C_{N_0}$	0.110 (0.27)	0.0727 (1.2)	0.0732 (2.4)
$C_{y\beta}$	1.88 (0.1)	1.32 (1.6)	1.310 (2.8)
$C_{y\delta_r}$	0.00791 (0.53)	0.00760 (0.7)	0.00770 (0.68)
$C_{z_a}$	2.227 (0.48)	1.53 (1.1)	1.525 (2.3)
$C_{z\delta_q}$	0.00872 (0.54)	0.00809 (1.4)	0.00823 (0.55)
$C_{M_a}$	10.71 (0.11)	8.57 (1.4)	8.76 (2.4)
$C_{M\delta_q}$	0.207 (0.29)	0.169 (1.6)	0.175 (2.4)
$C_{N_q}$	2903 (0.38)	2860 (0.5)	2867 (0.35)
$C_{N\beta}$	7.82 (0.05)	7.32 (1.6)	7.50 (2.5)
$C_{N\delta_r}$	1.83 (0.80)	0.155 (1.1)	0.160 (1.63)
$C_{N_r}$	2598 (0.33)	2527 (0.52)	2542 (0.50)



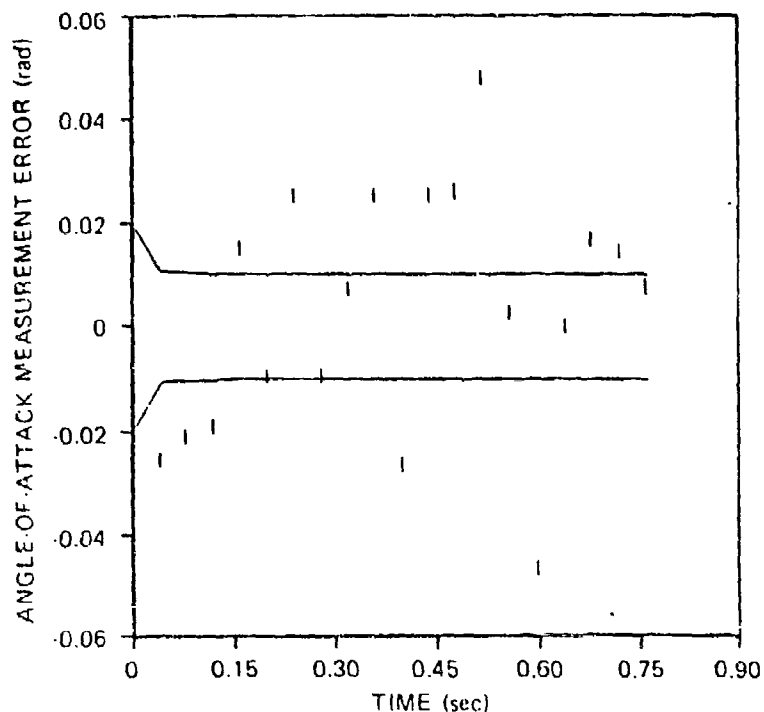


Figure 16. Residuals for Case 4

### SENSOR SELECTION

Sensors frequently used for gathering flight test data are discussed in Section III. The generality of the extended Kalman Filter facilitates transition between sensor sets, providing the appropriate measurement models and partial derivatives are included. As a demonstration of this sensor selection capability, identification results from different sensor sets are presented in this subsection. These sensor sets are given in Table 18.

Case 5 is the same as the nominal, except for the longitudinal accelerometer. In many cases missiles have operational requirements for only two accelerometers mounted orthogonal to the missile centerline. Thus, flight tests

TABLE 18. SENSOR SELECTION STUDIES

CASE	DESCRIPTION
5	Omit longitudinal accelerometer from nominal measurement set
6	Accelerometer measurements only
7	Rate gyro measurements only
8	Position and attitude measurements only

using only operationally required sensors would not include a longitudinal accelerometer. The primary utility of this accelerometer i.r parameter identification is in the determination of the drag related aerodynamic terms (e.g.,  $C_{x_0}$  in the linear airframe model).

Estimation performance for Case 5 is shown in Table 19. The predicted drag estimation accuracy is degraded from the nominal case; however, the initial drag uncertainty of 0.4 was improved to 0.17 -- indicating some drag information is available without a longitudinal accelerometer.

Drag information is apparently inferred from knowledge of the velocity profile -- velocity is "learned" along with the dynamic pressure through the known relationship and uncertainties governing the lateral accelerometer measurements, dynamic pressure and the uncertain parameters. The initial longitudinal velocity uncertainty is 100 ft/sec; this error is reduced to 10.7 ft/sec for the nominal case, and to 14.8 ft/sec without the longitudinal accelerometer.

Accelerometers and rate gyros are the most common sensors found on operational missiles. In Cases 6 and 7,

TABLE 19. PARAMETER ESTIMATION ACCURACY WITHOUT A LONGITUDINAL ACCELEROMETER

PARAMETER	NOMINAL $\sigma(n_0)$	CASE 5 NO LONGITUDINAL ACCELEROMETER $\sigma(n_0)$
$C_{x_0}$	0.6361 (1.6)	0.170 (0.18)
$C_{y_0}$	0.514 (1.6)	0.611 (1.4)
$C_{y_{cr}}$	0.00448 (0.26)	0.00451 (0.13)
$C_{z_0}$	0.392 (1.5)	0.742 (1.25)
$C_{z_{eq}}$	0.00601 (1.1)	0.00604 (1.1)
$C_{M_1}$	3.44 (1.3)	3.38 (1.1)
$C_{M_{eq}}$	0.0843 (1.07)	0.0862 (0.83)
$C_{M_Q}$	1032.0 (0.01)	1035 (0.02)
$C_{R_2}$	3.30 (0.01)	3.46 (1.5)
$C_{z_{cr}}$	0.0608 (1.3)	0.0628 (1.1)
$C_{N_y}$	850.0 (2.2)	852 (2.2)

sensor sets consisting of only accelerometers and only rate gyros, respectively, are considered. The parameter identification performance summary for these two cases is shown in Table 20. Estimation accuracies and values of  $n_0$  for Case 6 are shown at 0.8 second. Extreme filter divergence is evident (as indicated by the large values of  $n_0$ ) which prevented processing data beyond 0.8 second. No filter divergence was found when only rate gyros are used and the  $n_0$  values for this case indicate good filter performance.

Case 8 consists of measurement of only position and attitude. This set may result from phototheodolite data from a missile without onboard telemetry, or from free flight tests

TABLE 20. PARAMETER ESTIMATION ACCURACY WITH  
ACCELEROMETER AND RATE GYROS ONLY

PARAMETER	CASE 6 ACCELEROMETERS ONLY; T=0.8 sec $\sigma(n_\sigma)$		CASE 7 RATE GYROS ONLY; T=2.0 sec $\sigma(n_o)$	
$C_{x_0}$	0.120	(0.89)	0.393	(0.89)
$C_{y_\delta}$	1.37	(11.1)	1.40	(1.8)
$C_{y\delta_r}$	0.00073	(0.89)	0.0098	(0.55)
$C_{z_\alpha}$	0.975	(40.2)	1.76	(1.13)
$C_{z\delta q}$	0.00973	(1.62)	0.00996	(0.26)
$C_{M_\alpha}$	12.29	(5.28)	7.77	(0.11)
$C_{M\delta q}$	0.228	(4.8)	0.192	(0.49)
$C_{M_q}$	2370	(3.6)	520	(2.0)
$C_{N_\beta}$	8.92	(12.0)	7.06	(0.66)
$C_{N\delta_r}$	0.193	(1.6)	0.123	(0.31)
$C_{N_r}$	2786	(0.73)	533	(1.03)

of small-scale missile models fired within projectile test ranges (Reference 13). The aerodynamic force and moment coefficients enter directly into the dynamic equations for linear and angular acceleration-- thus, acceleration and angular rate provide more direct information about the aerodynamic parameters than do position and attitude measurements.

Nevertheless, highly accurate position and attitude measurements have been used with success to extract aerodynamic data in ballistic test ranges.

Three missile position measurements and three Euler angle attitude measurements were assumed with measurement noise levels of 5 feet and  $0.02^\circ$  radian, respectively, at a data rate of 50 hertz. These accuracies are representative of phototheodolite measurements. The resulting parameter estimation accuracies are compared with the alternate nominal results in Table 21. The filter performance in this case correlated well with predicted performance; however, the resulting parameter accuracies were degraded from the nominal measurement set. It is interesting to note, in comparing Cases 7 and 8, that more aerodynamic information is available from rate gyros alone than from position and attitude data, for the measurement accuracies investigated.

A significant issue with regard to sensor selection concerns the necessity of the  $\alpha$ - $\beta$  sensor. This issue will be addressed in more detail later in this report. The alternate nominal case was reprocessed using only accelerometers and rate gyros. No difference was noticed in the resulting parameter identification performance, indicating little additional information is contributed by the  $\alpha$ - $\beta$  sensor.

#### SENSOR MODELING

Several studies were performed to investigate the effects of systematic sensor errors on parameter identification. These systematic errors include accelerometer bias and scale factor error, and gyro bias and scale factor error, which are modeled as described in Section III. The cases presented here utilize identical measurement models and filter

TABLE 21. PARAMETER IDENTIFICATION PERFORMANCE WITH POSITION AND ATTITUDE MEASUREMENTS

PARAMETER	ALTERNATE NOMINAL $\sigma(n_o)$	CASE 8 POSITION AND ATTITUDE MEASUREMENT $\sigma(n_c)$
$C_{x_0}$	0.0464 (1.7)	0.0390 (0.54)
$C_{y_\beta}$	0.784 (1.2)	1.19 (0.80)
$C_{y\delta_r}$	0.0454 (0.663)	0.00997 (1.04)
$C_{z_\alpha}$	0.987 (1.29)	2.40 (0.02)
$C_{z\delta_q}$	0.00819 (0.61)	0.00996 (1.8)
$C_{M_\alpha}$	5.11 (1.03)	14.72 (1.4)
$C_{M\delta_q}$	0.0909 (1.17)	0.187 (0.40)
$C_{N_q}$	1186.0 (2.2)	2547.0 (0.61)
$C_{N_\beta}$	4.47 (0.87)	12.55 (0.71)
$C_{N\delta_r}$	0.0658 (0.44)	0.189 (0.74)
$C_{N_r}$	872.7 (1.4)	2381.0 (1.2)

models so that when bias errors, for example, are included in the measurement, they are also modeled and estimated within the filter.

The dynamic and statistical model used in generating the alternate nominal trajectory was utilized in the filters discussed in this subsection. The starting seed required for generating the random sequences used in measurement generation

was different from the seed used to produce the results for the alternate nominal case shown in Table 14. This results in different perturbation input time histories, parameter initializations, and measurement errors. The alternate nominal parameter estimation results were recomputed (without systematic errors) with the new seed for comparison.

The bias and scale factor levels studied are shown in Table 22. Each type of error was studied individually, for a total of four examples; each of the four cases included the three additional parameters associated with the corresponding systematic errors -- x, y, and z axis biases, for example. The predicted parameter identification accuracy for the four cases is shown in Table 23, together with the alternate nominal case having no systematic errors.

TABLE 23. SYSTEMATIC ERRORS SENSITIVITY STUDIES

CASE NO.	DESCRIPTION	
	ERROR TYPE	STANDARD DEVIATION
9	Accelerometer bias	2.0 ft/sec
10	Accelerometer scale factor error	0.02
11	Rate gyro bias	0.02 rad/sec
12	Rate gyro scale factor error	0.02

TABLE 23. THE EFFECTS OF SYSTEMATIC MEASUREMENT ERROR ON PARAMETER IDENTIFICATION

PARAMETER	PREDICTED PARAMETER STANDARD DEVIATIONS*				
	ALTERNATE, NOMINAL NO SYSTEMATIC ERROR	CASE 9 ACCELEROMETER BIAS ERRORS	CASE 10 ACCELEROMETER SCALE FACTOR ERRORS	CASE 11 GYRO BIAS ERRORS	CASE 12 GYRO SCALE FACTOR ERRORS
$C_{x_0}$	0.0237	0.0387	0.0373	0.0247	0.0250
$C_{y_0}$	0.880	0.917	0.874	0.990	1.021
$C_{y_{dr}}$	0.00886	0.00877	0.00745	0.00672	0.00694
$C_{z_0}$	1.168	1.209	1.190	1.340	1.322
$C_{z_{dr}}$	0.00628	0.00638	0.00710	0.00682	0.00675
$C_{M_0}$	6.23	6.37	6.40	6.62	6.90
$C_{N_{dr}}$	0.0903	0.0924	0.0910	0.0934	0.1086
$C_{M_q}$	1195.0	1206.0	1195.0	1208.0	1187.0
$C_{N_{\dot{\beta}}}$	6.32	6.37	6.46	6.68	6.68
$C_{N_{\dot{\alpha}}}$	0.1632	0.1635	0.1640	0.110	0.122
$C_{M_r}$	1246.0	1251.9	124	1255.0	1261.0
$\lambda$ sys- tematic error	0.0	1.35	0.00246	0.0132	0.0116
$\gamma$ sys- tematic error	0.0	0.900	0.0121	0.00260	0.00940
$\beta$ sys- tematic error	0.0	1.085	0.0128	0.00282	0.00893

\*  $C_{M_q}$  values are not shown for these cases though good statistical agreement between filter predictions and actual estimation errors was found in all cases.

## WIND STUDIES

A primary motivation for the requirement of  $\alpha$  and  $\beta$  sensors on flight vehicles lies in the consideration of atmospheric wind. Accelerometers and rate gyros sense motions with respect to inertial space. These motions are produced by forces and moments which result from missile and missile



control surface orientation with respect to the relative wind. The aerodynamic coefficients relate the relative wind to the forces and moments. To estimate the aerodynamic coefficients, estimates of force and moments and estimates of the relative wind must be inferred. Given the aerodynamic coefficients, the relative wind information ( $\alpha$  and  $\beta$ ) can be determined from acceleration and rate gyro measurement and known control surface deflections. Also, given good estimates of initial missile inertial velocity and a perfect measure of atmospheric wind -- the relative wind velocity can be estimated via integration of the acceleration over short time intervals. With uncertain wind and initial velocity errors as well as parameter uncertainty, it is not clear whether  $\alpha$  and  $\beta$  can be estimated with sufficient accuracy to improve the estimates of the aerodynamic parameters. Thus, it might be argued that  $\alpha$  and  $\beta$  sensors are required for parameter identification when atmospheric wind uncertainties are present. A brief study addressing this issue is discussed here. The test cases are listed in Table 24.

The capability of including a deterministic wind is included in the EKF generalized airframe model. The steady component of wind is modeled by a horizontal vector with magnitude and heading that are functions of altitude. The inclusion of a steady wind correctly modeled within the filter dynamics was found to have little effect on the parameter identification performance (a slight identification improvement was noticed, apparently from the additional  $\alpha$  and  $\beta$  variation resulting from the wind. A horizontal wind value of about 110 ft/sec\* oriented 45 degrees from the initial missile heading was assumed.

---

\*95 percentile wind at 20K feet altitude (Reference 14).

TABLE 24. WIND STUDIES

CASE	DESCRIPTION
13	Nominal case with deterministic wind added
14	Uncertain wind added to Case 13
15	Case 14 with poor $\alpha$ - $\beta$ sensors
16	Case 15 with poor initial attitude and velocity values
17	Case 16 with accurate $\alpha$ - $\beta$ sensors

In addition to the deterministic wind, a random (but constant) wind bias was modeled and estimated (Case 14). Random wind biases of up to 50 ft/sec in the three inertial axes were modeled. With nominal measurements and initial conditions, little change was observed in the parameter identification accuracy and the wind uncertainty was improved from 50 ft/sec to about 30 ft/sec in each of the three inertial directions. The nominal  $\alpha$  and  $\beta$  sensors were included in these cases.

The effects of the  $\alpha$  and  $\beta$  sensors on the identification accuracy with large deterministic wind and large wind uncertainty was determined by varying the measurement noise level on the  $\alpha$  and  $\beta$  sensors (Case 15). The nominal  $\alpha$  and  $\beta$  sensor noise level of 0.02 radian was increased to 0.2 radian, representing essentially no information provided by the  $\alpha$  and  $\beta$  sensors. For this case there was no noticeable decrease in the parameter identification accuracy. Some degradation in the ability to estimate wind was noticed, with wind uncertainties of about 40 ft/sec.

Some additional studies were conducted to isolate the relationship between initial state uncertainties and parameter identification in the presence of wind. Note that if good initial estimates of the lateral components of missile inertial velocity are available and if good initial estimates of missile attitudes are known, good initial estimates of  $\alpha$  and  $\beta$  can be computed. By propagating these initial estimates through the airframe dynamics,  $\alpha$  and  $\beta$  estimates may be inferred. For Case 16, the lateral velocity component uncertainties were increased from the nominal value of 20 to 80 ft/sec while the initial missile attitude uncertainties were increased from nominal values of 0.04 to 0.2 radian. With the large  $\alpha$  and  $\beta$  sensor rms noise level (0.2 radian), this case exhibited filter divergence. Figure 17 shows the resulting z-axis wind estimation errors as a function of time. Case 17 was performed with very low  $\alpha$  and  $\beta$  sensor noise levels (0.002 radian); the filter performance was near nominal with the z-axis wind estimation error shown by Figure 18. Thus, to avoid divergence in the presence of large state initial condition errors and uncertain wind, accurate  $\alpha$  and  $\beta$  measurements may be required.

#### ESTIMATION OF NONLINEAR AERODYNAMIC EFFECTS

The previous sections considered only the so called "linear" aerodynamic effects, however the resulting dynamic model is highly nonlinear in the augmented system state vector. The inclusion of additional "nonlinear aerodynamic effects" is conceptually no more difficult to handle in the parameter identification algorithms than the previous examples. Nevertheless, in order to demonstrate the capabilities of identifying a large number of parameters, a variety of nonlinear and cross coupling aerodynamic parameters are identified in this section.

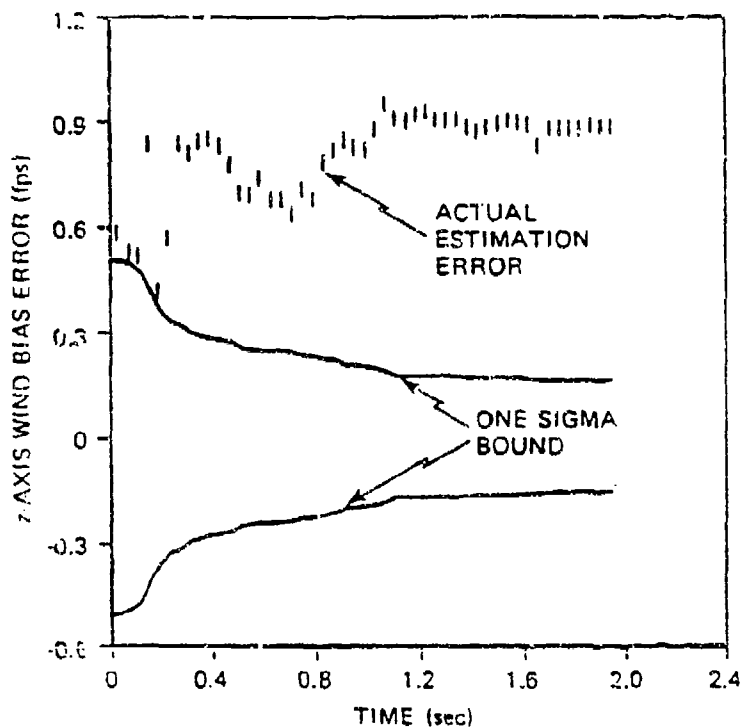


Figure 17. z-Axis Wind Estimation Error With Large Initial State Uncertainty and Large  $\alpha$ - $\beta$  Sensor Errors

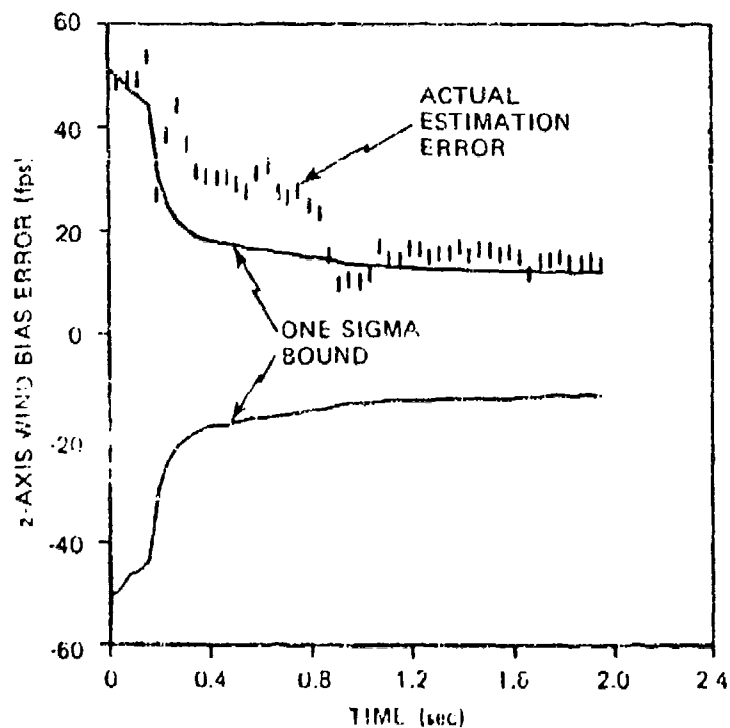


Figure 18. z-Axis Wind Estimation Error With Large Initial State Uncertainty and Small  $\alpha$ - $\beta$  Sensor Errors

One strategy for applying system identification to an airframe might include the following steps. First, attempt to fit the observed data using only the linear aerodynamic terms. Observe the resulting residual process, parameter estimates and the respective one sigma bounds and evaluate the filter performance from the standpoint of consistency. In many cases a linear aerodynamic model should provide reasonable correlation. Next isolate potential nonlinear aerodynamic effects likely required to improve the model. These additional nonlinear terms may be provided by the wind tunnel data or through insight gained by inspection of the residual process. For example, if a large discrepancy occurs in the lateral acceleration residual at a time when a large roll rate is observed, a roll coupling term might be added. This "intuitive approach" to model structure selection relies heavily on the experience of the user and requires a highly flexible identification algorithm so that aerodynamic coefficients can be removed or inserted easily.

Once a list of potential additional parameters has been selected to improve the linear model results, parameter uncertainty standard deviations must be selected to initialize the additional parameters. In some cases an uncertainty level might be ascertained from the wind tunnel data. Alternatively, uncertainties might be computed by considering the contribution of the additional aerodynamic terms to the total aerodynamic force and moment coefficients. For example, if the average angle-of-attack and sideslip over a segment selected for identification is observed to be  $\bar{\alpha}$  and  $\bar{\beta}$ , the average contribution to  $C_M$  from  $\alpha$  is about  $C_{M_\alpha} \bar{\alpha}$ . The uncertainty in a term such as  $C_{M_{\alpha\beta}}$  might be selected to produce an uncertainty in  $C_M$  of about 10 percent of the known primary contributor,  $C_{M_\alpha}$ . Thus, the standard deviation,  $c_{\alpha\beta}$ , in  $C_{M_{\alpha\beta}}$  is selected as,

$$\sigma_{\alpha\beta} = 0.10(C_{M_\alpha} \bar{\alpha})/(\bar{\alpha} \bar{\beta})$$

A test was conducted where 25 additional terms were included in the aerodynamic model used in the nominal cases, resulting in a total of 36 aerodynamic parameters. These parameters, their mean values, standard deviations and true values are given in Table 25. The standard deviations were selected so that each new term contributed on the order of 5 percent to the aerodynamic coefficients.

Different pitch and yaw control inputs were used for this test case. These inputs together with the resulting angle-of-attack and sideslip are shown in Figures 19 and 20. Only one second of data was processed, but the data rate was increased to 100 hertz. The large angle-of-attack and sideslip variations in this trajectory should provide good observability of the nonlinear terms.

An additional test case with 36 parameters was performed where the control inputs of Figures 19 and 20 were reduced by half. The resulting angle-of-attack and sideslip are also indicated in Figures 19 and 20. It is interesting to note that the addition of the nonlinear and coupling aerodynamic effects are not obvious from casual observation of Figures 19 and 20; the pitch and yaw planes do not appear coupled and the  $\alpha$  and  $\beta$  responses to control inputs could result from a linear aerodynamic model. The identification of subtle aerodynamic effects which contribute little to the basic linear airframe response provides an excellent demonstration of the capabilities of the postflight data processing algorithm discussed here.

TABLE 25. PARAMETER IDENTIFICATION SUMMARY  
FOR 36 PARAMETER CASE

PARAMETER	INITIALIZATION			PARAMETER ESTIMATION ACCURACY	
	MEAN VALUE	STANDARD DEVIATION	ACTUAL VALUE	LARGE CONTROL DEFLECTIONS $(\sigma_{n_1})$	REDUCED CONTROL DEFLECTIONS $(\sigma_{n_2})$
$C_{x_0}$	-1.63	0.4	-1.88	0.0676 (0.35)	0.0701 (0.38)
$C_{x_0^2}$	-8.0	4.0	-3.97	0.581 (1.6)	1.34 (0.39)
$C_{x_0^2}$	-8.0	4.0	-9.96	0.544 (1.1)	1.91 (0.89)
$C_{x_0 q^2}$	-0.0008	0.0004	-0.00074	0.000334 (0.6)	0.000304 (0.46)
$C_{x_0 r^2}$	-0.0008	0.0004	-0.00068	0.000300 (0.23)	0.000388 (0.52)
$C_{x_0 q r}$	-0.08	0.04	-0.057	0.0210 (0.28)	0.0352 (0.71)
$C_{x_0 r^2}$	-0.08	0.04	-0.058	0.0136 (0.43)	0.0327 (0.25)
$C_{x_M}$	0.0	0.5	0.243	0.326 (0.70)	0.246 (0.98)
$C_{x_r}$	-43.6	11.0	-51.1	1.03 (0.51)	1.46 (0.40)
$C_{y_0^2}$	0.0	400.0	233.0	5.05 (0.20)	27.41 (0.69)
$C_{y_0^2}$	0.0	400.0	-52.5	2.51 (1.6)	20.81 (0.39)
$C_{y_0^2}$	0.0	40.0	39.5	0.778 (1.5)	1.95 (1.53)
$C_{y_0 r}$	-0.044	0.011	-0.047	0.00270 (1.5)	0.00512 (0.76)
$C_{y_M}$	0.0	0.5	0.396	0.261 (0.7)	0.228 (1.7)
$C_{y_0}$	-43.6	11.0	-42.6	0.837 (0.65)	1.18 (0.10)
$C_{y_0^2}$	0.0	200.0	7.2	2.49 (0.41)	13.93 (0.21)
$C_{y_0^2}$	0.0	200.0	-15.7	3.04 (0.06)	21.22 (0.29)
$C_{y_0 q^2}$	-0.044	0.011	-0.03	0.00332 (1.1)	0.00542 (0.37)
$C_{y_0 r^2}$	0.0	0.0	-0.160	0.289 (0.12)	0.227 (0.48)
$C_{y_0}$	-290.6	50.0	-196.0	3.72 (0.78)	5.41 (0.11)
$C_{y_0^2}$	0.0	1000.0	-865.0	15.4 (0.08)	80.24 (0.63)
$C_{y_0^2}$	0.0	100.0	49.6	1.85 (0.08)	8.41 (1.2)
$C_{y_0^2}$	0.0	1000.0	1252.0	27.6 (0.85)	109.6 (0.69)
$C_{y_0 q}$	2.9	0.75	2.54	0.0597 (0.42)	0.0834 (0.55)
$C_{y_0 q^2}$	0.0	1.0	-0.063	0.0831 (0.60)	0.251 (0.26)
$C_{y_0^2}$	0.0	10.0	0.0074	3.06 (0.04)	3.25 (0.77)
$C_{y_0 q}$	-1250.0	3000	-1091.0	306.2 (0.76)	605.6 (1.7)
$C_{y_0^2}$	0.0	3.0	1.54	1.40 (0.21)	1.025 (0.89)
$C_{y_0^2}$	200.6	50.0	280.0	5.75 (0.97)	7.57 (0.65)
$C_{y_0^2}$	0.0	1000.0	-87.4	6.77 (0.88)	119.1 (0.40)
$C_{y_0^2}$	0.0	100.0	-57.0	1.861 (0.34)	6.31 (0.10)
$C_{y_0^2}$	0.0	1000.0	-208.1	16.14 (0.01)	119.8 (1.05)
$C_{y_0 r}$	-2.9	0.75	-2.86	0.0568 (0.98)	0.0824 (0.33)
$C_{y_0^2}$	0.0	10.0	-7.87	0.670 (1.3)	4.24 (0.48)
$C_{y_0}$	-1250.0	3000.0	194.2	187.0 (0.31)	339.8 (0.08)
$C_{y_0}$	0.0	3.0	-1.73	1.087 (0.65)	0.991 (0.66)

\*third order nonlinear terms

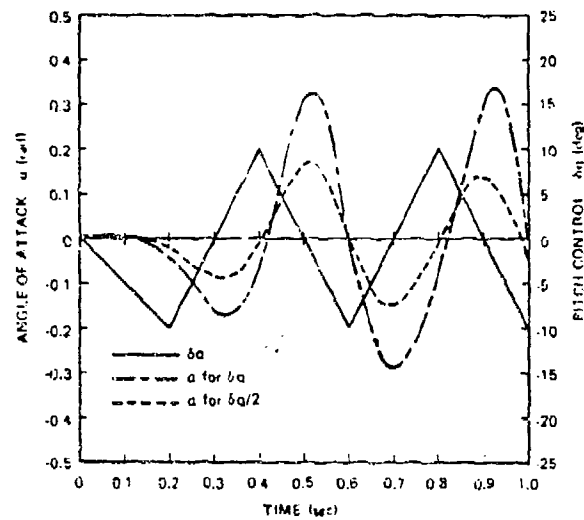


Figure 19. Angle-of-Attack Profile for the 36 Parameter Cases

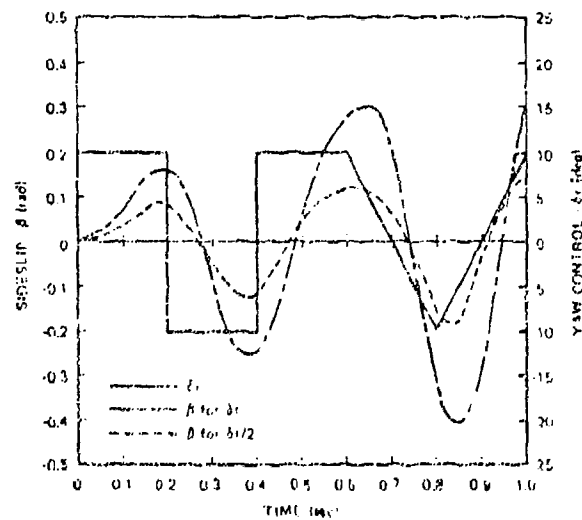


Figure 20. Sideslip Profile for the 36 Parameter Cases



The predicted parameter accuracy as well as the values of  $n_0$  are shown in Table 25 for both control input levels. The parameter estimation errors and the predicted one sigma bounds are shown in Appendix A, along with the residual processes. All consistency tests indicate the extended Kalman filter to be performing correctly; the residuals appear white and residual magnitudes are predicted accurately and the state and parameter errors behave according to the predicted bounds. The values of  $n_0$  indicated in Table 25 indicate excellent filter performance.

With the larger control input and the resulting larger  $\alpha$  and  $\beta$ , accurate estimates of the third-order terms are obtained rapidly. Note from Figure A-4 that the primary parameter accuracy improvement comes prior to about 0.4 second -- after about 0.5 second little additional improvement results. Yet the majority of the large  $\alpha$  and  $\beta$  variations occur after 0.5 second. The drag-related terms and the Mach number variation effects are less observable than the pitch and yaw dynamic terms. The drag terms produce relatively slight changes in longitudinal acceleration so that difficulty in identifying these effects is anticipated over short data segments.

The estimation accuracy achieved with reduced control magnitude was significantly reduced for ten third-order nonlinear terms, with the average degradation being a factor of about seven. Estimation error degradation for the remaining parameters was not significant. In fact, the five Mach number variation terms were improved with less  $\alpha$  and  $\beta$  variation.

#### ADDITIONAL PERFORMANCE STUDIES

A variety of additional studies have been conducted during the course of algorithm development. In particular,

parameter identification sensitivity to data rate, state initial condition magnitude, and process noise are discussed in this section (Table 26). These cases are variations of the alternate nominal trajectory. The predicted identification accuracies for these three demonstration cases are given in Table 27.

TABLE 26. ADDITIONAL PERFORMANCE STUDIES

CASE NO.	DESCRIPTION*
18	Halve the nominal data rate to 25 Hz
19	Double all initial dynamic state uncertainties
20	Set the process noise magnitude equal to zero

\*The measurement and filter model structures are identical on all cases.

Case 18 indicates that data rate reduction increased the parameter estimate standard deviations, but not significantly. Doubling the sample rate (data not shown) did not change the estimation accuracy -- indicating 50 hertz to be near the optimal data rate for this nominal case.

Doubling the dynamic state initial condition uncertainty (Case 19) also increases the parameter estimation error, but not significantly. This demonstrates an insensitivity of the estimates to state initial conditions, as well as showing that large initial condition uncertainty can be tolerated without indications of filter divergence.

TABLE 27. ADDITIONAL FILTER PERFORMANCE STUDIES

PARAMETER	INITIAL PARAMETER STANDARD DEVIATION	PREDICTED STANDARD DEVIATIONS			
		NOMINAL	CASE 18 HALVED DATA RATE	CASE 19 DOUBLE TC UNCERTAINTY	CASE 20 NO PROCESS NOISE
$C_{N_{\alpha}}$	0.1	0.046	0.060	0.056	0.033
$C_{Y_{\delta}}$	10.0	0.786	1.025	0.921	0.600
$C_{Y_{\delta r}}$	0.01	0.0045	0.0053	0.047	0.0043
$C_{Z_{\alpha}}$	10.0	1.987	1.27	1.15	0.76
$C_{Z_{\delta q}}$	0.01	0.0062	0.0071	0.0062	0.0054
$C_{M_{\alpha}}$	50.0	5.1	6.1	5.6	2.78
$C_{M_{\delta q}}$	0.7	0.091	0.113	0.102	0.054
$C_{N_q}$	3000.0	1186.0	1214.0	1189.0	265.0
$C_{N_r}$	50.0	4.47	5.39	5.02	2.72
$C_{N_{\delta r}}$	0.7	0.066	0.081	0.074	0.042
$C_{N_p}$	3000.0	973.0	1004.0	986.0	247.0

Case 20 shows identification accuracy with no process noise input. In some cases significant identification improvement results, particularly  $C_{M_q}$  and  $C_{N_r}$ . The process noise adds directly to the force and moment equations which include the aerodynamic parameters. As more noise is added, the deterministic structure of the model has relatively less effect so that the parameters become less observable.

An additional test case was performed in order to demonstrate the capability to fix certain well known parameters while estimating other terms. The less visible parameters from the nominal case are  $C_{Y_{\delta r}}$ ,  $C_{Z_{\delta q}}$ ,  $C_{M_q}$  and  $C_{N_r}$ . If the remaining 7 coefficients are fixed at the true values these less observable parameters should become more visible. The improved identification accuracy for this case is shown in Table 28.

TABLE 28. IDENTIFICATION ACCURACY WITH  
PARTIAL PARAMETER SET

PARAMETER	INITIAL UNCERTAINTY	PREDICTED STANDARD DEVIATIONS	
		11 PARAMETERS (NOMINAL)	4 PARAMETERS
$C_{N_{\dot{\alpha}}}$	0.01	0.00448	0.00288
$C_{L_{\dot{\alpha}}}$	0.01	0.00601	0.00432
$S_{N_{\dot{\alpha}}}$	3000.0	1032.0	1020.0
$C_{N_T}$	3000.0	850.0	795.0

#### SYNTHETIC DATA PROCESSING FOR A CASE EXHIBITING LARGE MACH NUMBER VARIATIONS

The algorithm verification exercise presented in the previous sections utilized simulated measurements produced with subroutines shared by the filter. For these cases the structure of the dynamics used for measurement generation was known to be identical to the structure assumed within the filtering algorithm.

An additional study was to be performed during this effort in order to exercise the general purpose airframe model and the filtering algorithm against synthetic measurement data provided by the Air Force. The data were to be generated by a missile exhibiting large variations in Mach number.

Synthetic data were provided by AFATL\* that were generated from a six-degrees-of-freedom simulation developed

---

\*Air Force Armament Laboratory, Eglin Air Force Base, Florida.

independently from the model discussed in Section 11. This data represents a 6.6-seconds trajectory from a high lift, bank-to-turn airframe for a short-range air-to-air interceptor. The trajectory contains a 2.6-seconds boost followed by four seconds of coast flight during which various pitch and yaw maneuvers are executed. The Mach number, angle-of-attack, and sideslip profiles are given on Figures 21, 22, and 23. Other trajectory variables -- accelerations, body rates, attitudes, etc -- were provided by AFATL to represent noise-free measurements.

The equations used for modeling the aerodynamic forces and moments were provided by AFATL and are shown in Table 29. Aerodynamic parameter values corrupted by "approximately 10 percent error" were provided by AFATL in the form of Table 30. The objective of this exercise was to identify an aerodynamic model which accurately reproduced the synthetic measurements during several segments of the trajectory.

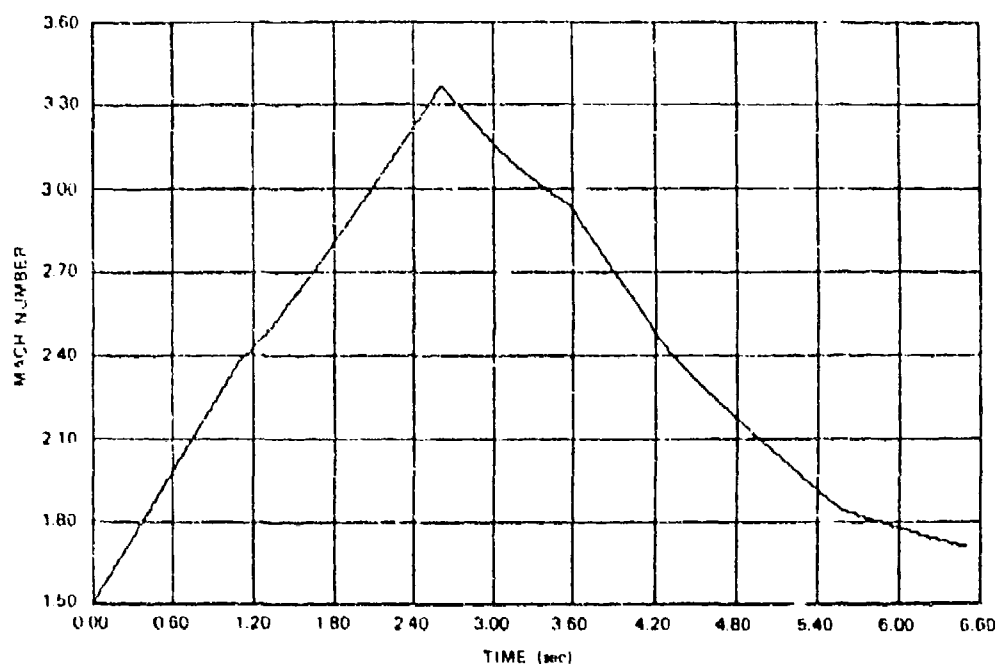


Figure 21. Mach Number Profile for AFATL Interceptor

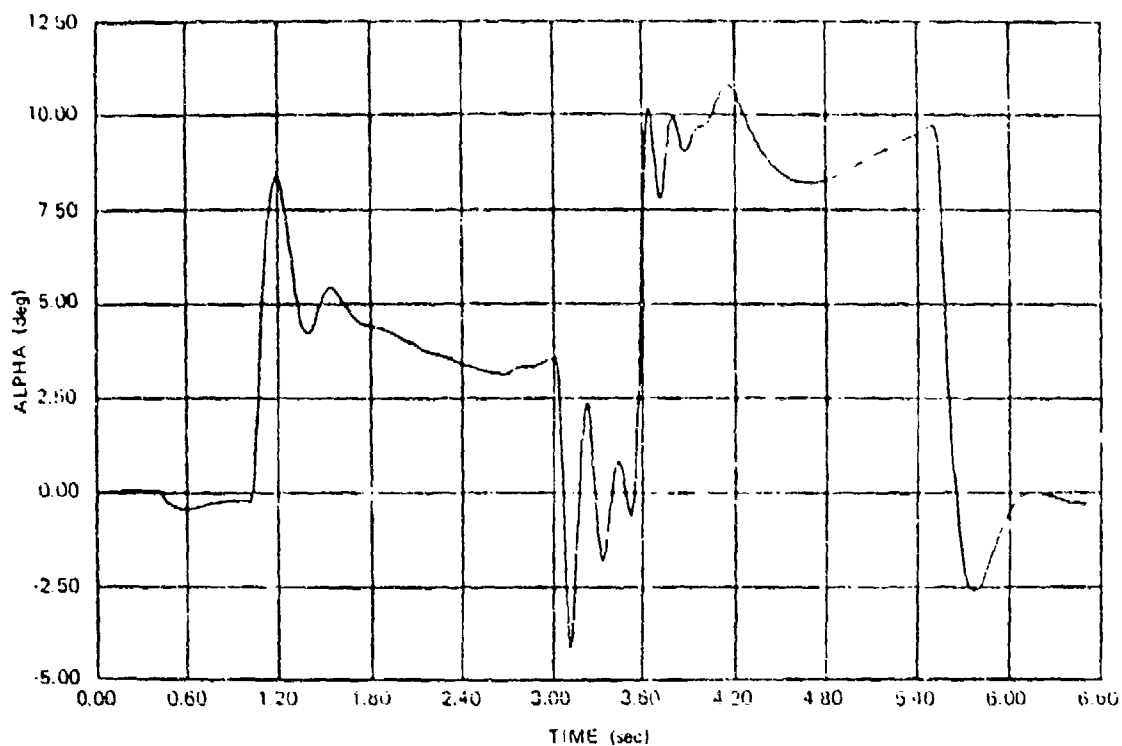


Figure 22. Angle-of-Attack Profile for AFATL Interceptor

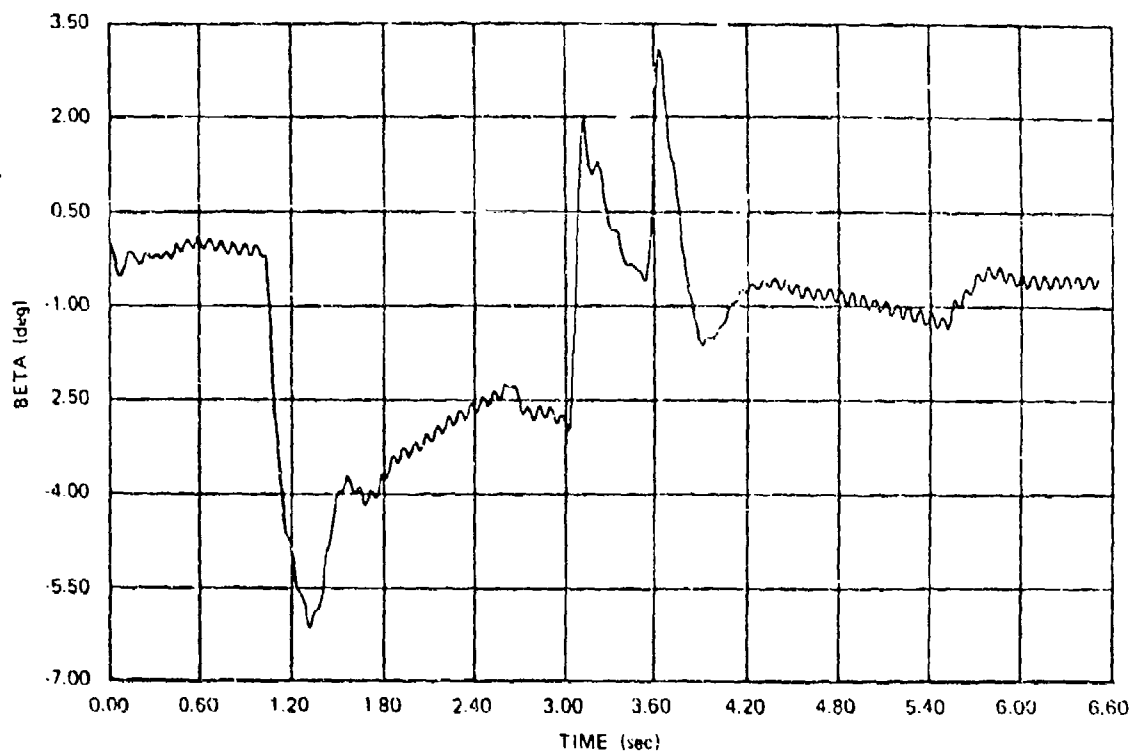


Figure 23. Sideslip Profile for AFATL Interceptor

TABLE 29. AERODYNAMIC MODEL FOR AFATL INTERCEPTOR

Aerodynamic Force Coefficients:

$$C_X = C_{X_0} + C_{X_\alpha} |\alpha| + C_{X_{\alpha^2}} \alpha^2 + C_{X_{\delta t}} |\delta t|$$

$$C_Y = C_{Y_\beta} \beta + C_{Y_{\delta r}} \delta r$$

$$C_Z = C_{Z_\alpha} \alpha + C_{Z_{\delta q}} \delta q$$

$$|\delta t| = (|\delta_q - \delta_p - \delta_r| + |\delta_q - \delta_p + \delta_r| + |\delta_q - \delta_r - \delta_p| + |\delta_p + \delta_q + \delta_r|)/4$$

Aerodynamic moment coefficients:

$$C_L = C_{L_{\alpha\delta}} \alpha\delta + C_{L_{\delta p}} \delta_p + C_{L_p} p D/2v_m$$

$$C_M = C_{M_\alpha} \alpha + C_{M_{\delta q}} \delta_q + C_{M_q} q D/2v_m$$

$$C_N = C_{N_\beta} \beta + C_{N_{\delta r}} \delta_r + C_{N_r} r D/2v_m$$

TABLE 30. APPROXIMATE AERODYNAMIC PARAMETER  
VALUES FOR AFATL INTERCEPTOR

AERODYNAMIC COEFFICIENT ( $C_i$ )	COEFFICIENT VALUES			% COEFFICIENT CHANGE AT $M = 2$ (PC) (PER SECOND)
	MACH = 1.1	MACH = 1.5	MACH = 3.5	
$C_{x_c}$	0.32	0.264	0.179	13
$C_{x_a}$	0.0068	0.0051	0.0011	50
$C_{x_{a2}}$	-0.00032	-0.00015	0.00011	10
$C_{x_{\delta r}}$	0.02	0.013	0.005	35
$C_{y_f}$	-0.125	-0.080	-0.047	19
$C_{y_{\delta r}}$	0.108	0.059	0.022	35
$C_{z_a}$	0.40	0.32	0.16	20
$C_{z_{\delta q}}$	0.103	0.056	0.019	35
$C_{L_{af}}$	-0.00495	-0.00326	-0.00104	35
$C_{L_{\delta r}}$	0.093	0.061	0.024	35
$C_{L_F}$	-6.35	-6.50	-3.60	20
$C_{M_a}$	-0.066	-0.024	0.0122	25
$C_{M_{\delta q}}$	-0.159	-0.093	-0.034	30
$C_{M_q}$	-29.8	-23.5	-12.7	20
$C_{N_{\delta}}$	0.146	0.074	0.015	40
$C_{N_{\delta r}}$	-0.168	-0.091	-0.036	35
$C_{N_r}$	-10.5	-5.7	-2.1	35



The significant characteristic of this data from the standpoint of parameter identification is the large variation of Mach number during boost and coast as well as the large variation of the aerodynamic coefficients with Mach number, as seen in Table 30. The percent rate of change in parameter magnitude (PC) at about Mach 2 is also indicated on Table 30. The quantity PC is computed according to,

$$PC_i = \left| \frac{\partial C_i}{\partial M} \frac{\partial M}{\partial t} / C_i \right| * 100$$

where

$C_i$  =  $i^{th}$  aerodynamic coefficient

$M$  = Mach number

$\partial M / \partial t$  = 0.723 per second

Note that for the majority of parameters, PC is greater than 30 percent per second for this trajectory.

The aerodynamic parameterization presented in Section II assumes only slight variation of the aerodynamic forces and moments with Mach number during any flight segment selected for identification. The allowable Mach variation can be expressed more quantitatively by considering the time required for accurate parameter estimation versus the time variation of the parameters with mach number. For example if the parameter uncertainty at Mach 2 were 10 percent and the parameter rate of change with Mach number is about 30 percent per second -- then the allowable time-interval for accurate identification should be small with respect to 1/3 second.

It becomes apparent that the aerodynamic parameterization of Section II is inadequate for the large Mach variation in the synthetic data provided by AFATL. Several alternative methods are proposed to allow aerodynamic modeling from flight

data in cases where all parameters may have large but linear time variations over the selected segment.

- Estimate the parameters as though they are constant -- assume the resulting parameter estimate to be an average value; i.e., associate the final estimate with the mach number at the center of the segment.
- Add parameters to model the linear variation of each coefficient with mach number; this will double the number of parameters to be estimated.
- Model the aerodynamic coefficients as time varying random processes -- i.e. dynamic states rather than parameters. This does not increase the dimensions of the required EKF. Reference 15 provides an example of identification of time-varying parameters using this method.
- Treat the aerodynamic model presented in Section II as a perturbation model which must be added to a more thorough a priori model containing the primary Mach number variation affects. The model used for identification would thus include the wind tunnel model used for preflight studies and would generate identical simulation results if all perturbation aerodynamic coefficients were set to zero. The perturbation model coefficients remain time invariant and yet should remain valid over larger flight segments provided the dominant Mach number trends are contained in the wind tunnel data. This procedure may require significant reprogramming from vehicle to vehicle depending on the particular forms of the wind tunnel models.

Each of these procedures, as well as certain combinations of them, should be investigated using appropriate controlled test cases. Such studies are recommended for future effort.

## SECTION VI

### AERODYNAMIC MODEL STRUCTURE IDENTIFICATION

#### BACKGROUND

The need for aerodynamic structure identification arises when the form of the missile dynamic model is uncertain. The design of an extended Kalman filter to estimate aerodynamic coefficients is based upon a specific stochastic model for the missile's motion. If this "filter model" is inconsistent with actual missile behavior, poor aerodynamic coefficient estimation accuracy may result. The objective of structure identification is to determine which model among a given class of models best represents the physical system of interest. Thus, the structure identification problem is one of approximation; i.e., determining which model within the given class best approximates the input-output response of the physical system. A method has been developed for identifying model structure when its uncertainty consists of several different models which might be best or correct. This method, based upon hypothesis testing theory, is demonstrated and evaluated in this chapter. Further examples of structure identification using this method are given in (Reference 16).

Structure identification is an important component of system identification and parameter identification for the following reasons:

- If the chosen structure is too complex (i.e., if too many parameters are included in the model), estimates of the relevant parameters (i.e., those parameters needed to describe the system response) will be degraded. This par-

ticular difficulty becomes severe when there is a limited amount of input-output data available

- If the structure chosen is too simple or incorrect, the physical system cannot be adequately represented for any values of the parameters in the selected model.

Researchers in the field of structure identification have recognized the obvious trade-off that exists between the number of parameters used in a model, and the ability of that model to fit a given set of data (References 17-19). Many of the techniques currently in use for selecting a model are based upon least squares fits of model parameters to the data. The model structure is chosen according to subjective statistical criteria which depend upon variables, such as "risk levels," that are specified in an ad hoc fashion. In addition, least squares approaches are theoretically deficient in that they are based upon certain assumptions about error statistics that are rarely satisfied in practical problems of structure identification. When these assumptions are not satisfied, the least squares estimates develop bias errors which can severely hinder the model selection process.

The motivation for the technique used here comes from previous work done on the parameter identification part of the system identification problem. Least squares techniques were initially employed for parameter identification due to their relative simplicity; however, they often produce biased, inaccurate estimates. Subsequently, more accurate techniques evolved such as maximum likelihood (e.g., as applied in Reference 20), and the extended Kalman filter (References 2 and 12). Inaccurate results have also been observed from application of least squares procedures to the structure identification problem (References 21 and 22); specifically there is a

tendency to select models having too many parameters. In this chapter a new technique based upon extended Kalman filtering is presented. It is used to obtain an improved solution to the problem of structure identification applied to missile aerodynamics.

The structure identification procedure used in this study is illustrated in Figure 24. A number of hypotheses,  $H_1, H_2, \dots, H_n$ , are defined, where  $H_i$  is the hypotheses that the model structure upon which the  $i^{\text{th}}$  filter is based is best. The choice of the set of hypotheses (or set of candidate models) is based upon the a priori information available about the system to be identified. The best model structure can be identified by operating  $n$  extended Kalman filters in parallel, as indicated in Figure 24, with each filter designed according to one of the candidate models. At the same time it is possible to recursively compute the probability  $P_{H_i}$  that the  $i^{\text{th}}$  model is correct; making use of the filter state estimates  $\hat{x}_i$  and the measurement data; the relative magnitudes of these probabilities provide a basis for selecting the model which best represents the data. The mathematical details of this procedure are presented in Appendix B.

The remainder of this section presents a structure identification study for an air-to-air missile. Several candidate models are selected, having different sets of aerodynamic parameters. One of these models, the "truth model", is used to generate synthetic measurement data. Extended Kalman filters are then constructed based upon each of the candidate models and used to process the measurement data. The probability that each model (each hypothesis) is the correct one is computed using the structure identification algorithm. The ability of this procedure to determine the correct system model is demonstrated by a number of simulations.

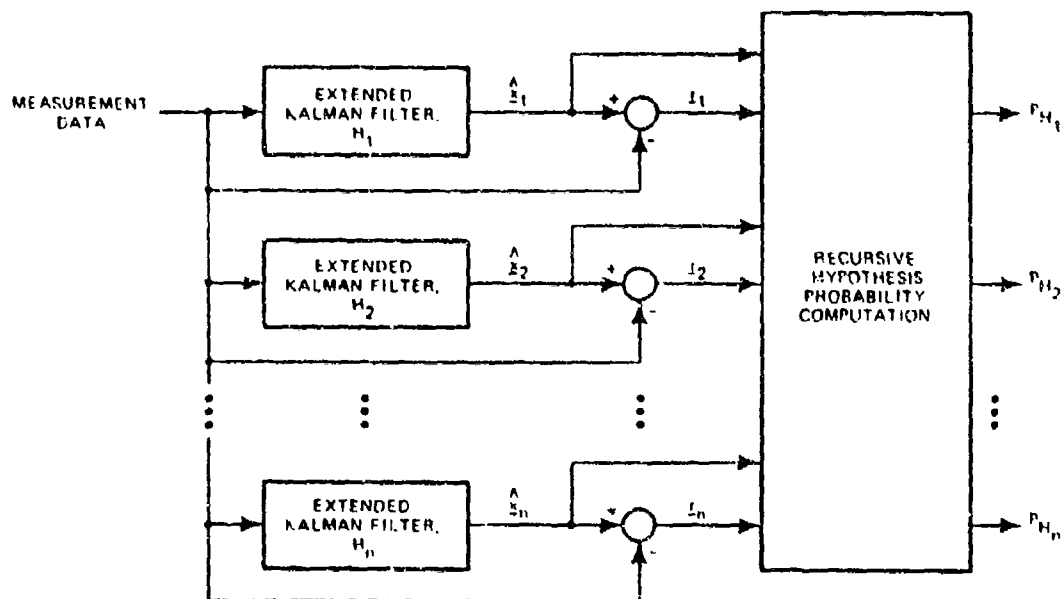


Figure 24. Functional Diagram of the Structure Identification Algorithm

## EXPERIMENTAL RESULTS

The experimental results presented in this section are based upon the air-to-air missile model described in Section V. Three versions of this model are employed here as truth models to generate synthetic measurement data. The first has 11 aerodynamic coefficients, the second has 16 and the third 20. Table 31 lists the parameter values for the three truth models. The control inputs, measurements, noise sources, dynamic initial conditions, and other model properties are the same as the model fully defined in Section V. Note that Model 1 has only linear aerodynamic parameters, while Model 2 has five additional nonlinear parameters, and Model 3 has four more nonlinear parameters than Model 2.

TABLE 31. TRUTH MODEL PARAMETER VALUES

PARAMETER	PARAMETER VALUES		
	TRUTH MODEL 1	TRUTH MODEL 2	TRUTH MODEL 3
$C_{x_0}$	-1.993	-1.993	-1.993
$C_{y_0}$	-37.468	-42.12	-42.12
$C_{y_{\delta r}}$	-0.048895	-0.0409	-0.0409
$C_{z_0}$	-42.120	-37.89	-37.89
$C_{z_{\delta q}}$	-0.04092	-0.0388	-0.0371
$C_{M_0}$	-172.24	-166.1	-234.6
$C_{M_{\delta q}}$	3.2617	2.809	3.591
$C_{N_0}$	-10432.0	-9538.0	-10521.8
$C_{N_{\delta}}$	166.53	206.6	205.17
$C_{R_{\delta r}}$	-2.4914	-2.835	-2.002
$C_{N_r}$	-12892.0	-12391.0	-12246.0
$C_{x_{\alpha 2}}$	-	10.08	10.08
$C_{x_{\beta 2}}$	-	-4.886	-4.886
$C_{M_{\alpha 3}}$	-	-680.4	583.7
$C_{M_{\beta 3}}$	-	583.7	-130.7
$C_{N_{\beta 3}}$	-	659.4	36.22
$C_{z_{\alpha 3}}$	-	-	103.34
$C_{M_{\alpha \delta q}}$	-	-	0.1212
$C_{N_{\alpha 2 \delta}}$	-	-	-683.2
$C_{N_{\beta 2 \delta r}}$	-	-	-2.663

Before proceeding with specific test cases it is important to emphasize the difference between the truth model and filter models in a given simulation. The truth model is used to generate a specific set of synthetic measurements. The filter model is the model upon which a particular filter design is based. In each case, for a particular measurement sequence, two or more extended Kalman filters are used to process the data. Each of these filters is based upon one of the models defined in Table 31. The outputs of these filters are then compared by the structure identification algorithm to determine which filter model best represents the truth model used to generate the data. The initial parameter statistics for the filters are given in Table 32. Other than these initial statistics, the filter design and implementation are the same as the nominal case described in Section V.

In the first test case of the structure identification procedure, Model 1 is used to generate the synthetic measurement data. Three hypotheses,  $H_1$ ,  $H_2$ , and  $H_3$  are formulated and defined with their corresponding probabilities as follows:

$H_i$  - Hypothesis that the  $i^{\text{th}}$  filter model corresponds to the truth model, for  $i=1, 2$ , and  $3$

$P_{H_i}$  - Probability that the hypothesis  $H_i$  is true, given the measurement data.

To compute the three probabilities of interest, the measurement data are processed independently by three extended Kalman filters, each designed in accordance with a different hypothesis (i.e., filter model). The estimates and error covariance matrix of each filter are then used by the algorithm described in Appendix B to compute the three hypothesis probabilities as a function of time.



TABLE 32. FILTER MODEL PARAMETER INITIAL STATISTICS

PARAMETER	INITIAL MEAN	INITIAL STANDARD DEVIATION		
	ALL FILTER MODELS	FILTER MODEL 1	FILTER MODEL 2	FILTER MODEL 3
$C_{x_0}$	-1.63	0.4	0.4	0.4
$C_{y_0}$	-43.55	10.0	10.0	10.0
$C_{y_{\delta r}}$	-0.044	0.01	0.01	0.01
$C_{z_a}$	-43.55	10.0	10.0	10.0
$C_{z_{\delta q}}$	-0.044	0.01	0.01	0.01
$C_{M_a}$	-200.55	50.0	50.0	50.0
$C_{M_{\delta q}}$	2.9	0.7	0.7	0.7
$C_{M_q}$	-12500.0	3000.0	3000.0	3000.0
$C_{N_0}$	200.55	50.0	50.0	50.0
$C_{N_{\delta r}}$	-2.9	0.7	0.7	0.7
$C_{N_r}$	-12500.0	3000.0	3000.0	3000.0
$C_{x_c 2}$	0.0	-	10.0	10.0
$C_{x_\beta 2}$	0.0	-	10.0	10.0
$C_{M_a 3}$	0.0	-	1000.0	1000.0
$C_{M_{\delta q} 2}$	0.0	-	1000.0	1000.0
$C_{N_{\delta r} 3}$	0.0	-	1000.0	1000.0
$C_{z_a 3}$	0.0	-	-	200.0
$C_{M_{\delta q} 2}$	0.0	-	-	1.0
$C_{N_{\delta r} 2}$	0.0	-	-	1000.0
$C_{N_{\delta r} 2}$	0.0	-	-	10.0

Figure 25 illustrates the result of the above procedure where the initial a priori probability of each hypothesis is assumed to be one-third. Note that initially, the probabilities remain constant and equal until approximately one-half second into the flight. During this period, the missile is in steady-state flight with zero control inputs, (see Figures 14 and 15). This behavior indicates that the data contains little or no information that can be used to discriminate between the three hypotheses. At about one-half second the control input begins and the probability of the correct hypothesis,  $P_{H_1}$ , rapidly goes to 1.0 as the others approach zero.

For the same measurement data as above, two additional cases were run using the structure identification procedure. Figure 26 illustrates the discrimination achieved between hypothesis  $H_1$  and  $H_2$  and Figure 27 presents a similar result for  $H_1$  and  $H_3$ . In each case the correct hypothesis is rapidly identified soon after the beginning of the missile control input.

In a second case study, Model 2 is used to generate the measurement data. Figure 28 shows the results of the structure identification procedure for the three hypotheses. Note that the algorithm rapidly identifies the correct hypothesis,  $H_2$ .  $P_{H_3}$  remains consistently higher than  $P_{H_1}$  because hypothesis  $H_3$  contains all of the parameters of  $H_2$ , whereas  $H_1$  contains only a part of the parameter set needed for Model 2.

As a further illustration, Figure 29 shows the result of computing  $P_{H_1}$  and  $P_{H_3}$  from the Model 2 data. Note, that in this case neither hypothesis is correct. Since, however, filter Model 3 contains Model 2 as a subset, whereas filter Model 1 does not, the probability calculation picks

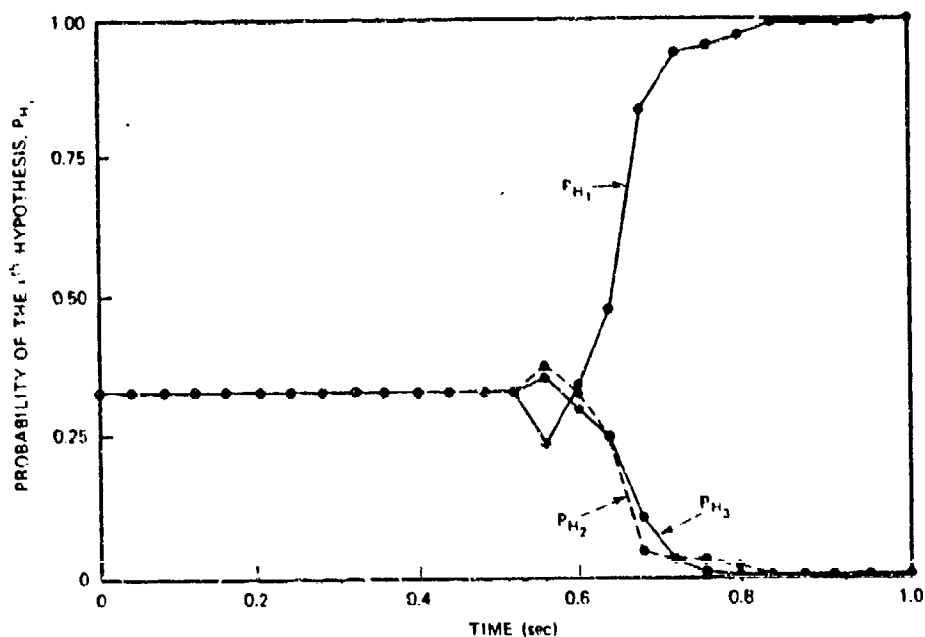


Figure 25. Probability that  $H_i$  is True when  $H_1$  is True, for  $i = 1, 2$ , and 3

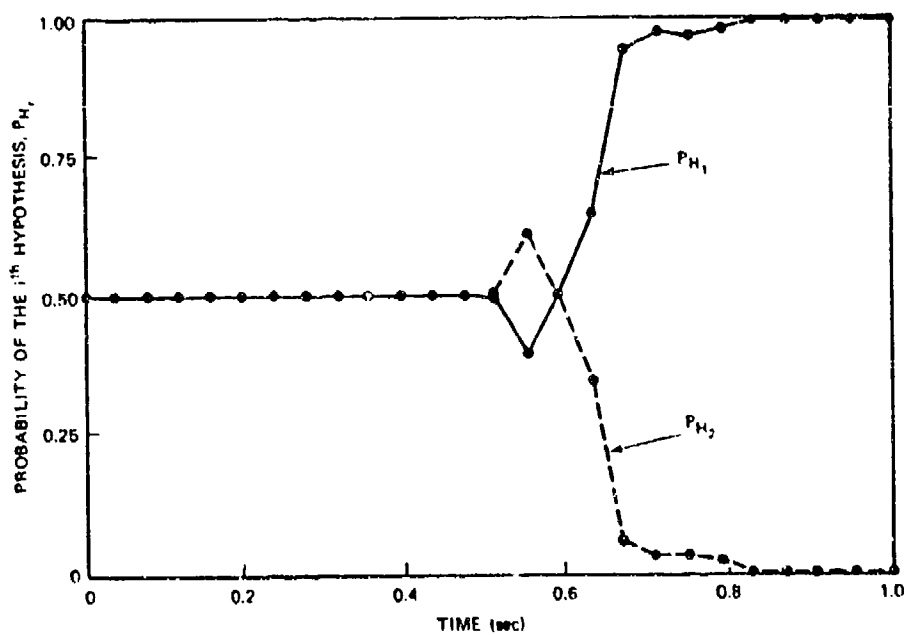


Figure 26. Probability that  $H_i$  is True when  $H_1$  is True, for  $i = 1$  and 2

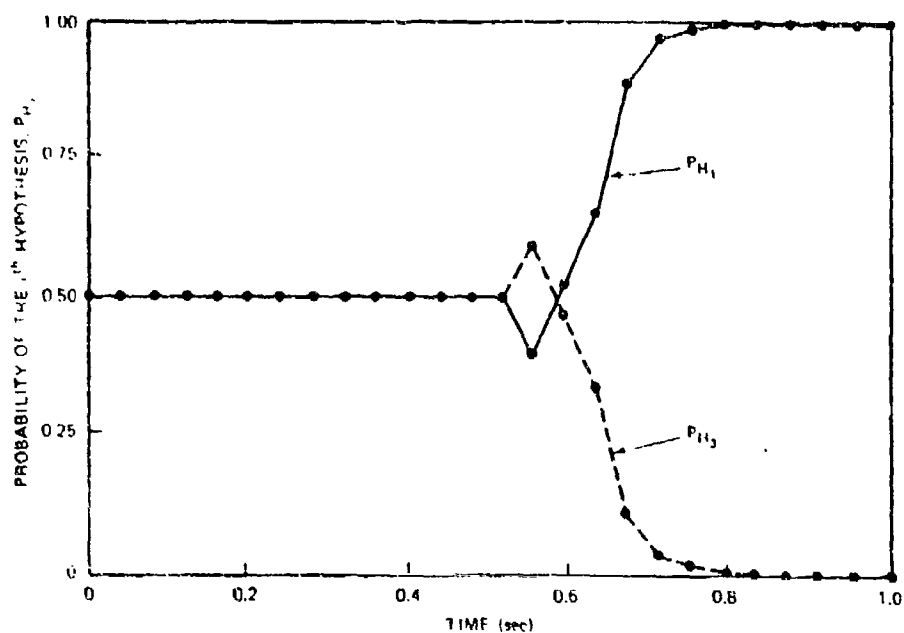


Figure 27. Probability that  $H_i$  is True when  $H_1$  is True, for  $i=1$  and  $3$

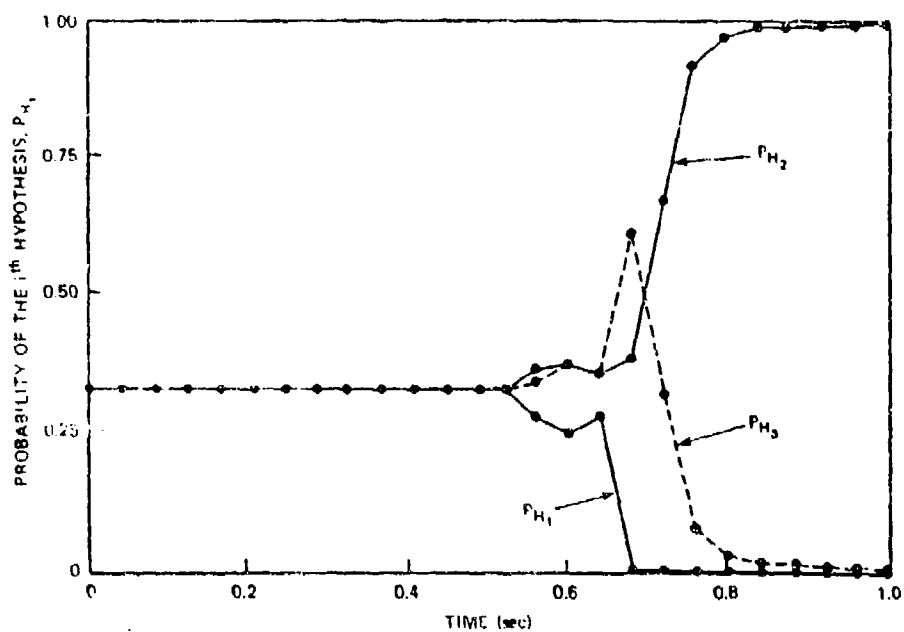


Figure 28. Probability that  $H_i$  is True when  $H_2$  is True, for  $i=1, 2$ , and  $3$

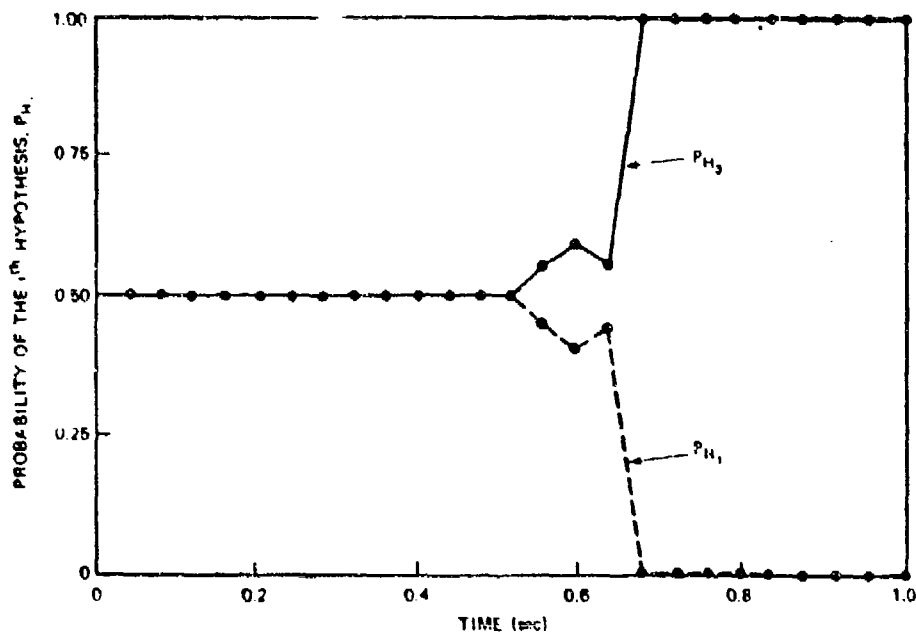


Figure 29. Probability that  $H_i$  is True when  $H_2$  is True, for  $i = 1$  and  $3$

that hypothesis which best represents the actual data. This demonstrates that the technique will not only select the correct hypothesis if it exists, but it tends to select the best or most likely hypothesis if the correct hypothesis is not known.

In the final test case, Model 3 is used to generate the measurements and the same three hypotheses are tested. Figure 30 shows that again the correct hypothesis is rapidly identified.

The above results clearly demonstrate the ability of the structure identification procedure to select the correct system model when the data contains information that allows the discrimination to be made. In practical cases, the technique can be used to evaluate the accuracy of a series of models, none of which may adequately described the system

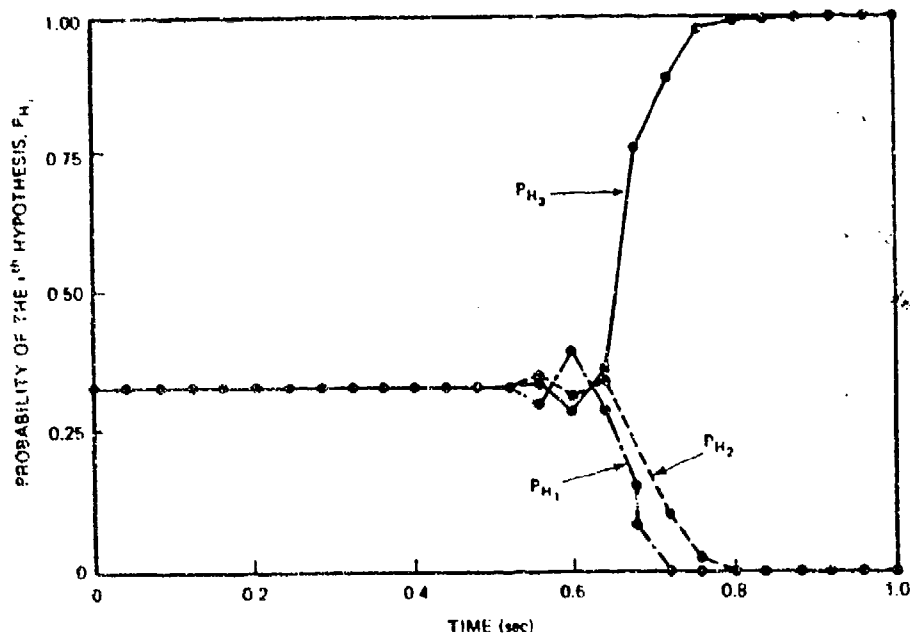


Figure 30. Probability that  $H_i$  is True when  $H_3$  is True, for  $i = 1, 2$ , and 3

which generates the data. The computational cost of this procedure is simply the cost of applying an EKF to the data for each proposed model, since the probability calculations require little additional computer effort.

## SECTION VII

### GBU-15 FLIGHT TEST DATA PROCESSING

#### BACKGROUND

The GBU-15 is a family of nonthrusting air-to-ground standoff weapons launched from an aircraft and steered during flight so as to impact a designated target. Among the GBU-15 family of modular glide weapons, the PWW (Planar Wing Weapon) is characterized by a high aspect ratio swept wing, cruciform tail and bottom mounted fin. Figure 31 gives the significant physical characteristics of this airframe. Extensive wind tunnel testing (over 250 hours) has been conducted in order to determine the aerodynamic model for autopilot design and performance evaluation. In addition, flight tests have been conducted to exercise the airframe throughout the flight regime and to verify performance predictions.

The data required for modeling the GBU-15 was provided by AFATL and included mass, CG and inertia characteristics, and the detailed wind tunnel aerodynamic model. This wind tunnel model includes over 60 static and dynamic terms, each of which requires a one-, two-, or three-dimensional table lookup. In spite of the complexity of this model, comparisons of in-flight measurements with computer simulated measurements show considerable discrepancy - particularly in regions where the vehicle exhibits rapid dynamic motions. Several configuration modifications were made after wind tunnel testing which were not modeled by the wind tunnel data -- a telemetry antenna was located aft of the bottom mounted fin and an  $\alpha$ - $\beta$  boom was mounted in the nose of the vehicle.

TECHNICAL DATA	
AIRFOIL SECTION	= NACA 65-410
THEORETICAL WING AREA	= 16.59 FT <sup>2</sup>
WING SPAN	= 136.3 INCHES
WING CHORD	= 18.48 IN. (STREAMWISE)
WING CHORD	= 16.00 (CHORDWISE)
SWEEP ANGLE	= 30 DEG
ASPECT RATIO	= 7.74
INCIDENCE ANGLE	= 2.6 (STREAMWISE)
	= 3.0 (CHORDWISE)
DIHEDRAL ANGLE	= -10 DEG
OVERALL LENGTH	= 154.50 INCHES
TAIL SPAN	= 56 INCHES
SWEEP ANGLE	= 25 DEG

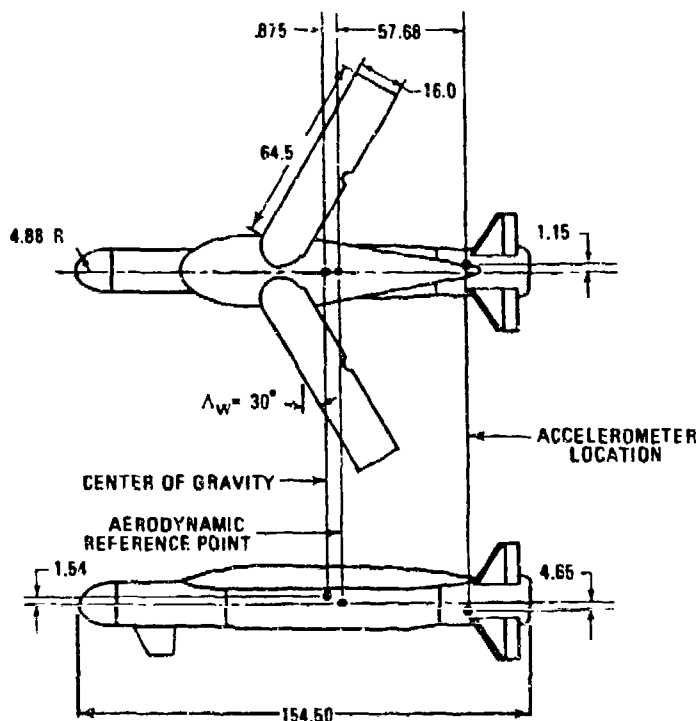
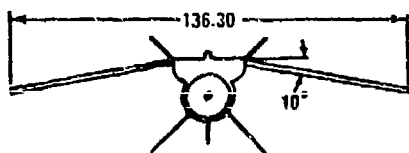


Figure 31. Physical Characteristics of the GBU-15

## FLIGHT TEST DESCRIPTION

All data from a single GBU-15 flight test was provided for use with the parameter identification algorithm discussed previously. This flight test (AFATL designation PPV-4) consists of a high altitude launch, followed by an altitude hold segment, a maximum L/D glide segment, and a rapid pitch down to a near vertical impact. Several roll and yaw maneuvers were executed during the flight to verify autopilot responses. In addition, two significant pitch maneuvers occurred, one at the transition from altitude hold to glide and another at the pitch down to impact.



The flight test data consists of,

- A data tape containing digitized telemetry records from onboard instrumentation at approximately a 20 hertz data rate
- Atmospheric data from instruments launched prior to flight test. This data includes wind, temperature and atmospheric density measurements as functions of altitude
- Radar data processed by an AFATL software package.

The GBU-15 onboard instrumentation included a lateral accelerometer and normal accelerometer, three body-fixed rate gyros, a free gyro indicating inertial roll and heading, an  $\alpha$ - $\beta$  boom, and control surface deflection sensors. Information on accelerometer accuracy and  $\alpha$ - $\beta$  boom wind tunnel calibration was provided.

The smoothed radar data was produced by an AFATL missile test range data processing package which utilized the atmospheric data, together with various radar inputs, to produce estimates of missile trajectory characteristics. Fixed interval smoothing methods were used to provide estimates of position and velocity with respect to inertial space and with respect to the relative air mass.

The telemetry data was plotted and visually inspected in order to determine segments suitable for aerodynamic parameter identification. Three segments, each of about ten-sec length, were selected based on the dynamic activity occurring during the trajectory. Selected telemetered flight measurements are given in Appendix C for each of the three segments. Segment I includes a large pitch maneuver at the transition to constant glide, Segment II includes a yaw maneuver with roll coupling, and

Segment III occurs during the pitch down to impact and includes a large pitch plane maneuver with some roll and yaw activity. Table 33 summarizes the initial and final trajectory characteristics from the radar data for each of the three segments.

The wind magnitude and heading from the atmospheric data are given in Figure 32. The three flight segments occur at altitudes from 15,000 to 24,000 feet. During this period the wind heading and magnitude are nearly constant with altitude so that a constant wind magnitude of 50 knots with heading of 305 degrees east of north was assumed. The missile initial heading was 326.6 degrees east of north and radar data indicates the heading was maintained closely throughout the flight. Each flight segment was initialized with zero initial heading, and with inertial wind approaching 21.6 degrees from the left at 50 knots. At nominal missile velocities, this lateral wind component can contribute about 3 degrees to the sideslip (whereas peak measured  $\beta$  values are about 5 degrees). Thus, wind modeling should play a key roll in the yaw plane representation.

TABLE 33. SUMMARY OF RADAR DATA PROCESSING FOR THREE FLIGHT SEGMENTS

TRAJECTORY VARIABLE	SEGMENT I		SEGMENT II		SEGMENT III	
	t=0	t=10	t=0	t=10	t=0	t=10
Altitude (ft)	23988	21752	19985	18148	19160	15609
Inertial Velocity Magnitude (fps)	550	628	672	685	478	642
Relative Velocity Magnitude (fps)	623	692	747	767	552	676
Mach Number	0.601	0.659	0.706	0.719	0.520	0.627
Flight Path Angle (deg)	-5.84	-30.426	-24.18	-8.34	-18.18	-68.67

The measured atmospheric temperature was used to compute the actual values for speed of sound. A comparison of these computed values and the standard atmosphere values are given in Figure 33, as well as a comparison of measured and standard air density. The standard values were used in the identification algorithm.

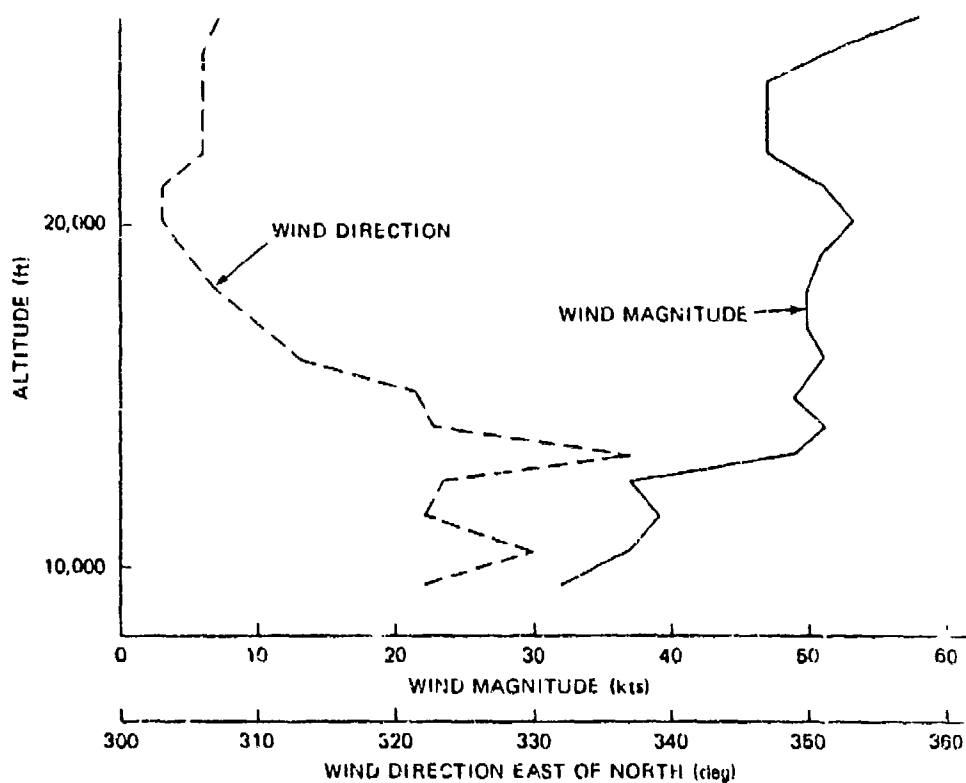


Figure 32. Measured Wind Data for GBU-15 Test Flight

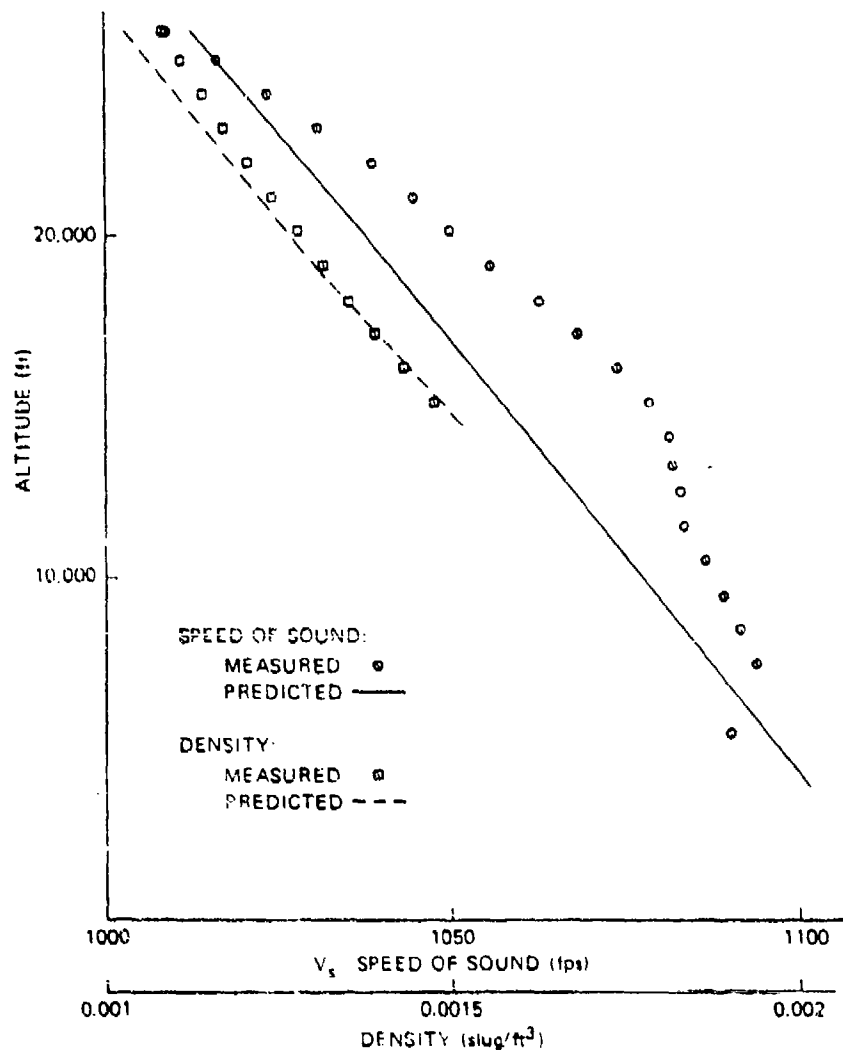


Figure 33. Comparison of Measured Speed of Sound and Density With Standard Values

#### THE A PRIORI MODEL

The GBU-15 mass properties consist of mass, CG location, and inertias. These data are given in Table 34. The lateral and normal accelerometers are located near the rear of the weapon at an average\* location as shown in the

\*The two accelerometers are actually located about 9 inches apart along the x-axis.

TABLE 34. GBU-15 AIRFRAME DATA

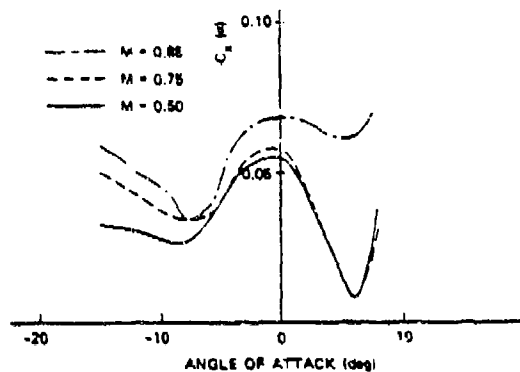
REQUIRED AIRFRAME DATA	GBU-15 VALUE
Mass (slugs)	86.354
x,y,z CG Location (in)	0.875, 0.0, -1.54
Roll Inertia (slug-ft <sup>2</sup> )	119.38
Pitch Inertia (slug-ft <sup>2</sup> )	675.55
Yaw Inertia (slug-ft <sup>2</sup> )	747.42
x,y,z Accelerometer Location (in)	-55.93, 1.15, 4.65

table. Instrument and CG locations are given with respect to the aerodynamic reference point in body axes, defined in Figure 31.

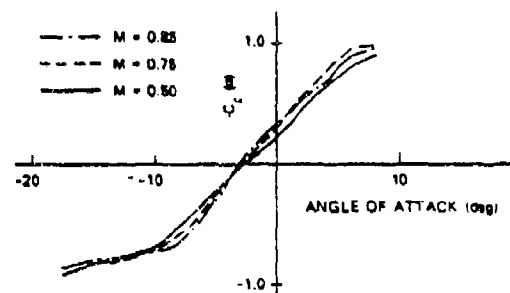
The a priori aerodynamic model for the GBU requires a parameterization of the detailed tabular data provided by AFATL, as well as the assignment of uncertainties to the resulting parameter values. This simplified model was constructed based on discussions with aerodynamicists familiar with the GBU-15, previous experience with winged aerodynamic vehicles, inspection of the actual flight data and analysis of the wind tunnel data.

A simplified EKF model was used for the initial trials, assuming pitch aerodynamics to be decoupled from the yaw and roll aerodynamics. Yaw and roll are known to be highly coupled so that all linear yaw-roll aerodynamic effects frequently encountered in aircraft are modeled (Reference 23). Additional parameters were investigated based on the initial identification trials.

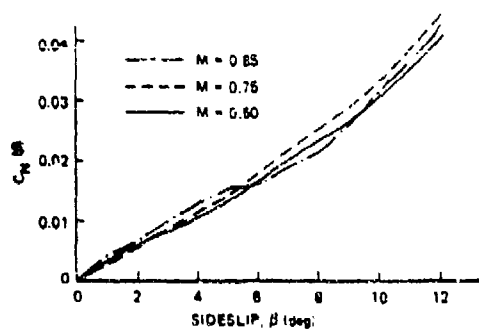
Figure 31 shows representative examples of the wind tunnel data. Figures 34(a) and 34(g) demonstrate the complex



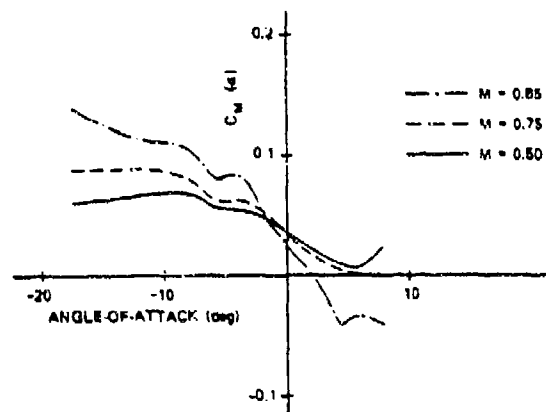
(a) Axial Force Coefficient vs Angle-of-Attack



(b) Normal Force Coefficient vs Angle-of-Attack

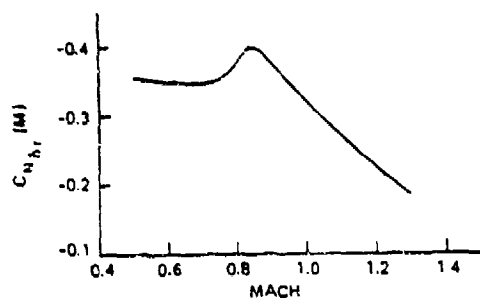


(c) Yaw Moment Coefficient vs Sideslip

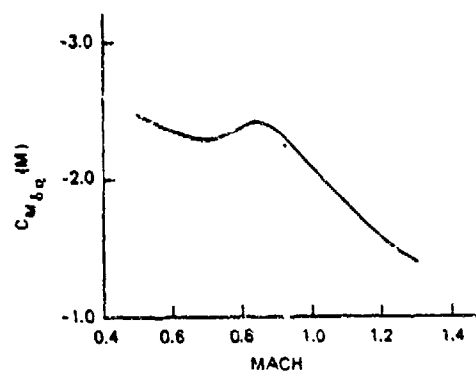


(d) Pitching Moment Coefficient vs Angle-of-Attack

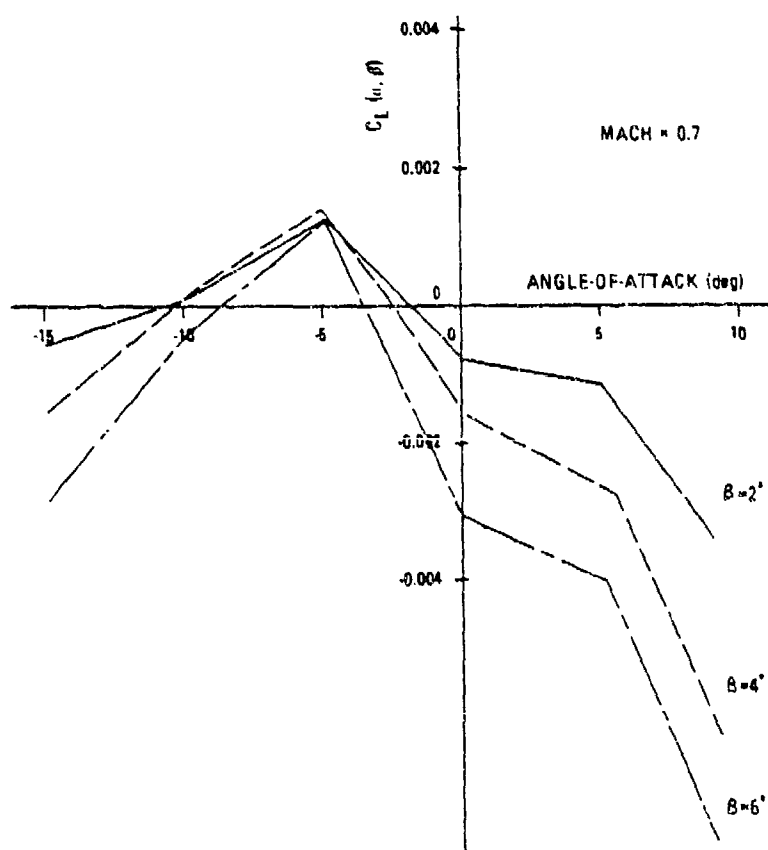
Figure 34. Representative Wind Tunnel Data



(e) Yaw Moment Control  
Effectiveness vs Mach No.



(f) Pitch Moment Control  
Effectiveness vs Mach No.



(g) Roll Moment vs Angle-of-  
Attack and Sideslip

nature of the aerodynamics for this vehicle. Only slight coefficient variation with Mach number below 0.75 is evident, so that coefficient invariance with Mach number is reasonable for Mach number ranges given in Table 34. The parameters investigated in this study are given in Table 35 along with the initial values and uncertainties.

The only measurements used for identification during this study are the two accelerometers, three rate gyros and the  $\alpha$ - $\beta$  sensors. A conservative initial estimate of measurement noise was obtained by observation of the actual data. These initial estimates were modified by inspection of the EKF residual process. The accelerometer, rate gyro and  $\alpha$ - $\beta$  sensor noises were initially given by  $2 \text{ ft/sec}^2$ ,  $0.01 \text{ rad/sec}$  and  $0.01 \text{ radian}$ , respectively.

The force perturbation inputs (process noise) were assigned values of  $2 \text{ ft/sec}^2$ . The moment perturbation inputs were given values representative of a 0.3-degree noise in control deflection measurement at a dynamic pressure of  $250 \text{ lb/ft}^2$ . All studies in this section assumed a wide-band (white) process noise input.

The transfer functions relating  $\alpha$  and  $\beta$  to the control inputs  $\delta_q$  and  $\delta_r$  were computed from the mass properties and the aerodynamic coefficients. This "open loop airframe response" indicates lightly damped pitch and yaw plane responses with damping ratios of approximately 0.18 and 0.08, respectively, and a natural frequency of about  $2.7 \text{ rad/sec}$  in both planes. Step responses from the 6-DOF a priori airframe model correlated well with these computations.

The GBU-15 utilizes both accelerometer and pitch rate feedback for stability augmentation. Well damped



TABLE 35. GBU-15 PARAMETER DATA

PARAMETER*	INITIAL VALUE	UNCERTAINTY ( $\sigma$ )
$C_{x_0}$	-0.04	0.02
$C_{y_0}$	0.0	0.10
$C_{y_B}$	-1.58	0.4
$C_{y_{\delta r}}$	0.83	0.15
$C_{z_0}$	-0.28	0.1
$C_{z_a}$	-6.25	4.0
$C_{z_{\delta q}}$	-0.42	0.10
$C_{L_0}$	0.0	0.02
$C_{L_e}$	0.0	0.02
$C_{L_{\delta p}}$	0.096	0.04
$C_{L_p}$	-0.45	1.0
$C_{L_r}$	0.16	0.40
$C_{M_0}$	0.03	0.20
$C_{M_a}$	-0.3	0.1
$C_{M_{\delta q}}$	-2.3	0.5
$C_{M_q}$	-20.0	20.0
$C_{N_0}$	0.0	0.003
$C_{N_B}$	0.120	0.03
$C_{N_{\delta r}}$	-0.35	0.10
$C_{N_r}$	-0.66	1.0
$C_{N_p}$	-0.04	0.40

\*All angles are expressed in radians.

responses to pitch and yaw plane acceleration commands are observed with settling times of about 1.5 and 2.5 seconds, respectively. Some concerns have been expressed in the literature about the identifiability of dynamic systems imbedded in closed loop systems (Reference 24), although studies discussed in Reference 24 indicate successful identification in systems operating in both open loop and closed loop modes.

No specific investigations into the effects of the closed loops on identification of the GBU-15 was made; all measurements result from the operational closed loop system.

## IDENTIFICATION RESULTS

Initial identification tests were performed using only ten measurement samples in order to isolate extreme a priori modeling problems. During this stage the data rate of 10 hertz (every other data point) was selected, dynamic state initial conditions of each data segment were adjusted and measurement noise levels were modified slightly from the a priori values. The measurement levels assumed in the EKF model are given in Table 36. After these initial trials, a 100-sample identification test was performed for each of the three segments discussed previously. The 21 parameters indicated on Table 35 were identified for each segment.

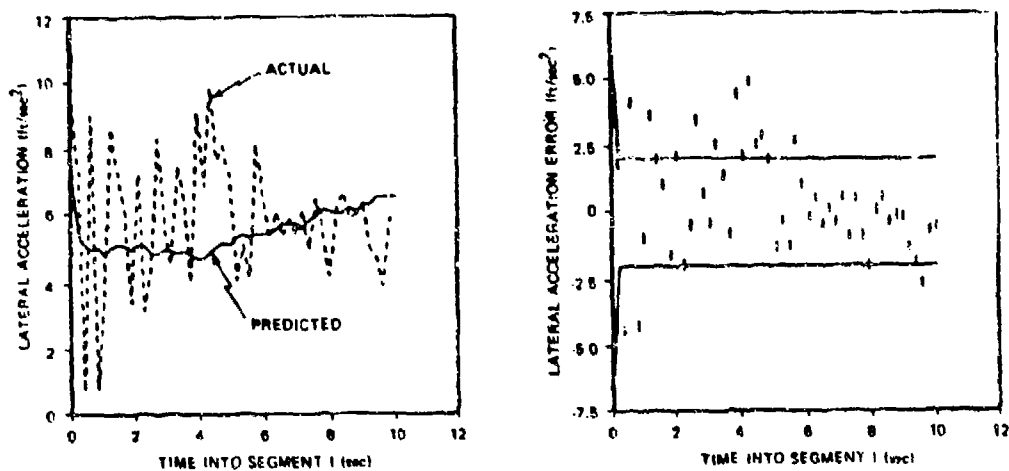
TABLE 36. ADJUSTED MEASUREMENT NOISE LEVELS

MEASUREMENT	UNITS	ERROR (1 $\sigma$ )
Lateral Accelerometer	ft/sec <sup>2</sup>	2.0
Normal Accelerometer	ft/sec <sup>2</sup>	2.0
Roll Rate	rad/sec	0.02
Pitch Rate	rad/sec	0.01
Yaw Rate	rad/sec	0.01
$\alpha$ Sensor	rad	0.005
$\beta$ Sensor	rad	0.01

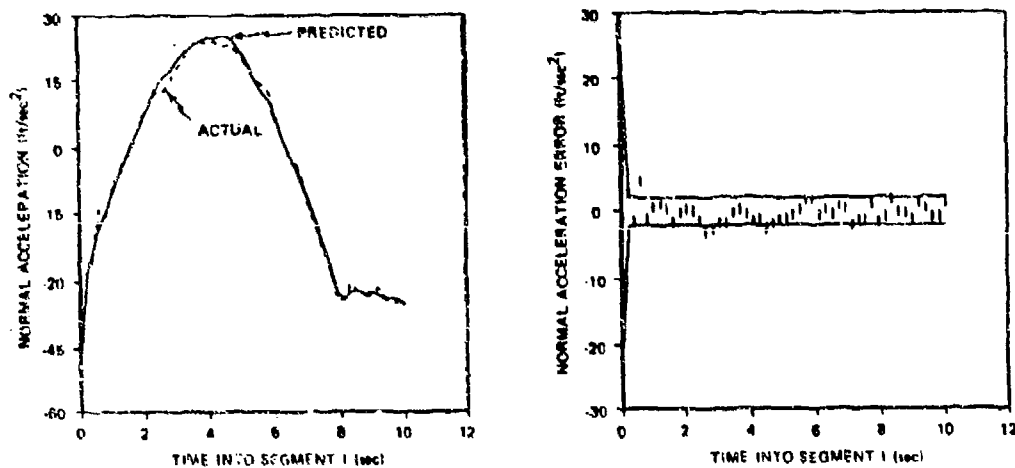
The predicted and actual measurement comparisons, the residual processes, and the predicted residual bounds which occurred during parameter identification are shown in Figures 35 through 37. The predicted/actual measurement comparison as shown in these figures must be interpreted carefully. If sufficient process noise is injected into a dynamic model, almost any set of parameter values may produce an excellent predicted measurement/actual measurement comparison. In addition, the dynamics which generated these measurements utilized time-varying parameters which resulted during the course of parameter identification. A more conclusive demonstration of the ability of the final parameter set to represent the data is given later. The final parameter estimate and the predicted standard deviations are shown in Table 37.

Because of the large angle-of-attack maneuvers during data segments I and III, the pitch plane aerodynamics should be highly observable. The pitch plane dynamics appear to be modeled accurately as indicated by the normal acceleration, pitch rate and angle-of-attack residuals.

Large values of the correlation coefficients between some parameters were observed, particularly between  $C_{Z_0}$  and  $C_{Z_\alpha}$  and between  $C_{M_0}$  and  $C_{M_\alpha}$ . Segments I and III produced correlation coefficients of 0.91 and 0.87, respectively, between  $C_{Z_0}$  and  $C_{Z_\alpha}$ . High correlations such as these make interpretation of actual parameter values difficult since a family of parameter values may produce near identical residual processes. The estimate of  $C_{M_\alpha}$  was consistent between the two segments and showed a slightly positive value -- indicating a less stable airframe than predicted by wind tunnel data.

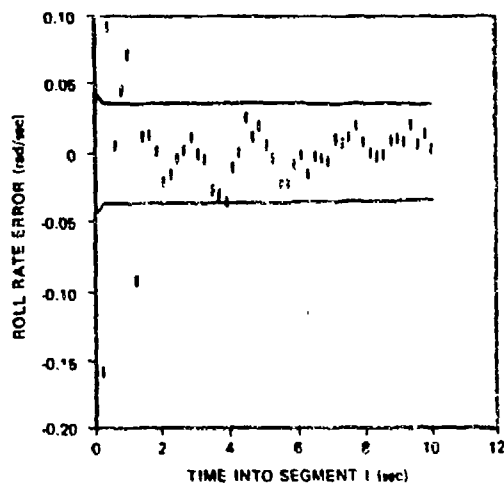
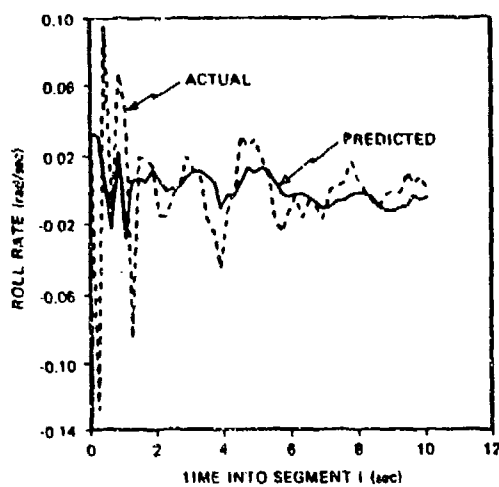


(a) Lateral Acceleration

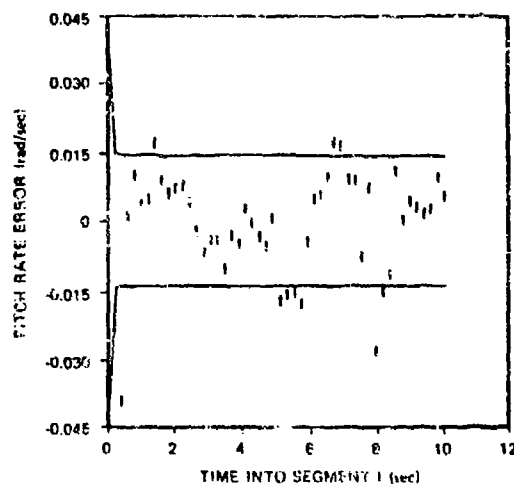
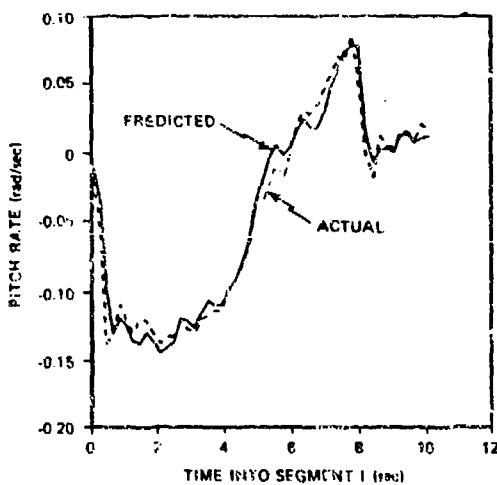


(b) Normal Acceleration

Figure 35. Predicted and Actual Measurement Comparison for Segment 1

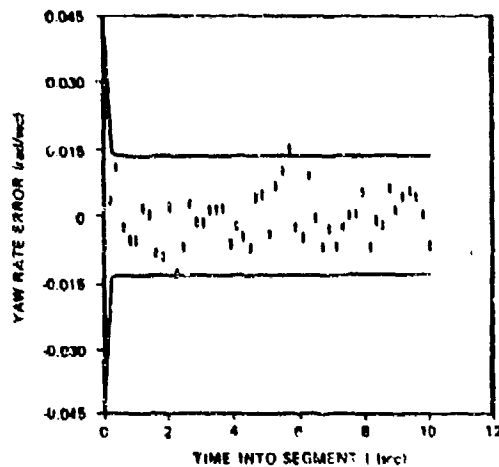
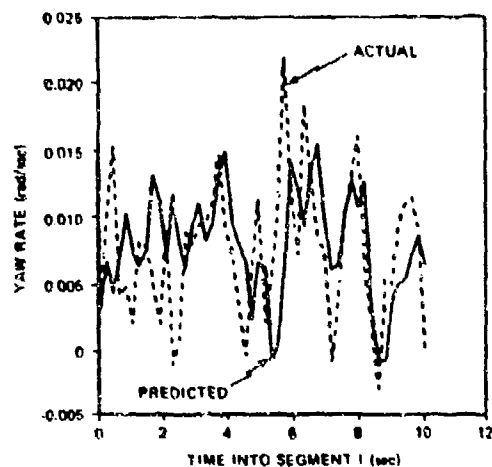


(c) Roll Rate

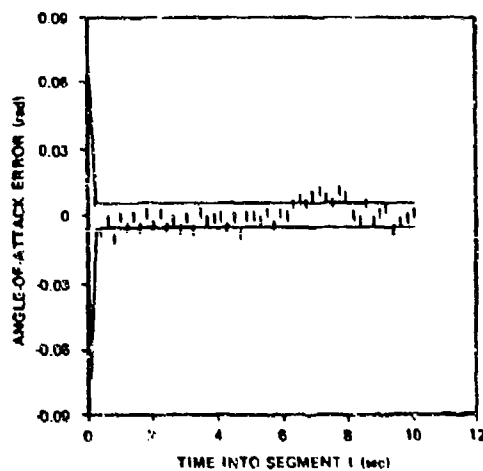
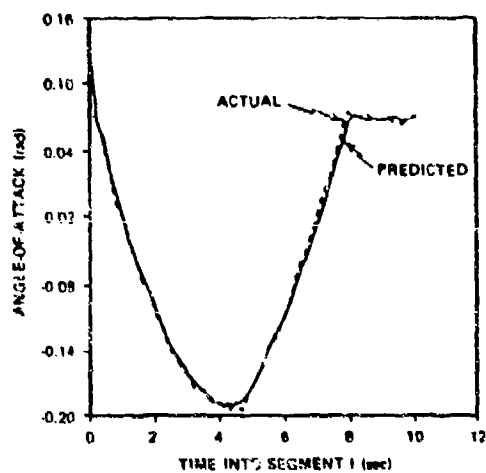


(d) Pitch Rate

Figure 35. Predicted and Actual Measurement Comparison for Segment I (Continued)

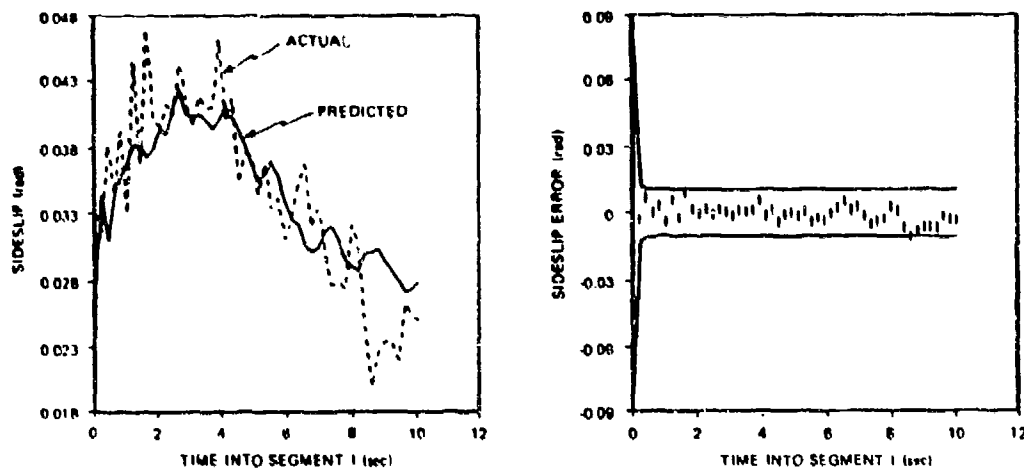


(e) Yaw Rate



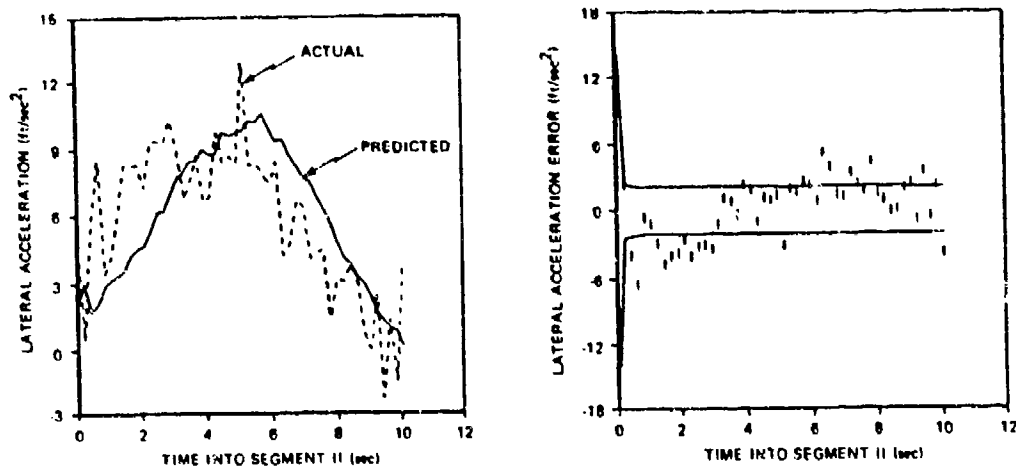
(f) Angle-of-Attack

Figure 35. Predicted and Actual Measurement Comparison for Segment I (Continued)

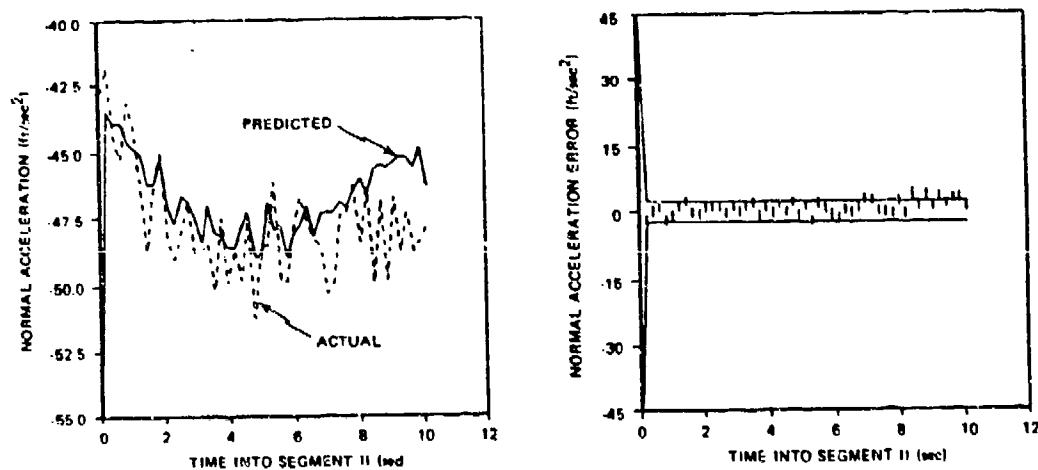


(g) Sideslip

Figure 35. Predicted and Actual Measurement Comparison for Segment I (Concluded)



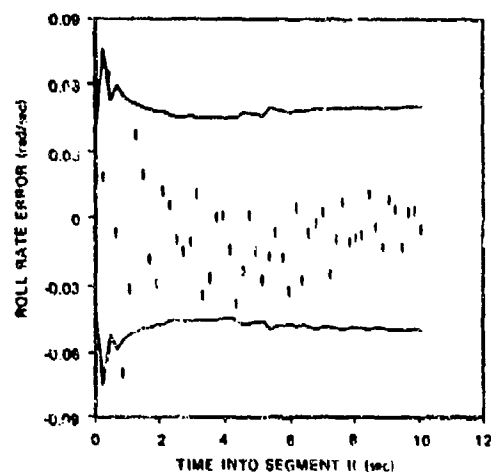
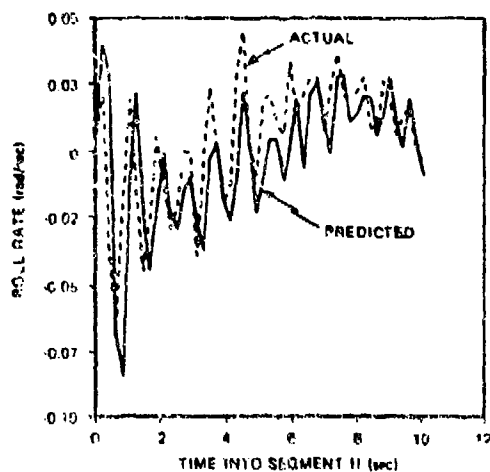
(a) Lateral Acceleration



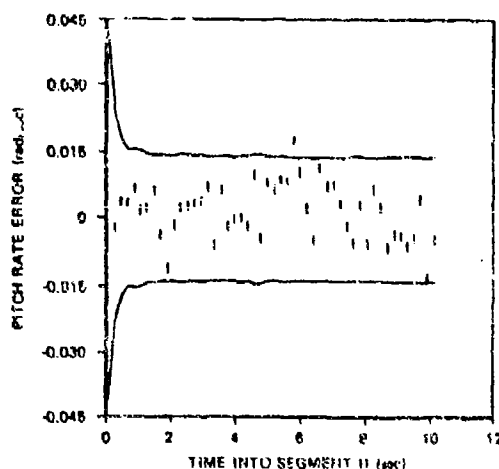
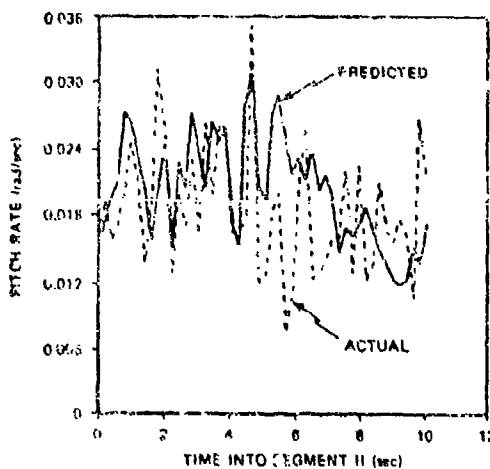
(b) Normal Acceleration

Figure 36. Predicted and Actual Measurement Comparison for Segment II



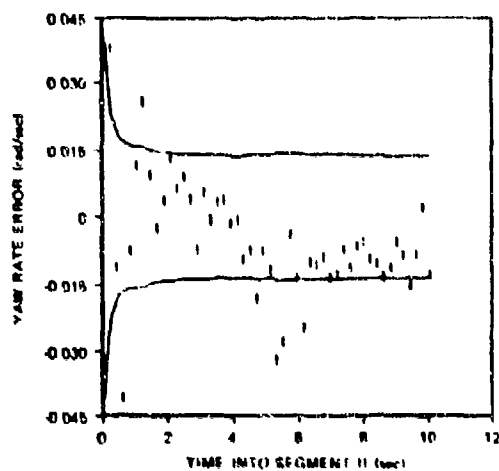
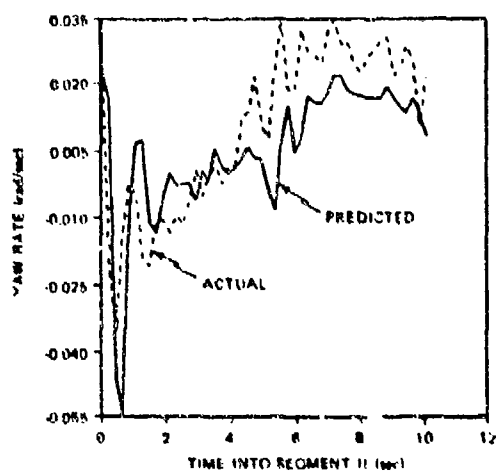


(c) Roll Rate

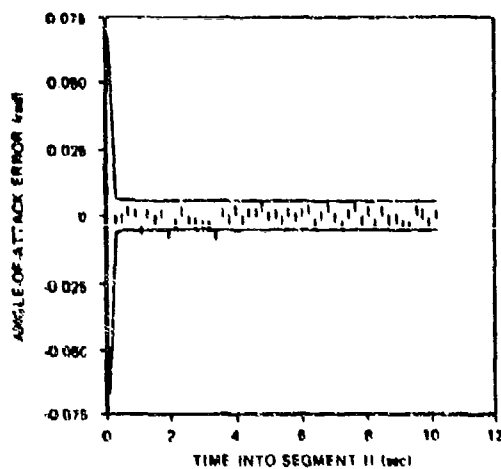
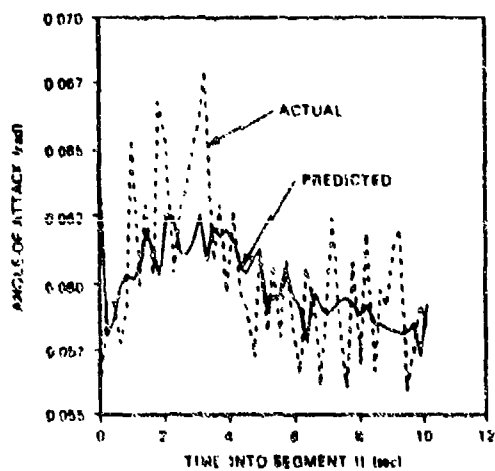


(d) Pitch Rate

Figure 36. Predicted and Actual Measurement Comparison for Segment II (Continued)

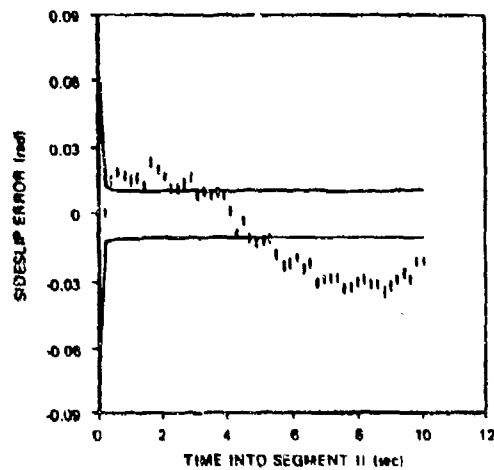
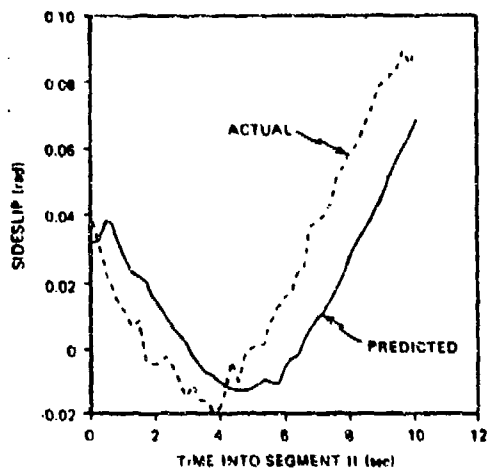


(e) Yaw Rate



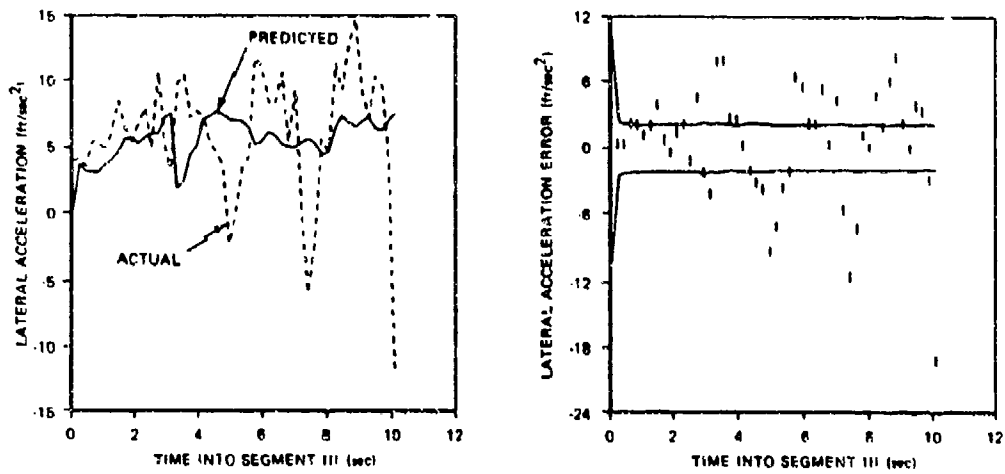
(f) Angle-of-Attack

Figure 36. Predicted and Actual Measurement Comparison for Segment II (Continued)

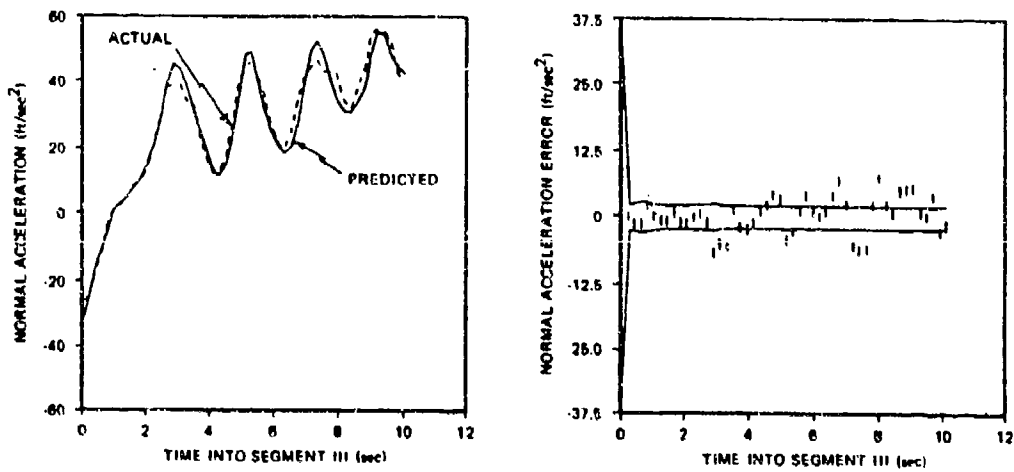


(g) Sideslip

Figure 36. Predicted and Actual Measurement Comparison for Segment II (Concluded)

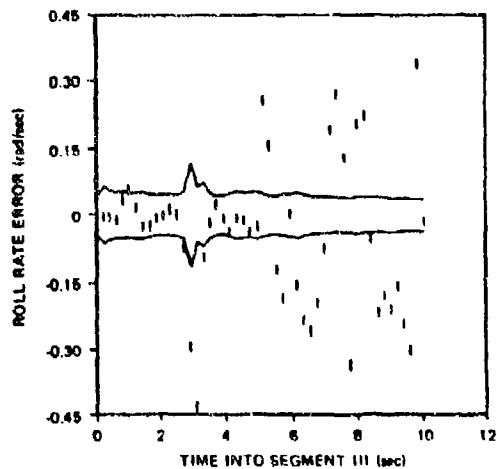
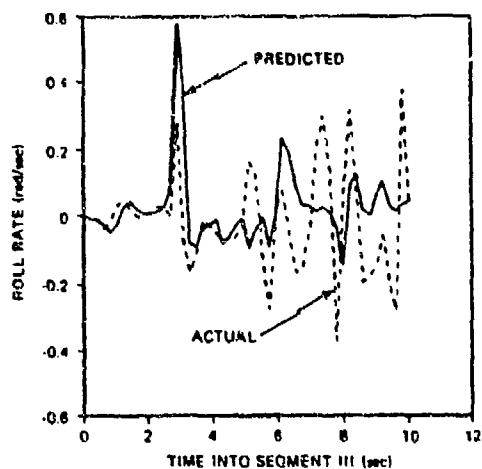


(a) Lateral Acceleration

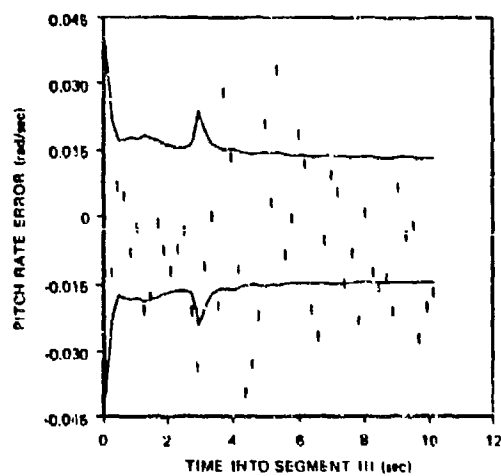
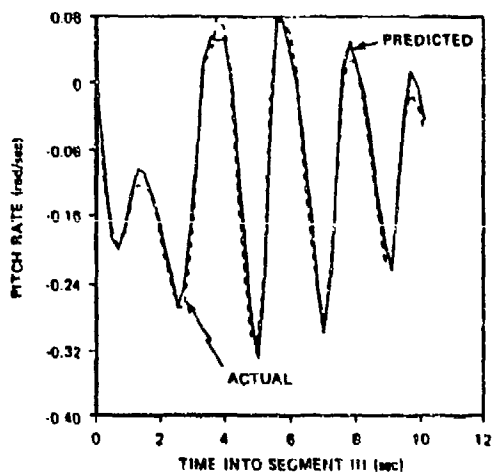


(b) Normal Acceleration

Figure 37. Predicted and Actual Measurement Comparison for Segment III

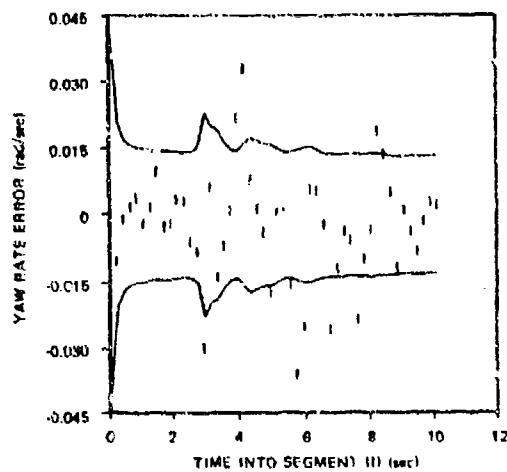
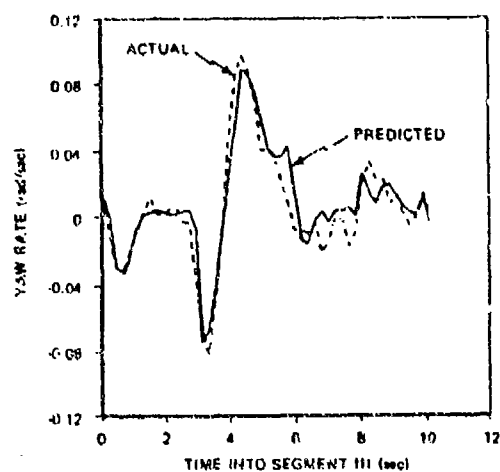


(c) Roll Rate

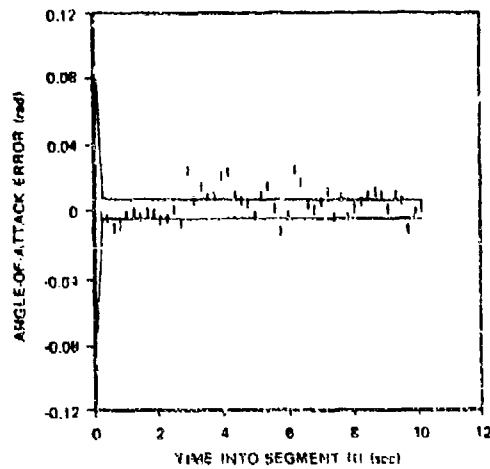
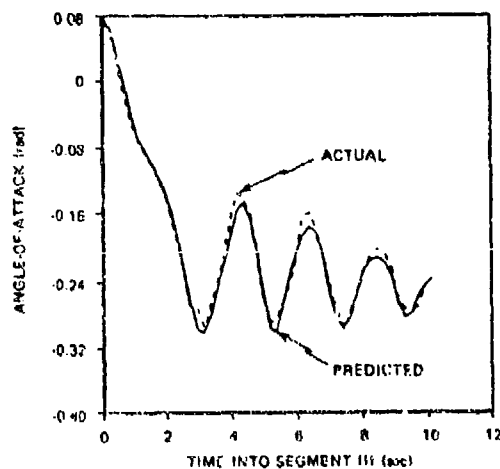


(d) Pitch Rate

Figure 37. Predicted and Actual Measurement Comparison for Segment III (Continued)

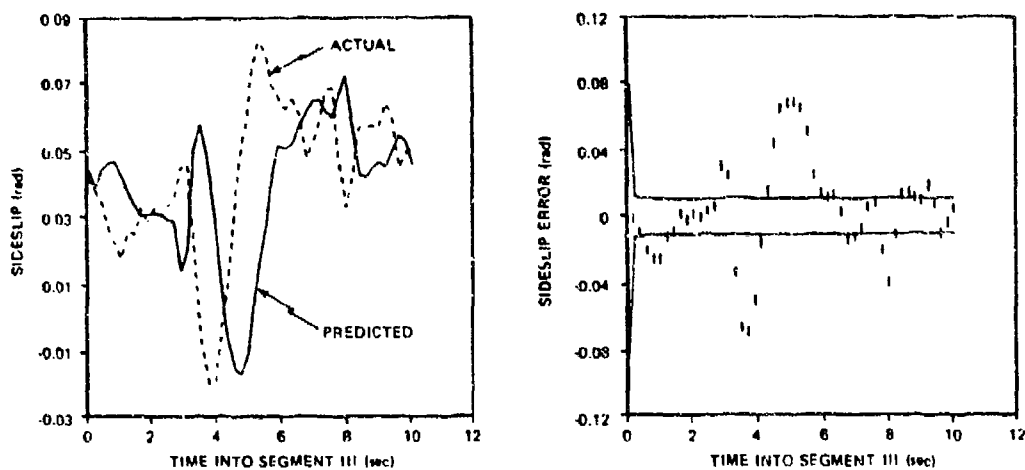


(e) Yaw Rate



(f) Angle-of-Attack

Figure 37. Predicted and Actual Measurement Comparison for Segment III (Continued)



(g) Sideslip

Figure 37. Predicted and Actual Measurement Comparison for Segment III (Concluded)

TABLE 37. FINAL GBU-15 PARAMETER ESTIMATES

PARAMETER	FINAL PARAMETER ESTIMATES (PREDICTED STANDARD DEVIATIONS)		
	SEGMENT I	SEGMENT II	SEGMENT III
$C_{x_0}$	-0.058(0.018)	-0.0021(0.016)	0.0038(0.015)
$C_{y_0}$	0.075(0.015)	0.30(0.0071)	0.12(0.008)
$C_{y_2}$	-1.2(0.37)	-3.1(0.19)	-0.60(0.16)
$C_{y_{\delta r}}$	0.85(0.15)	1.0(0.14)	0.69(0.15)
$C_{z_0}$	0.41(0.013)	-0.28(0.082)	-0.24(0.016)
$C_{z_a}$	-5.7(0.22)	-12.0(1.4)	-3.3(0.12)
$C_{z_{\delta q}}$	-0.42(0.10)	-0.43(0.10)	0.014(0.085)
$C_{L_0}$	0.0015(0.00078)	0.0019(0.00041)	-0.00023(0.00030)
$C_{L_2}$	0.012(0.017)	-0.0032(0.0094)	0.028(0.0064)
$C_{L_{\delta p}}$	0.025(0.030)	-0.0022(0.020)	-0.013(0.0038)
$C_{L_p}$	-2.6(0.82)	-0.29(0.54)	-1.7(0.12)
$C_{L_r}$	-0.033(0.00)	0.013(0.24)	-0.030(0.33)
$C_{M_0}$	0.018(0.0024)	0.046(0.011)	-0.0059(0.0032)
$C_{M_a}$	0.075(0.28)	-0.13(0.08)	0.0423(0.012)
$C_{M_{\delta q}}$	-0.97(0.14)	-0.65(0.22)	-0.90(0.039)
$C_{M_q}$	-12.8(12.0)	-28.0(20.0)	-59.6(5.1)
$C_{N_u}$	-0.0034(0.00095)	-0.0024(0.00048)	-0.00006(0.00039)
$C_{N_\beta}$	0.042(0.025)	0.092(0.012)	0.020(0.0081)
$C_{N_{\delta r}}$	-0.10(0.060)	-0.11(0.039)	0.060(0.049)
$C_{N_r}$	-1.32(0.96)	-1.2(0.79)	-2.3(0.56)
$C_{N_p}$	-0.059(0.39)	-0.42(0.36)	-0.65(0.13)



Data segments II and III should provide good parameter observability for the coupled roll and yaw planes. The residual processes from these segments appear to indicate modeling errors. Note, in particular, the low frequency component exhibited in the  $\beta$  residual for segment II in Figure 36(g). A variety of attempts were made to improve the roll-yaw model. The additional coupling terms indicated in Table 38 were investigated but little improvement was found. Early in the study some confusion arose in the correct signs of the input control deflections, particularly  $\delta r$  and  $\delta p$ . Switching signs on these inputs produced no improvement. Figure 37(g) suggests the sign of the  $\beta$  sensor may be incorrect. Changing this sign resulted in much better behavior of the  $\beta$  residual as shown in Figure 38.

Several factors may contribute to the modeling difficulties in the roll-yaw dynamics,

- The model assumed here may not accurately capture roll-yaw effects. The roll wind tunnel data of Figure 34(g) supports this premise.
- The initial parameter values may not be accurate enough to allow the filter to converge to the correct values.
- The yaw-roll maneuvers are of such low amplitude and frequency as to provide little information in the data about the yaw-roll coefficients.
- Signs of the measurements and/or control deflections may be wrong.

It is not readily apparent from the data presented thus far that the models resulting from parameter identification offer an improvement over the a priori models. In order to demonstrate that the collection of final parameter

TABLE 38. ADDITIONAL PARAMETERS INVESTIGATED

ADDITIONAL PARAMETERS INVESTIGATED	INITIAL VALUE	UNCERTAINTY ( $\sigma$ )
$C_{y_{as}}$	0	5
$C_{y_p}$	0.5	1.0
$C_{L_{a6}}$	0	0.2
$C_{L_{\delta r}}$	0	0.05
$C_{N_{pa}}$	-0.69	0.3
$C_{N_{\delta p}}$	0	0.2
$V_x^*$	0	10 (fps)
$V_y^*$	0	10 (fps)
$V_z^*$	0	10 (fps)

\*Wind components.

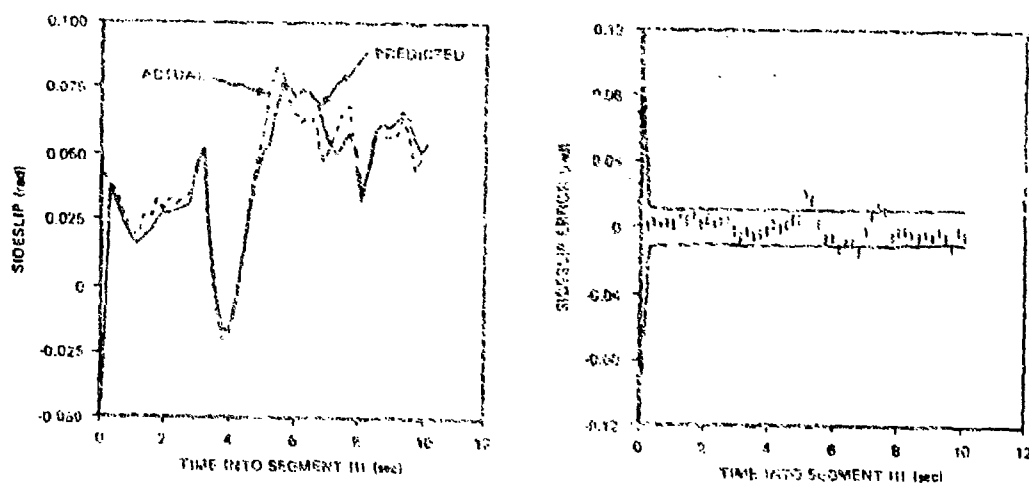
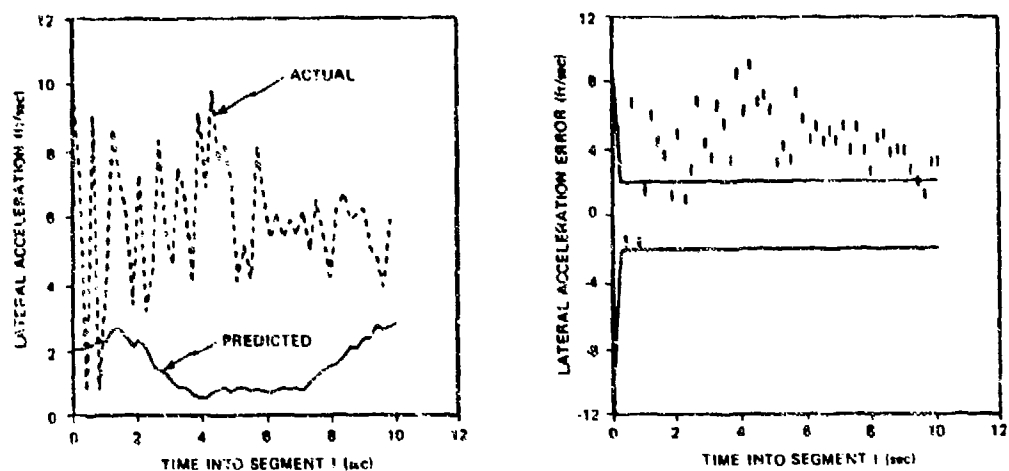


Figure 38. Comparison of Predicted and Actual Sideslip for Segment III With Input Measurement Assumed to Represent Negative Sideslip

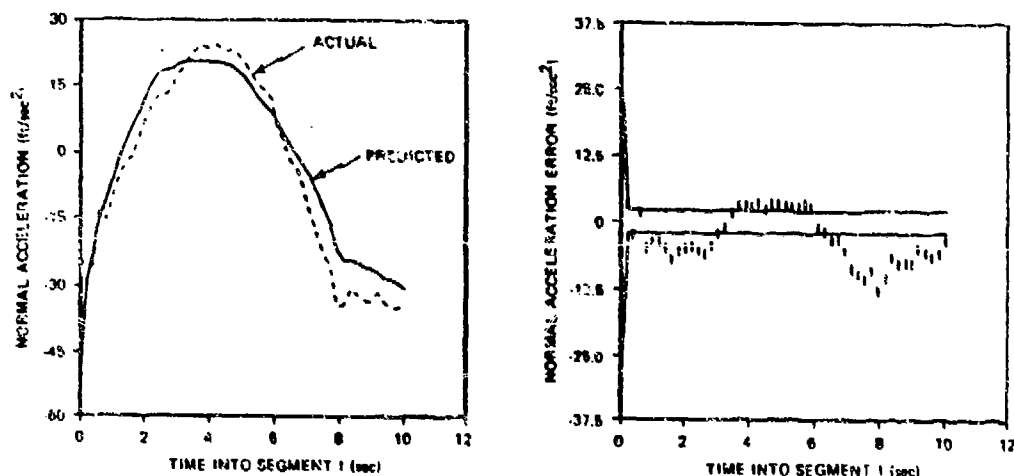
estimates represents an improved model, two predicted measurement profiles are presented -- one generated from the initial parameter values and a second from the final parameter estimates. The improvement in the agreement between the actual measurement and predicted measurements is a measure of the knowledge gained through system identification.

As demonstrated in Section V the initial condition errors and process noise inputs prevent comparisons resulting from a straightforward integration of the dynamics using the initial and final parameter estimates. Several of the results noted above suggest that process noise plays a significant role in the models which have been fit to the data. A method of comparison which treats unknown initial conditions and process noise consists of processing the measurement data via the EKF with the parameters assumed known, i.e., no parameter vector is augmented to the dynamic states. If the EKF is exercised in this manner, first with initial parameter values and then with final parameters, two measurement profiles are obtained which can be compared with the actual measurement data to show system model improvement.

The complete set of predicted measurements and residuals from data Segment I generated by the EKF using parameter estimates fixed at their initial values, is shown by Figure 39. These figures indicate considerable residual time-correlation indicating definite system modeling errors. The predicted measurements with fixed final parameter estimates are given by Figure 40. The excellent improvement in the residual processes demonstrates the increased modeling accuracy achieved with the parameter estimates obtained by the parameter identification algorithm. The initial and final parameter values from Segments II and III were not compared in this manner, though it is expected that a similar modeling improvement would be indicated.

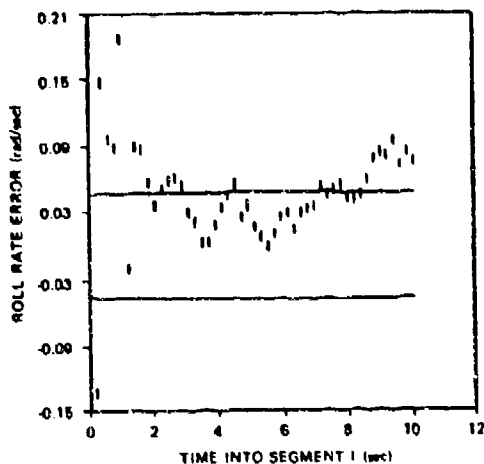
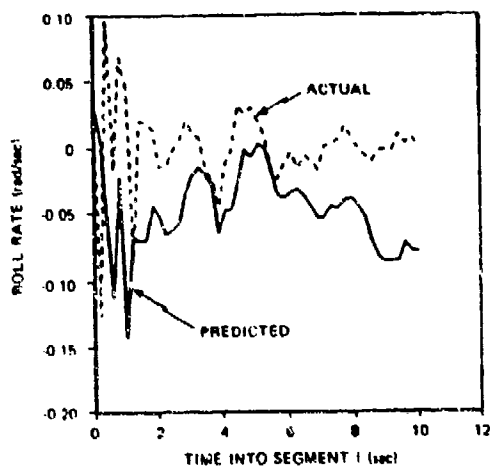


(a) Lateral Acceleration

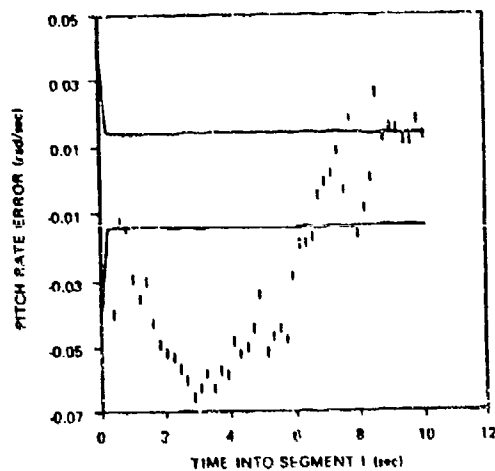
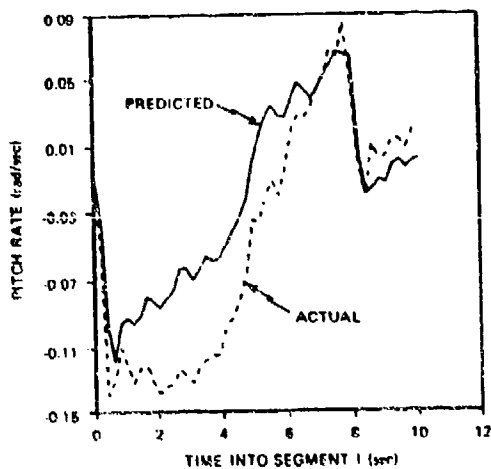


(b) Normal Acceleration

Figure 39. Predicted and Actual Measurement Comparison With Fixed Initial Parameter Values

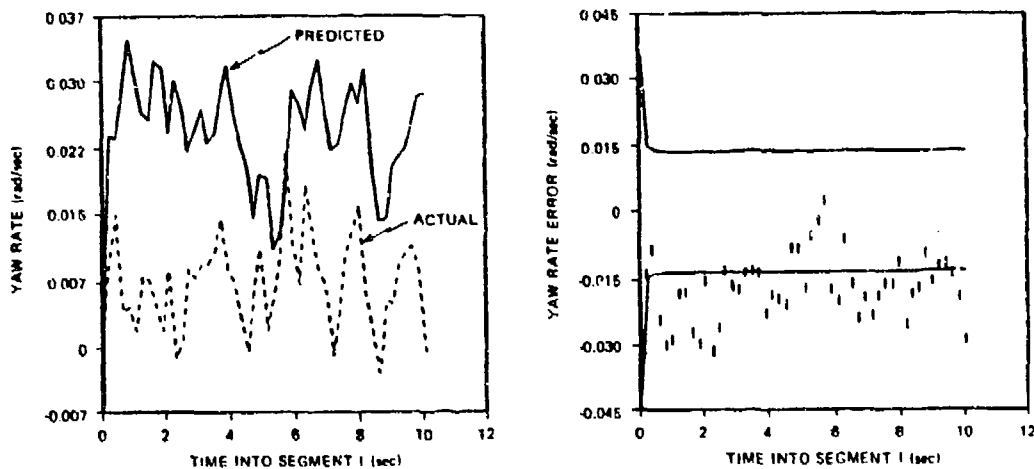


(c) Roll Rate

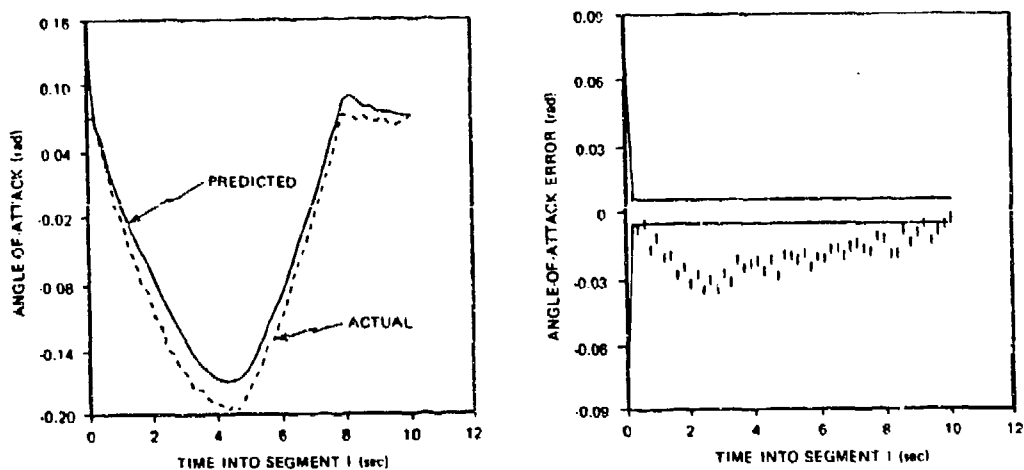


(d) Pitch Rate

Figure 39. Predicted and Actual Measurement Comparison With Fixed Initial Parameter Values (Continued)

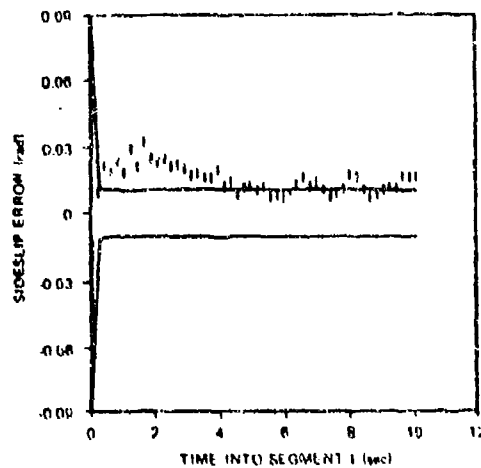
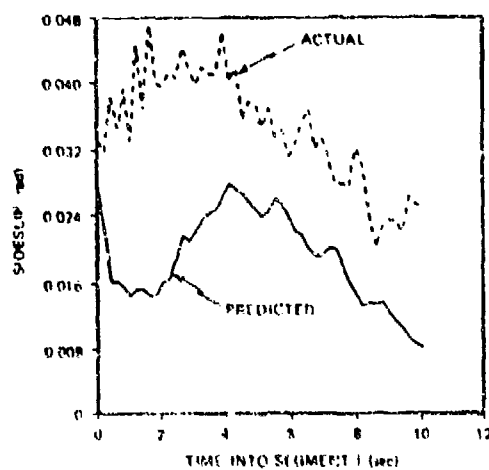


(e) Yaw Rate



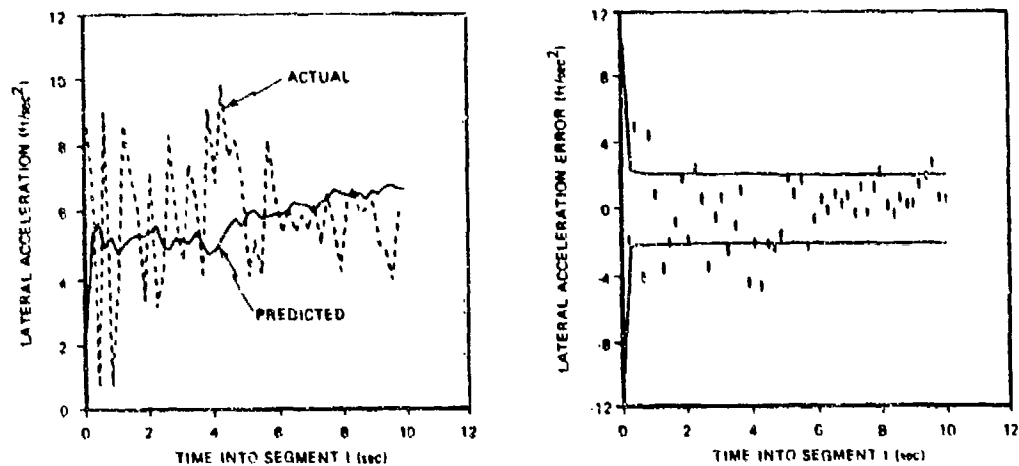
(f) Angle-of-Attack

Figure 39. Predicted and Actual Measurement Comparison With Fixed Initial Parameter Values (Continued)

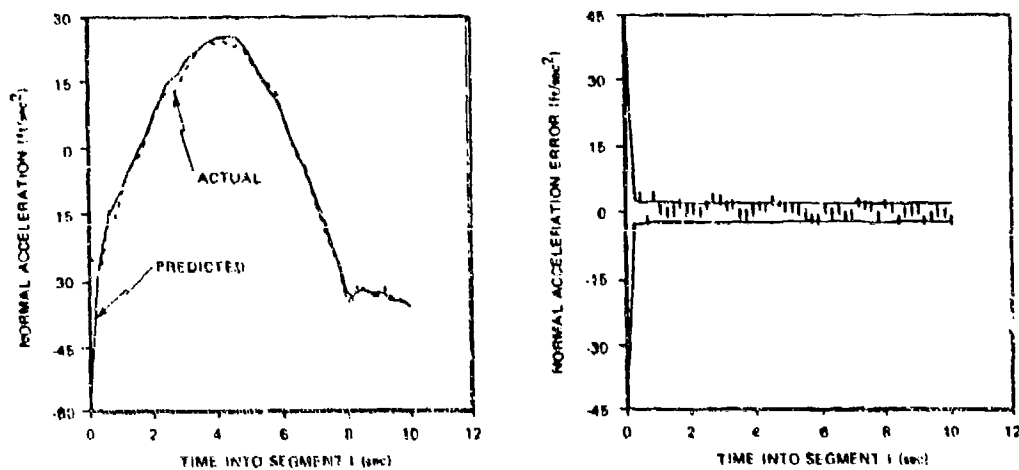


(g) Sideslip

Figure 39. Predicted and Actual Measurement Comparison With Fixed Initial Parameter Values (Concluded)



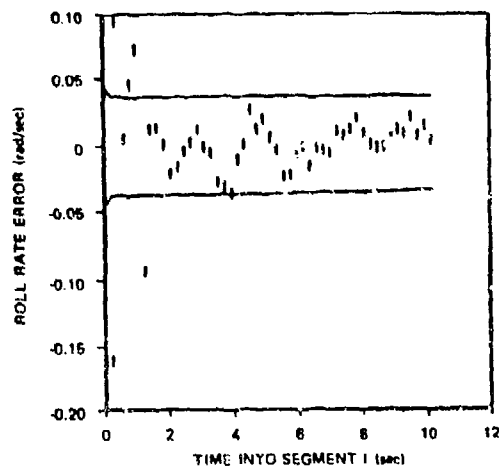
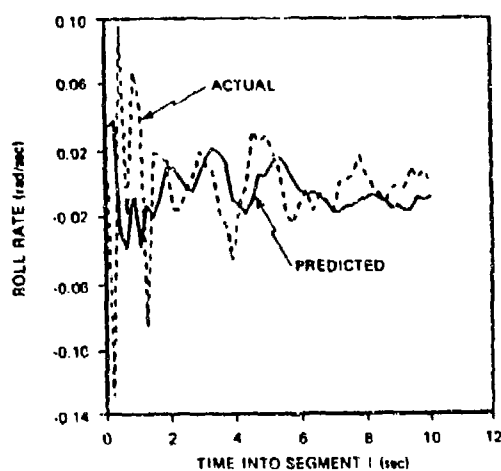
(a) Lateral Acceleration



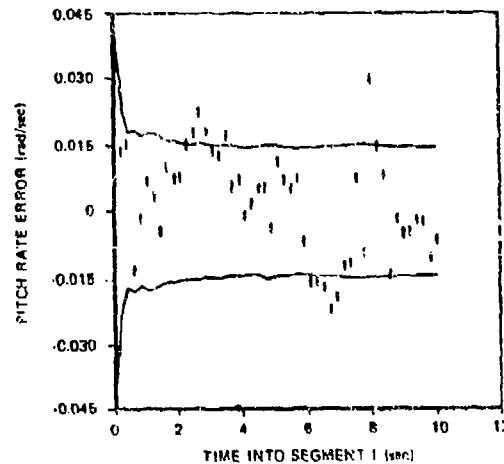
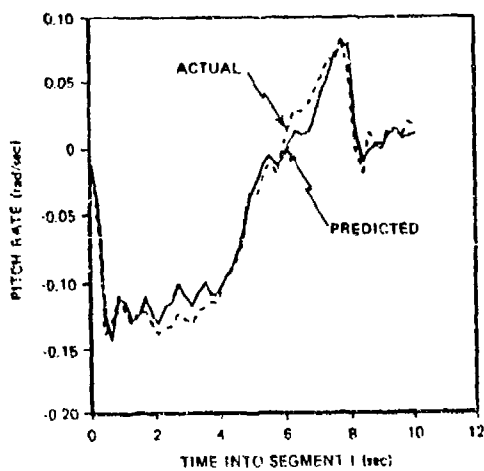
(b) Normal Acceleration

Figure 40. Predicted and Actual Measurement Comparison With Fixed Final Parameter Values



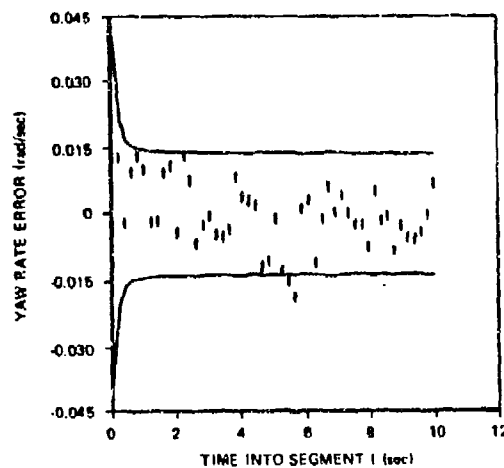
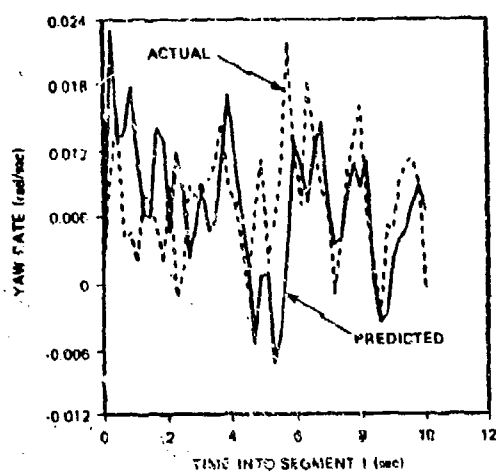


(c) Roll Rate

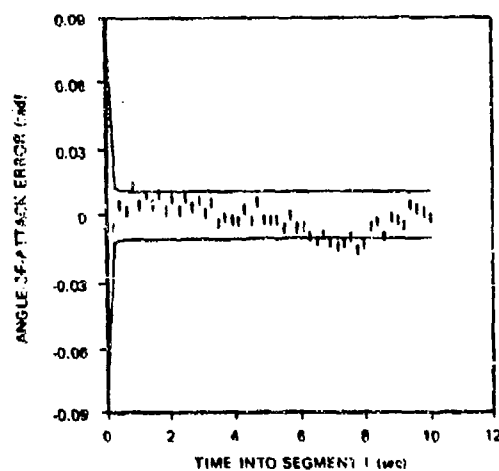
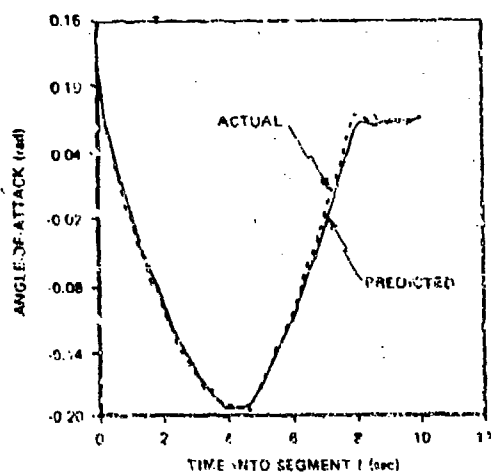


(d) Pitch Rate

Figure 40. Predicted and Actual Measurement Comparison With Fixed Final Parameter Values (Continued)

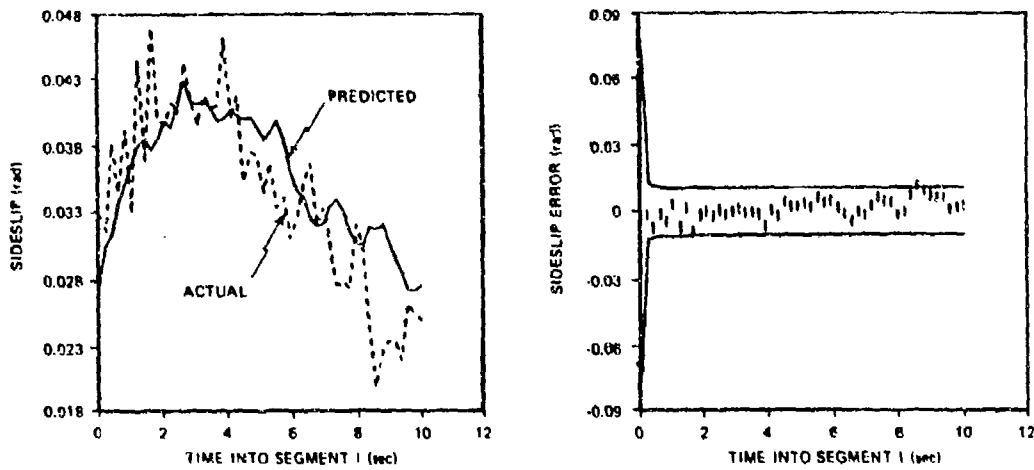


(e) Yaw Rate



(f) Angle-of-Attack

Figure 40. Predicted and Actual Measurement Comparison With Fixed Final Parameter Values (Continued)



(g) Sideslip

Figure 40. Predicted and Actual Measurement Comparison With Fixed Final Parameter Values (Concluded)

## SECTION VIII

### CONCLUSIONS AND RECOMMENDATIONS

#### SUMMARY AND CONCLUSIONS

An extended Kalman filter algorithm for estimating aerodynamic parameters from missile flight data has been developed and evaluated using both simulated and actual flight test data. The algorithm includes a general purpose 6-DOF missile airframe model suitable for representing a variety of missile configurations. Airframe modeling includes the effects of:

- Time-varying thrust profile
- Thrust variation with altitude
- Time-varying mass properties
- Standard atmospheric model
- Wind versus altitude profile
- Thrust misalignment
- CG offsets
- An extensive generalized aerodynamic parameterization.

The extended Kalman filter requires inputs from various flight data sensors. The measurement options investigated in this study are:

- Body-fixed rate gyros
- Body-fixed accelerometers
- Angle-of-attack and sideslip sensors

- Position measurement
- Attitude measurements.

Algorithm verification studies and filter sensitivity studies have been performed using synthetic data from a thrusting short range interceptor airframe model. Filtering performance variations resulting from various measurement sets, measurement modeling errors and measurement noise levels have been investigated. Aerodynamic representations consisting of a low order "linear" aerodynamic model as well as more extensive nonlinear models including up to 36 aerodynamic parameters were also studied. Conclusions resulting from the verification and sensitivity studies are:

- The extended Kalman filter is well suited as an aerodynamic parameter identification tool for large scale airframe modeling.
- The computational burden -- both in core size and computation time -- are not excessive for the realistically modeled example discussed here.

An additional study was to be performed using synthetic flight data provided by the Air Force Armament Laboratory. This data was produced by a six-degrees-of-freedom interceptor simulation developed independently from the model discussed here. No parameter identification was performed as a result of the large aerodynamic coefficient variations with Mach number during the flight. All aerodynamic coefficients varied on the order of 30 percent per second both during boost and during coast deceleration. Several recommended procedures for aerodynamic parameter identification with large Mach number variations are given in Section V.

A structure identification algorithm also has been developed and evaluated using synthetic measurement data. This algorithm, used in conjunction with the parameter identification algorithm, can select that model from a candidate family of aerodynamic models which most likely produced the input measurements. The capability of the structure identification procedure is demonstrated by test cases in which the algorithm consistently and rapidly selects the correct model structure from three aerodynamic representations -- an 11-parameter model, a 16-parameter model, and a 20-parameter model.

The identification algorithm has been used to process actual flight data from an aerodynamically controlled glide weapon. This experiment provided an operational test of the software and exercised all phases of the aerodynamic modeling procedure. The following tasks were performed in preparation for parameter identification:

- Interfacing with the flight test agency so that missile modeling data, flight measurement tapes, radar data, etc., could be obtained, interpreted, and placed in the proper format required by the identification software.
- An a priori airframe model for use in parameter identification was developed. Considerable simplification of the complex tabular aerodynamics was required.
- The flight data was visually inspected to isolate segments suitable for identification. Measurement noises, process noises and state initial conditions were approximated for three flight segments. Flexible data editing and plotting capabilities were developed to assist in this process.

Parameter identification of a 21-parameter model was performed for the three data segments. The resulting residual

process from the pitch plane measurements appeared well behaved -- indicating pitch plane modeling to be adequate. The roll and yaw plane measurement residuals indicated model deficiencies in the coupled roll-yaw dynamics. Various attempts to add additional parameters failed to improve the residual behavior. Possible causes of these identification difficulties are:

- The a priori model derived from the wind tunnel data is too simplistic. Complex aerodynamic behavior can be seen in the wind tunnel aerodynamic model, which was neglected in the a priori model used for identification.
- The airframe roll-yaw maneuvers during the three selected flight segments may be too low in amplitude and frequency to excite the airframe dynamic modes sufficiently to allow separation of the aerodynamic effects from process and measurement noises.
- The parameters may be initialized incorrectly. Large initial parameter errors together with statistically inconsistent initial uncertainty levels may not allow parameter estimates to converge to the "correct" values.
- Sign errors in control deflection inputs, and/or measurements may be present on the input data.

Irrespective of the difficulties indicated above, the overall GBU-15 modeling exercise was encouraging. A demonstration of modeling improvement after identification was given for which the extended Kalman filter with parameters fixed at their estimated values was used to process flight measurements. These results were compared to a similar case where the parameters were fixed at their initial values. A distinct model improvement was demonstrated by comparing the residual process behavior from these two cases.

## RECOMMENDATIONS

All studies to date indicate that the EKF parameter identification algorithm, together with the general purpose missile airframe model and the structure identification software, is a useful tool for aerodynamic modeling from flight data. Several recommendations for improvements and modification to the existing software are given below,

- Develop a well-documented, operational software package.
- Modify the software to allow identification of missile airframes during flight segments containing large Mach number variations. Specific recommendations are given in Section V.
- Include the capability to estimate additional airframe parameters such as CG offsets, thrust misalignments, sensor misalignments etc.
- Add a random wind model and perform additional studies into the effects of wind gusts.

Further study into GBU-15 parameter identification is also recommended. A major omission in the GBU-15 data processing effort was the failure to properly develop and verify the a priori model used for parameter identification. A more extensive a priori model is required and the resulting model should be verified against existing AFATL GBU-15 simulations. This exercise would ensure a thorough understanding of the significant features of the wind tunnel model and provide confidence in the overall accuracy of the a priori model.



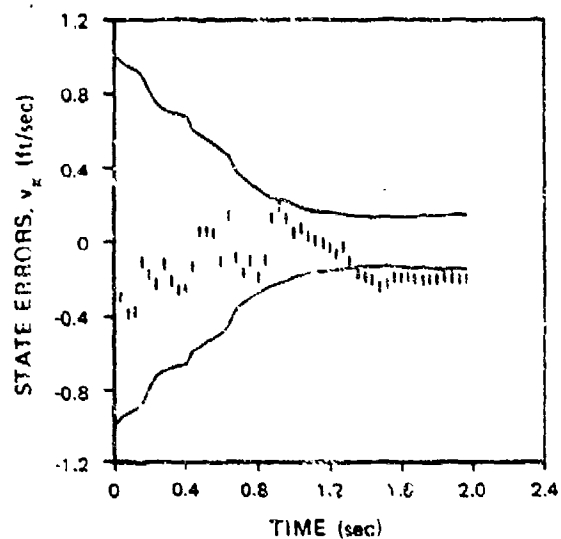
## APPENDIX A

### IDENTIFICATION ALGORITHM OUTPUT

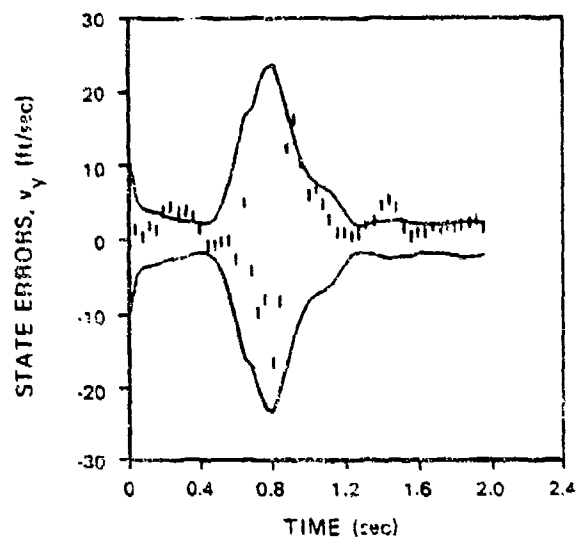
This appendix presents selected plots of significant variables computed during the parameter identification studies of Section V. Five groups of figures are included. These figures are:

- A-1 State estimation errors and predicted one sigma bounds for the 11-parameter nominal test case
- A-2 Parameter estimation errors and predicted one sigma bounds for the 11-parameter nominal test case
- A-3 Residual process and residual one sigma bounds from the 11-parameter nominal test case
- A-4 Parameter estimation errors and predicted one sigma bounds from the 36-parameter test case
- A-5 Residual process and residual one sigma bound for the 36-parameter test case

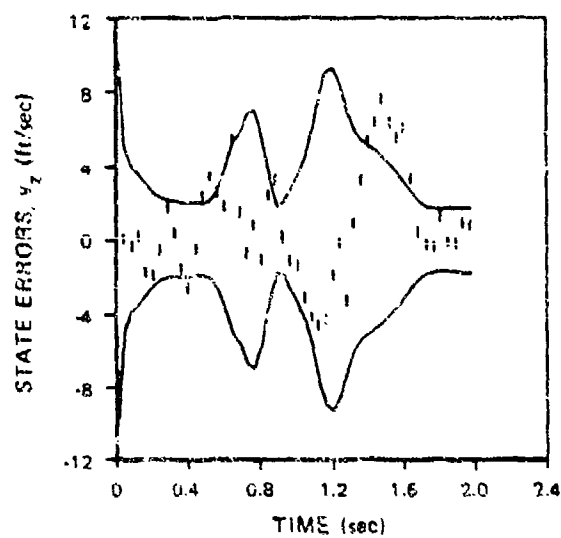
The solid lines shown on each figure represent the one sigma bounds as predicted by the EKF. The vertical dashes give the state error, parameter error or residual which occurred at the particular time during filtering.



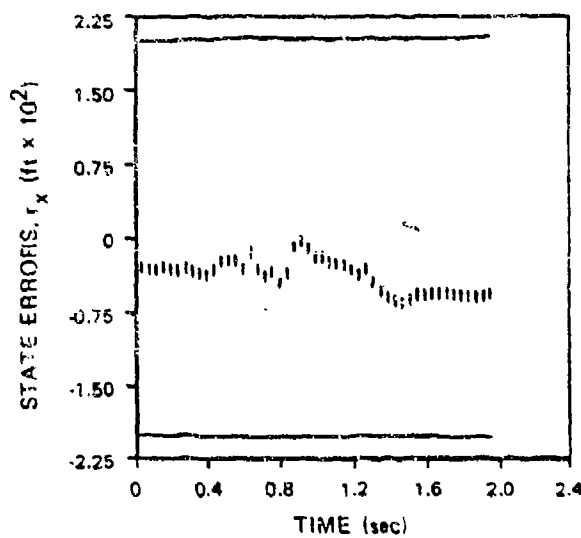
(a)  $v_x$  STATE ERROR



(b)  $v_y$  STATE ERROR

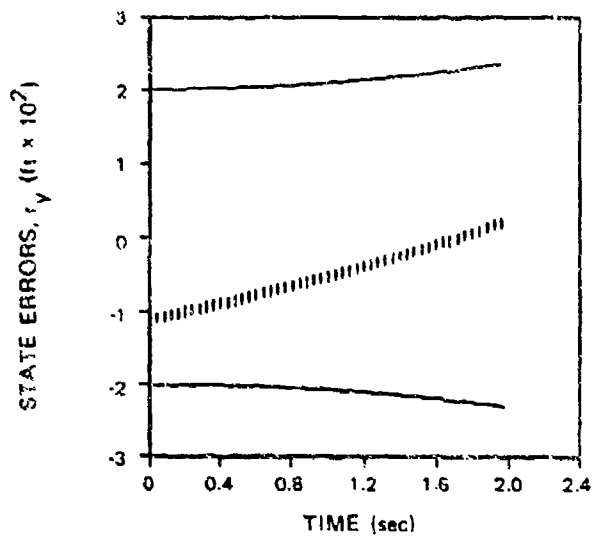


(c)  $v_z$  STATE ERROR

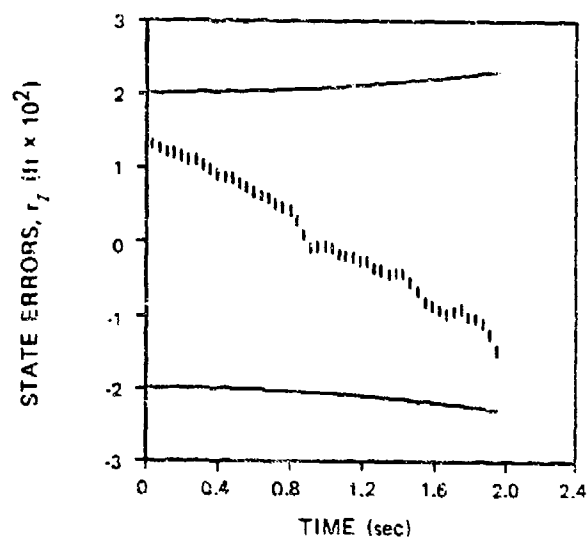


(d)  $r_x$  STATE ERROR

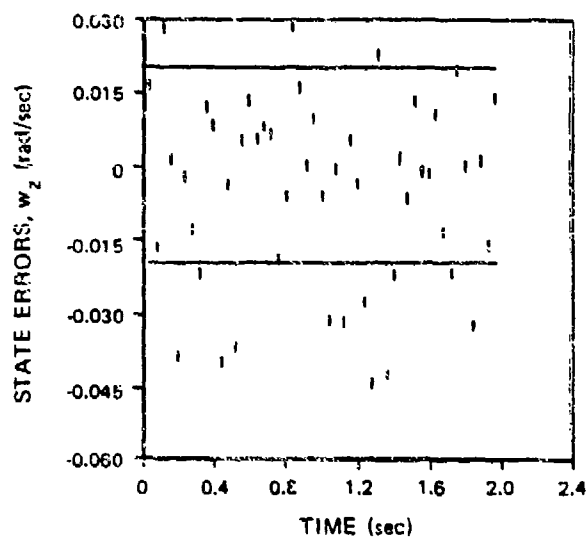
Figure A-1. State Estimation Errors for the Nominal Test Case



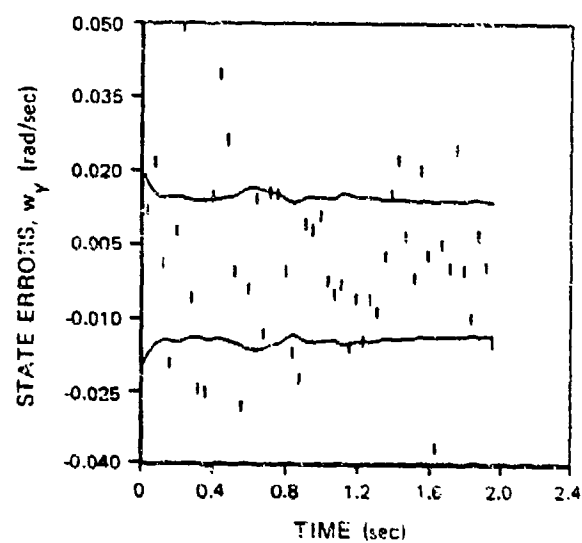
(e)  $r_y$  STATE ERROR



(f)  $r_z$  STATE ERROR

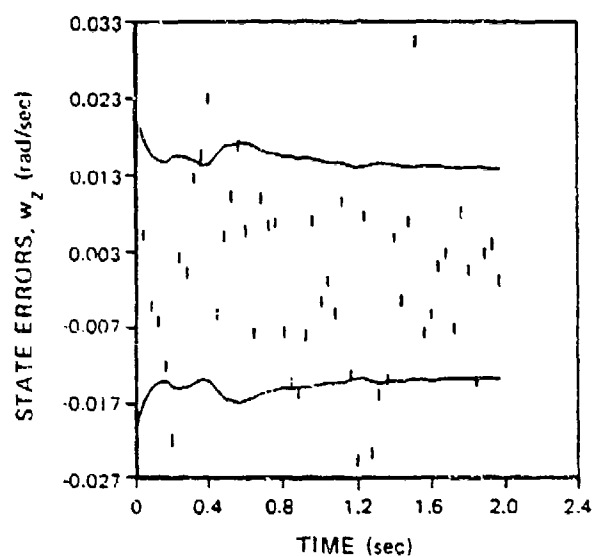


(g)  $w_z$  STATE ERROR

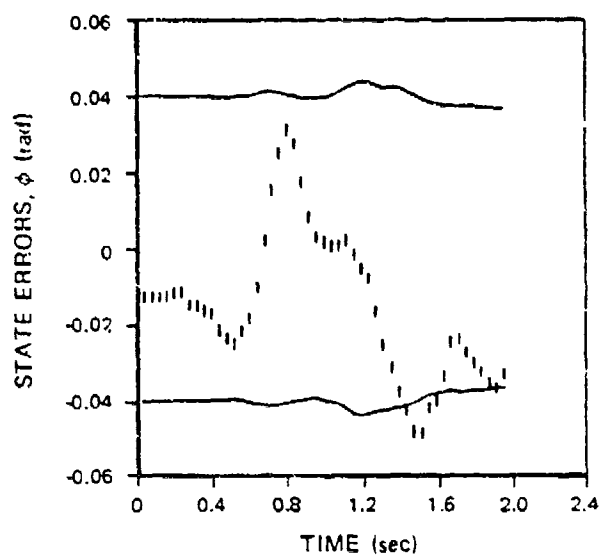


(h)  $w_y$  STATE ERROR

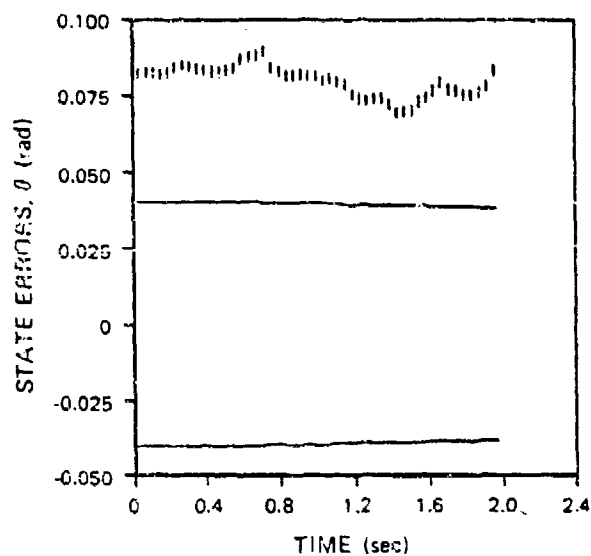
Figure A-1. State Estimation Errors for the Nominal Test Case (Continued)



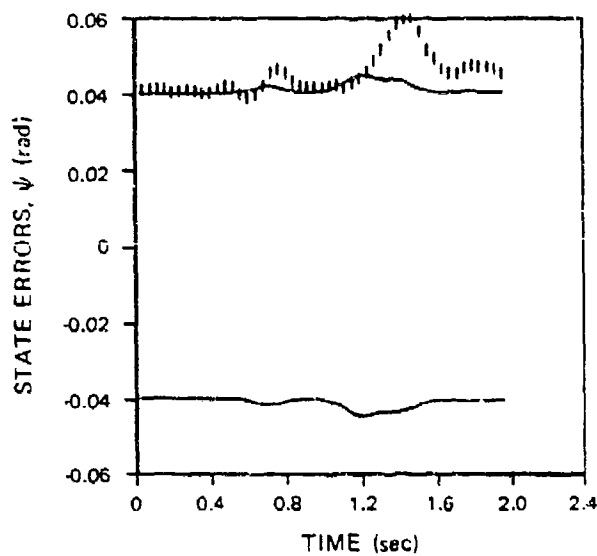
(i)  $w_z$  STATE ERROR



(j)  $\phi$  STATE ERROR

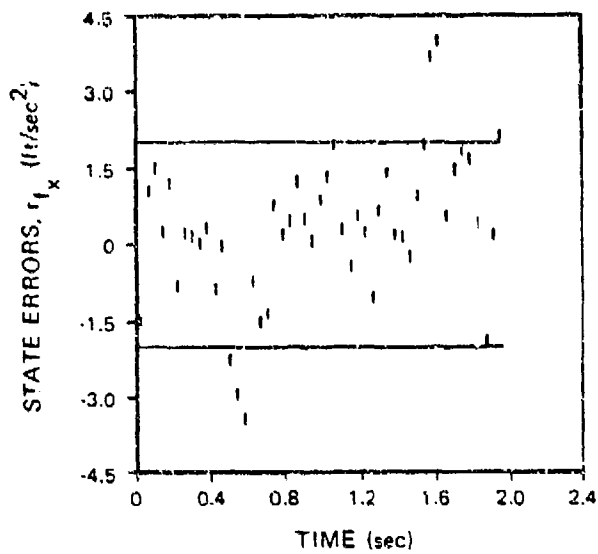


(k)  $\theta$  STATE ERROR

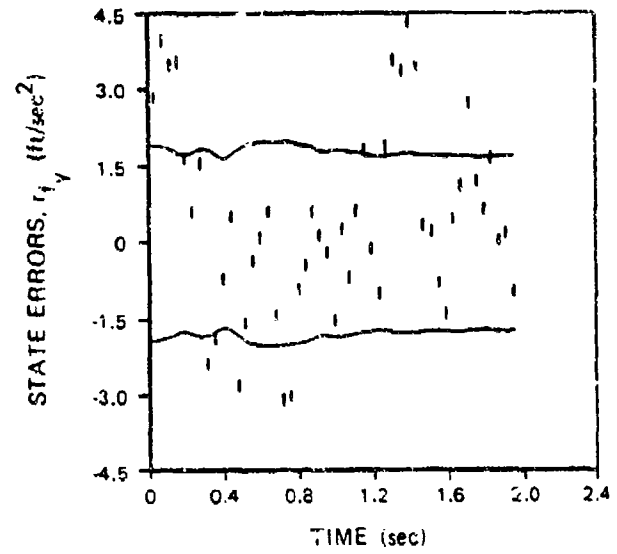


(l)  $\psi$  STATE ERROR

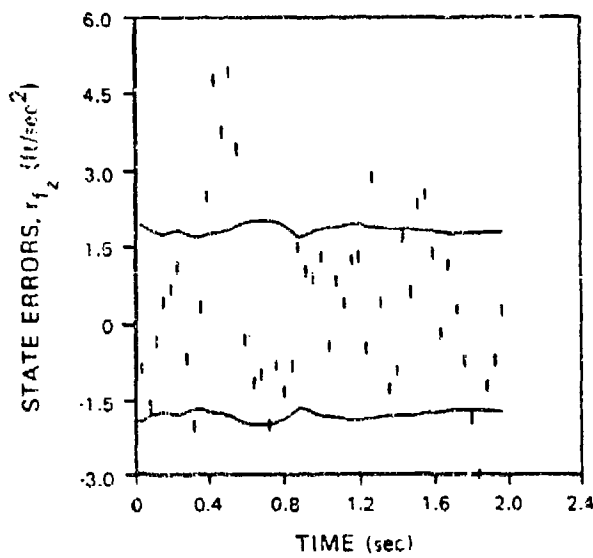
Figure A-1. State Estimation Errors for the Nominal Test Case (Continued)



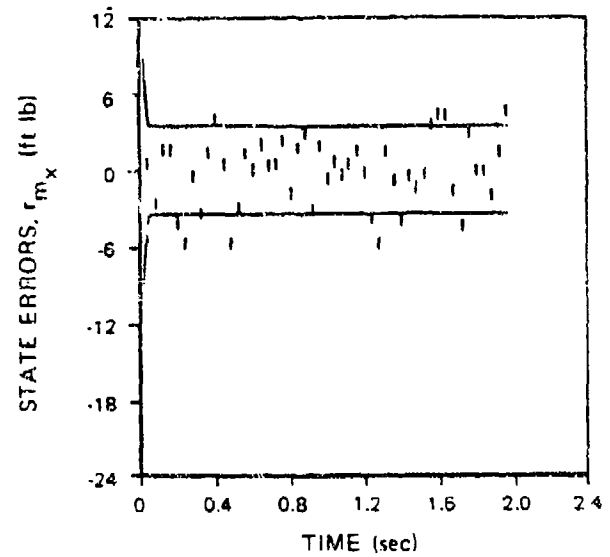
(m)  $r_{f_x}$  STATE ERROR



(n)  $r_{f_y}$  STATE ERROR

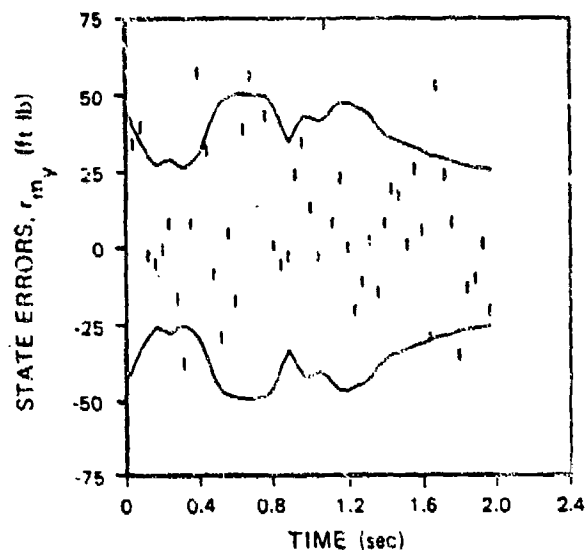


(o)  $r_{f_z}$  STATE ERROR

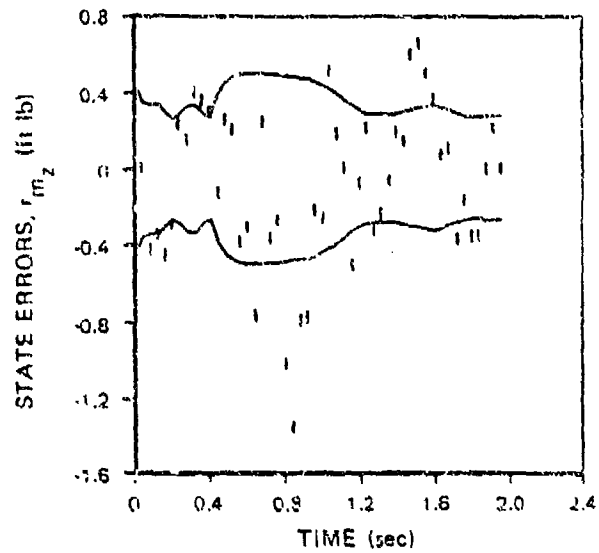


(p)  $r_{m_x}$  STATE ERROR

Figure A-1. State Estimation Errors for the Nominal Test Case (Continued)

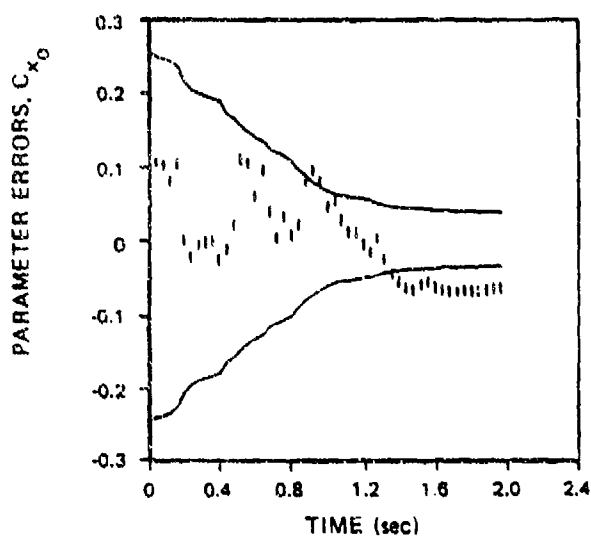


(p)  $r_{m_y}$  STATE ERROR

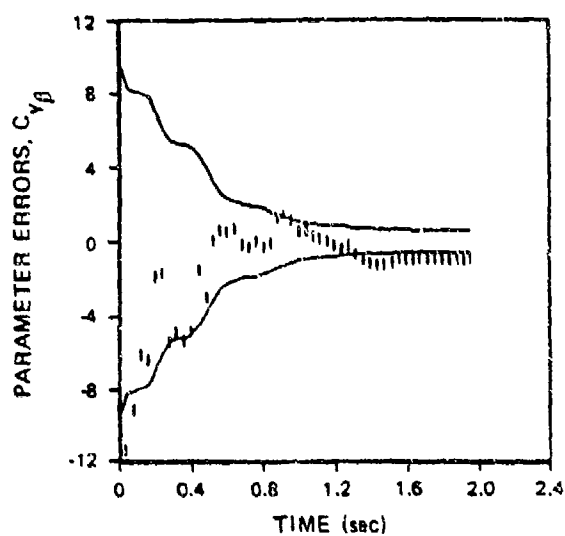


(n)  $r_{m_z}$  STATE ERROR

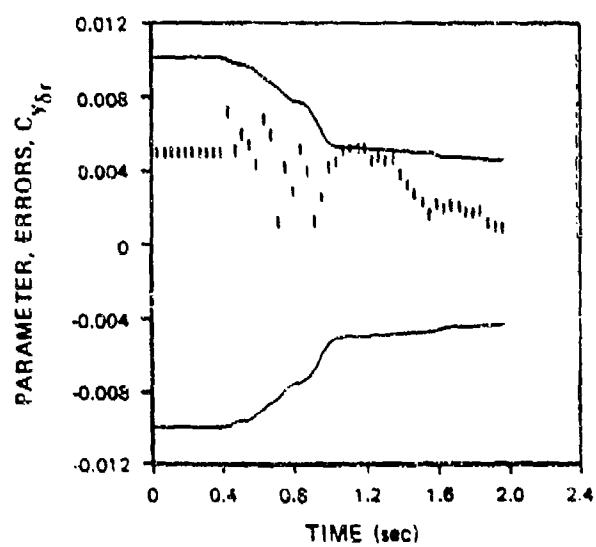
Figure A-1. State Estimation Errors for the Nominal Test Case (Concluded)



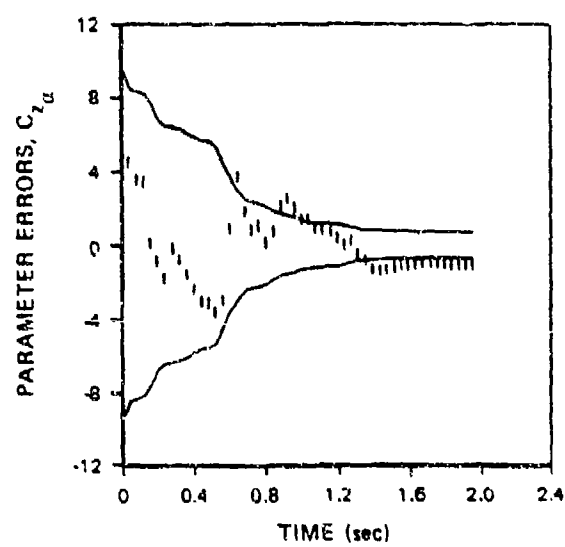
(a)  $C_{x_0}$  PARAMETER



(b)  $C_{y_{\beta}}$  PARAMETER

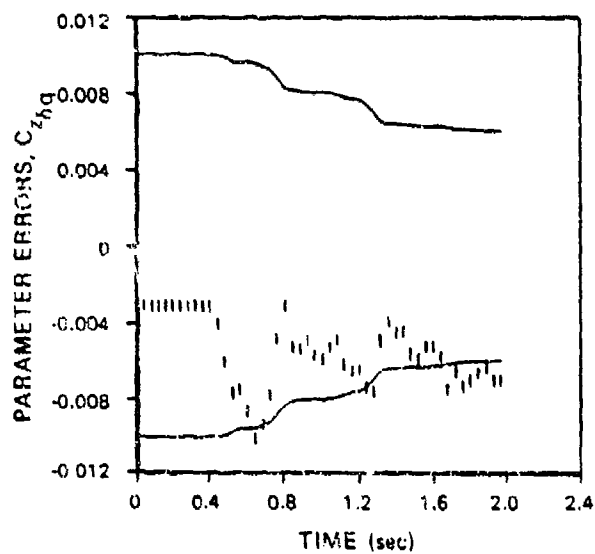


(c)  $C_{y_{\delta r}}$  PARAMETER

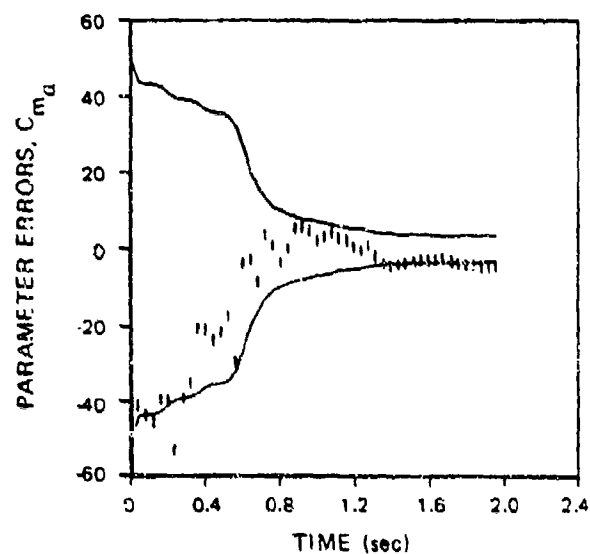


(d)  $C_{z_a}$  PARAMETER

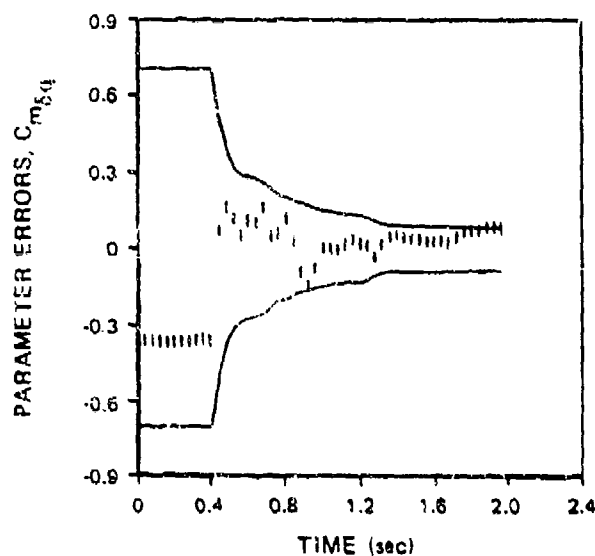
Figure A-2. Parameter Estimation Errors for the Nominal Test Case



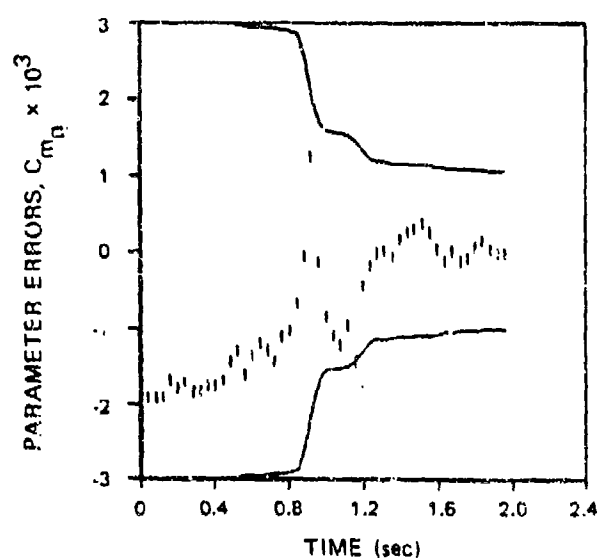
(e)  $C_{z\delta q}$  PARAMETER



(f)  $C_{m\delta}$  PARAMETER



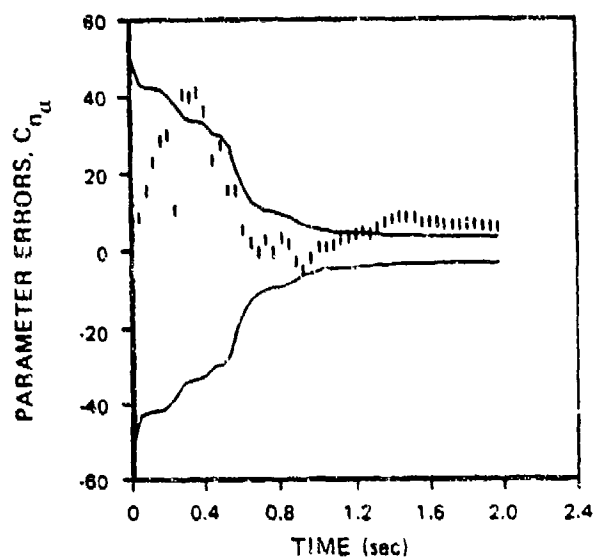
(g)  $C_{m\delta q}$  PARAMETER



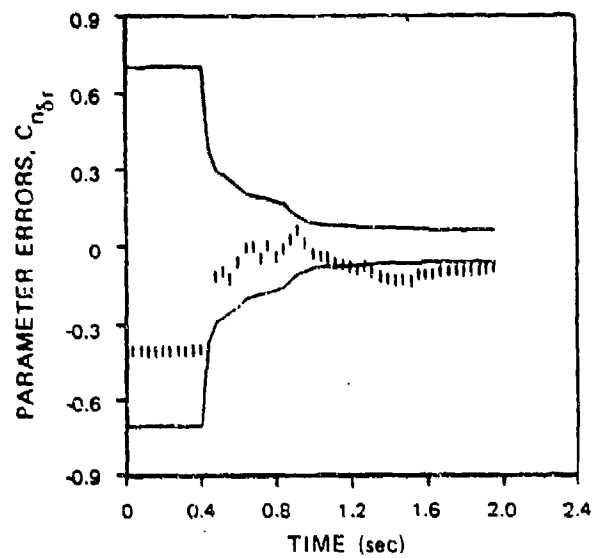
(h)  $C_{mq}$  PARAMETER

Figure A-2. Parameter Estimation Errors for the Nominal Test Case (Continued)

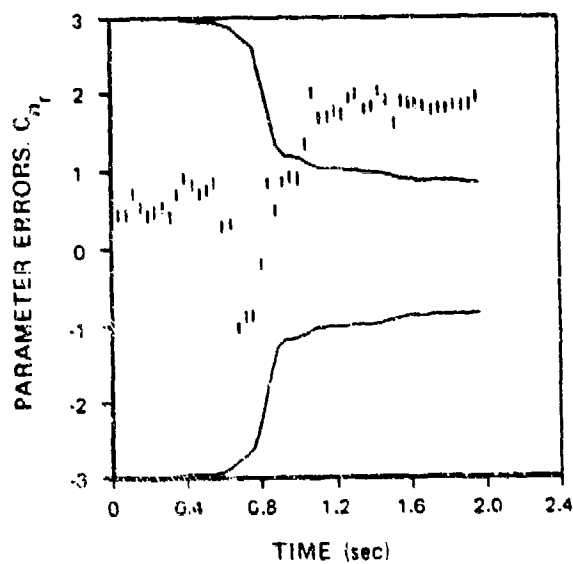




(i)  $C_{n_{\alpha}}$  PARAMETER

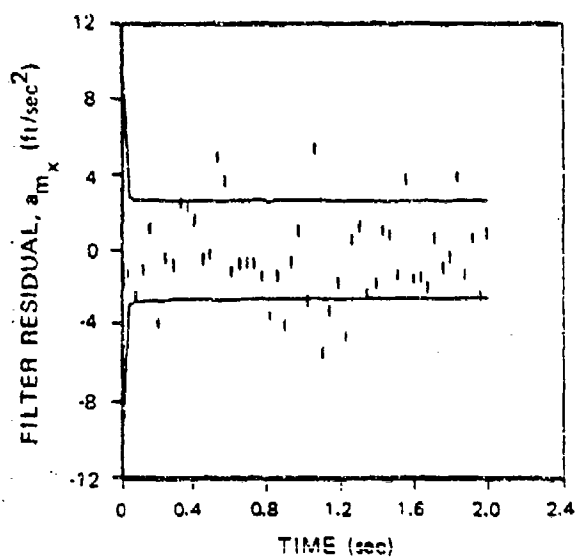


(j)  $C_{n_{\delta r}}$  PARAMETER

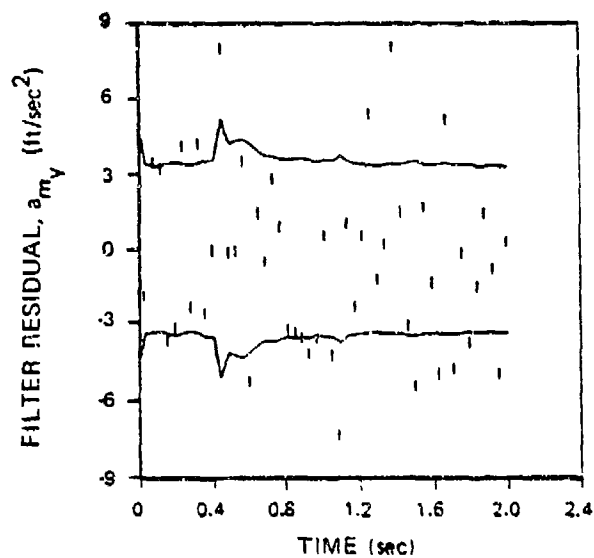


(k)  $C_{r_r}$  PARAMETER

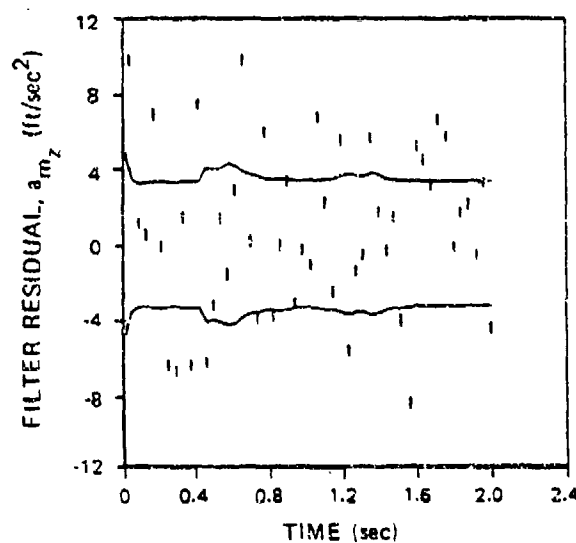
Figure A-2. Parameter Estimation Errors for the Nominal Test Case (Concluded)



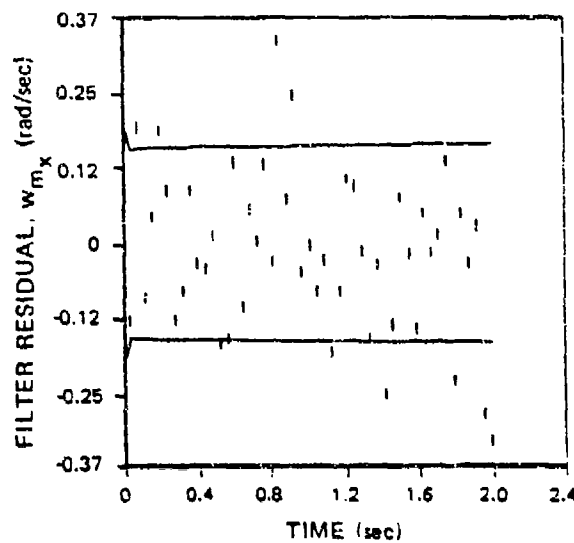
(a)  $a_{m_x}$  FILTER RESIDUAL



(b)  $a_{m_y}$  FILTER RESIDUAL

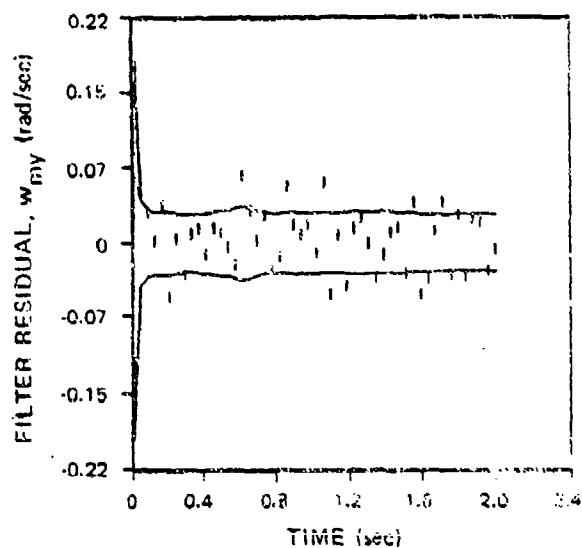


(c)  $a_{m_z}$  FILTER RESIDUAL

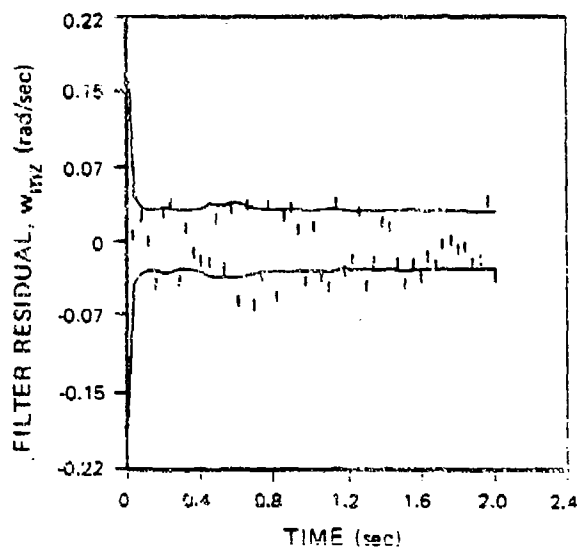


(d)  $w_{m_x}$  FILTER RESIDUAL

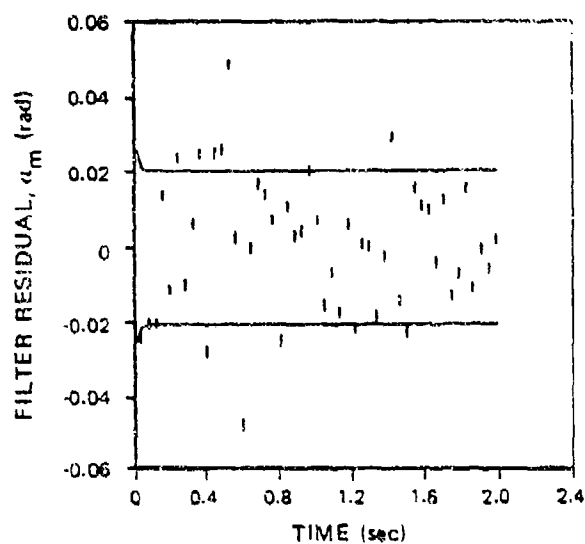
Figure A-3. Residual Processes from the Nominal Test Case



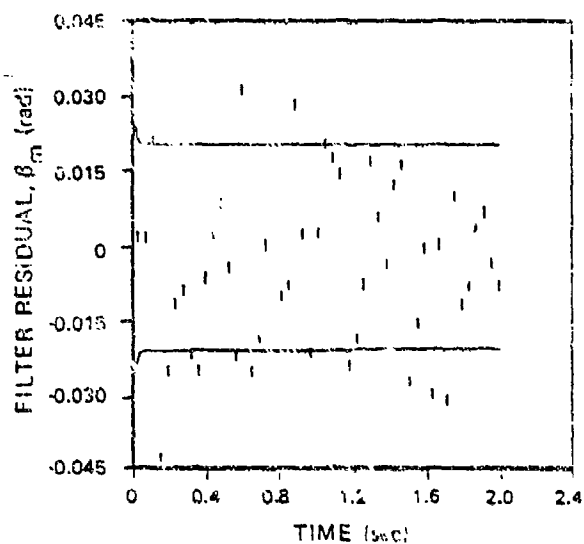
(e)  $w_{my}$  FILTER RESIDUAL



(f)  $w_{mz}$  FILTER RESIDUAL

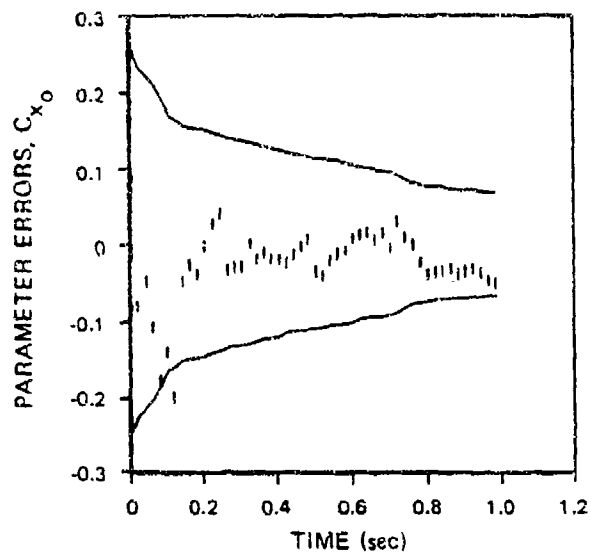


(g)  $\alpha_m$  FILTER RESIDUAL

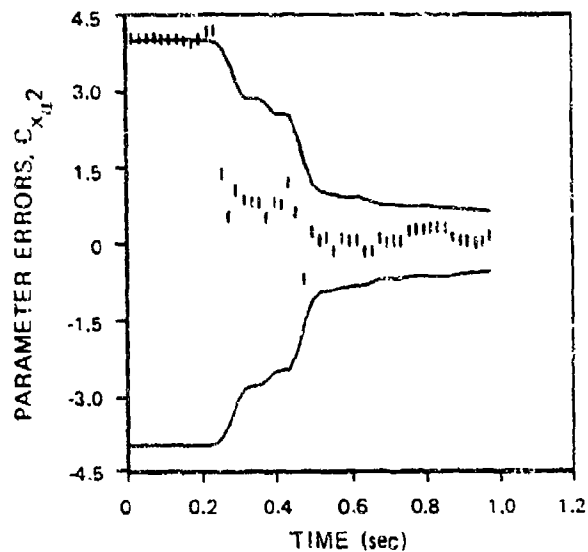


(h)  $\beta_m$  FILTER RESIDUAL

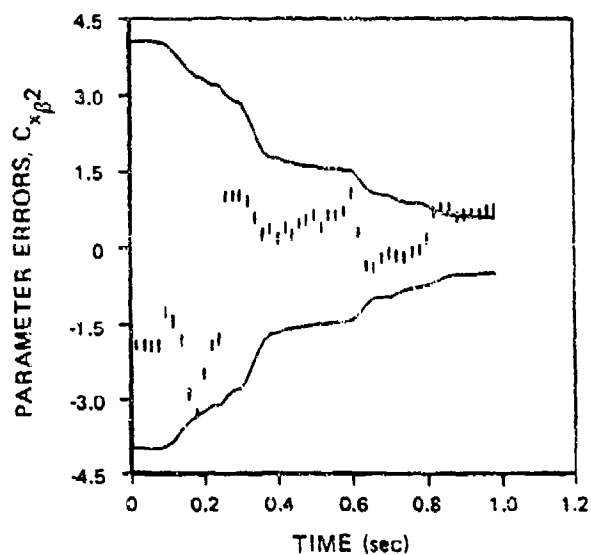
Figure A-3. Residual Processes from the Nominal Test Case (Concluded)



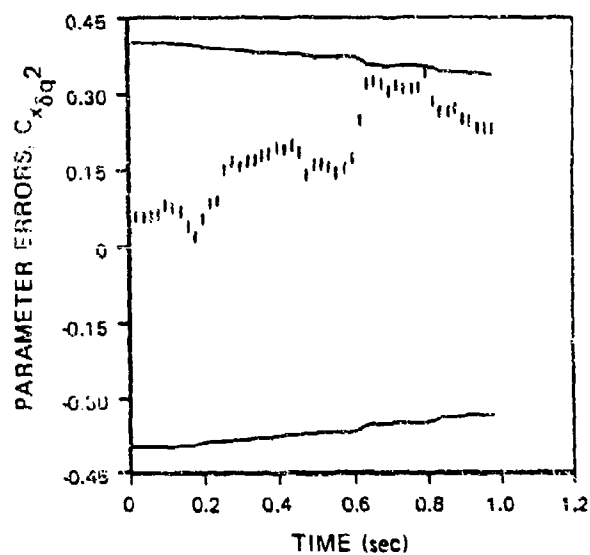
(a) PARAMETER ERRORS,  $C_{x_0}$



(b) PARAMETER ERRORS,  $C_{x_{d^2}}$

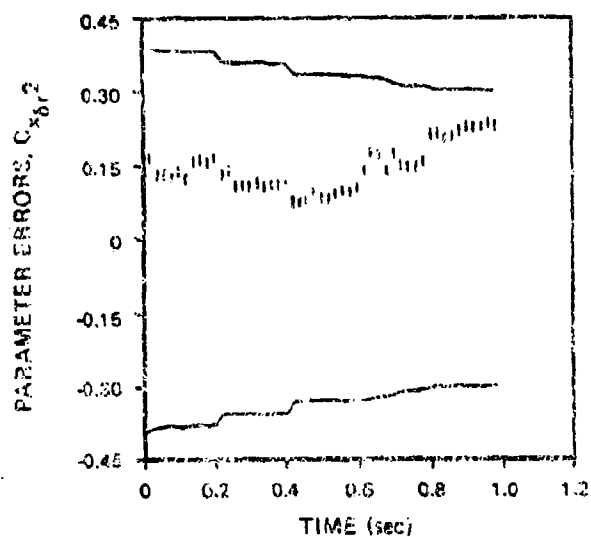


(c) PARAMETER ERRORS,  $C_{x_{\beta^2}}$

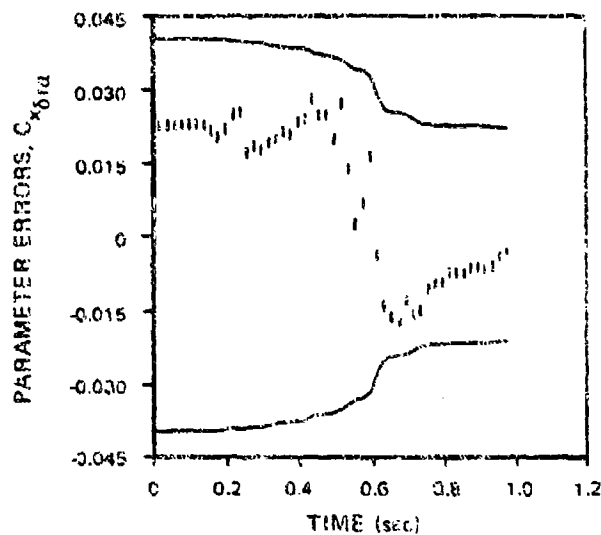


(d) PARAMETER ERRORS,  $C_{x_{\delta q^2}}$

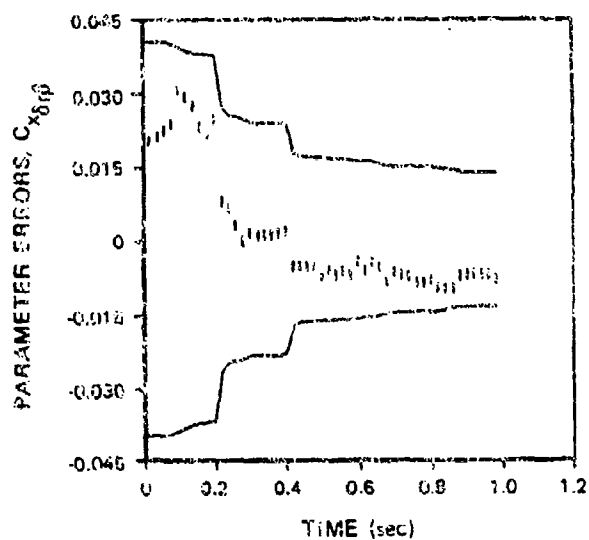
Figure A-4. Parameter Errors from the 36-Parameter Case



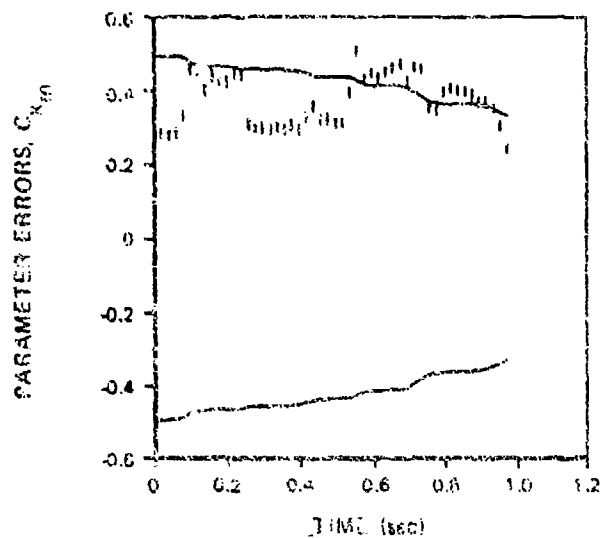
(e) PARAMETER ERRORS,  $C_{x\delta r2}$



(f) PARAMETER ERRORS,  $C_{x\delta ra}$

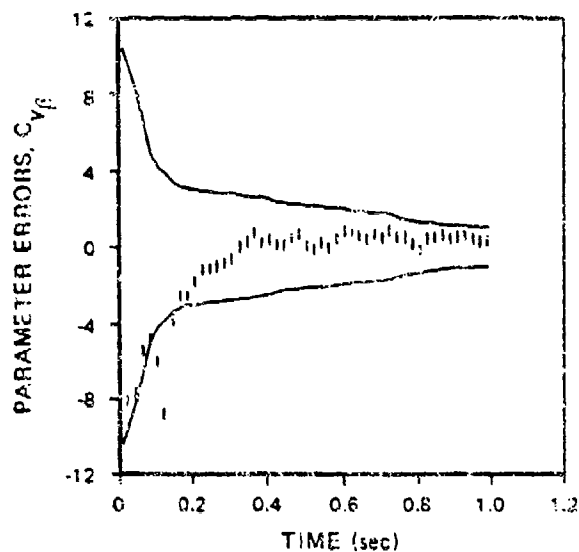


(g) PARAMETER ERRORS,  $C_{x\delta rp}$

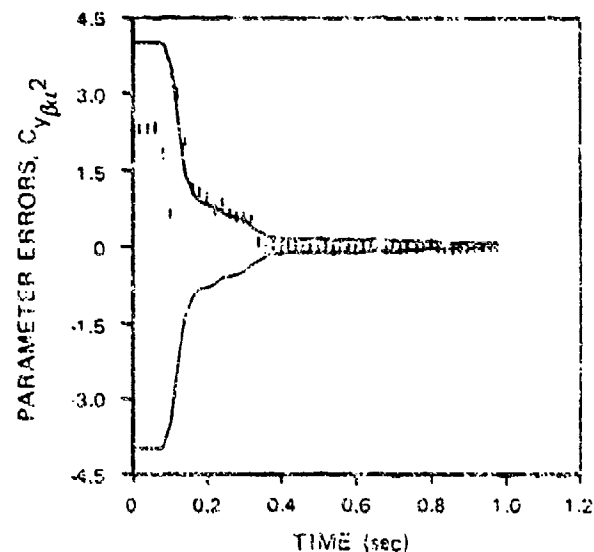


(h) PARAMETER ERRORS,  $C_{xm}$

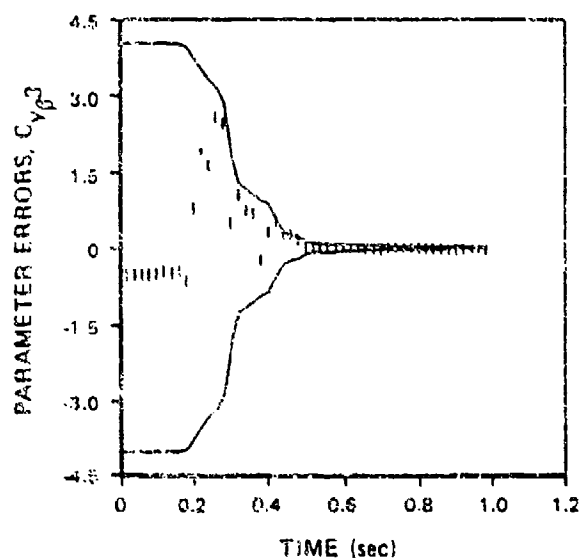
Figure A-4. Parameter Errors from the 36-Parameter Case (Continued)



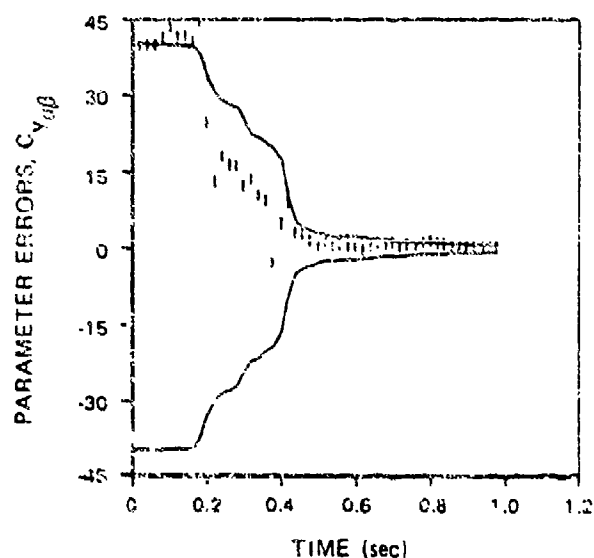
(i) PARAMETER ERRORS,  $C_{Y\beta}$



(j) PARAMETER ERRORS,  $C_{Y\beta a^2}$

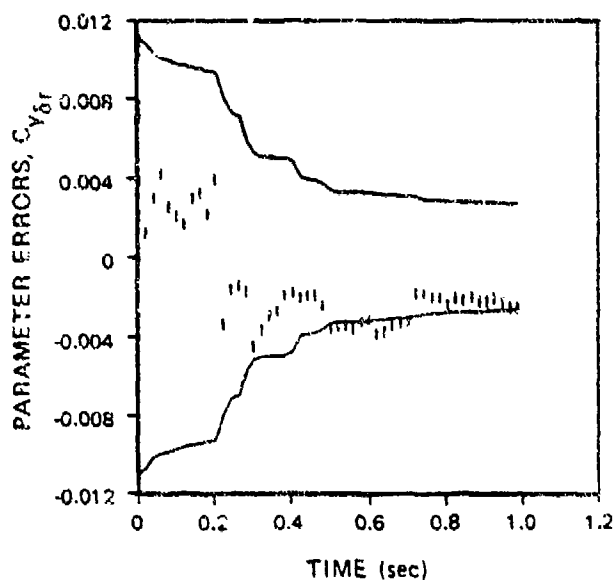


(k) PARAMETER ERRORS,  $C_{Y\beta^3}$

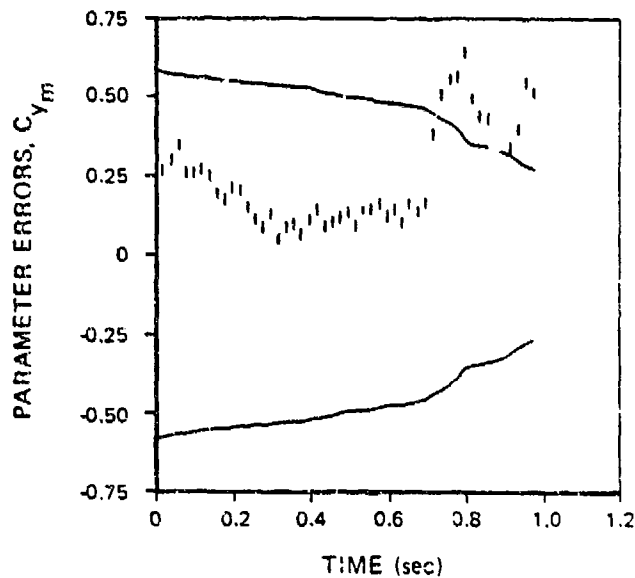


(l) PARAMETER ERRORS,  $C_{Y\beta a\delta}$

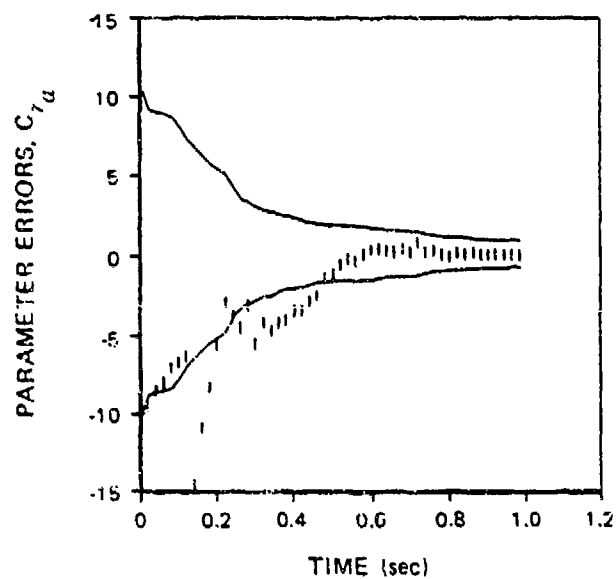
Figure A-4. Parameter Errors from the 36-Parameter Case (Continued)



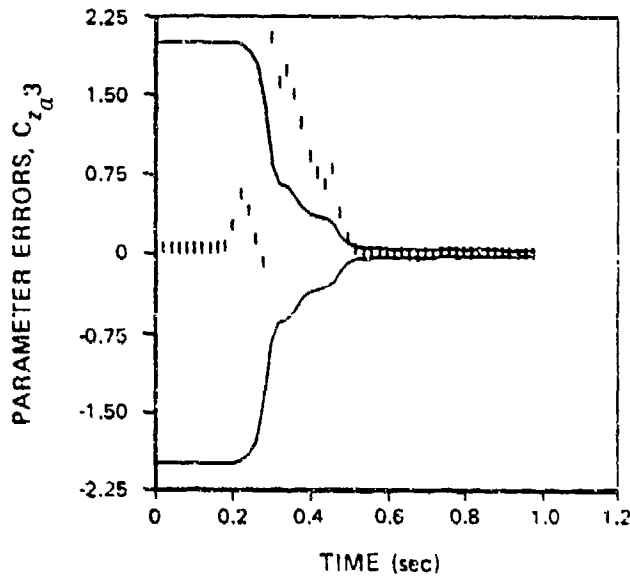
(m) PARAMETER ERRORS,  $C_{y\delta r}$



(n) PARAMETER ERRORS,  $C_{ym}$

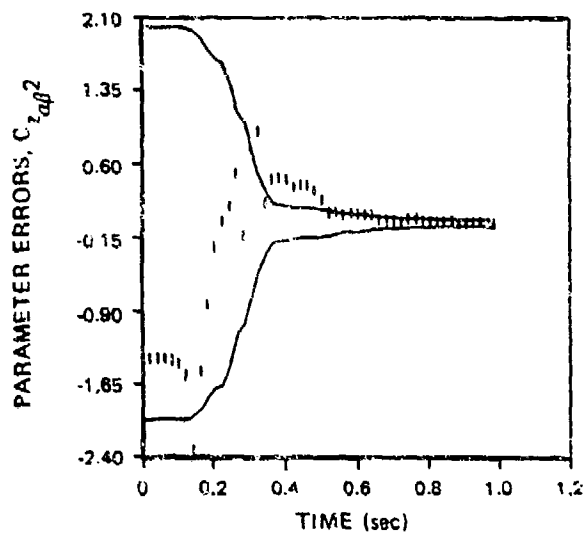


(o) PARAMETER ERRORS,  $C_{za}$

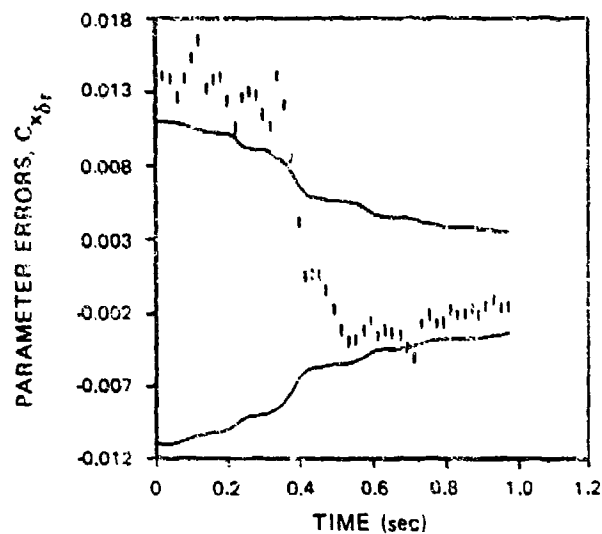


(p) PARAMETER ERRORS,  $C_{z\alpha 3}$

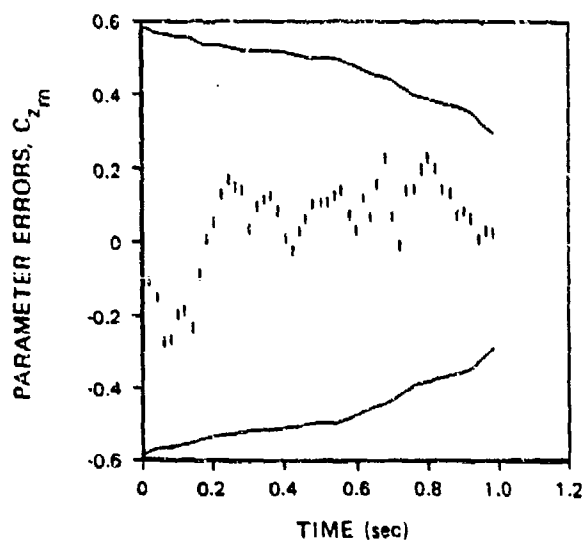
Figure A-4. Parameter Errors from the 36-Parameter Case (Continued)



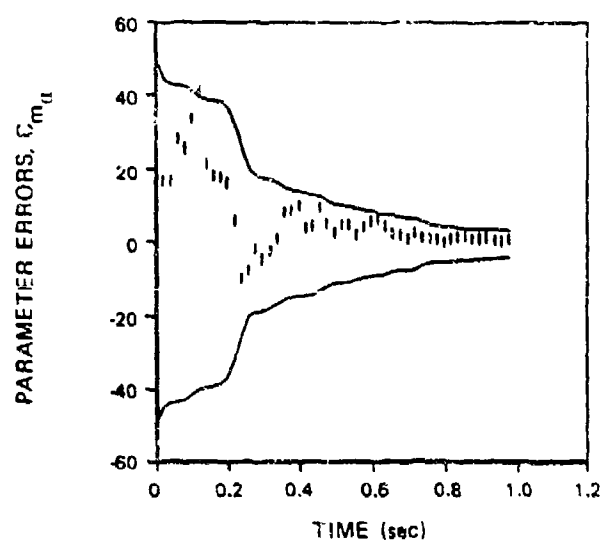
(q) PARAMETER ERRORS,  $C_{z_{\dot{\alpha}\beta}^2}$



(r) PARAMETER ERRORS,  $C_{x_{\delta r}}$



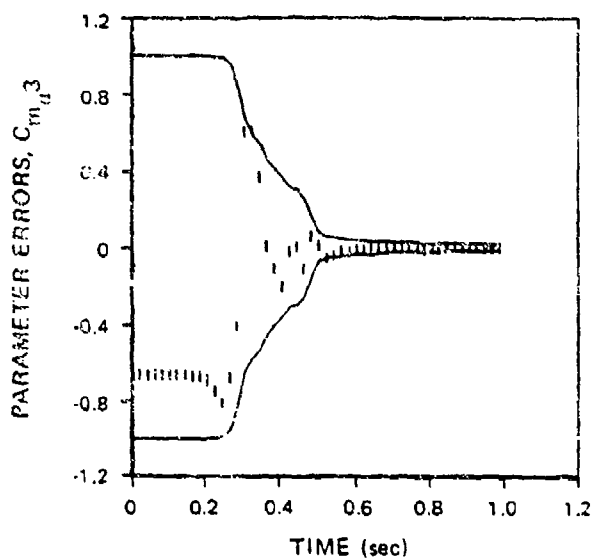
(s) PARAMETER ERRORS,  $C_{z_m}$



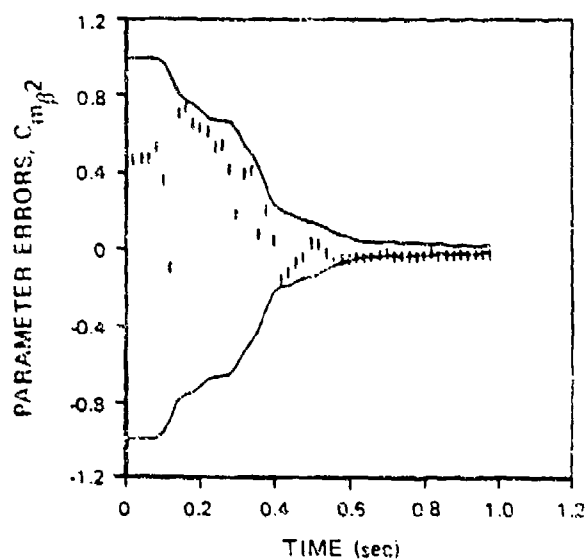
(t) PARAMETER ERRORS,  $C_{m_{\dot{\alpha}}}$

Figure A-4. Parameter Errors from the 36-Parameter Case (Continued)

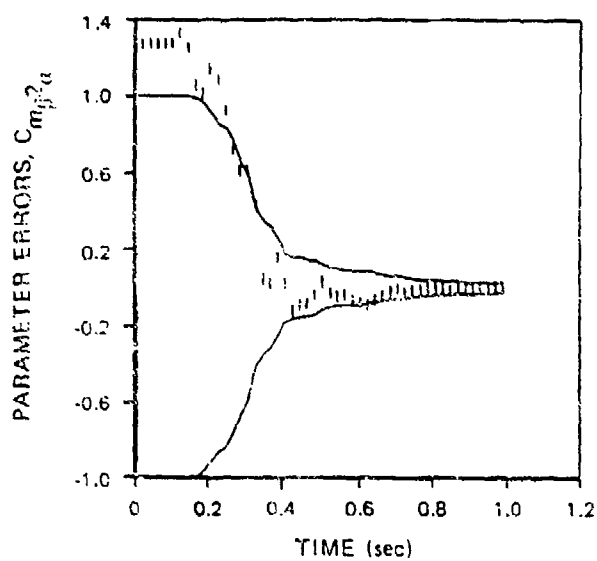




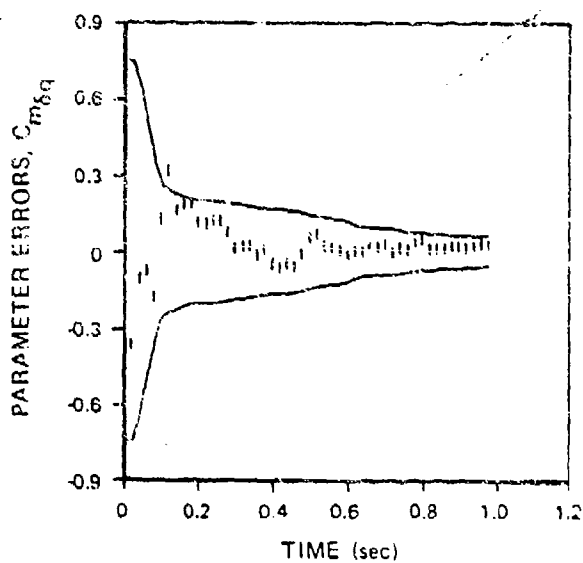
(u) PARAMETER ERRORS,  $C_{m_{\alpha}^3}$



(v) PARAMETER ERRORS,  $C_{m_{\beta}^2}$

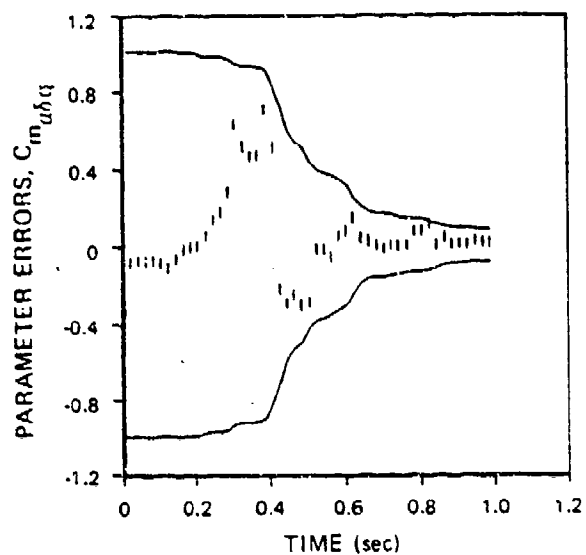


(w) PARAMETER ERRORS,  $C_{m_{\beta}^2 \alpha}$

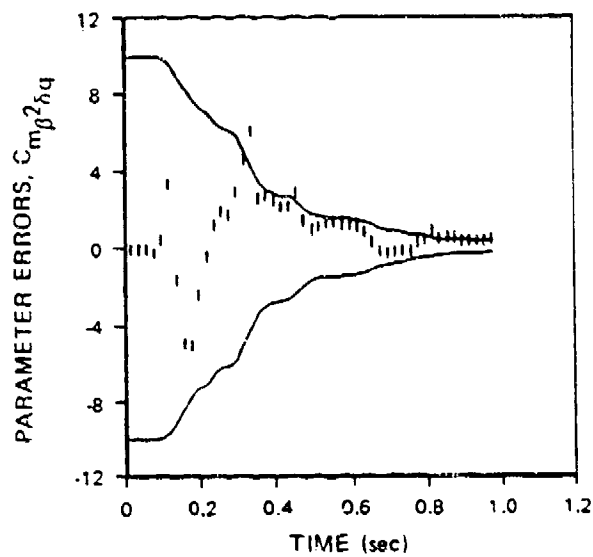


(x) PARAMETER ERRORS,  $C_{m_{\delta} \eta}$

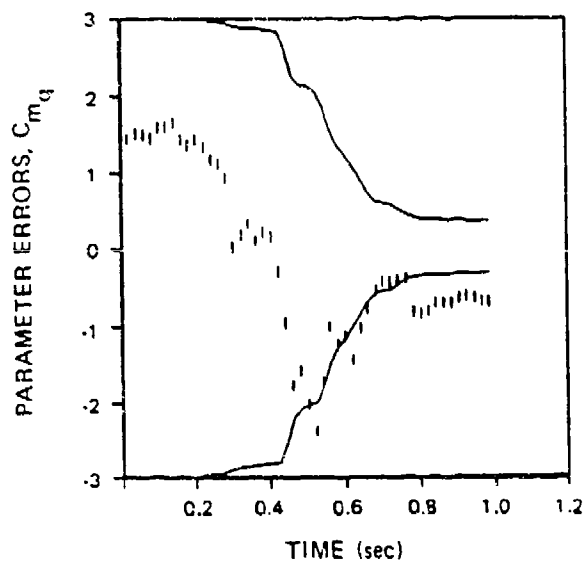
Figure A-4. Parameter Errors from the 36 Parameter Case (Continued)



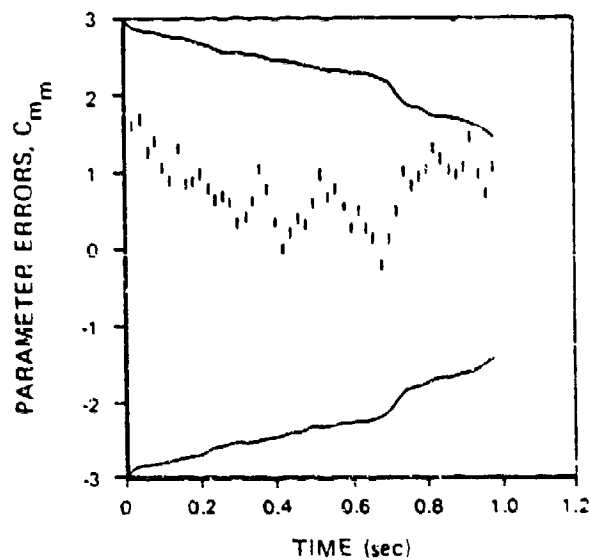
(y) PARAMETER ERRORS,  $C_{m_{\dot{\alpha}\delta q}}$



(z) PARAMETER ERRORS,  $C_{m_{\beta^2\dot{\delta}q}}$

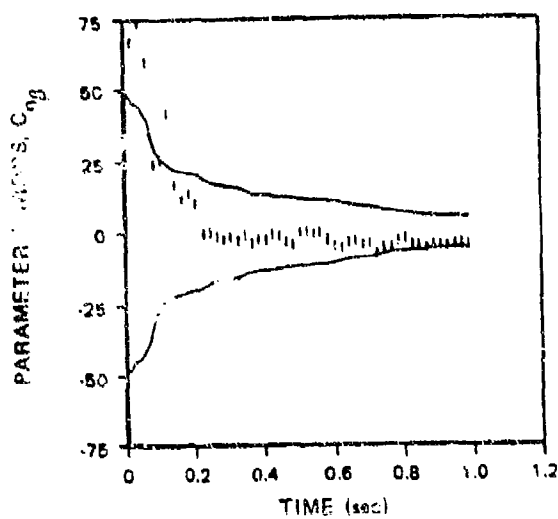


(aa) PARAMETER ERRORS,  $C_{m_q}$

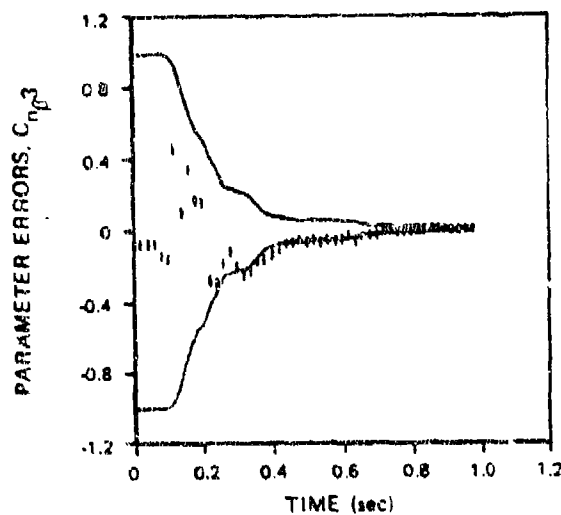


(bb) PARAMETER ERRORS,  $C_{m_m}$

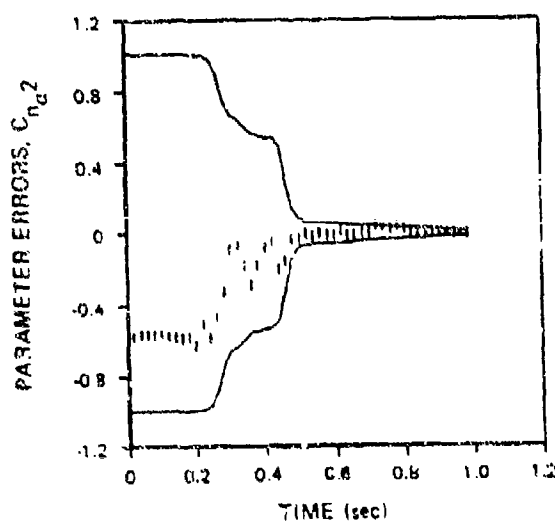
Figure A-4. Parameter Errors from the 36-Parameter Case (Continued)



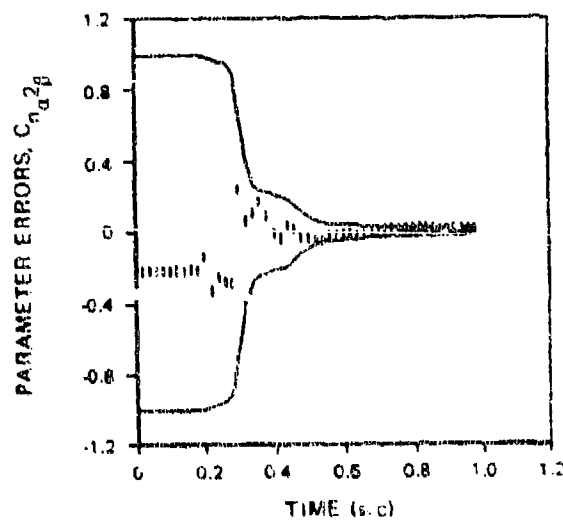
(cc) PARAMETER ERRORS,  $C_{n\beta}$



(dd) PARAMETER ERRORS,  $C_{n\beta 2}$

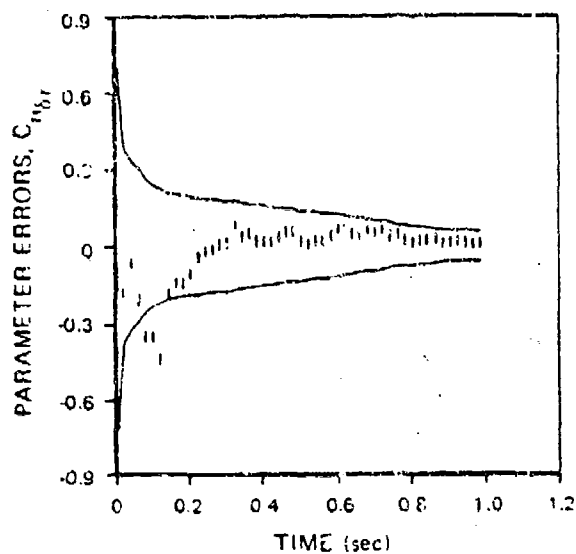


(ee) PARAMETER ERRORS,  $C_{n\alpha 2}$

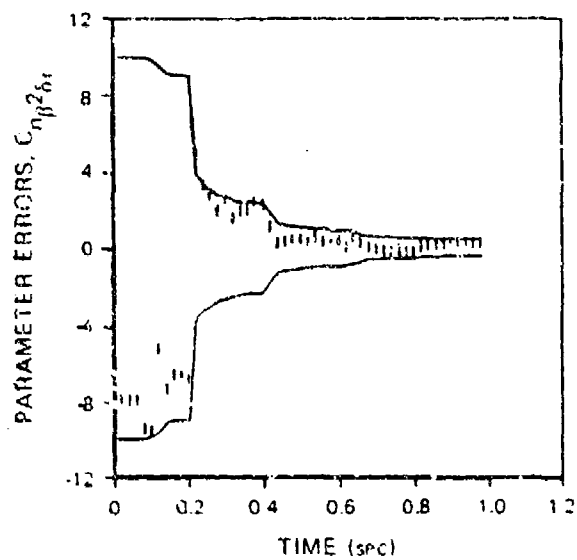


(ff) PARAMETER ERRORS,  $C_{n\alpha 2\beta}$

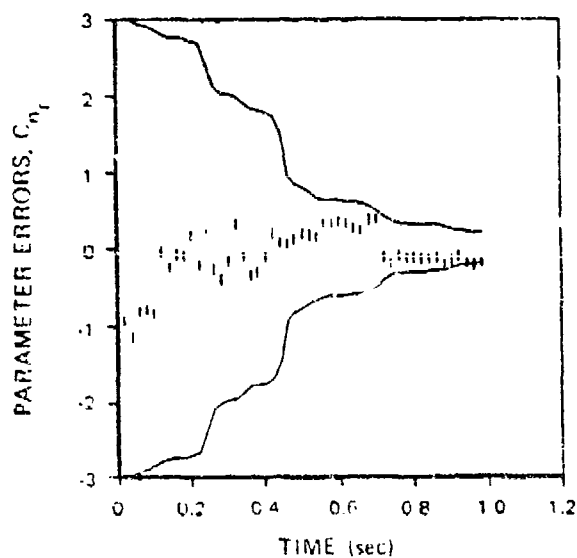
Figure A-4. Parameter Errors from the 36-Parameter Case (Continued)



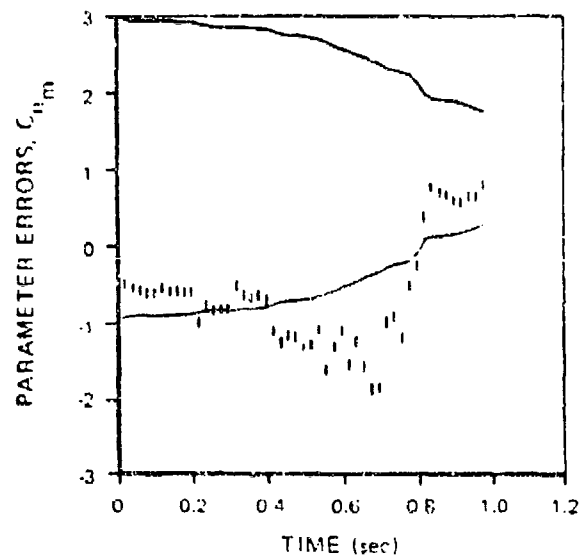
(gg) PARAMETER ERRORS,  $C_{n_{\delta r}}$



(hh) PARAMETER ERRORS,  $C_{n_{\beta^2 \delta r}}$

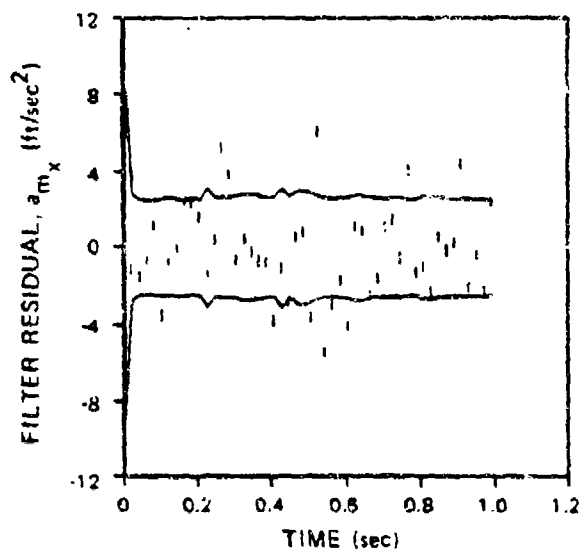


(ii) PARAMETER ERRORS,  $C_{n_r}$

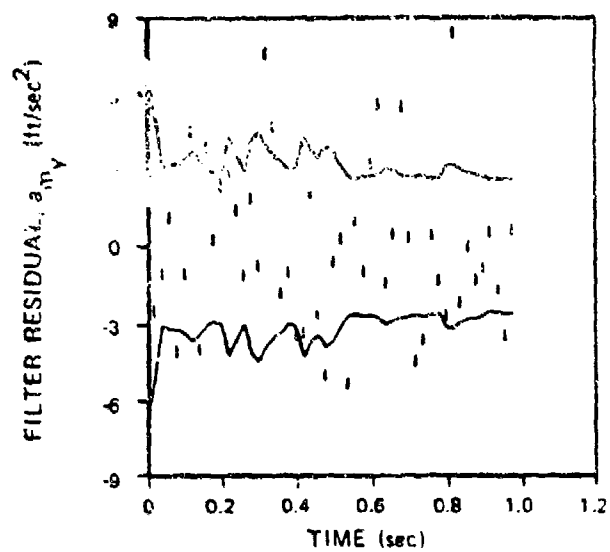


(jj) PARAMETER ERRORS,  $C_{n_m}$

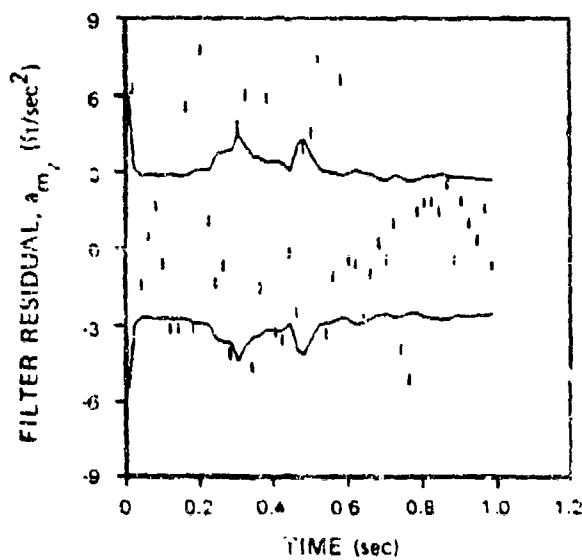
Figure A-4. Parameter Errors from the 36-Parameter Case (Concluded)



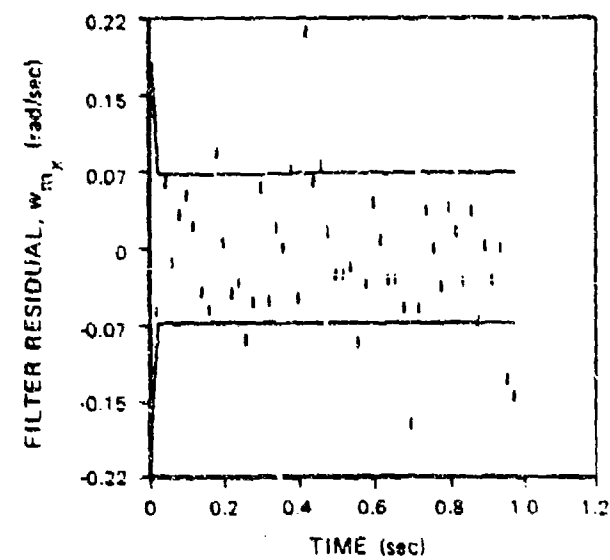
(a) FILTER RESIDUAL,  $a_{m_x}$



(b) FILTER RESIDUAL,  $a_{m_y}$

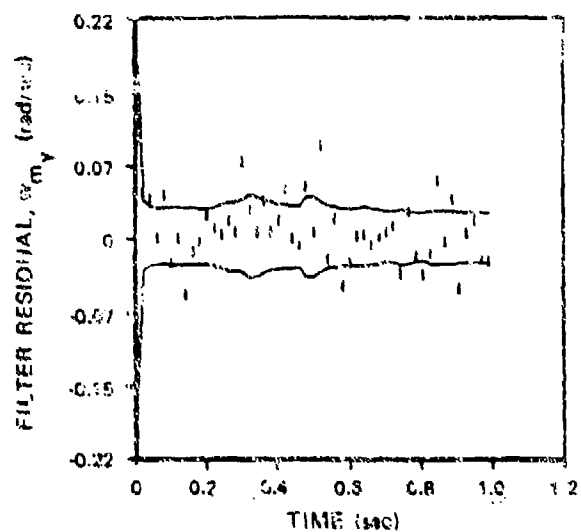


(c) FILTER RESIDUAL,  $a_{m_z}$

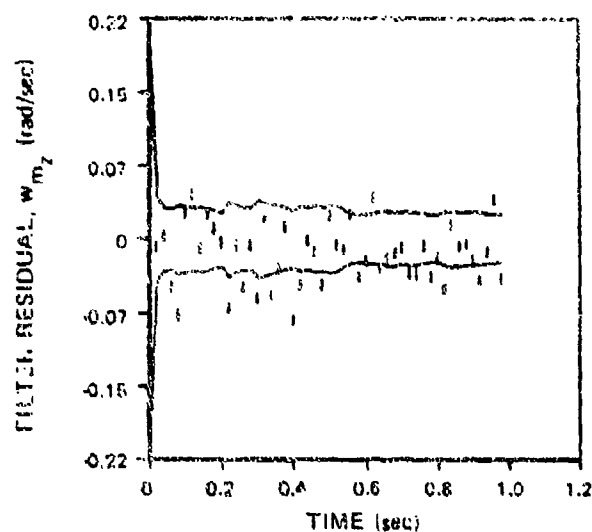


(d) FILTER RESIDUAL,  $w_{m_x}$

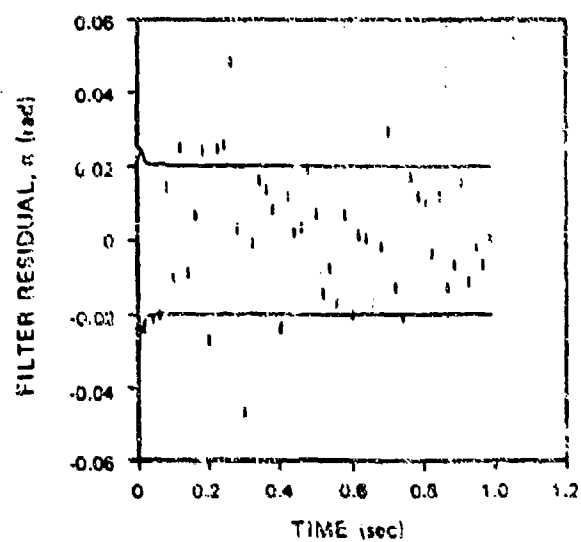
Figure A-5. Residual Processes from the 36-Parameter Test Case



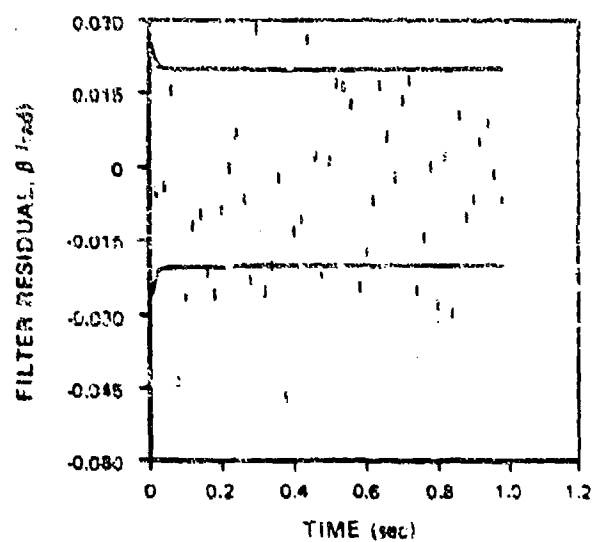
(e) FILTER RESIDUAL,  $w_{m_y}$



(f) FILTER RESIDUAL,  $w_{m_z}$



(g) FILTER RESIDUAL,  $\alpha$



(h) FILTER RESIDUAL,  $\beta$

Figure A-5. Residual Processes from the 36-Parameter Test Case (Concluded)

## APPENDIX B

### STRUCTURE IDENTIFICATION USING THE EXTENDED KALMAN FILTER

The structure identification technique used in this study is based upon the extended Kalman filter and hypothesis testing theory. A number of hypotheses,  $H_1, H_2, \dots, H_n$ , are defined; each are associated with a candidate model for the system structure to be identified.  $H_i$  is the hypothesis that the  $i^{\text{th}}$  model best represents the system. The choice of the set of hypotheses (or set of candidate model structures) is based upon the a priori information available about the system. The best model structure is that structure that best approximates the input-output response of the system. This structure is found by processing the measurement data independently with  $n$  extended Kalman filters, as indicated in Figure B-1, with each filter designed according to one of the candidate models or hypotheses. It is then possible to recursively compute the probability  $P_{H_i}$  that the  $i^{\text{th}}$  model is best or correct, making use of the filter state estimates, their filter computed covariances, and the measurement data. The relative magnitudes of these probabilities provide the basis for selecting the model which best represents the data in a statistical sense.

The notation used in Figure B-1 is defined as follows:

- $H_i$  Hypothesis that the  $i^{\text{th}}$  system model is correct
- $P_{H_i}(k)$  Probability that the  $i^{\text{th}}$  system model is correct given the measurements up to and including  $z_k$

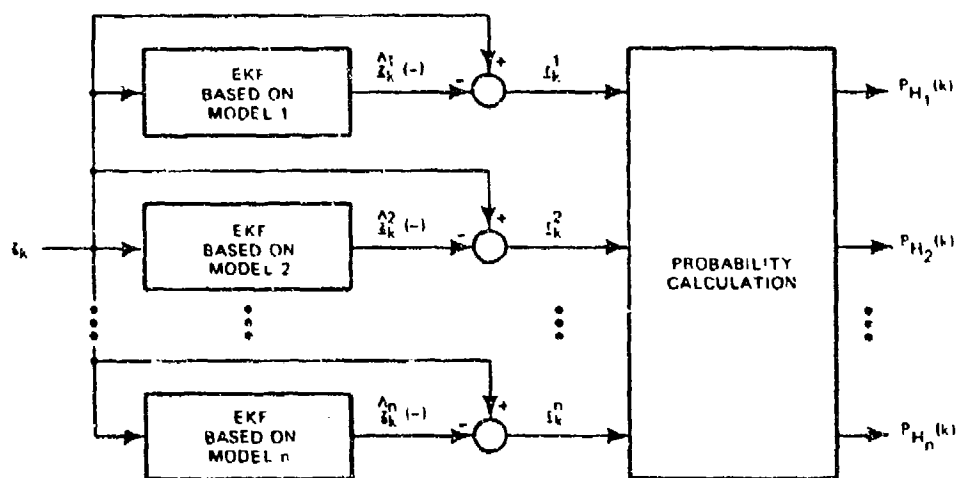


Figure B-1. Extended Kalman Filter Approach to Structure Identification

- $\underline{z}_k$  The system output measurement at time,  $t_k$
- $\underline{z}_k^i(-)$  The predicted value of  $\underline{z}_k$  based upon the data up to, but not including  $\underline{z}_k$ , for the EKF based upon the  $i^{\text{th}}$  model
- $\underline{r}_k^i$  The one-step predicted measurement residual at the  $k^{\text{th}}$  step for the EKF associated with the  $i^{\text{th}}$  model.

The output of the  $i^{\text{th}}$  extended Kalman filter immediately prior to the  $k^{\text{th}}$  measurement is a state estimate  $\hat{\underline{x}}_k^i(-)$  based upon the first  $k-1$  measurements and knowledge of the past and current system input. This estimate is used to predict the value of the  $k^{\text{th}}$  measurement using the nonlinear system output equation for the  $i^{\text{th}}$  model, i.e.,

$$\hat{\underline{z}}_k^i(-) = \underline{h}^i \left[ \hat{\underline{x}}_k^i(-) \right] \quad (\text{B-1})$$

The one step prediction residuals for the  $i^{\text{th}}$  EKF are then given by:

$$\underline{r}_k^i = \underline{z}_k - \hat{\underline{z}}_k^i(-) \quad (\text{B-2})$$



and the residual covariance by:

$$S_k^i = \text{Cov} \begin{bmatrix} \tilde{r}_k^i & \tilde{r}_k^{iT} \end{bmatrix} = H_k^i P_k^i (-) H_k^{iT} + R_k^i \quad (\text{B-3})$$

where

$$H_k^i = \left. \frac{\partial h^i \left[ \underline{x}_k \right]}{\partial \underline{x}_k} \right|_{\underline{x}_k = \hat{\underline{x}}_k^i(-)} \quad (\text{B-4})$$

and  $P_k^i(-)$  is the error covariance of  $\hat{\underline{x}}_k^i(-)$  computed by the  $i^{\text{th}}$  filter.

The objective is to use the above filter outputs and equations to compute the probability of each hypothesis. For notational purposes, let:

$$\underline{Z}_k = \{\underline{z}_1, \underline{z}_2, \dots, \underline{z}_k\} \quad (\text{B-5})$$

Applying Bayes' rule, we can write:

$$\begin{aligned} P_{H_i}(k) &\triangleq P(H_i | \underline{Z}_k) \\ &= P(H_i | \underline{z}_k, \underline{Z}_{k-1}) \\ &= \frac{P(\underline{z}_k | H_i, \underline{Z}_{k-1}) P(H_i | \underline{Z}_{k-1})}{P(\underline{z}_k | \underline{Z}_{k-1})} \\ &= \frac{P(\underline{z}_k | H_i, \underline{Z}_{k-1}) P(H_i | \underline{Z}_{k-1})}{\sum_{j=1}^n P(\underline{z}_k | H_j, \underline{Z}_{k-1}) P(H_j | \underline{Z}_{k-1})} \end{aligned}$$

thus,

$$P_{H_i}(k) = \frac{P(\underline{z}_k | H_i, \underline{Z}_{k-1}) P_{H_i}(k-1)}{\sum_{j=1}^n P(\underline{z}_k | H_j, \underline{Z}_{k-1}) P_{H_j}(k-1)} \quad (\text{B-6})$$

Based upon the assumptions that the system which generates the data is driven only by known inputs and white noise and the measurements are corrupted only by zero mean white sequences, then the residuals should be zero mean gaussian sequences if the EKF linearization assumption is valid. In this case,

$$P(\underline{z}_k | H_i, \underline{z}_{k-1}) \approx \frac{1}{(2\pi)^{\frac{M}{2}} |\det S_k^1|^{\frac{1}{2}}} e^{-\frac{1}{2} (\tilde{\underline{r}}_k^i)^T (S_k^i)^{-1} \tilde{\underline{r}}_k^i} \quad (B-7)$$

where  $M$  is the dimension of the residual vector  $\tilde{\underline{r}}_k^i$  and  $|\det S_k^i|$  denotes the absolute value of the determinate of the matrix  $S_k^i$ .

Equation B-6 is used recursively to compute the probability of each hypothesis  $H_i$  for  $i = 1, 2 \dots n$ . It must be initialized at assumed a priori values for the probability of each hypothesis, i.e.,

$$P_{H_i}(0) = P(H_i | (\text{no measurement})) \quad (B-8)$$

for  $i = 1, 2, \dots n$ . Based on  $k$  measurements, the decision procedure involves selecting the model or hypothesis which has the largest probability,  $P_{H_i}(k)$ .

Several comments can be made about the above procedure:

- The technique evaluates each model on the ability of the associated EKF to predict future observations (i.e., it is based upon the one-step prediction residuals)
- The decision procedure is totally objective

- The method provides a direct measure of the confidence levels  $\{P_{H_i}(k)\}$ . Furthermore, the probability calculations are recursive, so that considerable computational savings can be incurred in cases where the algorithm converges rapidly
- The technique treats the multiple hypotheses problem directly
- In dealing with a large-scale system, one can perform preliminary calculations to obtain insight as to the order of the system and thereby reduce the number of models that need be considered. Even with a large number of models, many of the  $P_{H_i}(k)$ 's will quickly converge to zero so that the associated models can be eliminated from consideration immediately
- The development of the extended Kalman filter for the  $i^{\text{th}}$  model is based on the assumption that one can effectively linearize the nonlinear functions about the state estimates  $\{\hat{x}_i\}$ . Little is known about the range of validity of this assumption. However, because of the generally good results that have been obtained with extended Kalman filters, vis-a-vis other methods in parameter identification, it is expected that they will offer a significant improvement for structure identification.

APPENDIX C  
TELEMETRY DATA FROM A GBU-15 FLIGHT TEST

The figures contained in this appendix represent typical telemetry records used as input measurements for the system identification exercise performed with the GBU-15 standoff glide weapon. Data from Segments I, II and III as defined in Section VII are included. Selected records of y- and z-axis accelerometers, pitch, yaw and roll rate gyros, the  $\alpha$ - $\delta$  sensors, and composite pitch, yaw and roll tail deflections are shown. All digitized records are plotted at 19.438 hertz as provided by AFATL with data points connected by straight lines.

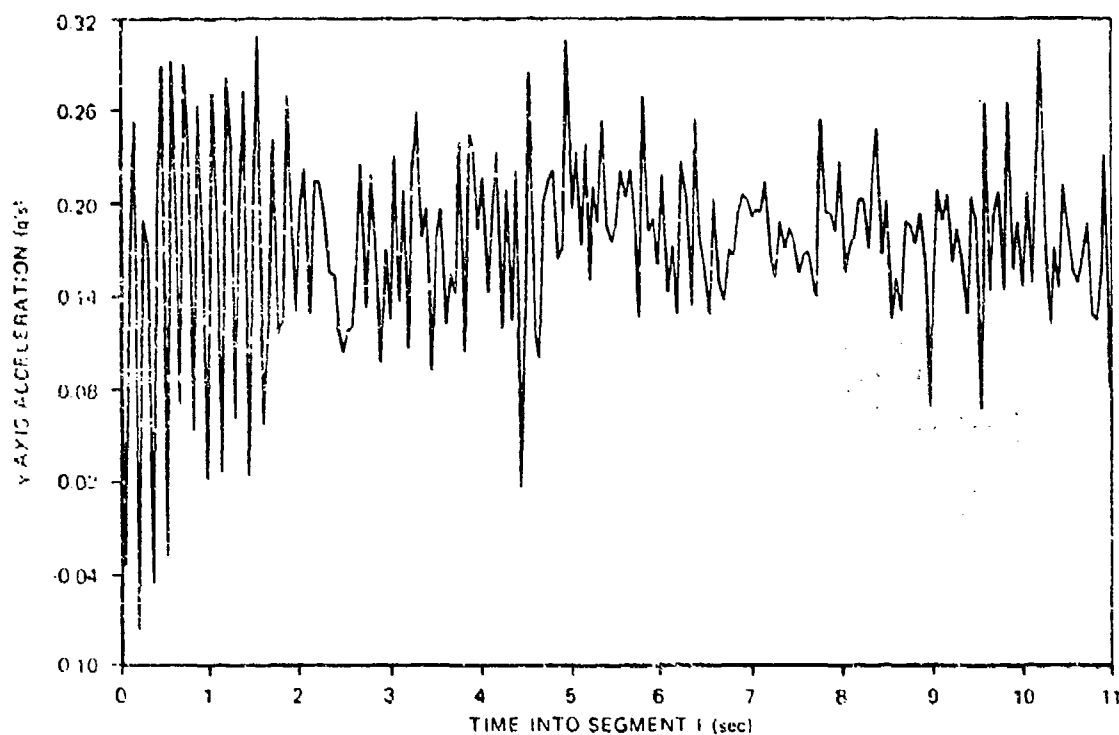


Figure C-1(a). Segment I y-Axis Acceleration

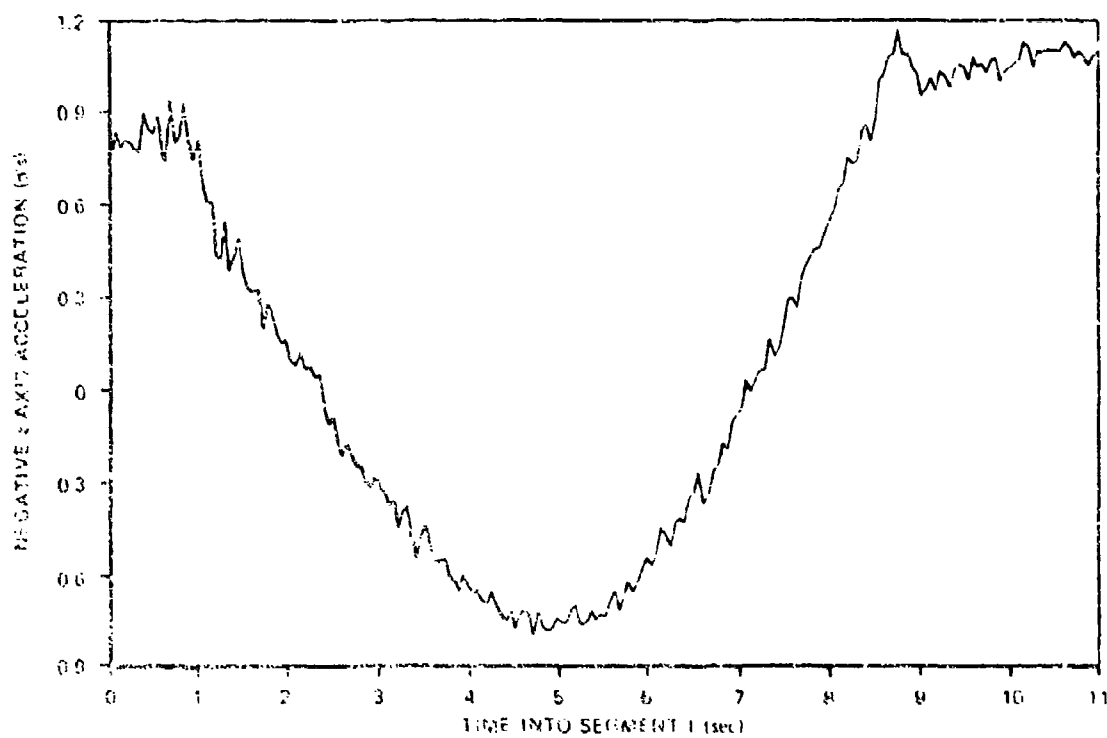


Figure C-1(b). Segment I z-Axis Acceleration

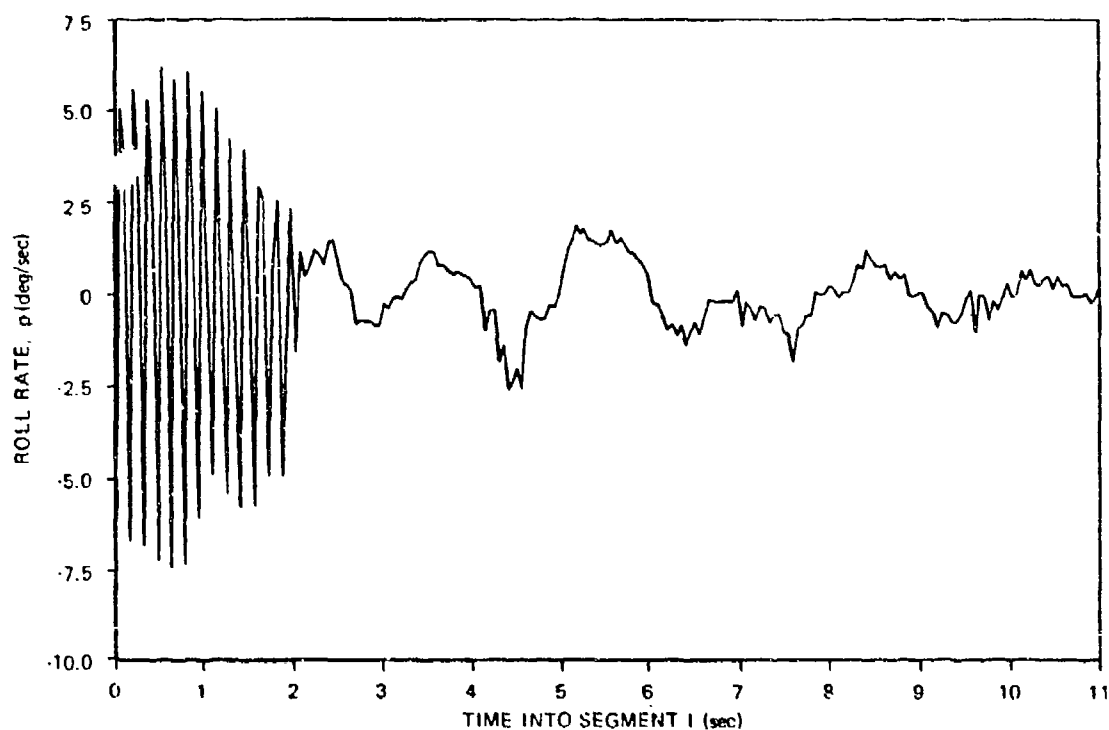


Figure C-1(c). Segment I Roll Rate

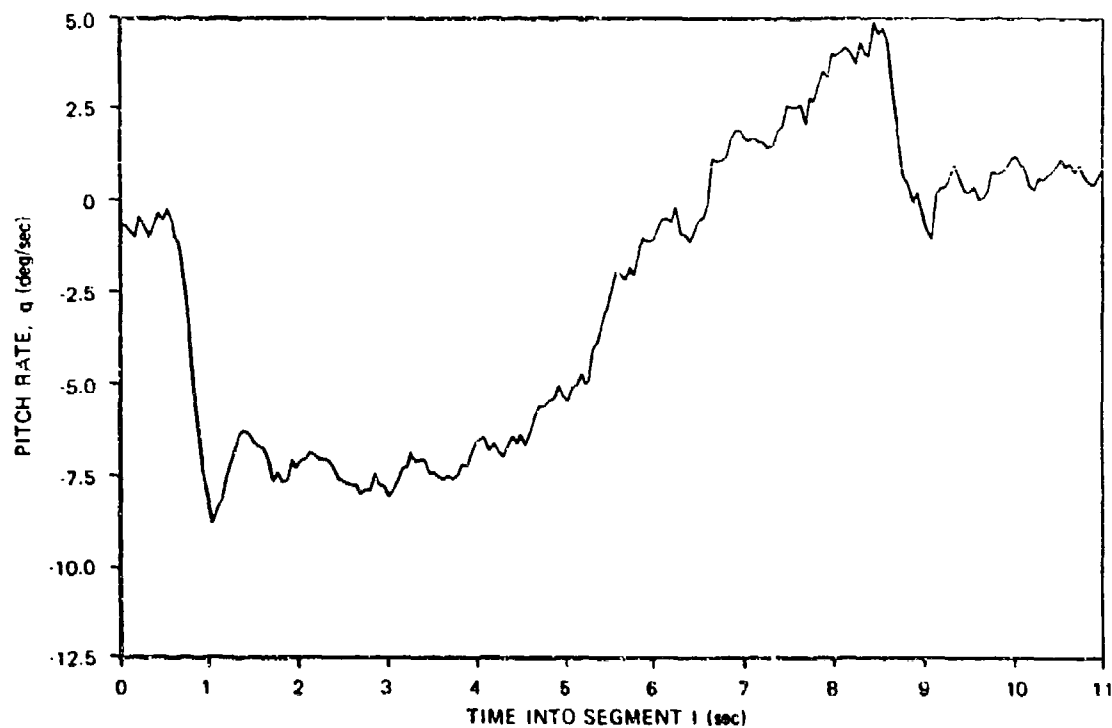


Figure C-1(d). Segment I Pitch Rate

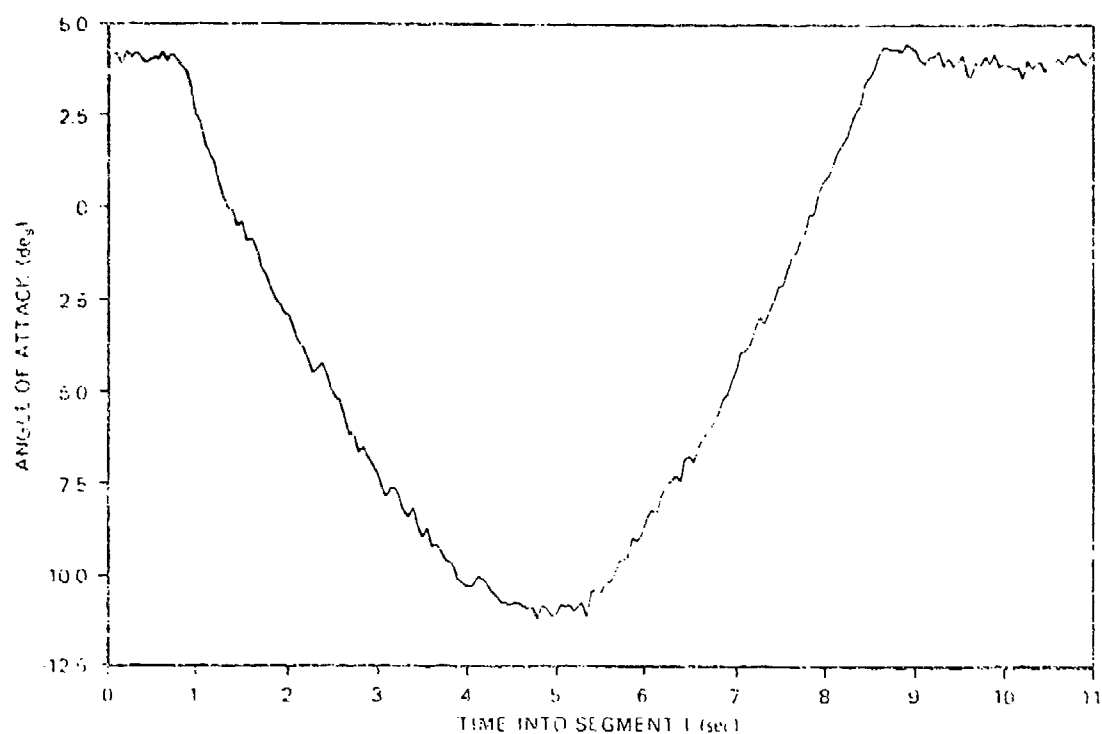


Figure C-1(e). Segment I Angle-of-Attack

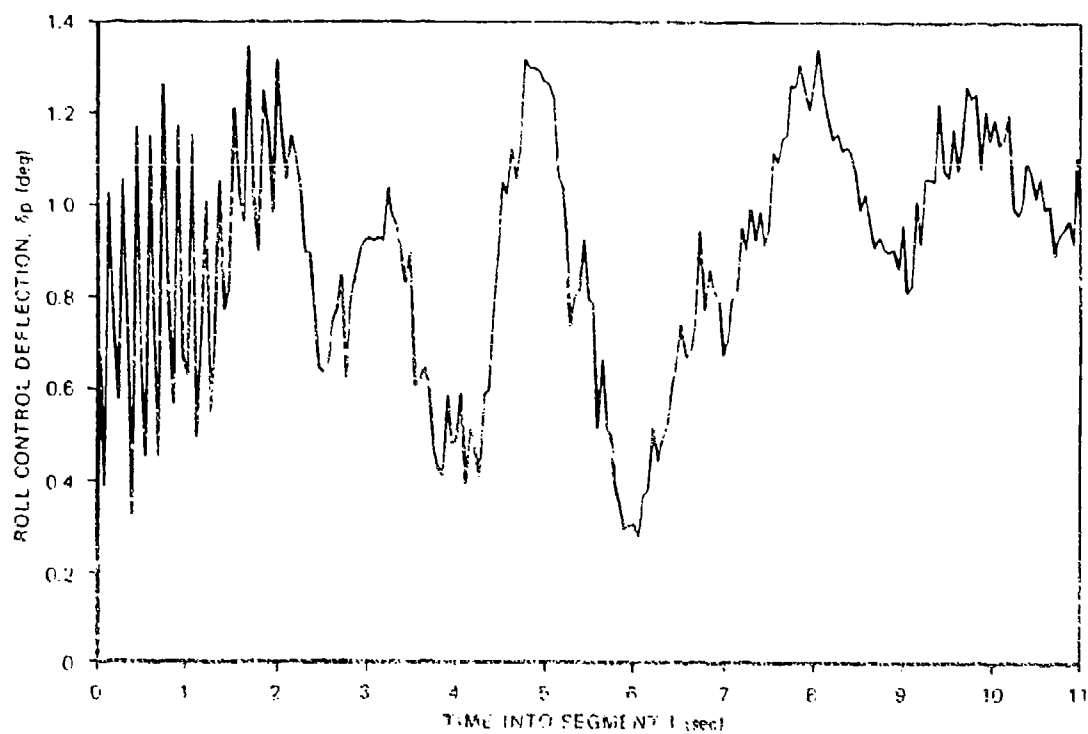


Figure C-1(f). Segment I Roll Control Deflection

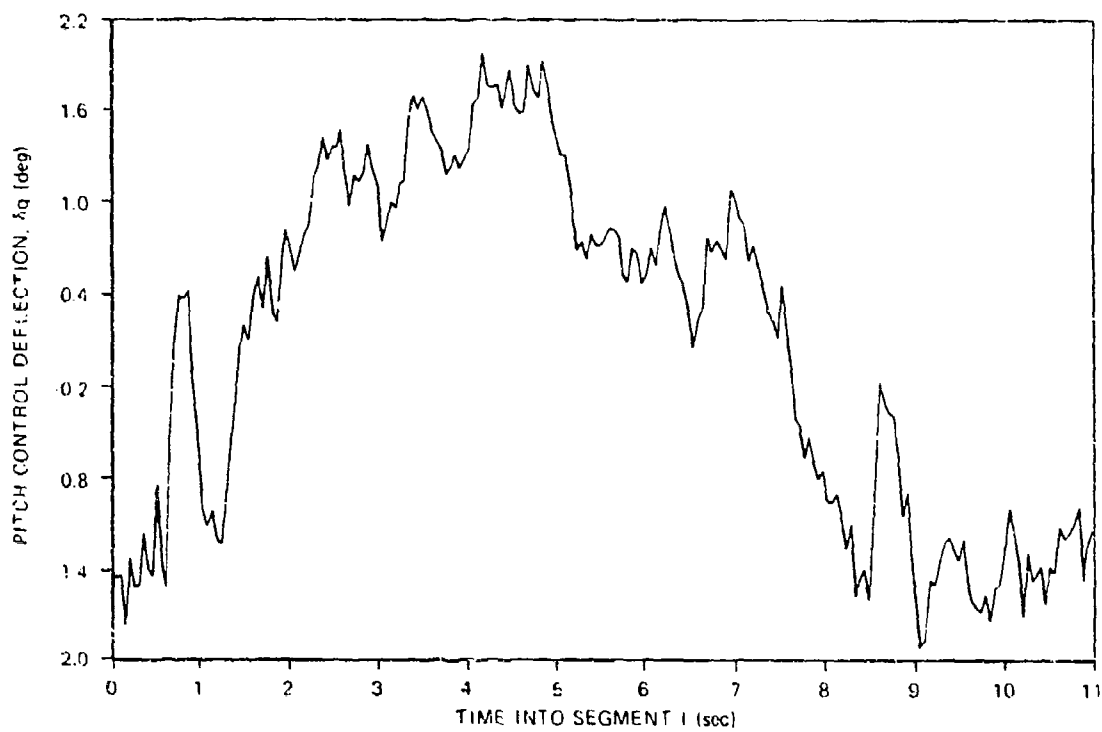


Figure C-1(g). Segment I Pitch Control Deflection



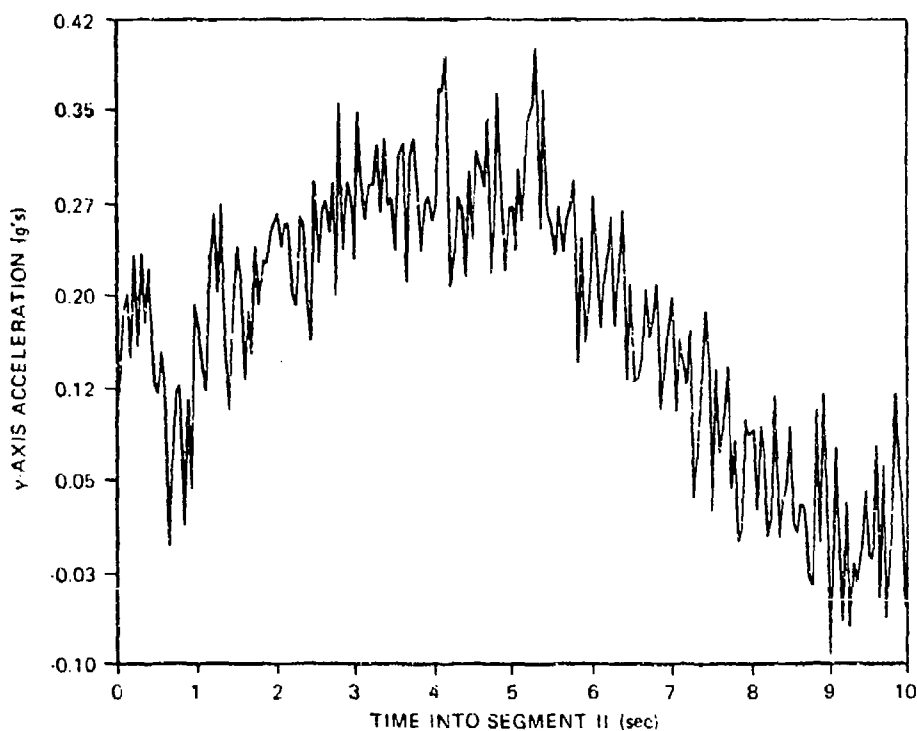


Figure C-2(a). Segment II y-Axis Acceleration

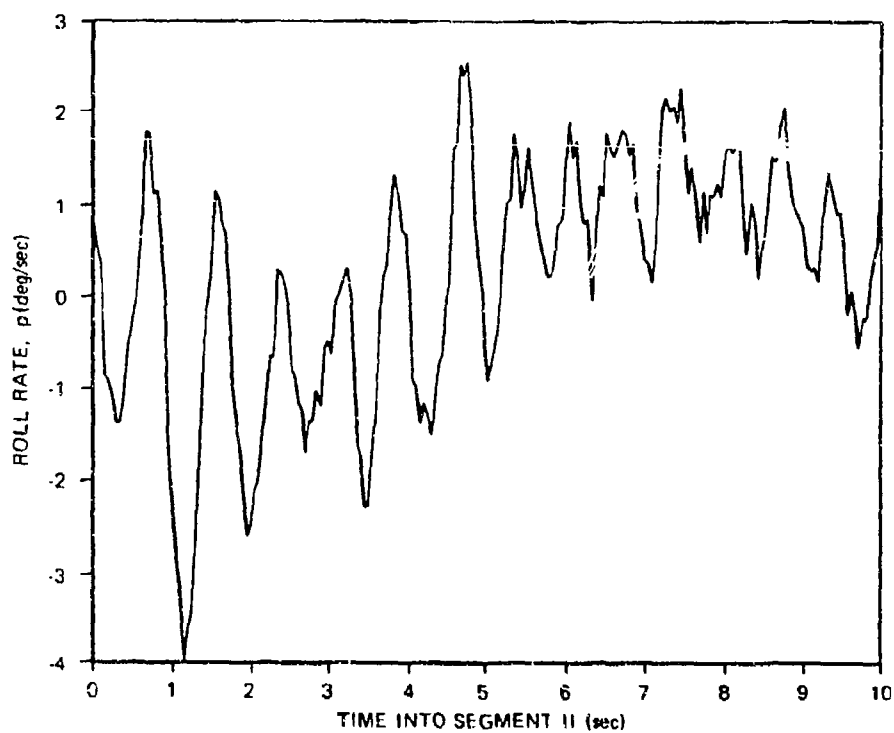


Figure C-2(b). Segment II Roll Rate

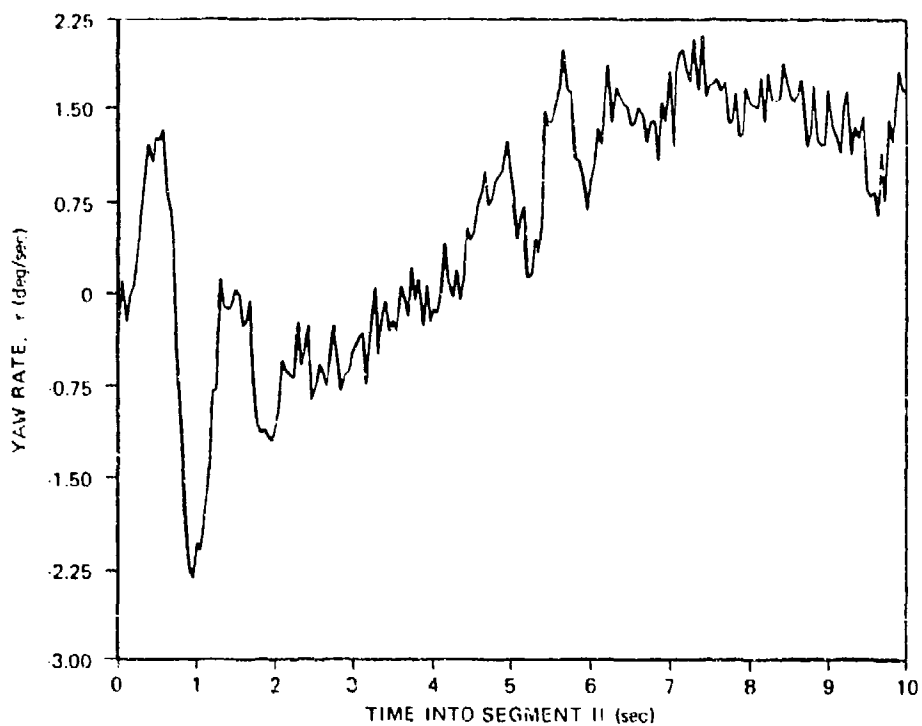


Figure C-2(c). Segment II Yaw Rate

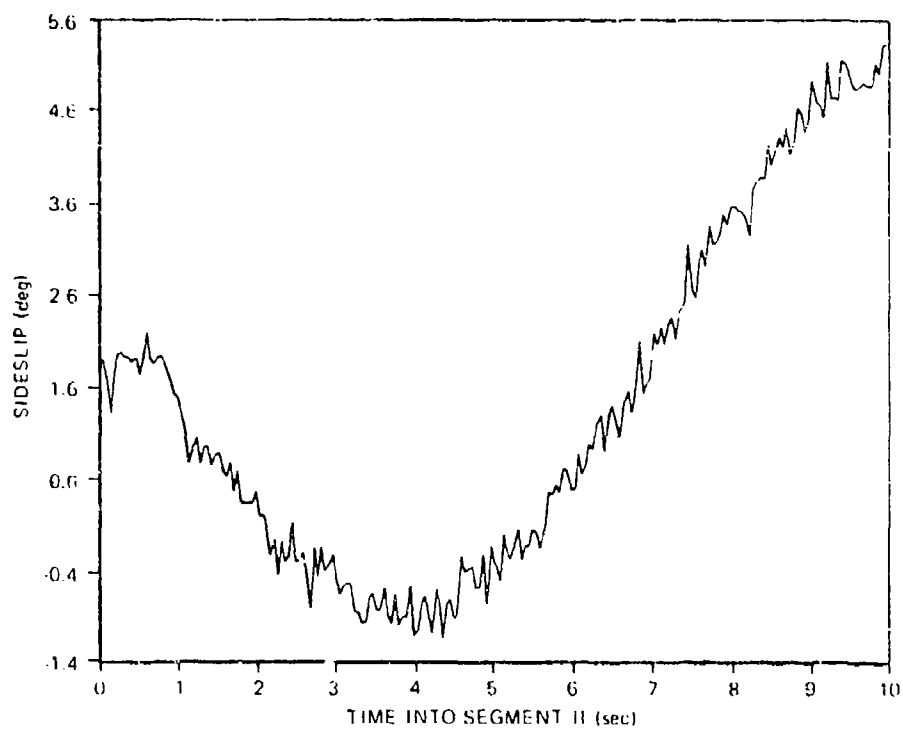


Figure C-2(d). Segment II Sideslip

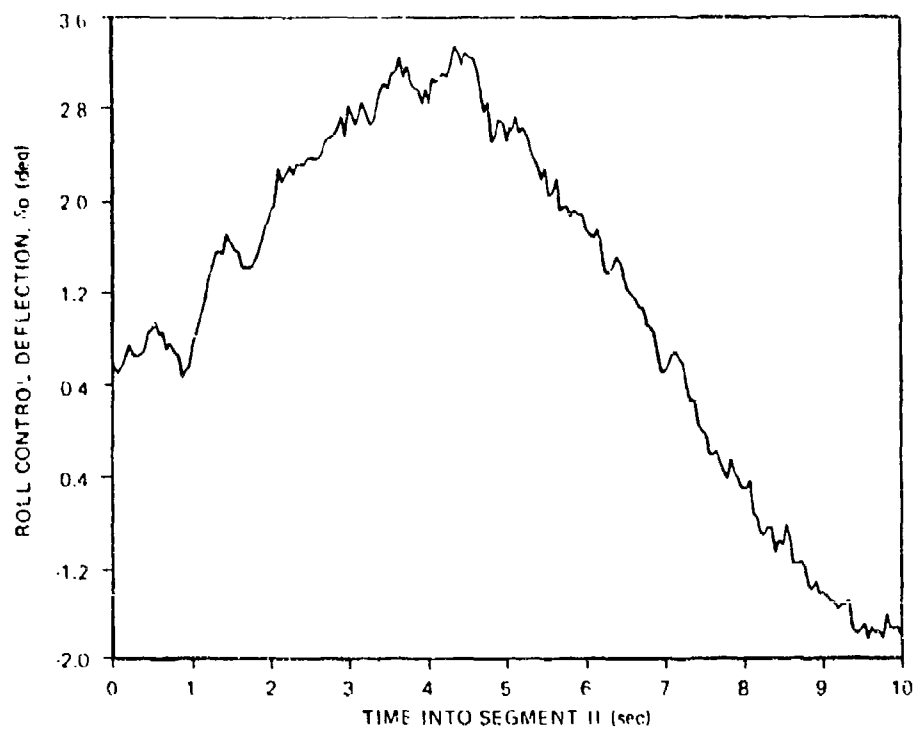


Figure C-2(e). Segment II Roll Control Deflection

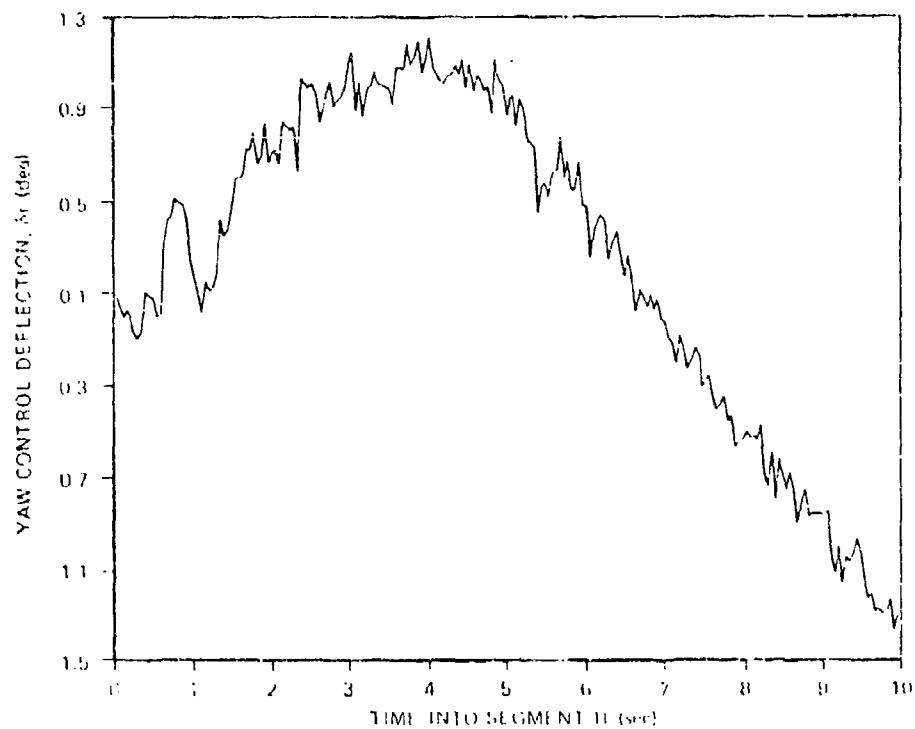


Figure C-2(f). Segment II Yaw Control Deflection

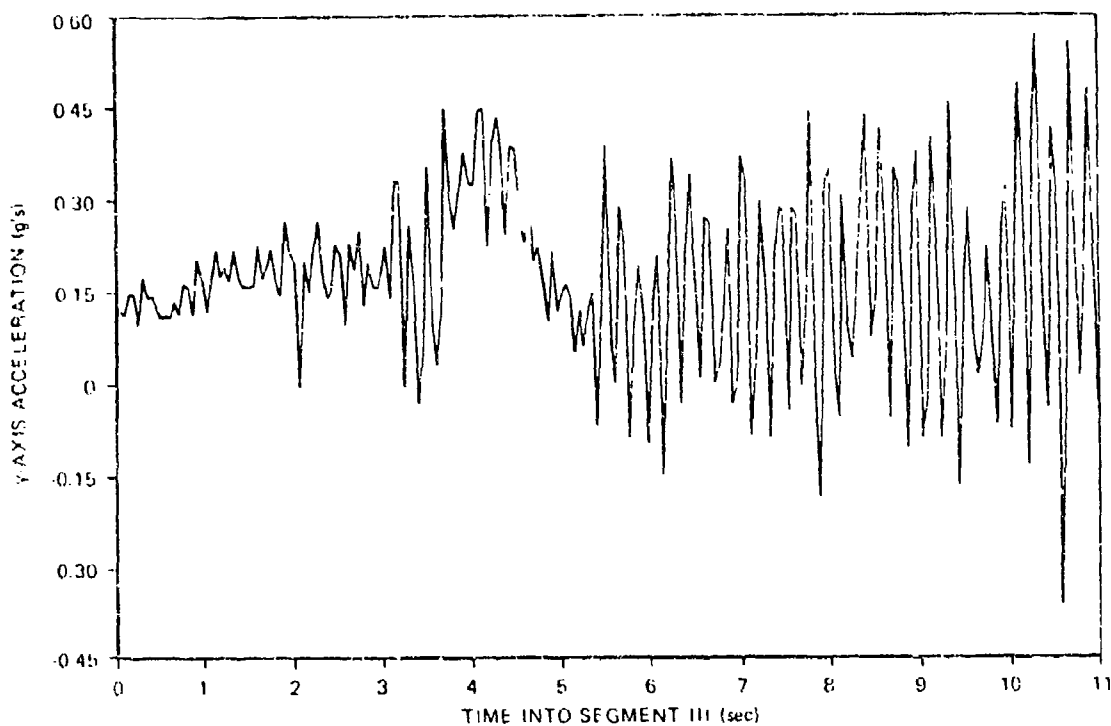


Figure C-3(a). Segment III y-Axis Acceleration

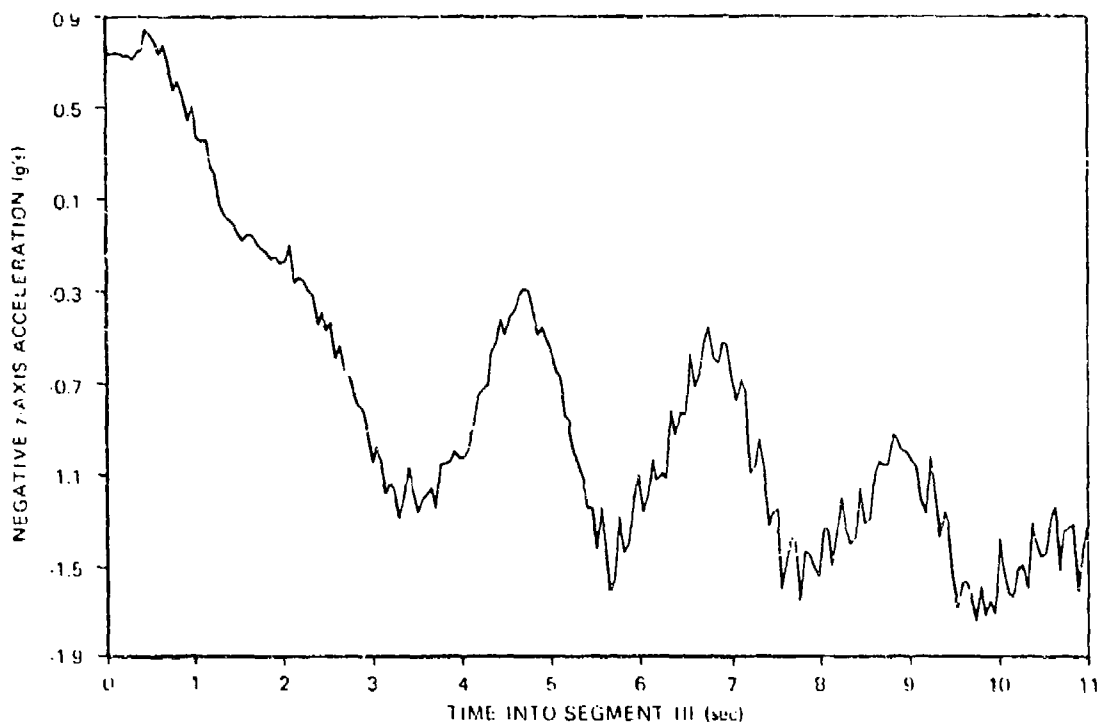


Figure C-3(b). Segment III z-Axis Acceleration

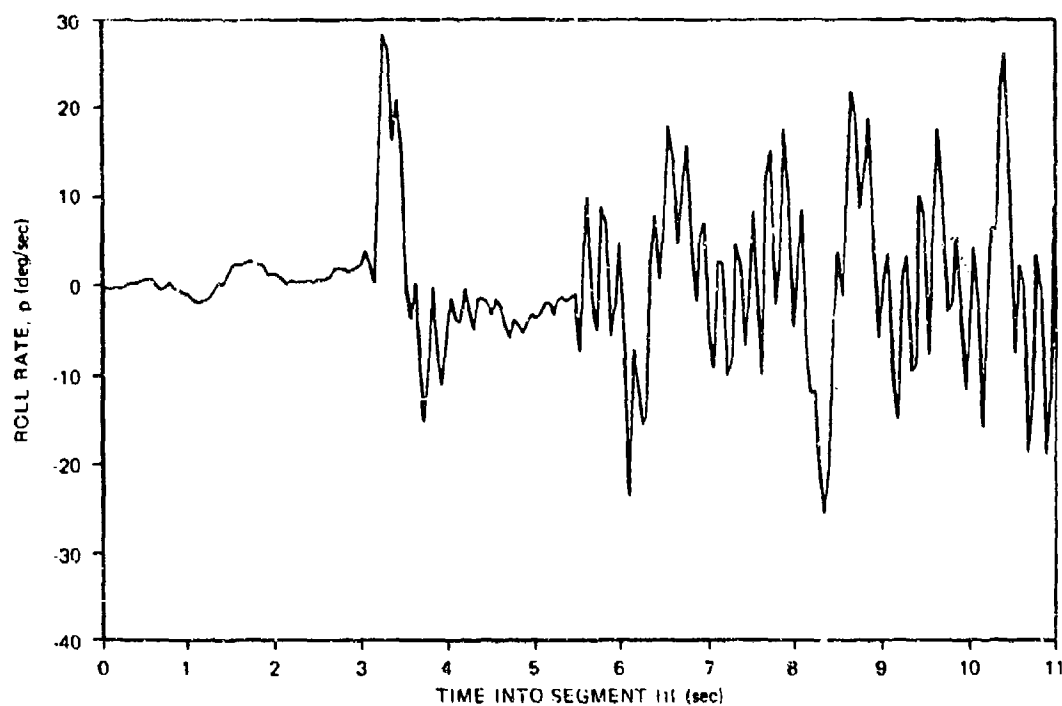


Figure C-3(c). Segment III Roll Rate.

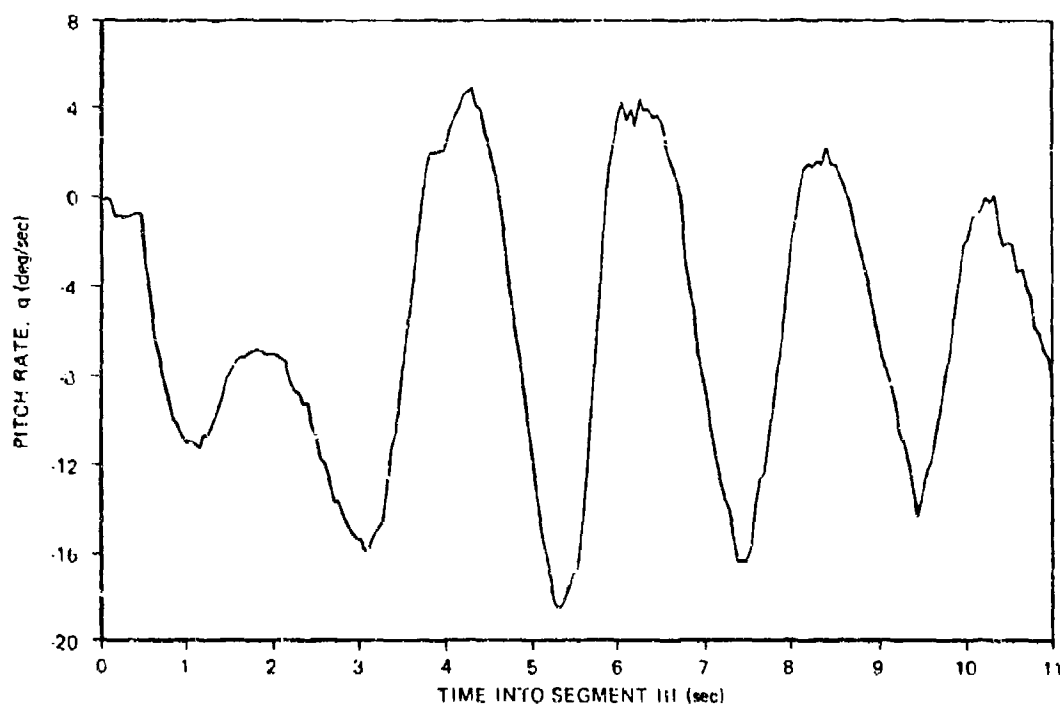


Figure C-3(d). Segment III Pitch Rate

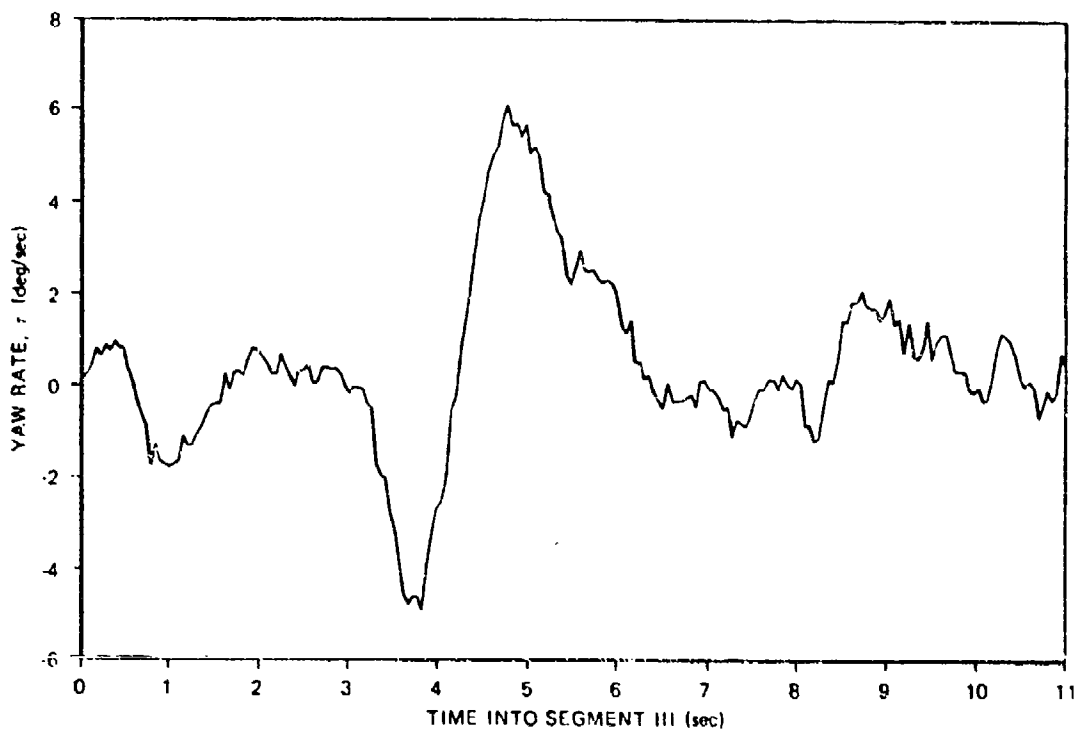


Figure C-3(e). Segment III Yaw Rate

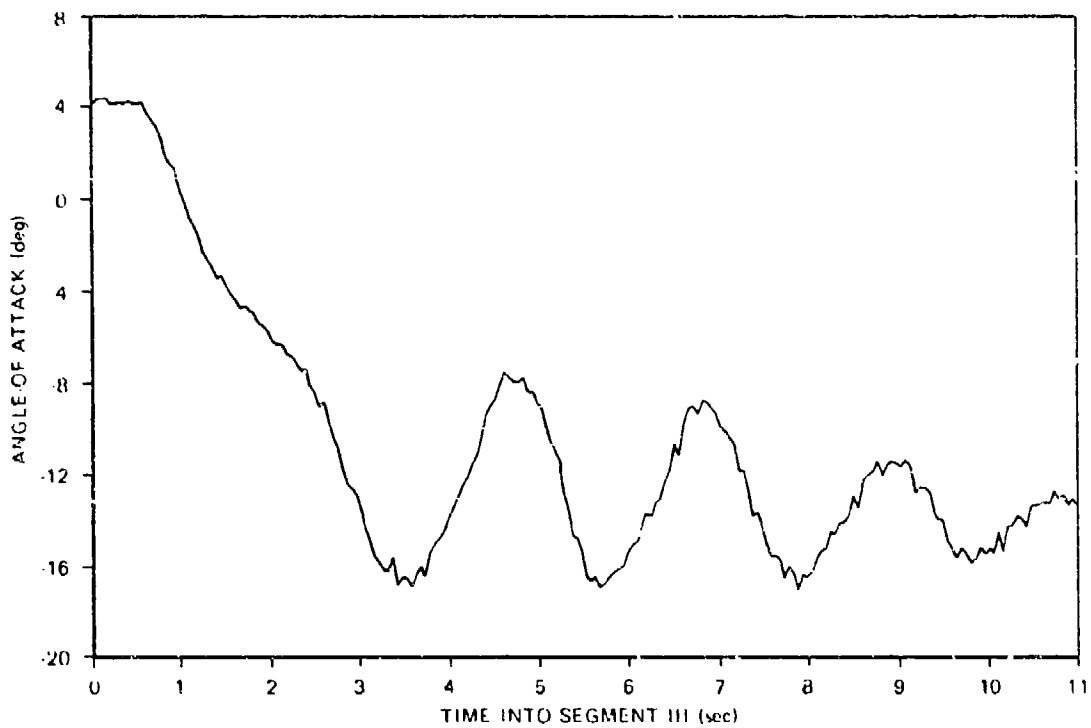


Figure C-3(f). Segment III Angle-of-Attack

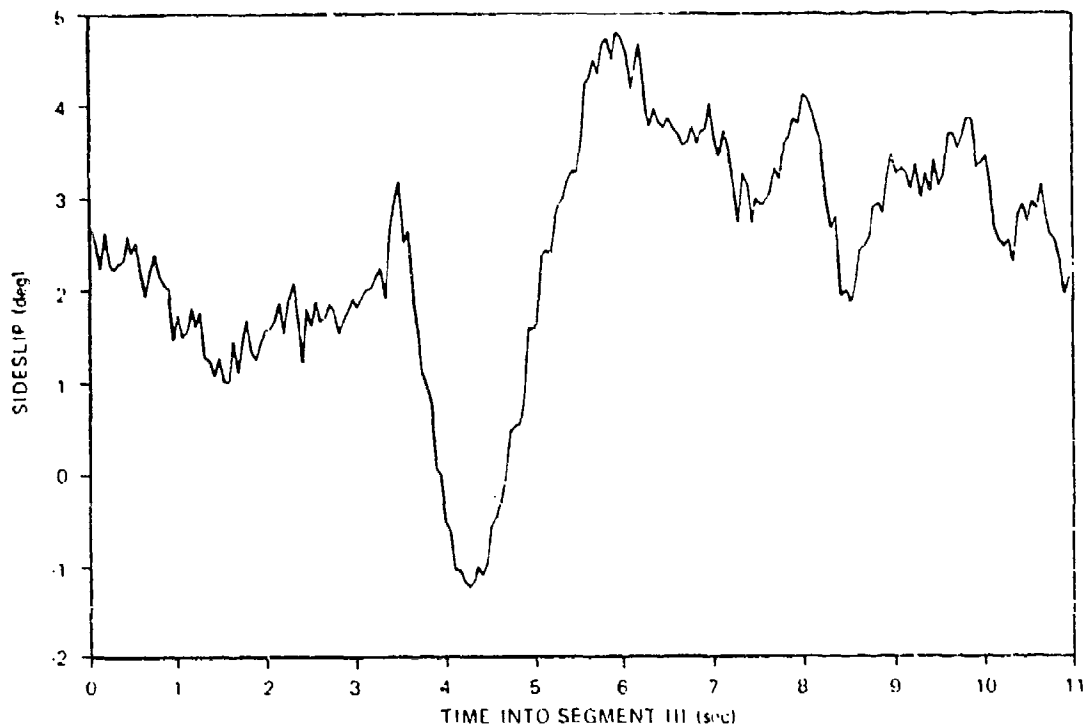


Figure C-3(g). Segment III Sideslip

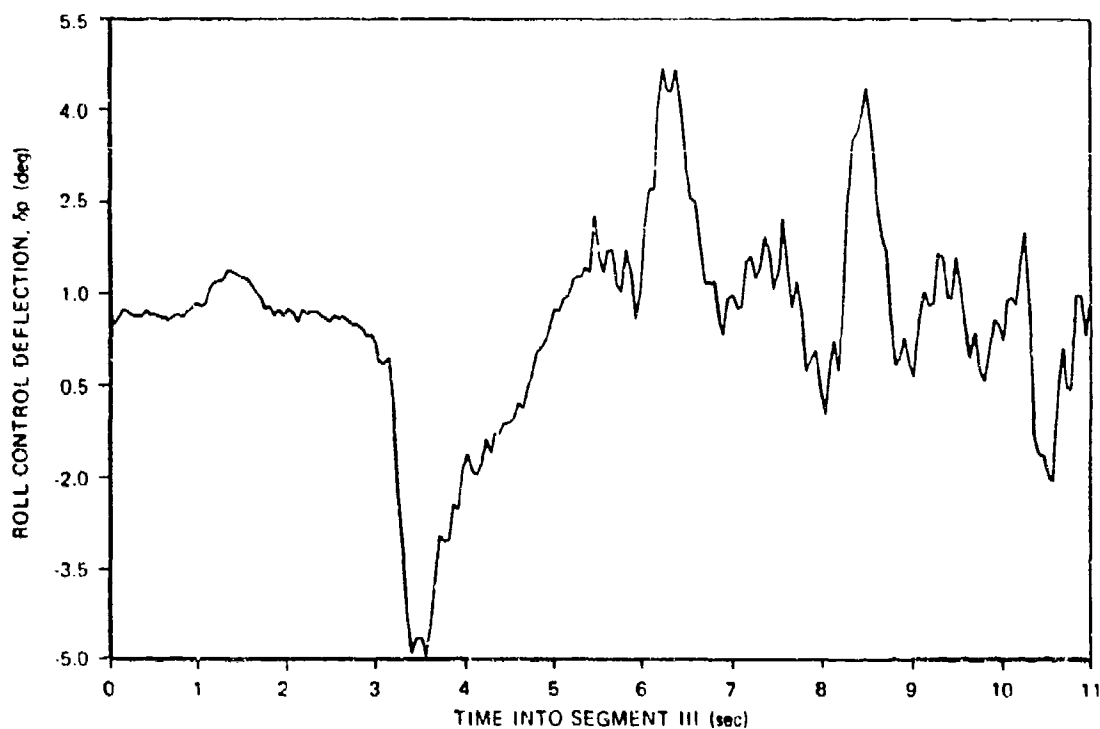


Figure C-3(h). Segment III Roll Control Deflection

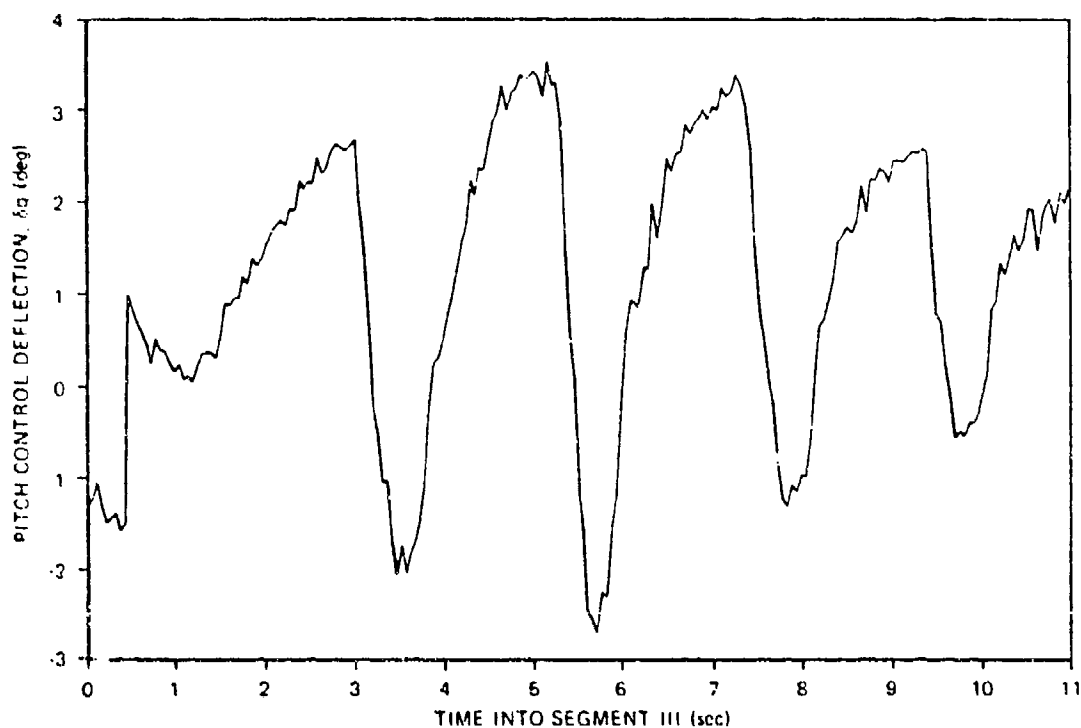


Figure C-3(i). Segment III Pitch Control Deflection

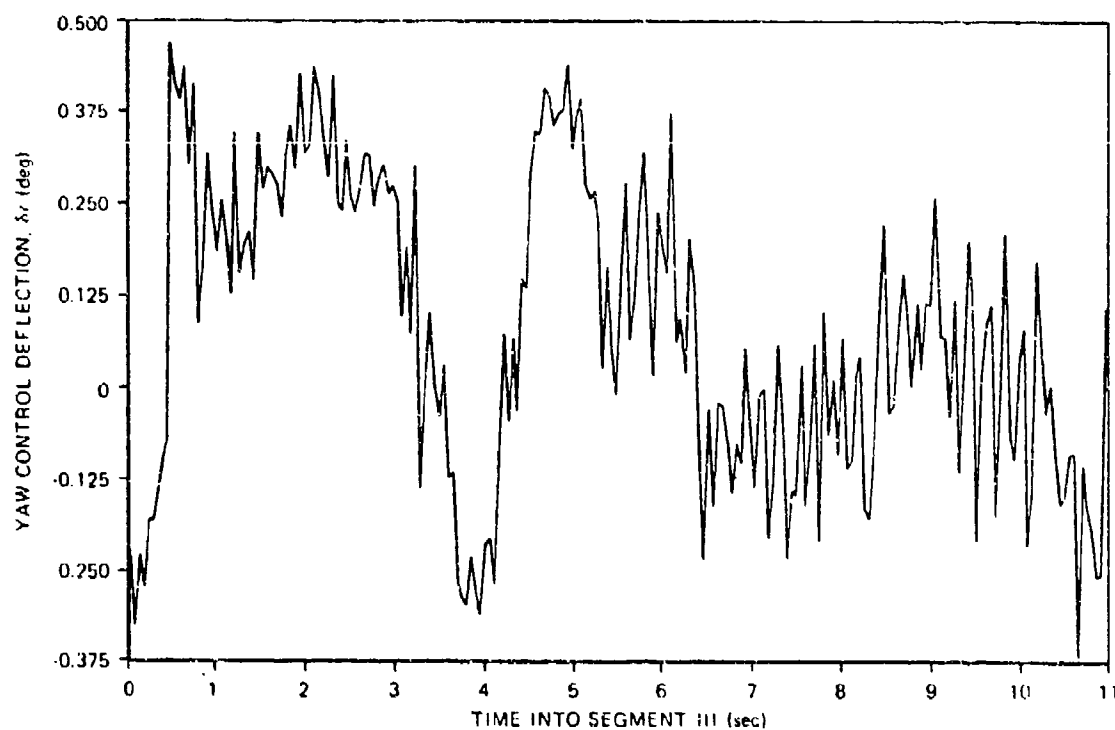


Figure C-3(j). Segment III Yaw Control Deflection



## REFERENCES

1. Symposium on Parameter Estimation Techniques and Applications in Aircraft Flight Testing, Flight Research Center, Edwards, Calif. NASA TN D-7647.
2. Gelb, A., (Ed.), Applied Optimal Estimation, M.I.T. Press, Cambridge, 1974.
3. Zipfel, P.H., "Aerodynamic Symmetry of Aircraft and Guided Missiles," Journal of Spacecraft and Rockets, Vol. 13, No. 7, pp. 470-475, July 1976.
4. Etkin, B., Dynamics of Atmospheric Flight, John Wiley & Sons, New York, 1972.
5. Oberkampf, W.L., Nicolaides, J.D., "Aerodynamics of Finned Missiles at High Angles of Attack," AIAA Journal Vol. 9, No. 12, pp. 2378-2384, December 1971.
6. Platus, D.H., "Dynamic Instability of Finned Missiles Caused by Unbalanced Fin Forces," AIAA Journal, Vol. 9, No. 3, pp. 378-381, March 1971.
7. Smith, L.H., Nonn, R.H., "Aerodynamic Characteristics of an Axisymmetric Body Undergoing a Uniform Pitching Motion," Journal of Spacecraft and Rockets, Vol. 13, No. 1, pp. 8-13, January 1976.
8. MacLanahan, D.A., "Calibration of Angle-of-Attack, Angle-of-Sideslip and Pilot-Static Pressure Sensors on the Modular-Guided Glide Bomb II at Transonic Mach Numbers," Arnold Engineering Development Center, AEDC-TR-75-17, February 1975.
9. Gilyard, G.B., Belte, D., "Flight Determined Lag of Angle-of-Attack and Angle-of-Sideslip Sensors in the YF-12A Airplane from Analysis of Dynamic Maneuvers," NASA-TN-07819, October 1974.
10. Elliot, J.R., "NASA's Advanced Control Law Program for the F-8 Digital Fly-by-Wire Aircraft," Proceedings of the 1976 IEEE Conference on Decision and Control, Paper TA8.45.

# REFERENCES (Continued)

11. Agee, W.S., Tarnse, R.H., "WSMR Best Estimate of Trajectory -- An Overview," Proceedings of the 1972 Army Numerical Analysis Conference, ARO-D, Report No. 72-3.
12. Jarzinski, A.H., Stochastic Processes and Filtering Theory, Academic Press, New York, 1970.
13. Brown, C.M., "An Extended Kalman Filter for Estimating Aerodynamic Coefficients," The Analytic Sciences Corporation, Report No. TR-636-1, December 1976.
14. "Terrestrial Environment (Climatic) Criteria Guidelines for Use in Aerospace Vehicle Development," Marshall Space Flight Center, NASA TM X-64757, July 5, 1973.
15. Koenigsberg, W.D. and Price, F.F., "Adaptive Control With Explicit Parameter Identification for Tactical Missiles," TR-170-3, The Analytic Sciences Corporation, December 1, 1971.
16. Fiske, P.H. and Price, C.F., "A New Approach to Model Structure Identification," Proc. of the AIAA Flight Mechanics Conference, (Hollywood, Fla.), August 1977.
17. Woodside, C.M., "Estimation of the Order of Linear Systems," Proceedings of the 2nd IFAC Symposium on Identification and Process Parameter Estimation, Prague, Paper 1.7, 1970.
18. Chan, C.W., Harris, C.J. and Wellstead, P.E., "Model Order Testing Techniques in Parameter Estimation," Proceedings of the 6th Triennial World Congress of IFAC, August 1975.
19. Chow, J.C., "On Estimating the Order of an Autoregressive Moving-Average Process With Uncertain Observations," IEEE Transactions on Automatic Control, Vol. AC-17, October 1972.
20. Aström, K. J., Bohlin, T. and Wensmark, S., "Automatic Construction of Linear Stochastic Dynamic Models for Stationary Industrial Processes With Random Disturbances Using Operating Records," Technical Paper 18.150, IBM Nordic Laboratory, Stockholm, June 1965.

# REFERENCES (Concluded)

21. <sup>O</sup> Aström, K.J. and Eykhoff, P., "System Identification - A Survey," Automatica, Vol. 7, No. 2, March 1971.
22. Eykhoff, P., System Identification, Wiley & Sons, New York, 1974.
23. Blakelock, J.H., Automatic Control of Aircraft and Missiles, John Wiley & Sons, New York, 1965.
24. Gustavsson, I., Wung, L., Soderstrom, T., "Survey Paper - Identification of Processes in Closed Loop - Identifiability and Accuracy Aspects," Automatica, Vol. 13, March 1976, pp. 59-75.

# INITIAL DISTRIBUTION

HQ USAF/SAMI	1	DARPA/TIO	1
HQ USAF/RDPA	1	NAVAIR SYS CMD/AIR-360E	1
HQ USAF/RDQRM	1	USAF/AFSC LIA CF/CODE 143	6
HQ USAF/XOO	1	NWC/CODE 456	2
AFSC/INA	1	NWC/CODE 533	1
AFSC/SDA	1	NWC/CODE 4063	1
AFSC/DLCAW	2	NWC/CODE 40903	3
AFIS/INTA	1	NWC/CODE 3301	1
AFSC/DPSI	1	NWC/CODE 335	1
AFSC/SDWM	1	REDSTONE SCI INFO CENT	3
TAC/DRA	2	USN WEAPNS LAB	1
TAC/XPSY	1	AMCPM-CT-E	1
AFAL/AA	1	DPC	2
AFAL/PHM	1	CINCPACAF/1GFW	1
AFAL/RWM	1	ADTC/PP	1
AFAL/RW	3	ADTC/TE	1
ASD/YHEV	1	ADTC/XR	2
ASD/XRG	2	SOF/DR	1
ASD/YFEI	1	TAWC/ERW	1
ASD/ENO	1	TAWC/TX	1
ASD/ENYW	1	AFATL/DL	1
ASD/ENA	1	AFATL/DLB	1
ASD/YPEX	1	AFATL/DLMA	13
ASD/AEW	11	AFATL/DLMI	5
ASD/AER	2	AFATL/DLMM	1
ASD/ENFEA	1	AFATL/DLOU	1
ASD/SD	1	AFATL/DLY	2
ASD/SD7	2	AFATL/DLYA	1
ASD/SD5E1	1	AFATL/DLYW	1
ASD/SD27	2	AFATL/DLJ	1
AFFDL/FE	1	AFATL/DLJF	1
AFFDL/FGL	1	AFATL/DLJC	1
AFFDL/FX	1	AFATL/DLJA	1
AFFDL/FY	1	AFATL/DLODL	2
AFML/MX	1	ADTC/SD	1
AFML/LL	1	ADTC/SDM	1
AFML/MB	1	ADTC/SDE	3
AFML/LP	1	ADTC/SD7	3
AFLC/MMWM	1	ASD/SDO	1
OO-ALC/MMWMP	1	ASD/SDM	1
6585 TG/GDP	1	AFFDL/FGC	1
AUL LSE 71-249	1	AFML/LTO	1
ATC/XPQS	1	DEAN USAF ACADEMY	
NAV AIR SYS CMD/AIR-5323	1	SAC/XPHN	2
NAV AIR SYS CMD/AIR-5324	1	SAC/DOXT	1
ODDR&E/TST&E	1	SAC/LGWC	1

AFAL/NVA-679A	2
ASD/SD-65	1
TAWC/TXA	1
FORD AERONUTRONICS DIV	1
ROCKWELL INTERNATIONAL	1
HUGHES AIRCRAFT CO	1
MARTIN-MARIETTA	1
RAND CORP	1
AFRPL/MK	1
RAYTHEON	1
GENERAL DYNAMICS	1
TAC/INA	1
ASD/XRP	1
MASS INST OF TECH	1
HQ USAFE/DOQ	1
USA TRADOC SYS ANA ACT	1
HQ PACAF/DOOFQ	3
COMIPAC/I-232	1
ALPHA RESEARCH INC	1
REDSTONE/CODE DRDMI-TDK	1
PICATINNY ARSENAL	1
US NAV ORD LAB/CODE 312	1
US NAV WPNS LAB/CODE GBJ	1
US NAV WPNS LAB/CODE TI-3	1
NASA AMES RESRCH CEN	1
NASA LANGLEY RESRCH CEN	2
BALLISTICS RESRCH LAB	1
GENERAL ELECTRIC CO	2
SANDIA CORP	1
CALIFORNIA INST OF TECH	1
JOHN HOPKINS U	1